Przemyslaw Bronowicki

Stability of Free Surface Flows in Capillary Channels with Rectangular Cross-Sections

Cuvillier Verlag Göttingen
Internationaler wissenschaftlicher Fachverlag

Stability of Free Surface Flows in Capillary Channels with Rectangular Cross-Sections

Stability of Free Surface Flows in Capillary Channels with Rectangular Cross-Sections

Dem Fachbereich Produktionstechnik
der
UNIVERSITÄT BREMEN

zur Erlangung des Grades
Doktor-Ingenieur
vorgelegte

Dissertation

von
Dipl.-Ing. Przemyslaw Bronowicki

Gutachter:
Prof. Dr.-Ing. habil. Michael Dreyer, Universität Bremen
Prof. Dr.-Ing. habil. Günter Brenn, Technische Universität Graz

Tag der mündlichen Prüfung: 07. Oktober 2016

Bibliografische Information der Deutschen Nationalbibliothek
Die Deutsche Nationalbibliothek verzeichnet diese Publikation in der Deutschen Nationalbibliografie; detaillierte bibliografische Daten sind im Internet über http://dnb.d-nb.de abrufbar.
1. Aufl. - Göttingen: Cuvillier, 2017
Zugl.: Bremen, Univ., Diss., 2016

Nonnenstieg 8, 37075 Göttingen
Telefon: 0551-54724-0
Telefax: 0551-54724-21
www.cuvillier.de

1. Auflage, 2017
Gedruckt auf umweltfreundlichem, säurefreiem Papier aus nachhaltiger Forstwirtschaft

ISBN 978-3-7369-9663-2
eISBN 978-3-7369-8663-3

Zusammenfassung

Diese Arbeit handelt von der erzwungenen Strömung durch teilweise offene Kapillarkanäle unter Schwerelosigkeit. Die untersuchten Kanäle bestehen aus zwei parallelen Glasplatten, welche durch eine oder zwei Flüssigkeitsoberflächen entlang der offenen Seiten begrenzt sind. Die Form des Kanals ähnelt den Kapillarkanälen, wie sie auch in Treibstoffhandhabungs-Systemen von Oberflächenspannungstanks von Satelliten Anwendung finden. Die Krümmung der Oberfläche, die dem Umgebungsdruck ausgesetzt ist, passt sich dem Druckunterschied auf der Grenzfläche entsprechend der YOUNG-LAPLACE-Gleichung an. Die Strömung im Kanal wird instabil, wenn die freie Oberfläche kollabiert und ein Gaseinbruch in die Flüssigkeitsströmung auftritt - ein Prozess der auch als “Choking”-Phänomen bezeichnet wird. Zweiphasenströmungen, die durch die Gasaufnahme verursacht werden, können ungünstig für bestimmte Anwendungen sein. Während der stabilen Strömung ist das Verhalten der freien Oberfläche von den Strömungsbedingungen, geometrischen Eigenschaften des Kanals, den Stoffeigenschaften und dem vordefinierten Systemdruck beeinflusst.

Kapillartechniken mit freien Oberflächen sind ein wichtiger Bestandteil für raumfahrtbezogene und terrestrische Anwendungen. Da sie aus keinen beweglichen Teilen bestehen, sind sie eine sehr verlässliche Methode der Flüssigkeitskontrolle. In dieser Arbeit wird die erzwungene, isotherme und inkompressible Kapillarströmung theoretisch, experimentell und numerisch untersucht. Die zuvor veröffentlichte Stabilitätstheorie wurde einer tiefgreifenden Überprüfung unterzogen. Ein Langzeitexperiment (über 60 Tage) wurde auf der ISS durchgeführt, um die Theorie zu validieren und deren Geltungsbereich in einem multidimensionalen Parameterraum zu bestimmen.

Im theoretischen Teil dieser Arbeit wird ein mathematisches Strömungsmodell, basierend auf dem eindimensionalen Bernoulli-Ansatz, dargestellt. Im Modell wird der Flüssigkeitsdruck in Beziehung zum Kapillardruck über die freie Oberfläche, unter Berücksichtigung beider Krümmungsradien, gesetzt. Das Modell berücksichtigt konvektive und viskose Verluste und zusätzliche Druckverluste, die durch die Veränderung des Geschwindigkeitsprofils im Eintrittsbereich entstehen. Es kann genutzt werden, um die Form des freien Oberflächenprofils für die Strömung unter stabilen Bedingungen vorherzusagen. Die Begrenzung der Strömung wird unter stabilen und zeitabhängigen Bedingungen diskutiert. Das Stabilitätskriterium für die stabile

Strömung basiert auf einem höheren Gradienten des Kapillardrucks im Vergleich zum Gradienten des konvektiven Drucks. Das Kriterium definiert einen kritischen Punkt, ab dem die Gradienten gleich sind und die Krümmung der freien Oberfläche den Druckunterschied an der freien Oberfläche nicht mehr ausgleichen kann. Die instabile Strömung bewirkt einen zusätzlichen Abfall des Volumenstroms aufgrund von Beschleunigungseffekten. Ähnlichkeiten mit der kompressiblen Kanalströmung werden aufgezeigt, bei der die begrenzende Geschwindigkeit von der Schallgeschwindigkeit definiert wird.

Das primäre Ziel des Capillary Channel Flow (CCF) Experiments auf der ISS ist es, die Form der freien Oberfläche und die maximalen Volumenströme, welche im Kanal erreicht werden können, ohne dass die freie Oberfläche kollabiert, zu bestimmen. Zwei Kanalgeometrien werden berücksichtigt: parallele Platten (zwei freie Oberflächen) und die Nut (eine freie Oberfläche). Die Stabilität der freien Oberfläche wird für stabile und instabile Strömungsbedingungen untersucht. Die CCF-Experiment-Ergebnisse werden evaluiert und stimmen mit den numerischen Vorhersagen überein. Eine klare Grenze zwischen stabiler und instabiler Strömung konnte bestimmt werden. Es wird gezeigt, dass das Modell die Form der freien Oberfläche unter verschiedenen Strömungsbedingungen vorhersagen kann. Der kritische Volumenstrom (maximaler Volumenstrom mit stabiler Strömung) wird als eine Funktion der Kanallänge definiert. Die konvektiven und viskosen Effekte beeinflussen die Form der freien Oberfläche. Mit zunehmender Strömungslänge steigt die Deformation der freien Oberfläche. Die dimensionslose Kanallänge $\tilde{l}$ (typisch für Kanalströmungsprobleme) wird für die Klassifikation der Strömungsregime vorgestellt. Darüber hinaus wird der Einfluss der dynamischen Strömungseffekte (Strömungsbeschleunigung) auf die Stabilität der freien Oberfläche untersucht. Die Grenzen der instationären Strömungen werden experimentell bestimmt. Eine gute Übereinstimmung zwischen den experimentellen Daten und dem kürzlich entwickelten Strömungsstabilitätsmodell wird ebenso dargestellt.

Zwei numerische Methoden werden verwendet, um das Kapillarkanal-Strömungs-Problem zu lösen. Die erste Methode ist ein eindimensionaler Code ccFlow (Eigenentwicklung), der auf dem mathematischen Strömungsmodell basiert. Die zweite Methode ist der dreidimensionale CFD-Code OpenFOAM (open source). Beide Instrumente lösen die stabilen und instabilen Probleme und liefern zufriedenstellende Ergebnisse. Die mit ccFlow vorhergesagte Stabilitätsgrenze (für “kleine” Kanallängen) ist jedoch im Vergleich zu den Daten aus dem Experiment überschätzt. Das mathematische Modell wird für einen großen Bereich von geometrischen Konfigurationen und Parametern validiert. Eine breite parametrische Studie mit ccFlow wird durchgeführt, um das mathematische Modell zu nutzen, und das allgemeine Verhalten der freien Oberflächen in Kapillarkanälen wird erforscht. Studien werden sowohl bezogen auf viskose und konvektive Strömungsbedingungen als auch für den Übergang zwischen den beiden Regimen durchgeführt. Schließlich wird gezeigt, dass der Druckverlust und die Strömungsentwicklung

im Eintrittsbereich des CCF Setups mit OpenFOAM dreidimensional modelliert werden kann, inklusive der Aspekte, die über die Möglichkeiten der experimentellen Messtechniken hinausgehen. Diese Modellierung wird für die Bestimmung der Randbedingungen, die erforderlich sind, um das eindimensionale mathematische Strömungsmodell zu lösen, genutzt.

Summary

This work is concerned with forced flow through partially open capillary channels under microgravity conditions. The investigated channels consist of two parallel glass plates and are bounded by either one or two free liquid surfaces along the open sides. The shape of the channel resembles the capillary vanes used in propellant management devices, commonly applied in satellite surface tension tanks. The curvature of the channel's gas-liquid interface, which is exposed to the ambient pressure, adjusts to the pressure difference across the interface in accordance with the YOUNG-LAPLACE equation. The flow within the channel becomes unstable when the free surface collapses and gas ingestion into the flow path occurs - a process that is also referred to as the "choking" phenomenon. Two-phase flow caused by the gas ingestion might be unfavorable for certain applications. During stable flow the behavior of the free surface is influenced by flow conditions, geometric properties of the channel, liquid properties and the pre-defined system pressure.

Capillary techniques with free liquid surfaces are an important element for space and terrestrial applications. Having no moving parts, they provide a very reliable method of liquid control. In this work, forced, isothermal, and incompressible capillary channel flow has been studied theoretically, experimentally, and numerically. A previously published stability theory has awaited a profound verification. A long-time experiment (over 60 days) aboard the International Space Station (ISS) was performed in order to validate the theory and probe limits within a multidimensional parameter space.

In the theoretical part of this work, a mathematical flow model based on the one-dimensional Bernoulli approach is outlined. In the model, the liquid pressure is related to the capillary pressure at the free surface including both principal radii of curvature. The model considers convective and viscous losses, and additional pressure loss due to the change of the velocity profile in the entrance region. It can be used to predict the shape of the free surface profile for the flow under stable conditions. The limitation of the flow is discussed for steady and time-dependent flow. The stability criterion for steady flow is based on a higher gradient of the capillary pressure in comparison to the gradient of the convective pressure. The criterion defines a critical point where the gradients are equal and the curvature of the free surface fails to balance the pressure difference across the gas-liquid interface. Unsteady flow yields an additional

decrease of the flow rate limit due to acceleration flow effects. Similarities with compressible duct flow are shown, where the limiting velocity is defined with the speed of sound.

The main goal of the Capillary Channel Flow (CCF) experiment aboard the ISS is to determine the shape of the free surfaces and the maximum flow rates which may be achieved in the channel without a collapse of the free surface. Two channel configurations are considered: parallel plates (two free liquid surfaces) and a groove (one free liquid surface). The stability of the free surface is investigated for steady and unsteady flow regimes. The CCF experiment results are evaluated and are found to agree well with numerical predictions. A clear limit is determined between stable and unstable flows. It is shown that the model can predict the shape of the free surface under various flow conditions. The critical flow rate (maximum flow rate resulting in the stable flow) is found to be a function of the channel length. The convective and viscous flow effects influence the shape of the free surface. With increasing flow length the deformation of the free surface increases. The dimensionless channel length $\tilde{l}$ (typical for duct flow problems) is introduced for the classification of the flow regimes. Furthermore, the influence of the dynamic flow effects (flow acceleration) on the stability of the free surface is investigated. The limits of transient flows are determined experimentally. Furthermore, a good agreement between the experimental data and recently developed transient flow stability model is shown.

Two numerical methods are employed to solve the capillary flow problem. The first method is a one-dimensional code ccFlow (in house developed) based on the mathematical flow model. The second method is the three-dimensional CFD code OpenFOAM (open source). Both tools solve the steady and unsteady problems and deliver satisfactory results. The stability limit estimated with ccFlow is however (for "small" channel lengths) overestimated compared to the data from experiment. The validity of the mathematical model is confirmed for a wide range of geometrical configurations and parameters. A broad parametric study with ccFlow is performed in order to exploit the mathematical model, and the general behavior of free surfaces in capillary channels is studied. Studies are conducted in both viscous and convective flow regimes and in the transition area between the two. Finally, it is shown that the pressure loss and the flow development in the entrance section of the CCF setup can be modeled three-dimensionally with OpenFOAM covering the aspects, which are beyond the capabilities of the experimental measurement techniques. Such modeling is utilized for the determination of the boundary conditions required to solve the one-dimensional mathematical flow model.

Preamble

The work described in this thesis was performed during my employment at the Center of Applied Space Technology and Microgravity (ZARM) at the University of Bremen in the years 2011 to 2015.

First of all I would like to express my gratitude to the head of the Multiphase Flow group at ZARM, Prof. Dr.-Ing. habil. Michael Dreyer, who gave me the possibility to perform this work. I would like to extend my gratitude to my colleagues who were involved in the CCF Project: Peter Canfield for the great cooperation and positive office atmosphere, Dr. Aleksander Grah for the comments regarding this manuscript and general support, and Dr. Yongkang Chen for the great cooperation during his time at ZARM. The support provided by Prof. Mark Weislogel during the preparation phases of the CCF experiment and during the operation is highly appreciated. I also wish to thank Ryan Jenson, William Blackmore, Dr. Jörg Klatte, and Lars Kiewidt who contributed to the CCF data collection.

Furthermore, I would like to thank my colleagues for the great time at work (and after): Ronald Mairose, Peter Prengel, Holger Faust, Frank Ciecior, Dr. Yvonne Chen, Diana Gaulke, Sebastian Schmitt, Willy Raider, Yulia Grebenyuk, André Pingel, Peter Friese and Zelimir Marojevic. I appreciate the involvement of Yulia Smiyukha especially during the preparation of the CCF online database. Special thanks to Stephanie Dackow for taking care of organizational matters and to my sister Aga for final readings. I acknowledge the DLR for funding the CCF experiment under grant No. 50WM1145.

Finally, I would like to express my gratitude to my lovely wife Christina for continuous support and patience especially during the last months of finalizing this manuscript. To my little boys, Henri David and Jakob Felix, whose smile encouraged me to keep going. *Kocham Was bardzo. Żadna praca ani projekt nie dały mi w życiu tyle radości co czas spedzony z Wami.*[1]

---

[1] I love you very much. There is no project or job that has given me so much joy as the time spent with you.

Contents

List of Symbols

Some variables exist in both dimensional and non-dimensional (scaled) form. A dimensional variable is marked with a prime ('). Dimensional variables required for the solution of flow model equations are non-dimensionalized according to scaling details given in Table 3.1.

Latin Lower Case Letters

a	gap distance of the channel		m
b	width of the channel		m
c'	area wave propagation velocity		m/s
d'	displacement of the free surface		m
f	flexibility function		
f_D	Darcy friction factor		
f_∞	flexibility coefficient		
g	gravitational acceleration	(g_x,g_y,g_z)	$\mathrm{m/s^2, m/s^2, m/s^2}$
h'	twice the mean curvature		$\mathrm{m^{-1}}$
k'	contour of the free surface		m
k'_{min}	minimum contour point		m
l'	length of the channel		m
l'_c	capillary length	$\sqrt{\sigma/(\rho g)}$	m
l_f	length of the FS in the vicinity of the inlet		
l_{f0}	length of the FS in the vicinity of the outlet		
l_0	length of the liquid column		
p'	liquid pressure		$\mathrm{kg/(m\ s^2)}$
p'_a	ambient pressure		$\mathrm{kg/(m\ s^2)}$
p_c	characteristic pressure	$2\sigma/a$	$\mathrm{kg/(m\ s^2)}$
r	feedback ratio		
r_t	diameter of the circular tube		m
s	standard deviation		
t'	time		s
s'_0	virtual channel length		m

v'	flow velocity		m/s
v_c	characteristic velocity	$\sqrt{2\sigma/(\rho a)}$	m/s
v_{ca}	capillary wave velocity		
x', y', z'	coordinates		m

Latin Upper Case Letters

A'	cross-sectional area		m^2
A'_c	area of the circular segment		m^2
A'_{cs}	area of the circular sector		m^2
A'_{tp}	area of the triangular portion		m^2
A_0	inlet/outlet area	ab	m^2
C_f	fanning friction factor		
D	dynamic index		
D_h	hydraulic diameter	$4A_0/P'$	
D_h^{GR}	hydraulic diameter for groove	$4ab/(a+2b)$	
D_h^{PP}	hydraulic diameter for parallel plates	$2a$	
D_h^{rc}	hydraulic diameter for rectangular channels	$2ab/(a+2b)$	
F_σ	surface tension force		$(\mathrm{kg\ m})/\mathrm{s}^2$
H'	mean curvature		m^{-1}
$\mathcal{H}$	curvature contribution		
$K_{c,\tau}$	friction coefficients		
K_f	pressure loss coefficient		
K_{Pf}	pressure loss coefficient for developed flow		
K_{Sf}	pressure loss coefficient for developing flow		
K_0	system pressure coefficient		
$K_{1,2,3}$	pressure loss coefficients (ccFlow nomenclature)		
L'_i	characteristic length		m
$L_{0,1}$	entrance factors		
P'	wetted perimeter		m
Q'	flow rate		m^3/s
Q'_c	critical flow rate		m^3/s
Q'_o	initial flow rate		m^3/s
R'	curvature radius in y, z-plane		m
R'_{CT}	radius of the compensation tube		m
$R'_{1,2}$	principal radii of curvature		m

S_{ca}	capillary speed index	
T'	temperature	°C
$\vec{U}$	velocity field vector	m/s
V'_c	calibration coefficient	m^3
V'_{cell}	volume of computational cell	m^3
V'_g	volume of gas in the PSC	m^3
V'_{vol}	volume of fluid	m^3

Greek Letters

α	first flow development coefficient	
α^{OF}	volume fraction	
β	second flow development coefficient	
γ	flow development ratio	
δ'	flow acceleration	$\mathrm{m}^3/\mathrm{s}^2$
δ'_c	critical flow acceleration	$\mathrm{m}^3/\mathrm{s}^2$
δ'_0	transient stability constant	$\mathrm{m}^3/\mathrm{s}^2$
η	contact angle	
θ	rotational angle	
μ	dynamic fluid viscosity	kg/(m s)
ν	kinematic fluid viscosity	m^2/s
ρ	fluid density	kg/m^3
σ	surface tension	kg/s^2
τ	viscous stress tensor	N/m^2
φ	angle of the circular segment	
χ	convective pressure	
Ψ	viscous contribution	

Dimensionless Numbers and Length Ratios

Bo	BOND number	$\rho g_i a L_i/\sigma$
Oh	OHNESORGE number	$\sqrt{\rho\nu^2/\sigma 2a}$
Po	POISEUILLE number	$\mathrm{Po} = C_f\mathrm{Re}$
Re	REYNOLDS number	$v' D_h/\nu$
$\tilde{l}$	dimensionless flow length	$\mathrm{Oh} l'/2D_h$
Γ	length aspect ratio	$D_h/(4l')$
Λ	aspect ratio	b/a

Sub- and Superscripts

a_0	inlet value at $x = 0$
a_1	outlet value at $x = 1$
a_a,a_g	value for ambient gas
a_l	value for liquid
a_{min}	minimum value
a_{max}	maximum value
a'	dimensional variable
a^*	value at minimal interface height
a^+	value at the equilibrium point
a^{an}	analytic solution
a^{EXP}	experimental value
a^{GR}	value for groove
a^{PP}	value for parallel plates
a^{var}	varied value
a^t	value for circular tube
a^{rc}	value for rectangular channel

Abbreviations

1D	One-dimensional
3D	Three-dimensional
CT	Compensation Tube
CCF	Capillary Channel Flow
CFD	Computational Fluid Dynamics
CFE	Capillary Flow Experiment
DT	Drop Tower
DLR	German Aerospace Center
EXP	Experimental
FS	Free Surface
FPC	Flow Preparation Chamber
FPS/Fps	Frames Per Second
GR	Groove
HSHRC	High Speed High Resolution Camera
ISS	International Space Station
MSG	Microgravity Science Glovebox
NASA	National Aeronautics and Space Administration
PMD	Propellant Management Device
PP	Parallel Plates
PSC	Phase Separation Chamber
PSU	Portland State University
VOF	Volume of Fluid
ZARM	Center of Applied Space Technology and Microgravity

Chapter 1

Introduction

Fluid management in compensated gravity environment is an important aspect of current and future space missions. The knowledge of liquid behavior in microgravity is essential for the development of space applications such as fluid management devices, life support systems or heat pipes. The simplicity, reliability and efficiency are here the key factors. Capillary techniques with free liquid surfaces are therefore an important element of fluid management in space. Having no moving parts, they provide a very reliable method of liquid control. Such devices are commonly two-phase systems, where free liquid surfaces are exposed to the gaseous phase. Hydrostatic pressure is negligible under microgravity conditions, and the influence of other forces dominates the behavior of the gas-liquid interfaces.

Typical applications are propellant management devices (PMDs) employed in satellite surface tension tanks (Figure 1.1). Propellant tanks are commonly spherical structures made of titan [65], where the ullage volume of withdrawn propellant is replaced by gas.

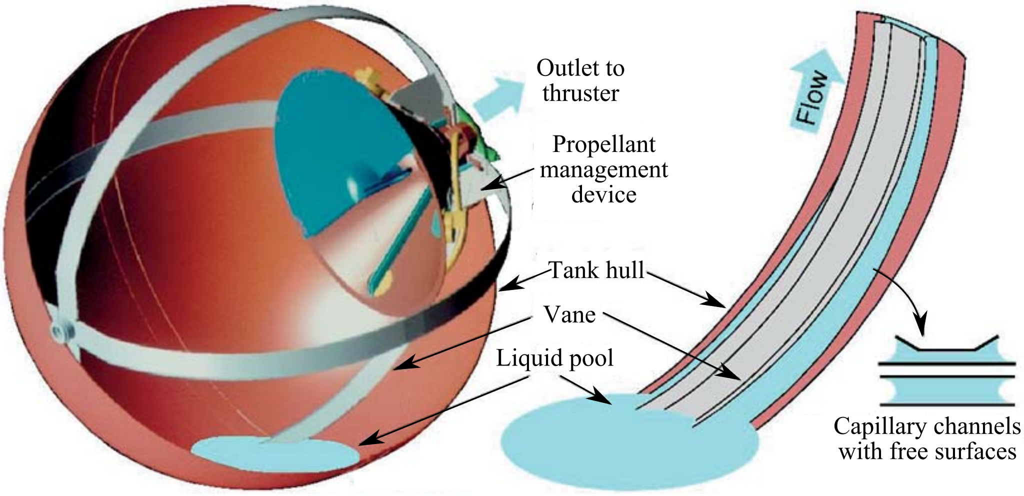

Figure 1.1: Satellite surface tension tank with a PMD consisting of capillary vanes.

The remaining propellant forms a bulk which is free to move within the tank depending on the spacecraft manoeuver. A continuous, bubble-free flow between the propellant bulk and an outlet to the thruster is required during the entire manoeuver phase. To achieve this, the tanks are equipped with propellant management devices. Because of chemical properties (aggressiveness) of the propellants, the choice of materials that can be used for the inner structure of the tank is very limited. The simplest PMD (Figure 1.1) consists of several metal plates aligned along the tank's inner walls [10, 43]. The plates are mounted close to the tank wall, forming vanes. The gap between the plates and the wall serves as a passage through which the propellant is transported towards the "funnel" part at the outlet of the PMD. From here, the propellant is driven directly to the thruster. Surface tension effects (capillary pressure) dominate the flow in the said passages where, depending on the design of the vanes, one or two free liquid surfaces are formed. The flow is driven by the pressure difference between the "funnel" and the propellant bulk. The curvature of the free surface adjusts to the changing pressure gradient between the liquid and the surrounding gas. Consequently, the free surfaces act as dampers compensating the pressure disturbances in case of the irregular propellant withdrawal. The propellant remains within the vanes due to adhesion and cohesion and the resulting capillary pressure. The stability of the flow in said vanes is essential for the mission performance. Under certain flow conditions, the free surface loses its stability and the flow becomes unstable. As a consequence, the surrounding gas is ingested into the flow path. Two-phase flow caused by the gas ingestion could be unfavorable for the application (lower efficiency or even damage of the thruster).

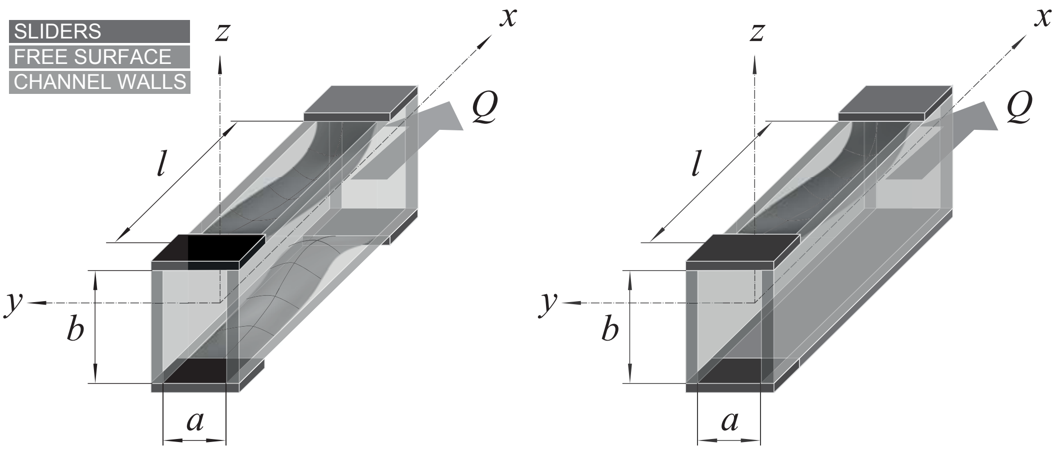

(a) Parallel plates (b) Groove

Figure 1.2: The capillary channel consisting of two glass plates (channel walls) and movable slide bars (sliders). The flow is driven along the x-axis by a pump which is located downstream of the channel. The free surfaces are pinned at the sliders edges.

The stability of the flow in said channels is the main subject of the Capillary Channel Flow (CCF) experiment. The PMD vanes shown in Figure 1.1 are simplified into capillary channels as shown in Figure 1.2. The capillary channel, investigated in this work, consists of two parallel plates. The channel's configuration can be changed with two movable sliders. Two channel configurations are considered: parallel plates (two free surfaces, Figure 1.2(a)) and groove (one free surface, Figure 1.2(b)). The capillary channel is implemented in a fluid circulation system to establish a continuous flow with variable parameters. A long time experiment was performed in the micrgravity environment of the International Space Station (ISS). The test channel with the free surface(s) is observed by a High Speed High Resolution Camera (HSHRC). The images are downlinked from the ISS and evaluated by image processing. The gathered results are used to validate the mathematical model developed prior to the experiment on board the ISS.

1.1 Motivation and Background

The motivation for this work arises from a deficit in experimental and theoretical work. Only few papers are found to deal with engineering solutions for applications in surface tension tanks. A recently developed stability theory awaited the experimental validation under long term microgravity conditions. The limited test duration of previous experiments (drop tower - order of seconds, suborbital flight - order of minutes) has left many important issues unaddressed. The CCF experiment aboard the ISS provided a unique opportunity to thoroughly validate the theory and probe limits within a multidimensional parameter space.

The CCF project is an international endeavor (ZARM, NASA, DLR, PSU). It is a first long term open duct flow experiment conducted in reduced gravity environment. The main goal of the CCF experiment is to determine the shape of the free surfaces and the maximum flow rates which may be achieved in the channel without a collapse of the free surfaces. The experience gathered during the previous short-time experiments in microgravity (within the multiphase flow group at ZARM) was employed to design a new unique experimental setup. The hardware, installed on board the ISS was controllable from the ground station in Bremen. Due to the limited astronaut involvement (only hardware installation), the CCF setup had to be a “plug and play” device. The hardware development was a challenging process due to the limited resources to test the component functionality in reduced gravity environment. Drop tower experiments and suborbital flight experiments were performed prior to the ISS experiment in order to probe the functionality of the major CCF components and to perform first observations of the flow behavior in the capillary channels.

1.2 Scope of this Work

The scope of this work covers the following points:

- execution of the CCF experiment aboard the International Space Station,
- evaluation of the gathered results,
- comparison with the predictions based on the mathematical model and its verification,
- numerical modeling (1D and 3D),
- implementation of the mathematical model to study the general flow behavior in the capillary channels (which is beyond the physical constraints of the CCF experiment).

This work is structured as follows. A literature overview is given in Chapter 2, where the development of the stability theory is summarized together with the limitations of steady and unsteady flows and the previously performed short-time experiments under microgravity conditions. Chapter 3 provides an overview of the capillary channel flow models (steady and time-dependent) known from literature. Governing equations and model equations are given in both dimensional and non-dimensional form. The CCF experiment hardware is described in Chapter 4 together with the operational scenarios and the performance of the experiment. Chapter 5 provides an overview on the numerical tools employed to model the flow in capillary channels (1D, in-house developed code ccFlow, and 3D open source CFD code OpenFOAM). The results of the steady flow experiments are discussed in Chapter 6 (including the comparison with the numerical predictions). Chapter 7 provides a discussion about the general behavior of the free surfaces in the capillary channels during the steady flow, where presented findings are based on the parametric study. The results of the transient flow experiments are discussed in Chapter 8 (including the comparison with the analytic model). Chapter 9 gives an overview of the 3D simulations performed with OpenFOAM. In Chapter 10, the conclusions from the work are drawn.

Chapter 2

State of the Art

An open capillary channel is a structure that establishes a liquid flow path when the capillary pressure caused by the surface tension force dominates over the hydrostatic pressure induced by gravitational or residual accelerations. The cross section of the flow in the open section of the capillary channel is totally or partly confined by free surfaces. Similarities exist between the flow in the investigated open capillary channels and compressible duct flows (high-speed wind tunels), flow in flexible tubes (arteries) or the flow in open channels (e.g. water open ducts). Each of these flows is governed by similar equations. The existence of limiting velocities is another similarity between the area-variable channel flow and compressible flows. For compressible flows, the speed of sound defines the choking velocity, whereas for the area-variable flows the limiting velocity can be defined with the speed at which waves propagate (will be discussed in Section 2.2).

In the following literature overview, both dimensional (denoted with a prime) and dimensionless quantities are presented. The scaling corresponds to the scaling of the mathematical flow model, which will be introduced in Chapter 3. The pressure $p = p'/p_c$ is scaled with the characteristic pressure $p_c = 2\sigma/a$, where a is the channel's gap distance. The velocity $v = v'/v_c$ is scaled with the characteristic velocity $v_c = \sqrt{2\sigma/(\rho a)}$. The cross-sectional area $A = A'/A_0$ is non-dimensionalized with the characteristic area $A_0 = ab$, where b is the channel's width. All lengths and the curvature h are scaled with the half of the channel's gap distance $a/2$. Complete scaling details relevant to the mathematical model considered in this work will be given in Section 3.4.

2.1 Propellant Management Devices

Propellant management devices are necessary for a spacecraft to control the position of the liquid propellant. The main function of the PMD is to keep the tank outlet to the thruster filled with fuel. The surface tension PMDs can be divided into three groups [65] (i) partial control, (ii) total control, and (iii) total communication devices. The partial control PMDs hold a fraction of the propellant in the tank over the outlet and leave the remaining liquid free. They are generally composed of not refillable traps (closed chamber) with a porous window or refillable sponges composed of metal sheets. These devices are used in vehicles that manoeuver considerably or use multiple engine firings. The total control surface tension PMDs hold all of the propellant over the tank outlet during all manoeuvers and are used when the slosh control is a concern. This type of device usually consists of a large compartmented container which contains almost all of the liquid when the tank is fully filled. The total communication PMDs are usually vane devices (subject of this work) designed to ensure that a flow path to the outlet is available from any position in the tank until the tank is depleted. The vanes are formed with

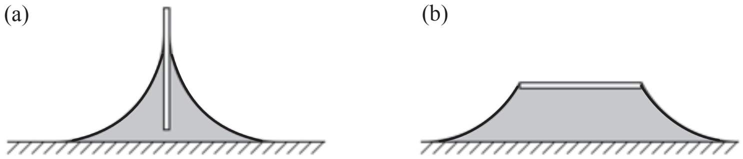

Simple Vane Ribbon Vane

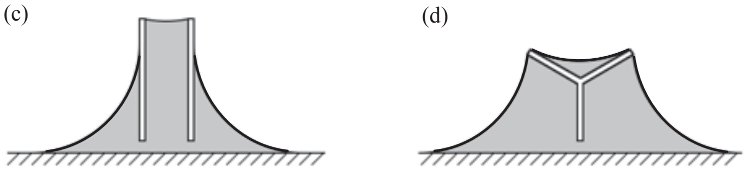

Double or Parallel Vane Complex Combination

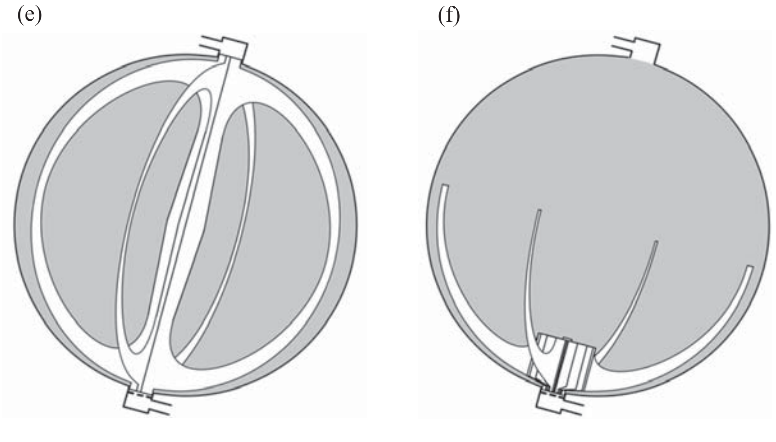

Vane Concept for a Flexible System Vane Concept for a Refillable System

Figure 2.1: Possible vane configurations in the surface tension tank (a-d). A vane device fitted into a typical propellant tank, flexible demand system (e) and refillable system (f). Based on Jaekle [43].

metal sheets aligned along the tank's inner walls. The simplest vanes consist of a single metal panel extending from and perpendicular to the tanks wall as shown in Figure 2.1(a).

Capillary flows along vanes are limited not only by the physical constraints of the system geometry and fluid properties, but also by spacecraft acceleration levels that can increase the BOND number[1]. The flow might be interrupted due to spacecraft maneuvers causing the destabilization of the liquid-gas interface. The flow becomes unstable if either limit is exceeded. In general, to avoid gas ingestion into the flow path two technical solutions are used (depending on the specific system requirements). For low flow rates and low acceleration, the vanes are used for direct supply (Figure 2.1(e)). For much higher flow rates and higher BOND numbers, the propellant is buffered in a refillable liquid reservoir that feeds the engine during the manoeuver (Figure 2.1(f)). After the manoeuver, the reservoir is refilled by means of the vanes.

Surface tension tanks are commonly used in telecommunication satellites such as GLOBALSTAR [56] (52 satellites), INSAT [57] (24 satellites), and EUROSTAR [21] (55 satellites). An example of the OST-2 surface tension tank applied in INSAT satellites is shown in Figure 1.1.

2.2 Current State of Understanding

Surface tension devices have been used in liquid propellant tanks for almost 55 years. In spite of the broad application of PMDs there is a lack of experimental work on their flow limitations. Since the physics behind the effect of the flow rate limitation is not known, the design of vanes is based on estimations (requiring high safety factors) and the theoretical work of Jaekle [43] and Der [14]. Jaekle performed a model computation of a liquid flow through a simple T-shaped vane (metal plate positioned perpendicular to the tank wall, Figure 2.1(a)). The one-dimensional momentum equation was solved numerically, yielding the radius of curvature in the cross-sectional plane and the corresponding flow rates of steady and time-dependent flows. The solution for the free surface interface shape, however, could not be computed for all flow rates. This effect was attributed to the choking effect, without any further discussion of its physical origin. The area wave propagation velocity down a simple vane was approximated as

$$c' = \sqrt{\frac{1}{2}\frac{\sigma}{\rho}\frac{1}{R'}}\,, \tag{2.1}$$

where R' is the radius of curvature. Jaekle used a term "choking velocity", assuming that c' might define an upper limit to manageable flow rates. The propagation of small disturbances traveling along the simple vanes was also studied theoretically by Der [14]. Neglecting the radius

---

[1] The BOND number Bo measures the importance of body forces to surface tension forces. The definition of the Bo number will be given later.

of curvature in flow direction, as well as the viscosity, a linear wave equation was derived. Der postulated that the wave speed depends on the liquid volume transported in the vane. Two cases were distinguished. The wave speed depends on the fluid properties and the radius of curvature if the radius of curvature is smaller than the vane height (first case). The wave speed additionally depends on the vane height itself if the radius of curvature is larger that the vane itself (second case).

First experiments on the forced flow in open capillary channels (resembling the vanes of the PMDs) date back to 1998 and were the work of Dreyer et al. [20]. In this work the flow rate limitations in parallel plates under microgravity conditions were investigated. In the theoretical part the steady state approach given by Jaekle [43] was followed. The mathematical model was based on the one-dimensional Bernoulli equation leading to a non-linear ordinary differential equation for the radius of curvature along the free surface of the test channel. Both laminar flow and entrance pressure flow conditions were taken into account, as well as the flow conditions before the channel inlet. The experiments were based on the work of Dreyer et al. [19] who investigated the rise of liquid between parallel plates under microgravity conditions in the drop tower and showed that the velocity of the rising liquid cannot exceed a certain critical value. Further experiments with parallel plates were carried out on board the ballistic rocket TEXUS-37 (Rosendahl et al. [67, 71]). An increasing demand on the liquid during the transition (stepwise increase of the flow rate) was compensated by the liquid stored in the liquid reservoir. An inlet nozzle was applied to control the flow conditions at the channel inlet. It was shown that the capillary wave speed can be derived from the experimentally determined free surface contour. The capillary channel and the free surface were observed with a high speed camera. Both Dreyer et al. and Rosendahl et al. (drop tower and sounding rocket experiments) pointed out that very small incremental increases in flow rates are required to minimize the transient inertial effects of the flow in the capillary channels. This could be accomplished during long-term experiments within a compensated gravity environment.

An extensive experimental, numerical, and theoretical study on the flow rate limitation in the open parallel plates channel was performed by Rosendahl et al. [70], who attributed the effect of surface instability to the capillary Speed Index. The definition of the capillary Speed Index

$$S_{ca} = \frac{v}{v_{ca}} = v\sqrt{-\frac{1}{A}\frac{\mathrm{d}A}{\mathrm{d}h}} \tag{2.2}$$

is based on the flow velocity v and the limiting longitudinal small-amplitude wave speed v_{ca}. A is the flow cross-sectional area, and h the mean curvature. The capillary wave velocity

$$v_{ca} = \sqrt{-A\frac{\mathrm{d}h}{\mathrm{d}A}} \tag{2.3}$$

is the generalized wave speed of Jaekle (Equation (2.1)). Choking occurs when the capillary Speed Index reaches unity $S_{ca} = 1$ and steady flow is possible only for flow rates below this critical value (subcritical flow). Stable, steady flow is possible in the subcritical regime and the free surface collapses at the critical point. In the one-dimensional flow model proposed by Rosendahl et al. the liquid pressure is related to the capillary pressure at the free surface including both principal radii of curvature. The model considers the convective and viscous losses, and the additional pressure loss due to the change of the velocity profile in the entrance region (entrance flow effects). For the discussion of the physical flow effects Rosendahl et al. introduced the dimensionless length $\tilde{l}$

$$\tilde{l} = \frac{\mathrm{Oh} l'}{4a}, \tag{2.4}$$

where OHNESORGE number Oh relates the viscous forces to inertial and surface tension forces. The definition of the Oh number will be given later. A numerical parameter study was performed aiming on the identification of three regions in which the flow limitation is caused by either convective or frictional pressure losses, leading to distinctly different interface profiles. For flow lengths $\tilde{l} < 10^{-3}$, the frictional pressure loss vanishes and choking is caused by the convective term (momentum equation). In the transition regime ($10^{-3} \leq \tilde{l} < 10^{-1}$) both effects control the flow (convective and frictional pressure losses). For very long channels ($\tilde{l} \geq 10^{-1}$), the flow is dominated by viscous momentum transport. For $\tilde{l} \to \infty$ (pure STOKES flow), the limit of application for the choking model was shown. The analytical formulation of the critical flow rate in the purely viscous regime $\tilde{l} > 0.1$ was approximated as

$$Q_c^{an} = \frac{2}{K_{Pf}\tilde{l}} \ , \tag{2.5}$$

where K_{Pf} is the friction factor for the flow between parallel plates.

Srinivasan [82] studied numerically the capillary self-driven liquid flows in open parallel plates channels. He proposed a semi-analytical method for the solution of the steady three-dimensional STOKES equations. Comparing with the experimental results from Rosendahl et al. [71], the computed flow rates were approximately three times lower, which the authors attribute to the inertia in the experiment.

The stability limits of unsteady open capillary channel flow were studied by Grah et al. [32]. The steady flow model of Rosendahl et al. [70] was extended to unsteady conditions. The unsteady effect was defined by a dynamic flow rate increase during a given time period causing an additional flow rate limitation. Grah et al. postulated that the unsteady flow can be temporarily choked, remaining however stable. Thus, the theory defines three flow regimes: subcritical flow, stable supercritical flow, and unstable (supercritical) flow. The stability in the supercritical regime is explained by a pressure balance at the free liquid surface. Grah et al. introduced the Dynamic Index defined as

$$D = 1 - \frac{h^* - \chi^*}{h^* - \chi_0^*} \ , \tag{2.6}$$

where h^* is the capillary pressure, χ^* convective pressure at the point of the flow minimum cross-section area and χ_0^* convective pressure at the beginning of the unsteady phase. The difference $h^* - \chi^*$ tends to zero at the stability limit, thus the dynamic index reaches unity for unstable (supercritical) flow.

The existence of the numerical singularity at the critical point of the steady flow instability, postulated in previous publications, was demonstrated in detail by Grah and Dreyer [31]. The numerical singularity was attributed to the stability criterion for steady flow and represents the numerical consequence of the liquid surface collapse. Furthermore, Grah and Dreyer introduced the Equivalent Steady System (ESS) technique assuming that every unsteady state which occurs during a flow transition can be substituted by an equivalent steady state. In his method the time derivatives of the differential equation system are considered as constant at the corresponding time point. Furthermore, in the work of Grah and Dreyer the liquid surface stability model, based on the capillary pressure h^* and the flow pressure χ^*, was extended to account for the viscous pressure loss.

Convective dominated flows in open capillary channels were studied theoretically and experimentally by Rosendahl et al. [69]. Flows of this type are of particular interest since the free surfaces possesses a quasi-symmetry in the flow direction enabling the application of a new method for evaluation of the flow limits. Contrary to former approaches, this method uses an approximation of the surface curvature by means of the empirical surface profiles. Moreover, Rosendahl et al. found that the choking effect occurs independently, whether the flow limit is approached by variation of the flow rate or by the variation of the flow length.

Klatte [50] and Klatte et al.[51] studied theoretically, numerically, and experimentally the flow in capillary channels with wedge-shaped cross sections. They postulated that the capillary Speed Index is effective for the convective dominated flow, but for viscous dominated flow in the wedge, the free surface loses stability even with the Speed Index below unity. Thus, an ingestion index was proposed for viscous dominated flows.

A related phenomenon, such as capillary-driven flows in slender containers with interior edges (wedges, rounded corners, and vane gapes), were extensively investigated theoretically and experimentally. All studies are motivated by passive manipulation of the fluid interfacial flows in absence of gravitational forces. The circulation and separation of large quantities of water in spacecraft life support systems was addressed in the work of Weislogel et al. [96]. He studied experimentally (low-g flight) a passive phase separation in a urine collection system. So far, capillary solutions for water based systems aboard spacecraft were ignored due to poor and unpredictable wetting properties which control fluid configurations in capillary dominated systems. It must be noted that, without the aid of gravity, for certain processes the principal challenge is simply the one of separating two fluid phases (e.g. condensate from humid air).

Weislogel et al. [93, 95] studied the flow behavior along the interior corners of spacecraft propellant tanks after the sudden reduction of gravitational forces. The numerical results were compared with the experimental data from the drop tower (2.2 s of μg) and low-g parabolic flights. The theoretical predictions of the liquid flow were based on a nonlinear one-dimensional diffusion equation, without the strong dependence on numerical data as in the work of Ayyaswamy et al. [2] and Ransohoff et al. [63].

A broad study on the capillary-driven flow in the low-gravity environment was performed within the series of Capillary Flow Experiments (CFE) aboard the International Space Station. The CFE are designed as a collection of quantitative fundamental and applied capillary phenomena experiments conducted using handheld (by astronauts) hardware. The flow in complex geometries is studied encompassing three experimental setups, Contact Line (CFE-CL), Interior Corner Flow (CFE-ICF), and Vane Gap (CFE-VG) configuration. The first investigates the properties of the contact line which controls the interface shape, stability, and dynamics of capillary systems [45]. The second studies capillary flow in interior corners resembling the structures inside the propellant tanks [94]. The third experiment studies capillary flow when there is a gap between interior corners, such as in the gap formed by an interior vane and a tank wall of a large propellant storage tank or the near intersection of vanes in a tank with complex vane control [11, 12].

2.3 Open Channel Flow Stability Criteria

The liquid surface stability is based on the pressure interactions across the free liquid surface in the open section of the capillary channel. The flow in the capillary channel is considered as shown in Figure 2.2. The liquid is confined to the channel in the open section by capillary forces only. The curvature of the free surface balances the pressure differences across the interface. The capillary pressure, defined with the Young-Laplace Equation $h^* = R_1^{*-1} + R_2^{*-1}$, has to compensate two flow-induced pressure flow effects. Firstly, the convective pressure χ^* caused by the convective acceleration $v\mathrm{d}v/\mathrm{d}x$. Secondly, an additional pressure effect, which is the difference $h^* - \chi^*$ caused by the the local acceleration $\mathrm{d}v/\mathrm{d}t$ of an unsteady flow. In general, the capillary pressure (surface tension) enhances the stability of the free surface, whereas the convective pressure and the effect of the local acceleration act contrarily. In the following, two criteria for the surface stability will be formulated of which at least one has to be fulfilled to assure the stability. The pressure balance at the point of the minimum cross-section x^* as shown in Figure 2.2 can be defined as [32]

$$\int_0^{x^*} \frac{\mathrm{d}v}{\mathrm{d}t}\mathrm{d}x = h^* - \chi^* \; . \tag{2.7}$$

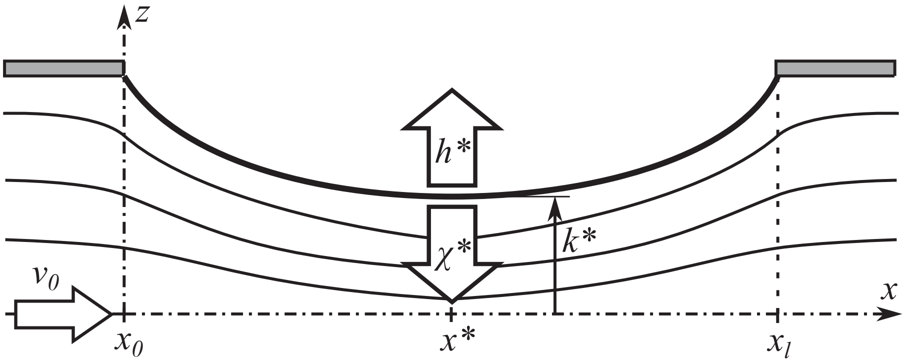

Figure 2.2: Steady equilibrium of the capillary pressure h^* and the convective pressure χ^*.

The irreversible pressure loss effects are neglected and the convective pressure (square function of the velocity) increases significantly at the channels throat. Hence, the convective pressure has a high potential for destabilization and plays a significant role in the liquid stability.

2.3.1 Flow Rate Limitation of Steady Flow

For steady flow, the pressure balance (2.7) at the channel position x^* simplifies to

$$h^* = \chi^* \ . \tag{2.8}$$

Figure 2.3(a) shows a generic steady pressure diagram at the point of the minimum cross section. The thin χ^*_Q lines represent the theoretical behavior of the convective pressure χ^* over the contour height k^* for a constant flow rate $Q = v^* A^*$. The bold line shows the capillary pressure h^*, which is the function of the curvature of the free surface. In general, with decreasing contour height k^* at the point $x = x^*$, the curvature of the free surface increases causing an increase of the capillary pressure h^*. A steady state can be defined at the intersection of the h^* and χ^*_Q lines, for a given flow rate Q (e.g., point **a** in Figure 2.3(a)). Qualitative comparison of the pressure curves in Figure 2.3(a) shows a higher gradient of the h^* line compared to the χ^*_Q lines. Even a small change of k^* caused by the free surface movements (due to external perturbations, e.g. change of boundary conditions) leads to a change of the capillary pressure along the h^* line and of the convective pressure along the χ^*_Q line (constant Q is assumed). Since the h^* line is steeper than the χ^*_Q line, the capillary pressure always acts in a stabilizing way and compensates the convective pressure. Hence, the stability criterion for steady flow can be formulated based on the gradients as

$$\left|\frac{\mathrm{d}h^*}{\mathrm{d}k^*}\right| > \left|\frac{\mathrm{d}\chi^*}{\mathrm{d}k^*}\right| \ . \tag{2.9}$$

With increasing flow rate, the point **a** in Figure 2.3(a) moves upwards along the h^* line (the free surface bends inwards, and the capillary pressure increases). The gradient of the h^* line decreases slightly and the gradient of the χ^*_Q line increases significantly for smaller k^* values.

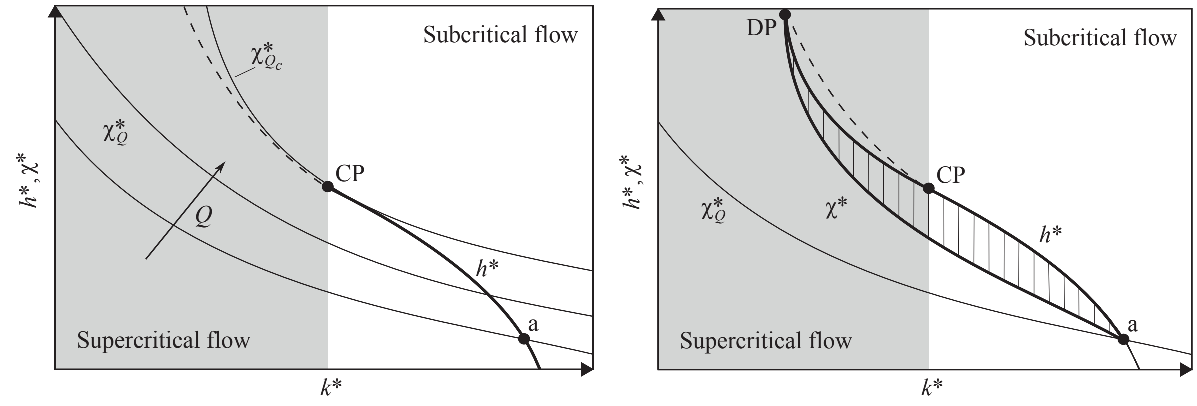

(a) Steady pressure diagram.

(b) Unsteady pressure diagram.

Figure 2.3: Pressure diagrams at the point $x = x^*$, where h^* is the capillary pressure, χ^* is the theoretical value of the convective pressure, and k^* is the free surface contour. The critical point CP defines the limit of the steady flow. For unsteady flow (b) the liquid surface collapse occurs at the destabilization point DP.

Consequently, the difference of the gradients in Equation (2.9) decreases. The gradients are equal when the critical point CP is reached, and the corresponding flow rate defines the critical rate (limit of the stable flow). The dashed line in Figure 2.3(a) represents the theoretical supercritical solution of no practical meaning for the steady flow theory. It will be shown later that it corresponds to the stability limit of unsteady flow.

Furthermore, rearranging inequality (2.9) and combining it with the small amplitude wave speed (2.3) yields the capillary Speed Index at the point of the minimum cross section

$$S_{ca} = \frac{v^*}{v^*_{ca}} = v^* \sqrt{-\frac{1}{A^*}\frac{\mathrm{d}A^*}{\mathrm{d}h^*}} \quad , \tag{2.10}$$

which bears similarities to Rosendahl et al. definition (2.2). The dependency of the S_{ca} on the flow rate is shown in Figure 2.4. At the critical point CP the velocities are equal $v^*_{ca} = v^*$, and the Speed Index reaches unity, $S_{ca} = 1$. Any disturbance traveling upstream at the speed of sound, e.g. an infinitesimal increase of the flow rate (pump located downstream from the channel outlet) cannot pass the minimum cross-section point $x = x^*$. In such case, the flow rate at the inlet remains unchanged. To satisfy continuity, surrounding gas has to be ingested into the channel. Thus, the free surface collapses and gas ingestion occurs. This phenomenon (choking) bears similarities to compressible duct flows e.g., flow in a De Laval nozzle or an orifice. Here, the limiting velocity is the speed of sound, and the Mach number approaches unity at the critical point.

The effect described above might be denoted as a “wave speed limitation” with the limiting mechanism of choking. For sufficiently long channels ($\tilde{l} > 0.1$), an effect of “viscous limitation” causes the flow rate limitation, as shown by Rosendahl et al. [69] .

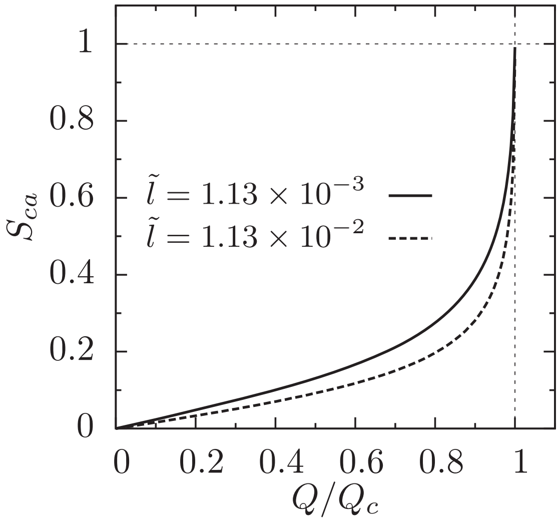

Figure 2.4: Numerically predicted Speed Index S_{ca} as a function of the flow rate Q for the parallel plates. Two flow lengths $\tilde{l}$ are chosen for comparison. The mathematical flow model (will be discussed in Section 3.4) is solved with finite differences (will be discussed in Section 5.1).

2.3.2 Flow Rate Limitation of Unsteady Flow

For unsteady flow, the acceleration pressure effect is taken into account. The capillary pressure h^* and the convective pressure χ_Q^* are not equal during the flow rate transition. Figure 2.3(b) shows a generic unsteady pressure diagram at the point of the minimum cross section. The point **a** (subcritical steady state) depicts the beginning of the unsteady phase. During the transition the free surface is drawn into the channel and the contour height k^* decreases. Consequently, the capillary pressure h^* moves along the bold line of the pressure diagram. The difference $h^* - \chi^*$ (marked with hatched lines in Figure 2.3(b)) represents the dynamic pressure effect, caused by the acceleration term in Equation (2.7). Owing to the unsteady terms no singularity occurs for the numerical solution at the critical point CP [32]. The flow remains stable and the supercritical flow regime on the left-hand side of the critical point CP can be reached in the case of dynamic flow. The Speed Index (2.10) is a function of the flow cross-sectional area A^* and the curvature h^* only and can be applied to the unsteady case as well. As for steady flow it reaches the value of $S_{ca} = 1$ at the CP in Figure 2.3(b). In the supercritical regime, the communication between the channel outlet and inlet is interrupted. Increasing flow rate demand on the outlet is not followed by the inlet flow rate. The imbalance between the outlet and inlet flow rate is compensated by liquid displacement. The difference $h^* - \chi^*$ decreases for decreasing k^* in the supercritical regime. In the supercritical regime the free surface is further drawn into the channel. This leads to an increase of the local curvature and a significant increase of the h^*-line gradient. When the convective pressure χ^* reaches the value of the capillary pressure h^*, the free liquid surface collapses (the destabilization point DP in Figure 2.3(b)). Hence, the supercritical unsteady stability limit criterion can be formulated as

$$h^* < \chi^* \ . \tag{2.11}$$

According to definition of the Dynamic Index given in Equation 2.6, χ_0^* is the convective pressure at the beginning of the unsteady phase. This corresponds with point **a** in Figure 2.3(b)). The difference $h^* - \chi^*$ tends to zero at the stability limit, thus an unsteady open capillary channel flow is stable if the Dynamic Index does not reach the value $D = 1$ in the supercritical area.

2.4 Limitation of Ground Based Experiments

Terrestrial experiments are limited by the hydrostatic pressure acting on the free liquid surfaces. Consequently, the OHNESORGE number is limited. Considering a horizontal flow between parallel plates (Figure 1.2(a)), the limits can be estimated with the following relation

$$\rho g_z a \approx \frac{2\sigma}{a} \ , \tag{2.12}$$

where the term on the left-hand side is the maximal hydrostatic pressure in the channel of gap distance a. The term on the right hand side represents the differential (capillary) pressure across the liquid interfaces. It is derived from the YOUNG-LAPLACE equation $p' - p'_a = -\sigma(R^{'-1} + R^{'-1})$, where the radius of curvature in flow direction x' is neglected ($R'_1 = -a/2, R'_2 \to \infty$). The ratio between the gravity and surface tension forces can be expressed with the BOND number defined as $\mathrm{Bo_z} = \rho g_z ab/2\sigma$, where $g_z = 9.8\ \mathrm{m/s^2}$ is the gravitational acceleration on Earth. The maximal gap distance in a ground based experiment and the minimal OHNESORGE number can be estimated as

$$a_{max} = \sqrt{\frac{2\mathrm{Bo_z}\sigma}{\rho g_z}} \quad , \quad \mathrm{Oh_{min}} = \frac{\mu}{\sqrt{2 a_{max} \rho \sigma}} \ . \tag{2.13}$$

Since the stability limit in considered channels is not known, $\mathrm{Bo_z} < 0.01$ is required. For the standard test liquids, the obtained limitations are shown in Table 2.1. For the test liquid HFE-7500 used in the CCF experiment, the maximal gap distance is $a_{max} = 0.1$ mm, and the minimal Oh number $\mathrm{Oh} = 12.5 \times 10^{-3}$. The range to be investigated aboard the International Space Station is however $5 \times 10^{-3} > \mathrm{Oh} > 5 \times 10^{-4}$. Large Oh number lead to a viscous dominated flow behavior and convective as well as inertia related effects cannot be studied.

Table 2.1: Maximal theoretical gap distance and the minimal OHNESORGE number in a terrestrial experiment. The test liquid properties are at 25 °C.

Liquid	ρ	ν	σ	a_{max}	$\mathrm{Oh}_{\min}\times$
-	kg/m^3	10^{-6} m^2/s	10^{-3} N/m	mm	10^{-3}
Heptane	679	0.57	19.9	0.2	4.8
SF 0.65	761	0.65	15.6	0.2	7.2
SF 1.0	818	1	16.9	0.2	11
HFE-7500	1600	0.66	15.7	0.1	12.5
FC-77	1789	0.8	14.7	0.1	17

2.5 Experiments in Microgravity

Forced flow in capillary channels under reduced gravity conditions has been extensively studied since the mid-nineties within the Multiphase Flow Group at ZARM. Prior to the experiment aboard the ISS, experiments were conducted in the drop tower and on board the sounding rocket TEXUS [73]. The drop tower in Bremen provides 9 s of μg, and the sounding rocket TEXUS 300 s of μg. Performed experiments are summarized in Table 2.2. The first experiments in the drop tower were performed by Dreyer et al. [20], who investigated the forced flow in the capillary channel.

Table 2.2: Overview of experimental studies concerned with capillary channel flow in a microgravity environment. DT - drop tower.

Year -	Geom. -	Dimensions mm	Environment & Test liquid	Objectives -	Outcomes -	References -
1998	PP	a: 2-5; b: 10-30 l: 48-96	DT FC77 SF0.65+1.0	filling, forced flow	1st observation of choking	[20]
2001	PP	a: 5 ; b: 25 l: 46.6	TEXUS-37 PDMS	steady flow, transition	critical flow, evaluation of v_c	[67, 71] [58, 70]
2005	PP	a: 12 ; b: 25 l: 12-19	TEXUS-41 HFE7500	extension to convective flow	$S_{ca} = f(Q)$ plot, pressure diagrams	[68, 66] [32]
2006	GR	a: 10 ; b: 25 l: 12	DT HFE7500	steady flow, choking	2nd geometry, k comparison	[35]
2010	GR	a: 10 ; b: 25 l: 28.9, 47.5	DT FC72	subcritical flow, surface profiles	comparison with model	[34]
2010	PP	a: 10 ; b: 25 l: 12	TEXUS-42 FC72	supercr. flow, Q and l variation	$S_{ca} = f(Q)$ plot, pressure diagrams	[69, 31]
2010	GR	a: 10 ; b: 25 l: 80	TEXUS-45 FC72	two-phase flow, bubble transport	comparison with model	[77, 76]
2011	WE	a: 8.4 ; b: 30 l: 48	DT HFE7500	steady flow, choking	3rd geometry, inertia and viscous collapse	[50]

2.6 Capillary-driven Flow in Terrestrial Applications

The outcomes of this work and the CCF experiment might be of interest not only for space applications (macrofluidic), but also for terrestrial systems that rely on capillary effects (microfluidic). Zhang et al. [100] proposed the capillary length $l_c = \sqrt{\sigma/(\rho g)} \lesssim O(1\text{ mm})$, which is the characteristic system dimension, to demonstrate the degree to which passive control may be achieved on Earth. For macrofluidic space systems significantly larger dimensions can be maintained $\lesssim O(1\text{ m})$. In cited work the fluid flow and heat transfer in dual-wet micro heat pipes was studied. Micro heat pipes are commonly long capillaries (triangular or rectangular) filled with a liquid and a long vapour bubble. Micro heat pipes find their application in micro electronic devices [33, 84].

Lab-on-a-chip platforms are another typical example of microfluidic devices [36, 90, 74], where capillary effects are employed to passively process the fluids. In such devices the single or multiple lab processes are scaled down to a chip-format in which effects such as capillary forces or wall roughness become more dominant.

The behavior of flow in partially open liquid microchannels was studied by Melin et al. [55]. The channels consist of a closed inlet part, a closed outlet part, and a section in between which is open to the surrounding gas. Such a structure enables direct liquid sampling which finds application in lab-on-a-chip devices [25]. The fluid behavior, based on the continuous pressure-driven flow and surface tension, was discussed in terms of cross sectional flow behavior, performance and its application to microfluidic interfacing.

A spontaneous capillary flow in uniform cross-section microchannels was studied by Berthier et al. [3]. Spontaneous capillary flow occurs when a liquid volume is moved by the effect of capillary forces, without the help of other devices such as pumps or syringes. A theoretical flow model was presented and the conditions for spontaneous capillary flow in any composite channels of uniform cross-sections (e.g. microchannels with non-homogeneous walls and partly open channels) were derived. The criterion for the establishment of said flow was based on the effective contact angle (CASSIE law). The work of Berthier was motivated by previous studies in which the influence of the channel geometry on the establishment of the capillary flow was investigated experimentally and numerically (Zimmerman et al. [101], Chen et al. [12]).

Capillary pumps are another typical application of capillary-driven flows. Zimmermann et al. [101] have shown how to control the capillary flow in the various geometrical configurations of capillary pumps. The performance of capillary pumps was studied in combination with the flow resistance, in which the capillary pressure was defined solely by the geometry. Design procedures of the capillary pumps with rectangular cross sections were shown in the work of van der Wijngaart [89]. Geometric parameters of the channel were derived ab initio, assuming constant volumetric flow rate and constant velocity profiles.

2.7 Computational Fluid Dynamics

The work of the British meteorologist Lewis Fry Richardson is believed to be the first approach of solving the fluid transport equations using finite differences and division of the physical space into cells [64]. Although, his weather prediction calculations were performed by hand, they are still the earliest type of computations resembling the modern CFD. Development of the electronic computers during the 1940s marks the start of the digital era of numerical computing. One of the earliest CFD computations were performed on ENIAC (Electronic Numerical Integrator And Computer) using methods similar to Richardson's meteorology models.

The earliest numerical solution for laminar flow past a cylinder was carried out in 1933 by Thom [86]. Two symmetrical eddies were obtained behind the cylinder and the values for drag and pressure distribution agreed with the experimental results. Kawaguti [48] obtained a similar solution for the flow around a cylinder in 1953 by using a mechanical desk calculator, working 20 hours per week for 18 months.

The first approach to solve the full Navier-Stokes equations with the finite element method for the flow with free surface dates back to 1965 and the marker-and-cell (MAC) method developed by Francis H. Harlow and Welch [38] and their group. Harlow is considered as one of the pioneers of CFD techniques. In his group during the 1950s and 1960s many of the currently used numerical methods: Particle-In-Cell (PIC), MAC, vorticity and stream function and Implicit Continuous Fluid Eulerian (ICE) were developed.

During the 1970s a group working under Brian Spalding at Imperial College (London, UK) developed other important numerical methods: SIMPLE (Semi-Implicit Method for Pressure Linked Equations) algorithm, stream function based codes and upwind difference discretization schemes. Spalding created PHOENICS - the first commercially available CFD software [1]. A further development of CFD techniques in the 1960s and 1970s is associated mainly with the research groups of space and aerospace industries. The first three-dimensional computations were achieved by discretizing the surface geometry with panels (panel methods) [39]. This technique for airfoil analysis, ship hulls and aircraft fuselages was extensively developed, including lifting models and boundary layer models (viscous effects).

Most commercial CFD codes available today (Fluent, CFX, Star-CD, Flow 3D, Polyflow) originated from the 1980s and 1990s. The use of commercial CFD software started to become accepted by major companies around the world rather than development of in-house CFD codes. Extensive documentation and user support are the main benefits of the commercial codes. The main disadvantages are the limited possibility to modify the code and license fees. An alternative to commercial software are open-source CFD codes, among which the most popular are: OpenFOAM [44] (general purpose CFD code), REEF3D [47] (focus on complex free surface flows in hydraulic, coastal, offshore and environmental engineering), SU2 [61] (focus on aerodynamic shape optimization), FeatFlow [42] (general purpose code for the numerical solution of the incompressible Navier-Stokes equations in two and three space dimensions) and Gerris [62] (focuses on marine and ocean flow applications).

2.7.1 Interface Tracking

Simulating liquid motion with free surfaces introduces the complexity of having to deal with solution regions (interfaces) whose shapes are changing. Existing methods for the computation of free surfaces can be classified into two groups [23]: (i) surface methods (surface fitting), and (ii) volume methods (surface capturing). With surface methods (particles on interfaces, height functions, level set method, surface fitted methods) [87], the interface is represented and tracked explicitly, either by marking it with special marker points, or by attaching it to a mesh surface which is forced to move with the interface. The advantage of this approach is that the interface remains sharp and its position is known throughout the flow field. Surface methods are limited to interfaces which are not subjected to large deformations due to the restrictions on the prediction of merging (coalescence) or rupturing (breakup) interfaces as in the case of choking in capillary channels. With volume methods, the fluids on either side of the interface are marked by either massless particles or an indicator function. The exact position of the interface is not known explicitly and special techniques need to be applied to capture a well defined interface as a part of the solution algorithm [88]. A comprehensive review of numerical methods to track interfaces in multiphase flows is given in the work of Gopala and van Wachem [27].

The Volume of Fluid (VOF) method is probably the most widely used volume method. It is based on the idea of recording in each grid cell the fractional portion of the cell volume occupied by liquid. The main advantage of this method is the capability to model non-linear problems in which the free surface experiences sharp topological changes. The VOF method is computationally friendly, as it introduces only one additional equation and does not require mesh deformation algorithms as in case of surface-tracking methods. More details on the VOF method will be given in Section 5.2.

2.7.2 Two-Phase Simulations With OpenFOAM

OpenFOAM (Open source Field Operation And Manipulation) is a C++ toolbox for the development of customized numerical solvers and pre-/post-processing utilities for the solution of continuum mechanics problems, including computational fluid dynamics (CFD) [44]. The code is released as free and open source software under the GNU General Public License. By being "open", the code offers complete freedom to customise and extend existing functionality. OpenFOAM (originally FOAM) was created by Henry Weller and co-workers [97] in the late 1980s at Imperial College (London, UK). OpenFOAM is being constantly developed, and it contains over 80 solver applications that simulate specific problems in engineering mechanics. In this study, OpenFOAM was chosen for the three-dimensional modeling of the flow in capillary channels because of its multiphase capabilities (interFOAM solver based on the VOF method), no license fees and possibility to run simulations on an unlimited number of cores. More details on solver properties, performed simulations and results will be given in Sections 5.2 and 9.

The two-phase solver interFOAM was described and validated for various application cases. A comprehensive review can be found in the work of Deshpande et al. [15]. Complex multiphase flow problems, such as a circular water jet plunging at shallow angles into a quiescent pool, were modeled. Excellent agreement between the numerical predictions (including coalescence of air cavities) and experimental findings was obtained [16]. The effect of velocity modulation imposed on a cylindrical liquid jet falling into stagnant gas was modeled by Srinivasan et al. [83]. Sinusoidal velocity fluctuations of finite frequency and amplitude were applied at the liquid jet inlet, and the resulting jet deformation (i.e., surface waves) was captured with the interFOAM methodology. The stability of the gas-liquid meniscus was studied numerically and experimentally by Maiwald and Schwarze [53] who analyzed the flow-induced gas entrainment in a roll coating system.

Another phenomenon studied with OpenFOAM is microfluidic flow. Hoang et al. [41] showed that the movement and formation of confined bubbles and droplets can be predicted in very good agreement with experimental data using VOF simulations. Numerous test cases are considered, and the ability of interFOAM to handle large interfacial tension, topological changes and large separation of characteristic length and time scales was demonstrated. Computationally demanding tasks, such as the formation of a lubricating film (typically two orders of magnitude smaller than the channel width) or the breakup of a bubble in three-dimensional T-junctions were accurately predicted. A two-phase capillary flow in microfluidic channels at very low Capillary numbers was investigated experimentally and numerically with interFOAM by Saha et al. [75]. The channels consist of two parallel glass plates with integrated pillars. Passive capillary filling process was considered by applying a constant pressure at the channel inlet and outlet. Good agreement of simulated meniscus profiles with the experimental work was obtained.

Falling liquid films were studied widely with OpenFOAM. Dietze et al. [17] investigated the nonlinear wave and flow dynamics of vertically falling films with three-dimensional regular surface waves of large-amplitude humps preceded by capillary ripples. It was shown that the dynamics in three-dimensional films differ significantly from those in two-dimensional films due to the absence of gravity in the third (spanwise) direction. Dietze showed that complex inertia- and capillary-dominated flow structures can be resolved with the DNS (direct numerical simulation) technique coupled with interFOAM. Other examples of numerical validation of flow film models can be found in the work of Martin et al. [54]. The gravity-driven, thin wavy films are modeled assuming only one computational cell over the film height. With such approach, the computational time can be reduced and film flow over large surfaces of complex geometrical shape can be considered. Doro and Aidun [18] show that the flow inside the film can be modeled by discretising the film over its thickness. The formation and evolution of backflow regions for the sinusoidal and teardrop-shaped surface regimes of laminar falling liquid films were studied with interFOAM. It was shown that falling liquid film disturbances grow into waves as they travel downstream. The dynamic aspects of backflow were successfully resolved with the VOF technique.

Grah and Dreyer [30, 31] used interFOAM solver to study the forced flow in capillary channels under microgravity conditions. The channel configuration (parallel plates), and the liquid and flow properties corresponded to the experimental conditions during the TEXUS-42 sounding rocket flight. For the verification, the numerical results were compared with quasi-steady and unsteady data from experiment. Good qualitative agreement in the numerically determined shape of the free surfaces compared to the experimental data was shown. Particularly in the unstable supercritical regime, the choking process was well reproduced by numerical modeling.

Klatte [50] employed OpenFOAM to model the forced flow in the wedge channel. His model resembles the setup of the experiments with wedge performed in the drop tower. His computational domain consists of the flow preparation chamber, the entrance nozzle, and the capillary channel. He applied a mesh adaptation algorithm in order to reduce the computational time. With this method, a relatively coarse grid can be used for the simulation. The mesh in the vicinity of the free liquid surface is automatically re-meshed (re-fined) during the computation, depending on the position of the interface. The numerical results (critical flow rate and free surface contour) coincided well with the experimental data. Furthermore, a parametric study was performed with OpenFOAM in which the dependency of the flow rate on the velocity field (flow profiles) and its development for the flow in the wedge in the inertia and viscous dominated regimes was studied. Also the influence of the OHNESORGE number and the wedge dimensions on the critical flow rate was shown.

Chapter 3

Modeling the Flow in the Capillary Channel

Forced liquid flow through an open capillary channel consisting of two parallel plates is considered, as shown in Figure 1.2. The channel has a width b, and a gap distance a. The flow enters the channel at $x = 0$ and exits at $x = l$. One (groove) or two (parallel plates) free liquid surfaces are formed along the open flow path l. In the stable flow regime, the capillary pressure at the free surface causes the pressure difference across the gas-liquid interface. The liquid pressure decreases in the flow direction, thus the curvature increases in the vicinity of the channel outlet. For an internal pressure lower than ambient pressure, the free liquid surface(s) are concave at any cross-section as shown in Figures 3.1(c) and 3.1(e) for parallel plates and groove, respectively. The flow along the channel axis x is characterized by the mean velocity v and the liquid pressure p and is modeled with the unsteady, one-dimensional flow model based on the momentum and continuity equations. The model predicts the free surface contour $k(x)$ along the channel at stable flow conditions.

In the following, the mathematical model of the flow in capillary channels (parallel plates and groove) is given. The governing equations and relevant mathematical relations are introduced in dimensional form. Furthermore, the non-dimensional numbers and scaling are presented and applied to the dimensional model, resulting in the set of a coupled differential equations that can be solved with finite differences. The notation used in the figures is valid for dimensional and non-dimensional quantities (primes are dropped for the sake of simplicity).

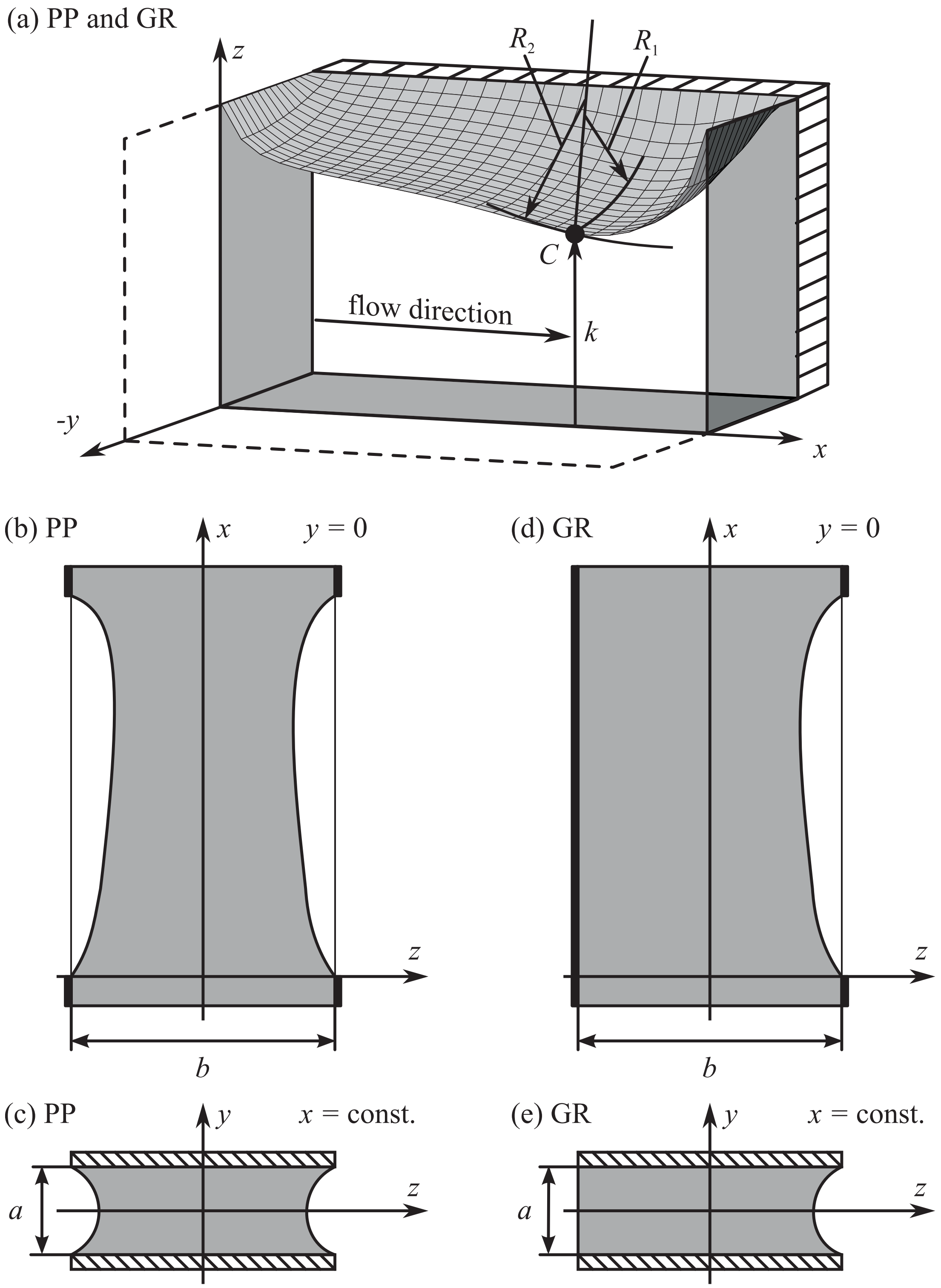

Figure 3.1: Schematic of the considered capillary channel (PP - parallel plates; GR - groove channel). (a) Free surface with two principal radii of curvature R_1 and R_2 and the interface contour k in the x, z-plane as a function of x. (b) and (d) are the cross-sectional views in the x, z-plane. (c) and (e) are the cross-sectional views in the y, z-plane (for $x =$ const. and $0 < x < l$.).

Basic Definitions

In the following, the basic geometrical relations required for the formulation of the mathematical model are given. The channel length is defined as a longitudinal length of the free surface extended between the pinning points x_0 and x_1 (Figure 3.2). The free surface contour $k(x)$ is defined by the intersection line of the free surface with the plane $y = 0$, and it defines the innermost position of the liquid surface. For any flow cross section it defines the minimum of $z = z(x = \text{const}, y)$. For any x between x_0 and x_1, the contour k is a function of the coordinate x. The free surface profile is defined as the graphical representation of the function $k = f(x)$. The minimum contour point $k_{min}(x^*, k^*)$ coincides with the location of the minimum cross-sectional area where the first derivative of the contour is zero. The free surface displacement is defined as its vertical offset $d = b/2 - k$. The free surface deformation (asymmetry) $\Delta x = x^* - l/2$ can be identified for the non-symmetrical free surfaces for which the minimum contour point is shifted towards the channel outlet. For symmetrical profiles, the point k_{min} is located in the channel's center $x^* = l/2$ and $\Delta x = 0$.

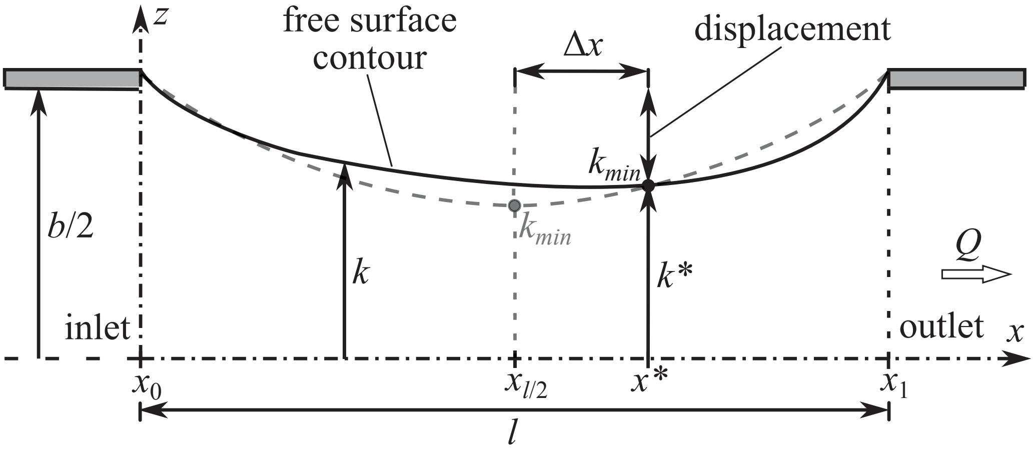

Figure 3.2: Geometrical definitions in the symmetry x, z-plane of the rectangular channel. The grey dashed line and black solid line represent a symmetrical, and a non-symmetrical free surface profile, respectively. k - free surface contour, k_{min} - minimum contour point with its spatial coordinates x^* and k^*, l - channel length, b - channel width, x_0 - channel inlet, x_1 - channel outlet.

Model Assumptions

In the following, the dimensional quantities, denoted with (') are presented (unless otherwise specified). The dimensions a and b are not supposed to be scaled for the non-dimensional model, thus the prime is dropped. The origin of the coordinate system is located at the center of the inlet cross-section area. The flow is assumed to be one-dimensional along x'. The test liquid is Newtonian, and perfectly wetting with the contact angle of 0°. The incompressible flow and isothermal conditions are assumed. The Reynolds number is defined as

$$\mathrm{Re} = \frac{v' D_h}{\nu} \ , \tag{3.1}$$

where v' is the average flow velocity, D_h is the hydraulic diameter of the cross section and ν is the kinematic viscosity. In the experiment below 900, therefore the flow is assumed to be laminar. The hydrostatic pressure caused by acceleration g is considered to be negligible. The Bond number is defined as

$$\mathrm{Bo} = \frac{\rho g_i a L_i'}{2\sigma} \ , \tag{3.2}$$

where ρ is the liquid density and σ the surface tension. In the experiment the characteristic lengths are $L_i' = a, b, l'$ and characteristic axis $i = x', y', z'$. Assuming the acceleration $g_i = 10^{-5}$ m/s^2 the Bond number in experiment is below 10^{-4}.

3.1 Basic Equations

The shear stress at the gas-liquid interface is neglected and the gas phase is considered as passive. The differential pressure at the interface can be determined by the YOUNG-LAPLACE equation

$$p' - p_a' = -2\sigma H' = -\sigma \left(\frac{1}{R_1'} + \frac{1}{R_2'} \right) . \tag{3.3}$$

The capillary pressure is proportional to twice the mean curvature $2H'$, which is defined by the principal radii of curvature R_1' and R_2' (Figure 3.1(a)). For further considerations the curvature is defined as the variable

$$h' = 2H'. \tag{3.4}$$

Momentum Balance

The one-dimensional, unsteady momentum equation in dimensional form writes

$$\frac{\partial v'}{\partial t'} + v' \frac{\partial v'}{\partial x'} = -\frac{1}{\rho}\frac{\partial p'}{\partial x'} - \frac{1}{\rho}\frac{\partial w_f'}{\partial x'} \ , \tag{3.5}$$

where v' is the flow velocity, x' the coordinate in flow direction, t' the time, p' the pressure, ρ the liquid density and $\mathrm{d}w'_f$ the friction factor. Combining the pressure term from equation (3.5) with the YOUNG-LAPLACE equation (3.3) yields

$$\frac{\partial p'}{\partial x'} = -2\sigma \frac{\partial H'}{\partial x'} = -\sigma \frac{\partial h'}{\partial x'} \ , \tag{3.6}$$

where the mean curvature term is substituted with (3.4) and $p_a = \text{const}$ is assumed. The final form of the one-dimensional, unsteady momentum equation writes

$$-\frac{\partial v'}{\partial t'} = -\frac{\sigma}{\rho}\frac{\partial h'}{\partial x'} + v'\frac{\partial v'}{\partial x'} + \frac{1}{\rho}\frac{\partial w'_f}{\partial x'} \ . \tag{3.7}$$

Mass Balance

The volumetric flow rate balance writes

$$-\frac{\partial A'}{\partial t'} = \frac{\partial A'}{\partial x'}v' + \frac{\partial v'}{\partial x'}A' \ . \tag{3.8}$$

The flow cross-section area A' is a function of x' due to the change of the free surface profile along the flow direction. Consequently, the mean flow velocity is also a function of x' such as

$$v'(x') = \frac{1}{A'}\int_{A'} v'_x(x', y', z')\mathrm{d}y'\mathrm{d}z' \ , \tag{3.9}$$

where v'_x is the component of the velocity in the x' direction (flow direction).

3.2 Modeling of the Free Liquid Surface

A relation between the mean curvature of the free surface h' and the flow cross-sectional area A' is required in order to solve the transport equations (3.7) and (3.8). It will be shown that h' and A' can be defined as a function of k' and its derivatives with respect to x'. The first and second derivatives are defined as $\mathrm{d}_{x'}k' = \mathrm{d}k'/\mathrm{d}x'$ and $\mathrm{d}_{x'x'}k' = \mathrm{d}^2k'/\mathrm{d}x'^2$, respectively. The following considerations apply for the groove and parallel plates since the mathematical model is almost identical for both geometric configurations. What differs is the determination of the flow cross-sectional area A' and the friction loss term $\mathrm{d}w'_f/\mathrm{d}x'$ in the momentum Equation (3.7). The cross-section is greater for the groove than for the parallel plates because the narrowing of the cross-section area occurs only on one side for the groove (Figure 3.1(e)).

In the following considerations, it is distinguished between two cases: (i) the contact line of the free surface is pinned along the edges of the channel walls, and (ii) the free surface is not pinned and free to move with a zero degree contact angle (free contact line). In the second case, the free surface moves inwards between the channel walls, and the cross-sectional area decreases further.

Free Surface Curvature

In general, the mean curvature of the free surface $z' = z'(x', y')$ can be derived as [6]

$$H'(x', y') = \frac{z'_{y'y'}[1 + z'^2_{x'}] - 2z'_{x'}z'_{y'}z'_{x'y'} + z'_{x'x'}[1 + z'^2_{y'}]}{2[1 + z'^2_{x'} + z'^2_{y'}]^{3/2}} \ , \tag{3.10}$$

where $z' = f(x', y')$ is the position of the liquid surface over the area of the open channel with $x \in [0, l]$ and $y \in [-a/2, a/2]$. The subscripts denote partial derivatives $z'_i = \partial z'/\partial i$, $z'_{ij} = \partial^2 z'/\partial i \partial j$, with $i, j \in \{x', y'\}$. For the parallel plates, the lower and upper free surfaces are assumed to be symmetric with respect to the plane $y = 0$ (justified by the low Bo numbers). Assuming the free surface contour $k' = z'(x', y' = 0)$ the Equation (3.10) reduces to

$$H' = \frac{k'_{y'y'}[1 + k'^2_{x'}] + k'_{x'x'}}{2[1 + k'^2_{x'}]^{3/2}} \; . \tag{3.11}$$

Combining the above equation with (3.3) and (3.4) yields

$$2H' = h' = \frac{1}{R'_1} + \underbrace{\frac{k'_{x'x'}}{[1 + k'^2_{x'}]^{3/2}}}_{R'_2{}^{-1}} \tag{3.12}$$

with the derivatives $k'_{x'} = \mathrm{d}k'/\mathrm{d}x'$ and $k'_{x'x'} = \mathrm{d}^2k'/\mathrm{d}x'^2$. For an arbitrary point C of the profile (Figure 3.1(a)) the second term in equation (3.12) defines the portion of the curvature in the principal normal plane x, z, which is given by the inverse principal radius of curvature $1/R'_2$ (curvature in flow direction). The first term, gives the portion of the curvature in the principal normal plane $(y, \hat{z})$ defined by the inverse principal radius of curvature $1/R'_1$ (orthogonal to $1/R'_2$).

Area Function of the Flow Cross Section

The flow cross-sectional areas at the channel inlet and outlet are constrained/defined with the geometric properties of the channel (gap distance a and the width b). The area A' decreases between $x = 0$ and $x = x^*$ and increases between $x = x^*$ and $x = l$. The flow cross-sectional area can be related to the radius R' and the free surface contour k'. Two cases are distinguished: (i) the contact line is pinned along the edge of the channel walls (Figure 3.3(a)), and (ii) the contact line is not pinned and free to move with a zero contact angle (Figure 3.3(b)). For the pinned contact line assumption, the flow cross-sectional area for parallel plates can be defined as

$$A' = ab - 2A'_c \; , \tag{3.13}$$

where A'_c is the area of the circular segment as shown in Figure 3.3(a). A'_c can be defined as $A'_c = A'_{cs} - A'_{tp}$, where A'_{cs} is the area of the circular sector with the radius R' and A'_{tp} is the area of the triangular portion. Assuming the angle (in Figure 3.3(a))

$$\varphi = 2\text{arcsin}\frac{a}{2R'} \tag{3.14}$$

the area of the circular sector can be written as

$$A'_{cs} = \pi R'^2 \frac{\varphi}{2\pi} = R'^2 \text{arcsin}\frac{a}{2R'} \; . \tag{3.15}$$

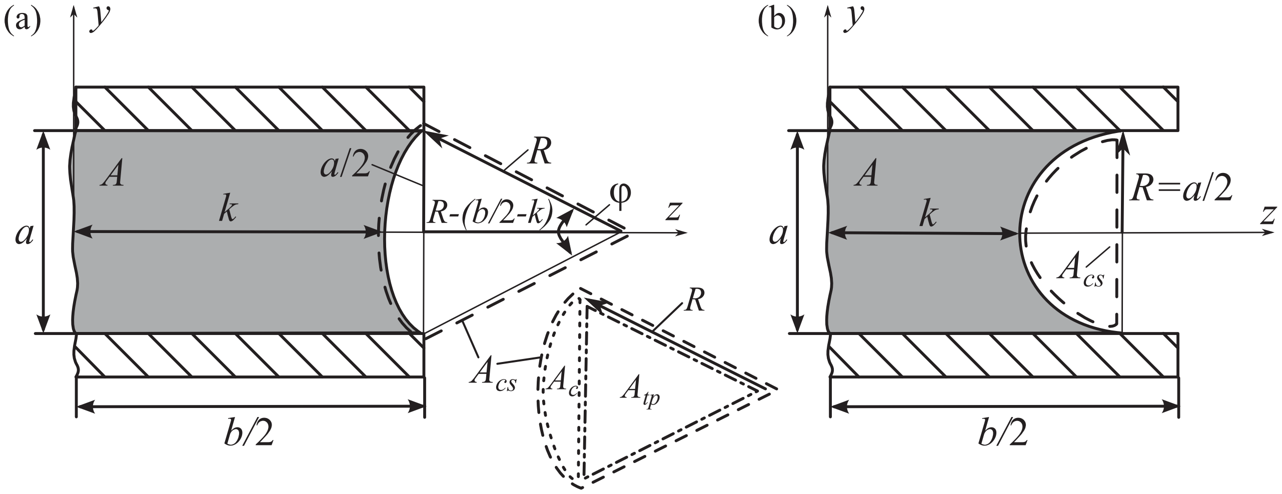

Figure 3.3: Cross-section of the channel in the (y, z)-plane. Due to the symmetry with respect to $y = 0$ only the upper half (z positive) of the channel is shown. (a) pinned contact line assumption (constant contact line position); (b) free contact line assumption (constant contact angle), where the area of the circular sector A_{cs} is equal to the half of the area of the circle with the radius $R' = a/2$.

The area of the triangular portion is defined as

$$A'_{tp} = \frac{a}{2}\left(R' - \frac{b}{2} + k'\right) . \tag{3.16}$$

Combining equations (3.13), (3.15), and (3.16) yields

$$A' = ab - 2\left[R'^2 \arcsin\frac{a}{2R'} - \frac{a}{2}(R' - \frac{b}{2} + k')\right] \tag{3.17}$$

for $k' \geq b/2 - a/2$ (pinned contact line assumption). For the free contact line assumption, the flow cross section area can be determined as (Figure 3.3(b))

$$A' = 2k'a + a^2 - \frac{\pi}{4}a^2 . \tag{3.18}$$

In this case the radius is constant $R' = a/2$ (Figure 3.3(b)). Finally, the flow cross-sectional area function for the parallel plates can be written as

$$F'_A(k')^{PP} = A'^{PP} = \begin{cases} ab - 2R'^2 \arcsin\left(\dfrac{a}{2R'}\right) + a\left(R' - \dfrac{b}{2} + k'\right) & ; \; k' \geq \dfrac{b}{2} - \dfrac{a}{2} , \\ 2k'a + a^2 - \dfrac{\pi}{4}a^2 & ; \; k' < \dfrac{b}{2} - \dfrac{a}{2} . \end{cases} \tag{3.19}$$

The flow cross-sectional area in the groove channel differs from the parallel plates since only one free surface is present. The area function for the groove channel can be defined as

$$F'_A(k')^{GR} = A'^{GR} = \begin{cases} ab - R'^2 \arcsin\left(\dfrac{a}{2R'}\right) + \dfrac{a}{2}\left(R' - \dfrac{b}{2} + k'\right) & ; \; k' \geq \dfrac{b}{2} - \dfrac{a}{2} , \\ \dfrac{a^2}{2} + k'a - \dfrac{\pi}{8}a^2 + \dfrac{ab}{2} & ; \; k' < \dfrac{b}{2} - \dfrac{a}{2} , \end{cases} \tag{3.20}$$

where also two cases are distinguished: pinned contact line for $k' \geq b/2 - a/2$ and free contact line for $k' < b/2 - a/2$.

Furthermore, the radius R' can be defined accounting for geometric relations shown in Figure 3.3(a) as

$$\left(\frac{a}{2}\right)^2 + \left(R' - \frac{b}{2} + k'\right)^2 = R'^2 \ . \tag{3.21}$$

Rearranging the above equation yields the definition of the radius

$$R'(k') = \begin{cases} \dfrac{a^2 + (b - 2k')^2}{4(b - 2k')} & ; \quad k' \geq \dfrac{b}{2} - \dfrac{a}{2} \ , \\ \dfrac{a}{2} & ; \quad k' < \dfrac{b}{2} - \dfrac{a}{2} \ , \end{cases} \tag{3.22}$$

where upper and lower part represent pinned and free contact line assumptions, respectively.

First Principal Radius of Curvature

The first principal radius of curvature R'_1 can be identified in the $y, \hat{z}$-plane (Figure 3.4(b)) which is tilted by the angle θ from the cross-sectional y, z-plane. The angle θ can be derived from the geometric relation in Figure 3.4(a)

$$1 = \sin^2\theta + \cos^2\theta \ . \tag{3.23}$$

Multiplication of the equation (3.23) with $\cos^{-2}\theta$ yields

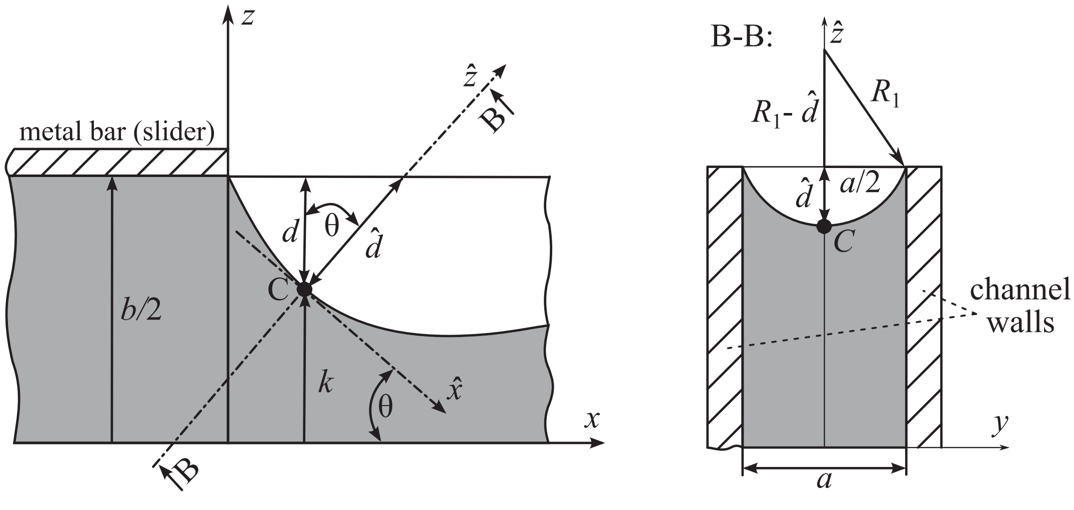

(a) (b)

Figure 3.4: (a) Section of the channel in the (x, z) - plane. (b) Section B-B through the channel in the $(y, \hat{z})$ - plane containing the point C.

$$\cos^{-2}\theta = \tan^2\theta + 1 \ , \tag{3.24}$$

where the angle

$$\cos\theta = d'/\hat{d}' \tag{3.25}$$

relates both displacements d' and $\hat{d}'$ in the x, z and $\hat{x}, \hat{z}$ planes, respectively. The slope of the free surface contour k' shown in Figure 3.4(a) can be defined as

$$\tan\theta = k'_{x'} \ , \tag{3.26}$$

where $k'_{x'}$ is the first derivative of the contour k' along x'. Combining equations (3.24) and (3.26) yields

$$\left(\frac{\hat{d}'}{d'}\right)^2 = k'^2_{x'} + 1 \ . \tag{3.27}$$

Equation (3.27) yields the displacement $\hat{d}'$ in the $y, \hat{z}$ - plane

$$\hat{d}' = d'[1 + k'^2_{x'}]^{1/2} = \left(\frac{b}{2} - k'\right)[1 + k'^2_{x'}]^{1/2} \ , \tag{3.28}$$

where $d' = b/2 - k'$ is the free surface displacement in the x, z-plane. The equation relates the displacement $\hat{d}$ (in the $\hat{x}, \hat{z}$-plane) to the free surface contour k visible in the x, z plane.

The radius R'_1 can be defined as

$$\left(\frac{a}{2}\right)^2 + (R'_1 - \hat{d}')^2 = R'^2_1 \tag{3.29}$$

what follows from the geometric constraints shown in Figure 3.4(b). Rearranging the equation (3.29) yields

$$R'_1 = \frac{\left(\frac{a}{2}\right)^2 + \hat{d}'^2}{2\hat{d}'} \ . \tag{3.30}$$

Equation (3.30) holds for $\hat{d}' \leq a/2$, which means that the free surface is pinned at the edges of the channel walls and R'_1 may change between infinity (plane surface) and $R'_1 = a/2$ (maximum curvature). Combining equations (3.28) and (3.30) yields the definition of the first principal radius

$$R'_1 = \begin{cases} \dfrac{a^2 + (b - 2k')^2[1 + k'^2_{x'}]}{4(b - 2k')[1 + k'^2_{x'}]^{1/2}} & ; \quad k \geq \dfrac{b}{2} - \dfrac{a}{2}[1 + k'^2_{x'}]^{-1/2} \ , \\ \dfrac{a}{2} & ; \quad k < \dfrac{b}{2} - \dfrac{a}{2}[1 + k'^2_{x'}]^{-1/2} \ , \end{cases} \tag{3.31}$$

where the upper and lower parts represent the pinned and free contact line assumptions, respectively. By applying equation (3.31) to the Young-Laplace equation (3.12) the capillary pressure is given as a function of k' and its derivatives with respect to x' ($h' = f(k', \mathrm{d}_x k', \mathrm{d}_{xx} k')$). For any point of the profile along x, the first principal radius of curvature is defined according to Equation (3.31). A special case is the point of the minimum cross section (k_{min}) where $R' = R'_1$.

3.3 Pressure Losses

The irreversible pressure loss in Equation (3.7) depends on the geometry of the channel, but also on whether the flow is developed. It will be shown that the friction coefficient $\mathrm{d}w'_f$ is well determined for a fully developed flow in the channel. When the flow is still developing, $\mathrm{d}w'_f$ is a complex function of the location x' along the channel.

In general, when a flow with a constant velocity profile enters a duct, it takes a certain distance for the flow to fully develop. This length is called the entrance length L_e and the entrance region is defined between the duct inlet and the location where the flow is fully developed (Figure 3.5(c)). Said transformation is caused by molecular momentum transport from the wall into the liquid. The friction coefficient in Equation (3.7) can be defined as

$$\mathrm{d}w'_f = \mathrm{d}w'_{Pf} + \mathrm{d}w'_{Sf} \ , \tag{3.32}$$

where $\mathrm{d}w'_{Pf}$ is the component for the fully developed Poisuille flow and $\mathrm{d}w'_{Sf}$ the component for the entrance region.

Pressure Drop of the Fully Developed Flow

The fully developed laminar flow between parallel plates can be treated as a Poiseuille flow. The component for the fully developed flow in Equation (3.32) can be then modeled as [98]

$$\frac{\mathrm{d}w'_{Pf}}{\mathrm{d}x'} = \frac{\rho v'^2}{2}\frac{K_{Pf}}{\mathrm{Re}D_h} \ , \tag{3.33}$$

where K_{Pf} is a geometry-dependent coefficient. It can be defined, in terms of the Poiseuille Number $\mathrm{Po} = C_f\mathrm{Re}$, where C_f is the fanning friction factor, as $K_{Pf} = 4\mathrm{Po}$. For the ducts with rectangular cross section, White's et al. relation can be used to determine the Po values in dependency on the channel aspect ratio $\Lambda = b/a$ [99]. The parallel plates configuration is a limiting case of the rectangular channel, where the channel gap distance a approaches zero. The Poiseuille number for parallel plates is then $\mathrm{Po}^{\mathrm{PP}} = 24$ and the corresponding friction factor $K_{Pf}^{PP} = 96$. The groove can be treated as a half rectangular section (due to the symmetry and negligible shear stress on the free surface). The aspect ratio $\Lambda^{-1} = 0.2$ for the groove can be translated to ratio $\Lambda^{-1} = 0.1$ as for a full rectangular section. In this case, $\mathrm{Po} = 21.6$, and accordingly $K_{Pf}^{GR} = 86.4$.

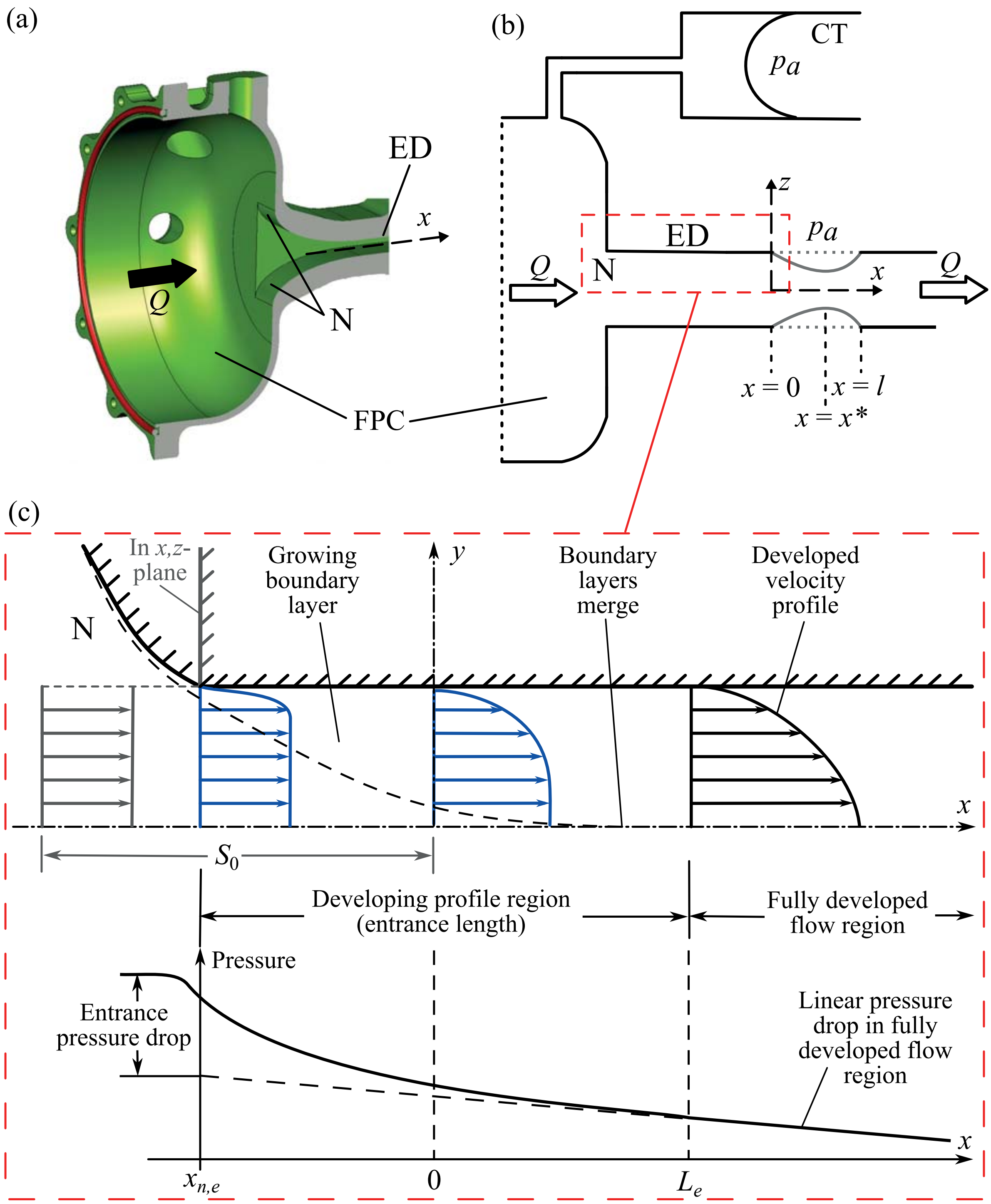

Figure 3.5: Inlet section of the CCF experimental setup. (a) 3D rendering of the flow preparation chamber FPC and the inlet nozzle N converting into the entrance duct ED (cross-sectional view). (b) Schematic of the flow configuration with the main components, where CT is the compensation tube. $x = 0$ and $x = l$ are the open channel inlet and outlet, respectively. $x = x^*$ is the point of the minimum cross-section area. Free liquid surfaces in the test channel and in the CT are exposed to ambient pressure p_a. (c) Developing velocity profiles and pressure evolution in the inlet section of the CCF channel. Partially developed velocity profiles at the nozzle outlet ($x_{n,e}$), and the channel inlet ($x = 0$) are depicted with blue color.

It must be noted that the above determination of the coefficient K_{Pf} applies for the rectangular channel with $\Lambda^{-1} = 0.2$. In the open section of the capillary channel the flow cross-section area A' changes due to the free surface retraction. Consequently, K_{Pf} changes locally, depending on A'. In the following consideration, however, a constant value of K_{Pf} is assumed.

Pressure Drop of the Developing Flow

The inlet section of the CCF channel consists of the nozzle and the flow preparation chamber to regulate the flow before it enters the open section of the channel (Figure 3.5(a)). The boundary layer develops already along the walls of said contraction such that the flow at the inlet of the channel ($x = 0$) does not possess a constant velocity profile (Figure 3.5(b)). Three-dimensional simulation of the flow in the inlet section of the CCF channel confirms this assumption (will be discussed in Section 9.2.2). The development of the flow profile leads to the additional pressure loss modeled with the method of Sparrow [80]

$$\frac{\mathrm{d}w'_f}{\mathrm{d}x'} = \frac{\rho v'^2}{2} \frac{1}{\mathrm{Re} D_h} (K_{Pf} + 16\hat{K}_{Sf}(x')) \;, \tag{3.34}$$

where the coefficient $\hat{K}_{Sf}$ depends on the length x' along which the flow develops. This length x' is transformed into a scaled length $\hat{x}$

$$\hat{x} = \frac{16x'}{\mathrm{Re} D_h} \;, \tag{3.35}$$

for which the dependence of $\hat{K}_{Sf}$ can be fitted as

$$\hat{K}_{Sf}(\hat{x}) = c_1 c_2 c_3 \exp\left(c_2 \hat{x}^{c_3}\right) \hat{x}^{(c_3 - 1)}, \tag{3.36}$$

with the constants $c_1 = -0.6203$, $c_2 = -9.9948$, $c_3 = 0.6576$. It is assumed that the flow is fully developed at the at $\hat{x} = 0.24$. In such a case Equation (3.36) yields $\hat{K}_{Sf}(\hat{x} = 0.24) = 0$ and consequently the right term in the brackets of Equation (3.34) vanishes.

In the CCF experiment however, the velocity profile at the channel inlet ($x = 0$) is not constant. Therefore it is necessary to virtually extend the channel upstream by a certain length denoted with $\hat{s}_0$ over which the flow velocity would develop from a constant profile to one which is the same as in real flow (Figure 3.5(c)). Therefore, two additional parameters are introduced

$$\alpha = \frac{\hat{s}_0}{\hat{x}} \;, \tag{3.37}$$

and

$$\beta = 1 - \alpha \;, \tag{3.38}$$

so that

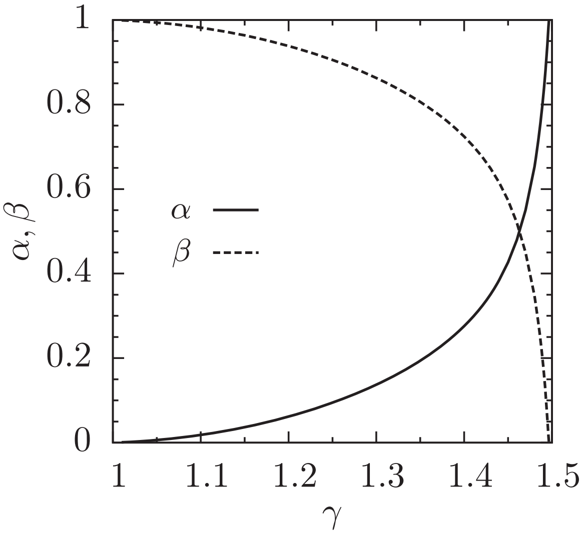

Figure 3.6: Parameters α (Equation (3.41)) and β (Equation (3.38)) versus the flow development ratio γ.

$$\hat{s}_0 = \alpha \hat{x} = \hat{x}(1 - \beta) \ . \tag{3.39}$$

The parameters α and β are related to the flow development ratio γ (Figure 3.6) defined as the ratio of local maximum velocity over the average velocity

$$\gamma = \frac{u(y = 0)}{v} \ . \tag{3.40}$$

The parameter α can be approximated as

$$\alpha = (\gamma - 1) \left(\gamma - 1 - \frac{c_4}{\gamma - c_5} \right) , \tag{3.41}$$

with the constants $c_4 = 0.0345$ and $c_5 = 1.5192$. For fully developed flow at $\hat{x} = 0.24$ the flow development ratio reaches the value $\gamma = 1.5$ for the parallel plates [80]. In such a case $\alpha = 1$ and $\beta = 0$ (Figure 3.6).

The velocity profile at the open channel inlet is dictated by the geometry of the duct upstream of the channel and can be determined with three-dimensional CFD simulations. The factor β can be defined as a function of the flow rate at the channel inlet as

$$\beta = L_0 + L_1 \frac{\mathrm{Oh}}{2 v_0 A_0} , \tag{3.42}$$

where v_0 and A_0 are the velocity and the cross section area at the channel inlet ($x = 0$). It will be shown later that the flow rate $Q = A_0 v_c$ is a characteristic quantity used to scale the flow rate for the non-dimensional mathematical model. Three cases can be distinguished in terms of the flow condition at the capillary channel inlet ($x = 0$): (i) undeveloped flow (constant velocity profile), where $L_0 = 1$ and $L_1 = 0$; (ii) developing flow: $L_0 = 1$ and $L_1 < 0$; and developed flow (parabolic velocity profile), where $L_0 = 0$ and $L_1 = 0$. It will be shown in Section 6.2.1 that for the flow in the considered capillary channel the parameter L_1 is usually $-900 < L_1 < 0$.

3.4 Dimensionless Model

Scaling and Characteristic Numbers

Dimensionless quantities are used to solve the model equations. Model constants and scaling details are given in Table 3.1. The prime ($'$) indicates the dimensional variables. All lengths (except the x coordinate which is scaled with the channel length l') and the curvature h are scaled with the half of the channel's gap distance $a/2$. The cross sectional area is non-dimensionalized with the characteristic area $A_0 = ab$. The pressure is scaled with the characteristic pressure $p_c = 2\sigma/a$ which arises from the scaling of the YOUNG-LAPLACE Equation (3.3). The velocity is scaled with the characteristic velocity $v_c = \sqrt{2\sigma/(\rho a)}$ which is a characteristic property determined in the experiments on the capillary rise of liquids between parallel plates [19]. It scales the maximum velocity of spontaneous, or capillary-driven flows. The hydraulic diameter is defined as $D_h = 4A/P$, where $A = A_0$, and the wetted perimeter $P^{PP} = 2b$, and $P^{GR} = a + 2b$, for parallel plates and groove channel, respectively. The critical flow rate can be written as a function of following dimensional parameters

Table 3.1: Model constants and scaled variables of the 1D model, where: A_0 - characteristic area; p_c - characteristic pressure; D_h - hydraulic diameter; v_c - characteristic velocity; h' - mean curvature; Q' - flow rate; R_i' - radius of curvature; p' - liquid pressure; k' - free surface contour; A' flow cross-sectional area; d' - free surface displacement. A prime $'$ indicates a dimensional variable scaled for the non-dimensional model.

Lengths	Other variables	Model constants
$x = x'/l'$	$v = v'/v_c$	$A_0 = ab$
$y = y'/(a/2)$	$p = p'/p_c$	$p_c = 2\sigma/a$
$z = z'/(a/2)$	$A = A'/A_0$	$v_c = \sqrt{2\sigma/(\rho a)}$
$k = k'/(a/2)$	$t = t'/(l/(2v_c))$	$D_h^{PP} = 2a$
$R = R'/(a/2)$	$Q = Q'/(A_0 v_c)$	$D_h^{GR} = 4ab/(a+2b)$
$R_{1,2} = R'_{1,2}/(a/2)$	$s_0 = s'_0/l'$	
$d = d'/(a/2)$	$\delta = \delta^{'}/(2bv_c^2)$	
$l = l'/(a/2)$	$h = h'/(2/a)$	

$$Q_c' = f(\rho, \mu, \sigma, \eta, a, b, l') \ , \tag{3.43}$$

with eight dimensions

$$\begin{array}{cccccccc} Q_c' & \rho & \mu & \sigma & \eta & a & b & l' \\ \left[\dfrac{\mathrm{m}^3}{\mathrm{s}}\right] & \left[\dfrac{\mathrm{kg}}{\mathrm{m}^3}\right] & \left[\dfrac{\mathrm{kg}}{\mathrm{m\ s}}\right] & \left[\dfrac{\mathrm{kg}}{\mathrm{s}^2}\right] & [-] & [\mathrm{m}] & [\mathrm{m}] & [\mathrm{m}] \end{array} ,$$

and three fundamental units

$$\begin{array}{ccc} \text{mass} & \text{length} & \text{time} \\ [\mathrm{kg}] & [\mathrm{m}] & [\mathrm{s}] \end{array} .$$

In this work perfectly the wetting liquid with a contact angle $\eta = 0$ is assumed. This parameter is skipped in the following considerations. According to the Π-theorem of BUCKINGHAM there are five $(8-3=5)$ independent dimensionless parameters describing the flow in the considered capillary channels. The dimensionless critical flow rate $Q_c = Q_c'/A_0'v_c$ is therefore a function of four characteristic numbers

$$Q_c = f(\mathrm{Oh}, \tilde{l}, \Gamma, \Lambda) \ . \tag{3.44}$$

The OHNESORGE number relates the viscous forces to inertial and surface tension forces. Oh is inversely proportional to the REYNOLDS number $\mathrm{Re_c}$ based on the characteristic velocity v_c

$$\mathrm{Oh} = \sqrt{\frac{\rho\nu^2}{\sigma 2a}} = \frac{2\nu}{D_h v_c} = \frac{2}{\mathrm{Re_c}} \quad \text{with} \quad \mathrm{Re_c} = \frac{D_h v_c}{\nu} \ . \tag{3.45}$$

The dimensionless flow length corresponds to the length introduced in entrance flow problems [80]

$$\tilde{l} = \frac{\mathrm{Oh}\, l'}{2D_h} \ . \tag{3.46}$$

The length aspect ratio defines the aspect ratio between the length of the channel and the hydraulic diameter

$$\Gamma = \frac{D_h}{4l'} \quad ; \quad \Gamma^{\mathrm{PP}} = \frac{a}{2l'} \quad ; \quad \Gamma^{\mathrm{GR}} = \frac{ab}{l'(a+2b)} \ . \tag{3.47}$$

The channel aspect ratio is defined as

$$\Lambda = \frac{b}{a} \ . \tag{3.48}$$

Final Equations

Applying scaling and dimensionless numbers to the momentum and continuity Equations (3.7), (3.8) yields a set of governing equations

$$-\frac{\partial v}{\partial t} = -\frac{\partial h}{\partial x} + v\frac{\partial v}{\partial x} + \frac{K_f}{2}\,\tilde{l}\; v, \tag{3.49}$$

$$-\frac{\partial A}{\partial t} = v\frac{\partial A}{\partial x} + A\frac{\partial v}{\partial x}, \tag{3.50}$$

where K_f is the friction factor. The capillary pressure h is related to the the cross-sectional area A and the free surface contour k. The area functions (Equations (3.19) and (3.20)) in non-dimensional form write

$$F_A(k)^{PP} = \begin{cases} 1-(2\Lambda)^{-1}\left(R^2\arcsin R^{-1}+R-\Lambda+k\right) & ; \quad k \geq \Lambda-1 \ , \\ (\Lambda)^{-1}\left(1+k-\dfrac{\pi}{4}\right) & ; \quad k < \Lambda-1 \ , \end{cases} \tag{3.51}$$

$$F_A(k)^{GR} = \begin{cases} 1-(4\Lambda)^{-1}\left(R^2\arcsin R^{-1}+R-\Lambda+k\right) & ; \quad k \geq \Lambda-1 \ , \\ (2\Lambda)^{-1}\left(1+k-\dfrac{\pi}{4}\right)+\dfrac{1}{2} & ; \quad k < \Lambda-1 \ , \end{cases} \tag{3.52}$$

for the parallel plates and groove channel, respectively. Scaling of the radius of curvature (Equation (3.22)) yields for both geometries

$$R(k) = \begin{cases} \dfrac{1+(\Lambda-k)^2}{2(\Lambda-k)} & \text{for} \quad k \geq \Lambda-1 \ , \\ 1 & \text{for} \quad k < \Lambda-1 \ . \end{cases} \tag{3.53}$$

The pressure is related to the curvature of the free surface by the scaled YOUNG - LAPLACE Equation (3.12) which in dimensionless form writes

$$h(k) = \frac{1}{R_1} + \underbrace{\frac{\Gamma^2 \mathrm{d}_{xx}k}{\left[1+\Gamma^2(\mathrm{d}_x k)^2\right]^{3/2}}}_{R_2^{-1}} \ , \tag{3.54}$$

where the first principal radius (Equation (3.31)) in dimensionless form writes

$$R_1 = \begin{cases} \dfrac{1+(\Lambda-k)^2\left[1+\Gamma^2(\mathrm{d}_x k)^2\right]}{2(\Lambda-k)\left[1+\Gamma^2(\mathrm{d}_x k)^2\right]^{1/2}} & \text{for} \quad k \geq \Lambda-\left[1+\Gamma^2(\mathrm{d}_x k)^2\right]^{-1/2} \ , \\ 1 & \text{for} \quad k < \Lambda-\left[1+\Gamma^2(\mathrm{d}_x k)^2\right]^{-1/2} \ . \end{cases} \tag{3.55}$$

This coupled partial differential equation set of second order (first order in h and second order in k) is solved with finite differences with the `ccFlow` solver (description in Section 5.1).

Boundary Conditions

The boundary conditions are given by the flow velocity at the channel outlet v_1, the position of the liquid surface contour k at the channel inlet and outlet, and the pressure (curvature) at the channel inlet h_0

$$v(x=1) = v_1 \ , \tag{3.56}$$

$$k(x=0) = k(x=1) = \Lambda \ , \tag{3.57}$$

$$h(x=0) = h_0 \ . \tag{3.58}$$

The flow is driven by the pump located downstream from the channel outlet. Due to the scaling of the flow rate Q with the characteristic area A_0, the flow velocity at the channel outlet can be assumed as $v_1 = Q$. The cross-sectional area A_0 at the channel inlet is equal to the cross-section area A_1 at the channel exit. The liquid surface is pinned (at the channel inlet and outlet) along the edges of the closed duct. Thus, the k position is defined with the aspect ratio Λ. The capillary pressure at the channel inlet $h_0 = p_a - p_0$ is defined by the capillary pressure of the meniscus in the compensation tube plus convective and frictional flow losses in the inlet section of the CCF setup. It can be expressed by

$$h_0 = \frac{\partial v_0}{\partial t} l_0 + K_0 + K_1 \frac{\mathrm{Oh} v_0}{4} + K_2 \frac{v_0^2}{2} + K_3 \mathrm{Oh} \left[v_0 - v_1 \right] , \tag{3.59}$$

where $v_0 - v_1$ is the velocity difference between channel inlet and outlet velocity, which causes liquid to move into the compensation tube (CT). K_0 defines the pressure induced by the meniscus of the compensation tube (Figure 3.5(b)) and is defined as

$$K_0 = \frac{(p'_a - p')a}{2\sigma} . \tag{3.60}$$

The meniscus in the CT defines the system pressure at the point where it is connected to the flow preparation chamber. Along the fluid loop the pressure adapts corresponding to the flow conditions. K_1 and K_2 describe the pressure loss in the nozzle up to the channel inlet ($x = 0$) and are determined numerically by three-dimensional simulations of the flow in the inlet section of the CCF setup (will be discussed in Section 9.2.2). The factor K_3 describes the pressure loss due to the displacement of the liquid column between the compensation tube and the channel inlet and is approximated with a circular tube flow as $K_3 = \mathrm{Oh}^{-1}$ [32]. The length $l_0 = 155.2$ ($l'_0 = 388$ mm) is the length of the intersection between the CT and the channel inlet.

3.5 Transient Flow Stability Model

Compared to steady flow, additional flow effects take place when the flow is transient. These effects are caused by the dynamic liquid transition. Depending on whether the flow is accelerated or decelerated, the demand on the liquid in the fluid loop changes. This is compensated by the liquid stored in the compensation tube. The inertia of the liquid column in the intersection between the CT and the test channel (Figure 3.5(b)) influences the pressure at the channel inlet.

Furthermore, during the CCF experiment it was observed that the length of the free surface (Figure 3.7) in the test channel contributes to the transient flow stability. This effect is based on the flexibility of the linear part of the free surface.

Another effect specific for closed fluid loop systems (as the CCF experiment) is the feedback effect of the fluid loop. In the CCF setup, the flow is driven by the pump located downstream from the channel outlet. The liquid is not only drawn out of the channel outlet, but is also forced through the intermediate components into the channel inlet. In case of transient flow this may increase the local pressure at the channel inlet, and consequently the stability of the free surface during the transient flow. For steady flow the CT defines the pressure of the system (will be discussed in Chapter 6).

In the following, a short overview of the transient stability model, which was recently published, is given [29]. The above mentioned transient flow effects are modeled based on theoretical considerations, numerical simulations, and experimental observation. In the transient model, which is an extension of the steady model, the inertia of the accelerated liquid column and the geometry of the free surface are taken into account. The dimensional variables are scaled according to the steady model scaling data (Table 3.1).

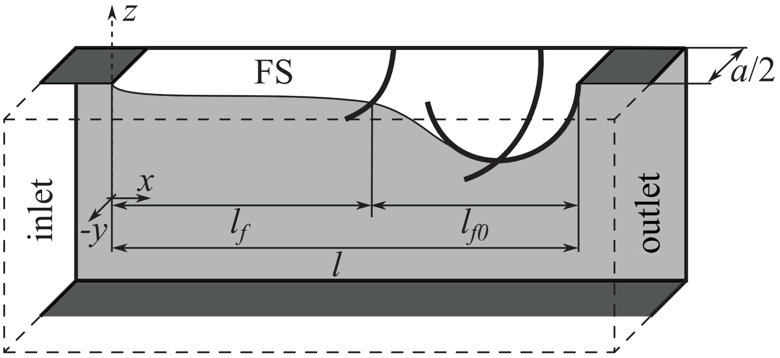

Figure 3.7: The capillary channel with free surface FS (view in the symmetry plane x, z at $y = 0$). Half of the free surface (y-positive) is shown. The flow is from left to the right. Bold lines are circular arcs approximating the free surface contour at a given point.

3.5.1 Transient Stability Limit

The acceleration of the liquid at the channel outlet (dynamic transition) is defined as $\delta = \Delta Q/\Delta t$, where ΔQ is the change of the flow rate over the given period of time Δt. The final flow rate after transition is defined as $Q = Q_{t=0} + \Delta Q$.

Both steady (convective acceleration) and transient (local acceleration) flow effects contribute to the free surface stability during the transition. The critical flow rate after the transition (steady flow) and the critical acceleration (transient flow) are inversely proportional. In general, with increasing flow rate, the liquid pressure decreases, and consequently the free surface collapses at the lower acceleration. In other words, the lower the flow rate at which transition takes place, the higher the maximum stable acceleration is. Therefore, the maximum stable acceleration δ_0 is defined for $Q = 0$, which means that there is no flow at the end of the transition. This requires a negative initial flow rate, which is beyond the CCF experiment capabilities. Neglecting the terms for the velocities in the pressure boundary condition Equation (3.59) yields

$$h_0 = \frac{\partial v_0}{\partial t} l_0 + K_0 \ , \tag{3.61}$$

where K_0 is the system pressure defined by the meniscus in the compensation tube CT (Figure 3.5(b)). The length l_0 is the liquid column length connecting the CT and the channel inlet $(x = 0)$.

The momentum change during the transition is balanced by the free surface indentation at the channel outlet (Figure 3.7). Thus, the stability limit is assumed to be at the maximum curvature of the indentation (point of the minimum cross-section). Integrating the momentum equation (3.49) between the channel inlet $(x = 0)$ and the point of the minimum cross-section $(x = x^*)$ for $v = 0$ and assuming the pressure according to Equation (3.61) yields

$$\int_0^{x^*} \frac{\partial v}{\partial t} dx = h^* - \frac{\partial v_0}{\partial t} l_0 - K_0 \ . \tag{3.62}$$

The integral on the left hand side can be neglected since the liquid column length $l_0 \gg (x^* - x_0)$. As a consequence, Equation (3.62) does not depend on the channel length. It will be shown later that the liquid in the vicinity of the channel inlet plays another role (flexibility). Furthermore, the liquid acceleration can be simplified as $\delta_0 = \partial v_0/\partial t$, so the momentum balance (3.62) can be written as

$$l_0 \delta_0 = h^* - K_0 \ . \tag{3.63}$$

It can be assumed, that the free surface indentation in the vicinity of the channel outlet is of almost hemispherical shape, as the liquid surface tends to minimize its surface energy. This was confirmed during the CCF experiments. The principal radii of the hemispherical indentation are equal to the half of the channel's width $R_1 = R_2 = 1$ (due to scaling with

$a/2$). Consequently, the maximum curvature at $x = x^*$ is $h^* = 2$. Based on these geometrical properties, the balance in Equation (3.63) yields the stability limit

$$l_0\delta_0 < 2 - K_0 \ . \tag{3.64}$$

and the transient stability constant

$$\delta_0 = \frac{h^* - K_0}{l_0} = \frac{2 - K_0}{l_0} \ . \tag{3.65}$$

The δ_0 is the maximum stable acceleration with the final flow rate $Q = 0$. The δ_0 is defined by geometric and fluid properties only and is considered as a system constant.

3.5.2 Augmented Stabilization (Flexibility Effect)

The channel length l defines the longitudinal length of the free surface. As shown in Figure 3.7 the free surface can be divided into two parts: the left part l_f (in the vicinity of the channel inlet) and the right part l_{f0} (in the vicinity of the channel outlet). For sufficiently long channels the left part is almost linear along the channel x-axis (with one principal radius of curvature) and is free to move during the liquid flow. The flexibility of the linear part of the free surface may enhance the flow stability. During the transition the flow rate in the test channel increases due to increased demand on the outlet (pump drives the flow downstream the channel outlet). Liquid from the "l_f-part" of the surface is relocated towards the outlet due to its "flexibility", satisfying the demand. As a consequence, the capillary pressure at the indentation decreases and the probability that the surface remains stable increases. The longer the channel the higher the compensatory effect of the flexible surface.

In the CCF experiment, it was observed that the changeover from the linear part of the free surface to the hemispherical takes place over a length of $a/2$ (one half of the channel's width). The curved part of the hemispherical free surface is estimated to be $l_{f0} = 3/2a = 3$ (due to scaling with $a/2$). The remaining part of the surface $l_f = l - l_{f0}$ is assumed to be flexible and therefore contributing to the relaxation of the acceleration effect. For $x \leq l_f = l - l_{f0}$ the free surface is supported by one radius which is *one half* in comparison to the surface area at the indentation where the limit δ_0 is defined. As a consequence of the *one radius* to *two radii* relation the flexibility coefficient yields

$$f_\infty = 0.5\delta_0 \ , \tag{3.66}$$

which is the maximum possible additional stability due to the surface flexibility for a sufficiently long channel ($l_f \to \infty$). Finally, the flexibility function for a finite channel length is defined as

$$f = f_\infty \frac{l_f}{l} \ , \tag{3.67}$$

where $f \neq 0$ for $l > l_{f0}$.

3.5.3 The Feedback Effect of the Fluid Loop

As already mentioned, during the transition the liquid is withdrawn from the test channel and forced into the channel inlet. This increases the inlet pressure and in consequence enhances the stability of the free surface. In the model the transient stability constant δ_0 (representing the maximum possible stable acceleration) is multiplied by an enhancement factor r. In the CCF setup, a flow separation chamber is located between the channel outlet and inlet. It is applied for the gas separation from the liquid loop. The technical aspects of the CCF hardware will be discussed in Section 4.1.1. The gas stored in the chamber (in the form of the gas bubble) influences the feedback effect. The chamber acts as a damping system due to the compressibility of the gas. The complete feedback effect takes place when there is no gas present in the flow preparation chamber. Such a scenario was tested during the CCF experiment. It is found that the maximum stable acceleration is 12 times higher when the flow separation chamber is empty ($V_g = 0$ and consequently $r = 12$). If there is gas present in the flow separation chamber, the damping effect occurs. As a consequence the feedback effect decreases. Dependency of the feedback ratio r on the gas volume V_g is shown in Figure 3.8(a). The feedback ratio r is defined as

$$r = \frac{r_0 - r_\infty}{1 + V_g/V_c} + r_\infty, \tag{3.68}$$

where V_c is a calibration coefficient for the setup defined by fitting the model between the r_0 and r_∞.

For a fully decoupled system no feedback effect is assumed (flow separation chamber full with gas). Consequently, the $V_g \to \infty, r \to r_\infty = 1$. This would be the case for the technical application, e.g. capillary vanes of a propellant management device as presented in Figure 1.1.

3.5.4 Formulation of the Transient Stability Model

The transient stability model can be formulated upon the model assumptions presented above. In the following, the six characteristic scenarios in terms of the transient flow state are presented. These illustrate the formulation of the transient stability model.

1. $Q = 0,\ r = 1,\ f = 0$ (point **A**, Figure 3.8(b))
   No flow at the end of transition (no steady flow effects). No flexibility ("short" channel) and feedback effects. The stability limit is defined by the transient stability constant

$$\delta = \delta_0. \tag{3.69}$$

2. $Q = 0,\ r > 1,\ f = 0$ (point **B**, Figure 3.8(b))
   No flow at the end of transition (no steady flow effects). No flexibility effect ("short" channel). Feedback effect due to liquid re-circulation is considered. The stability limit is

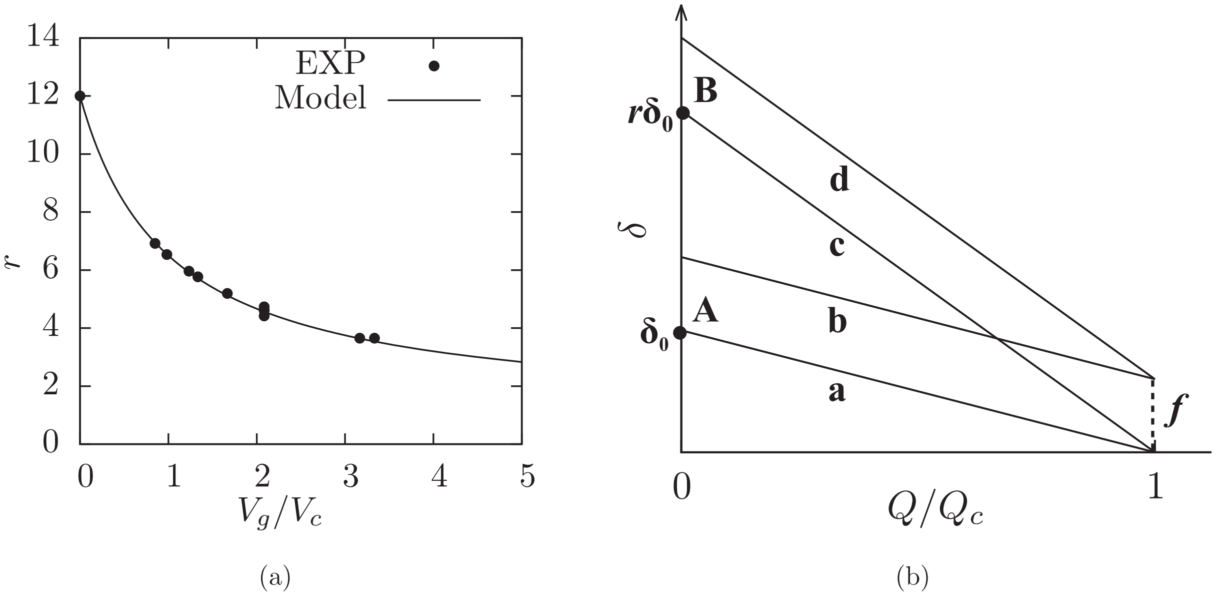

Figure 3.8: (a) The feedback ratio r due to the damping effect of the gas V_g in the PSC. The circles represent the actual feedback ratio of the performed transient stability measurements. The solid line represents the model based Equation (3.68). (b) The generic stability diagrams illustrating the transient stability model. (a) The maximum stable acceleration δ is a function of the flow rate Q. Points A (no feedback effect) and B (feedback effect) correspond to the maximum stable acceleration when no flow is present at the end of the transition ($Q = 0$). With increasing flow rate the maximum stable acceleration decreases (line a). The flexibility effect (line b), the feedback effect (line c) or a combination of both effects (line d) provide an enhancement of the stability.

defined as

$$\delta = r\delta_0. \tag{3.70}$$

3. $Q > 0,\ r = 1,\ f = 0$ (line **a**, Figure 3.8(b))
   Flow is present at the end of transition. No flexibility ("short" channel) and feedback effects. The stability limit is defined as

   $$\delta = \delta_0 \left(1 - \frac{Q}{Q_c}\right) . \tag{3.71}$$

   The stability limit δ decreases with increasing flow rates (due to increasing flow effects) until the critical steady flow rate Q_c is reached for $\delta = 0$.
4. $Q > 0,\ r = 1,\ f > 0$ (line **b**, Figure 3.8(b))
   Flow is present at the end of transition. No feedback effect. The flexibility effect is considered. The stability limit is defined as

   $$\delta = \delta_0 \left(1 - \frac{Q}{Q_c}\right) + f . \tag{3.72}$$

5. $Q > 0,\ r > 1,\ f = 0$ (line **c**, Figure 3.8(b))
   Flow is present at the end of transition. No flexibility effect ("short" channel). Feedback effect due to liquid re-circulation is considered. The stability limit is defined as

$$\delta = r\delta_0 \left(1 - \frac{Q}{Q_c}\right) \ . \tag{3.73}$$

6. $Q > 0,\ r > 1,\ f > 0$ (line **d**, Figure 3.8(b))
   Flow is present at the end of transition. The flexibility and the feedback effects are considered. The stability limit is defined as

$$\delta = r\delta_0 \left(1 - \frac{Q}{Q_c}\right) + f \ . \tag{3.74}$$

Rearranging Equation (3.74) yields the normalized transient stability model

$$\frac{\delta - f}{r\delta_0} = 1 - \frac{Q}{Q_c} \ . \tag{3.75}$$

Such a scaling provides a common description of all stability limits within one diagram, where the distorting influence of the feedback effect (CCF setup specific) is eliminated.

Chapter 4

CCF Experiment on ISS

Two CCF Experiments Units (EUs) were developed and transported to the ISS on board the space shuttle Discovery in year 2010. The first unit (EU#1) contains a test channel with two parallel glass plates and is designated for the investigation of the flow between parallel plates and in the groove. The second unit (EU#2) contains a wedge shaped test channel. It must be noted that the subject of this work is only the first unit EU#1.

The CCF experiment is designed to be controlled from the ground station in Bremen. For the CCF operation, the involvement of astronauts is needed only during the integration of the experiment unit into the designated environment on board the ISS and commissioning. The commissioning procedure includes several activities which are performed for initializing the flow loop and performing a functional test of the hardware. After the installation and commissioning, the entire CCF experiment operation is performed remotely via telescience (experiment patch is shown in Figure A.1 in Appendix A). The first unit EU#1 was operating for 66 days in 2011.

The CCF experiment hardware consists of three subsystems: (i) Experiment Unit (EU), (ii) Optical Diagnostic Unit (ODU), and (iii) Electronic Subsystem (ESS). The EU contains the Test Unit (TU) with the investigated Test Channel (TC), and the Fluid Management System (FMS). The ODU is used for video observation. It contains a parallel light source (background illumination) and the High Speed High Resolution Camera (HSHRC) used for the test channel observation. The ESS contains the electrical power system (EPS) and data handling system. In the following, a brief overview of the first subsystem - Experiment Unit (EU#1) will be given.

The CCF experiment unit is accommodated within the Microgravity Science Glovebox (MSG) in the ISS US lab Destiny [81]. The MSG is a double rack facility with 255 dm^3 work volume (Figure 4.1(e)).

4.1 Experimental Setup

A detailed description of the CCF experiment hardware was published in [8]. In the following, a brief overview of the experimental setup is given, with the focus on the fluid loop (closed loop as shown in Figure 4.2), data acquisition, and experiment operation and performance. The most important CCF experiment parameters are summarized in Table 4.1.

Table 4.1: Summary of the CCF experiment parameters. Liquid properties are at (30 ± 5)°C.

Parameter	Dimensionless numbers	Model constants
$a = 5$ mm	$\mathrm{Oh} = 2.26 \times 10^{-3}$	$A_0 = 1.25\ \mathrm{cm}^2$
$b = 25$ mm	$\Lambda = 5$	$p_c = 6.5$ Pa
$5 \leq l' \leq 48$ mm $(2 \leq l \leq 19.2)$	$5.64 \times 10^{-4} \leq \tilde{l}_{PP} \leq 5.42 \times 10^{-3}$	$v_c = 6.33$ cm/s
$\rho = (1610 \pm 10)\ \mathrm{kg/m^3}$	$6.21 \times 10^{-4} \leq \tilde{l}_{GR} \leq 5.96 \times 10^{-3}$	$D_h^{PP} = 1$ cm
$\nu = (0.72 \pm 0.06) \times 10^{-6}\ \mathrm{m^2/s}$	$0.052 \leq \Gamma \leq 0.5$	$D_h^{GR} = 0.9$ cm
$\sigma = (16.2 \pm 0.5) \times 10^{-3}$ N/m	$\eta = 0$	

4.1.1 Hardware

The key part of the CCF experiment unit is the test channel with fixed gap distance $a = 5$ mm and width $b = 25$ mm (Figures 1.2 and 4.1(a)). Movable sliders are used to vary the length of the open sections of the channel in a range of $5 \leq l' \leq 48$ mm. If both sliders are open, the parallel plates channel is formed (two free liquid surfaces). If only one slider is open, the groove channel is formed (one free surface). The fluid loop of the CCF experimental setup EU#1 is shown in Figure 4.2. The capillary channel (formed by two glass plates, as shown in Figure 4.1(a)) is located in the test section (TS). In the presented schematic, the groove configuration with the free surface (FS) contour (visible in the x, z-plane) is shown. The flow is driven by the gear pump (P) located downstream the channel and the flow meter is used to monitor the flow rate (F). The flow direction is depicted with arrows. The liquid enters the setup at the bottom (Figure 4.2) and is led through the following components: the phase separation chamber (PSC) with a screen (S) to withhold gas (separates gas from the liquid loop) and vanes (V) for the positioning of the gas bubble, the flow preparation chamber (FPC) with deflectors (D) to establish rotational flow and a perforated sheet (PS) for uniform velocity distribution, the compensation tube (CT), the nozzle (N), and the sliders (S1, S2). Plungers (K1, K2, K3) and valves (C1, C3, C4, C9, C11) serve for fluid control. The valve C9 prevents liquid leaking during shuttle launch and remains open during the experiment. The liquid plunger K2 and the gas plunger K3 are used for the maintenance of the fluids. Valve C3 can be used for the withdrawal of the gas stored in the FPC.

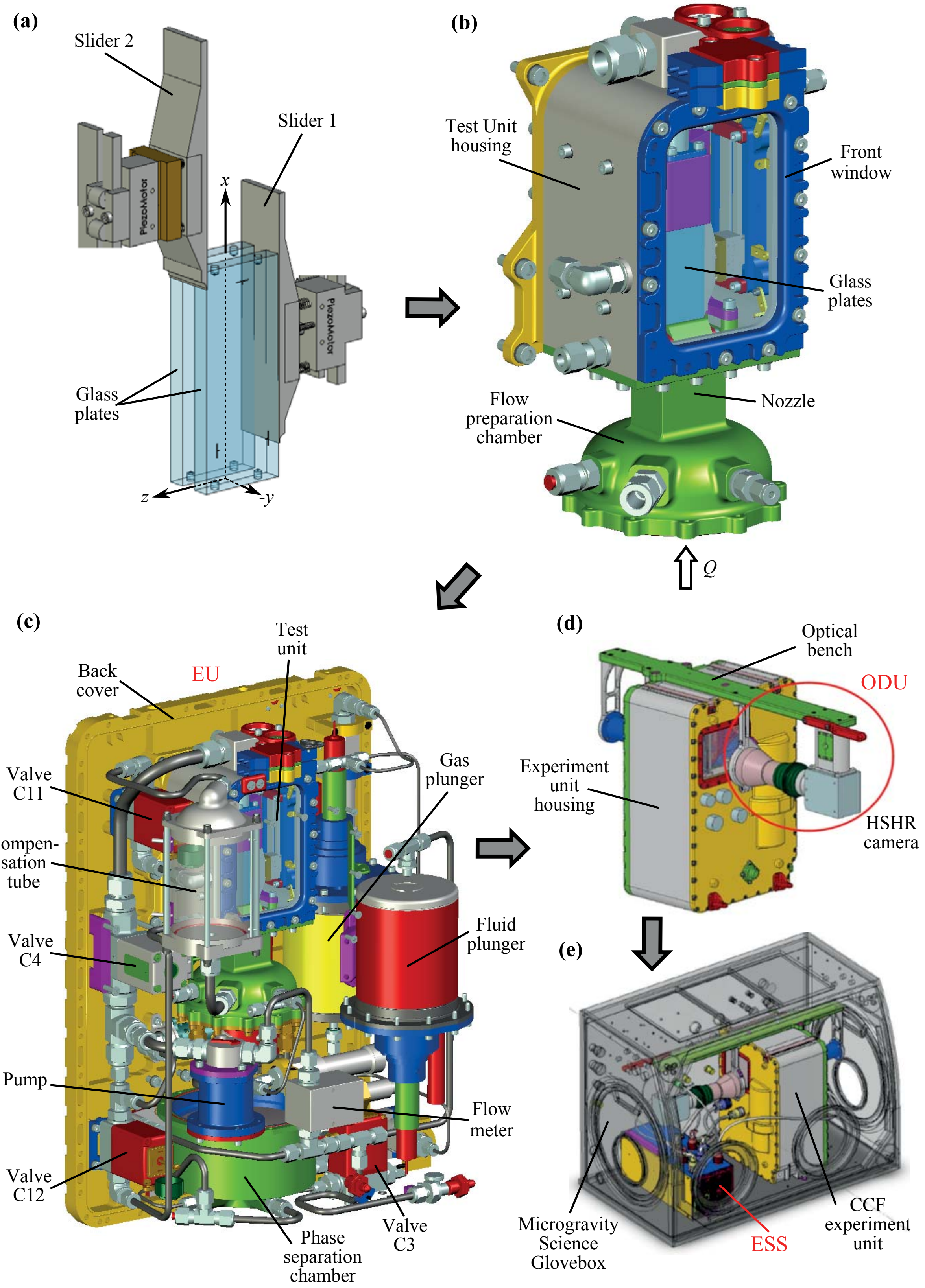

Figure 4.1: CCF hardware (CAD rendering). (a) test channel. (b) test unit housing the test channel. (c) main components of the CCF experiment unit (EU subsystem). (d) EU and ODU subsystems. (e) MSG facility hosting the CCF experiment hardware (EU, ODU, and ESS subsystems).

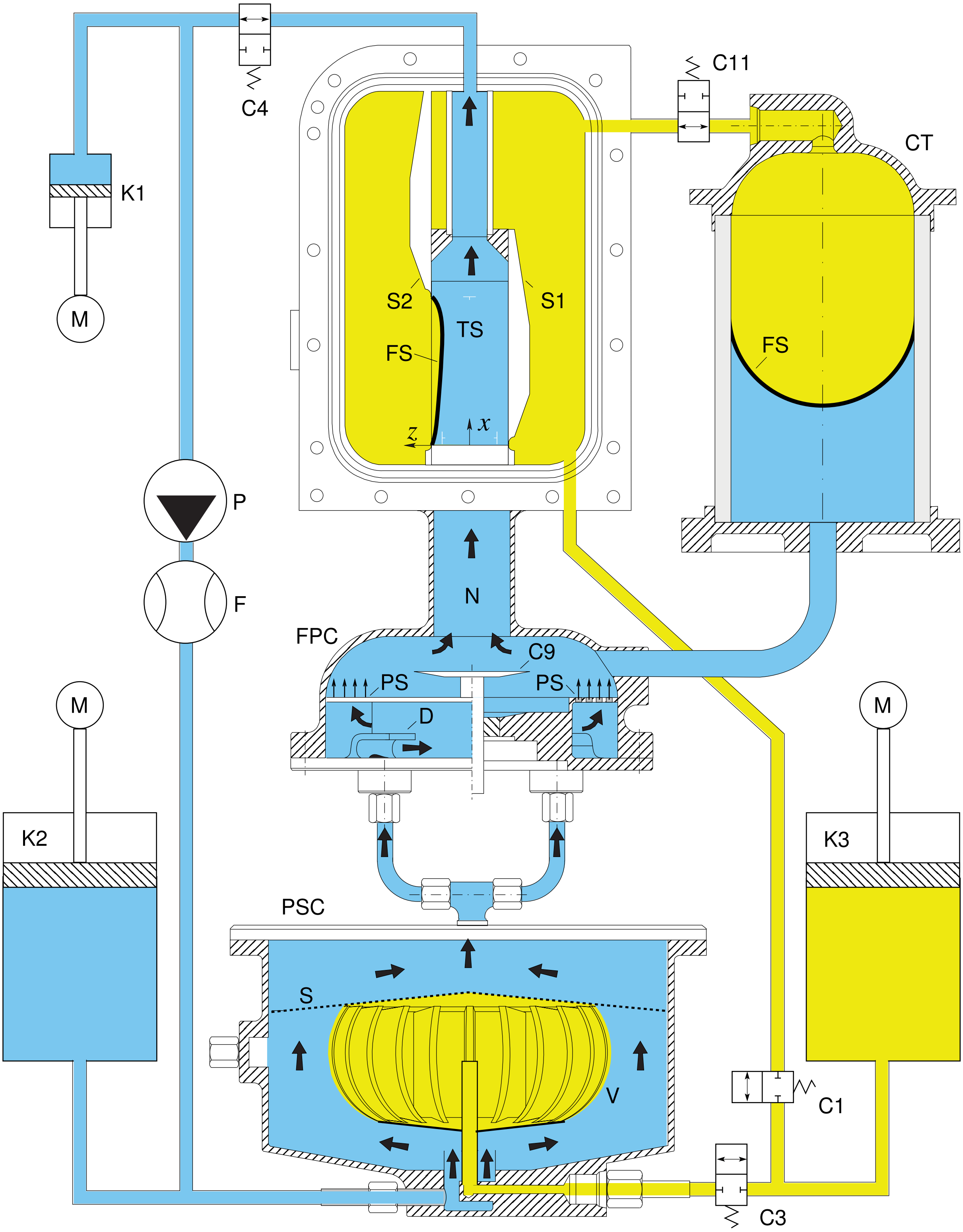

Figure 4.2: Schematic view of the fluid loop in the CCF experimental setup (EU#1). Cyan and yellow colors represent liquid and gas, respectively. The capillary channel is located in the test section (TS). In the depicted case, one slider (S2) is open and one free liquid surface (FS) is formed (groove configuration). The flow direction is depicted with arrows.

Compensation Tube

The free liquid surface(s) of the open channel and the compensation tube are exposed to the ambient pressure p'_a. The ambient gas in the test unit and the gaseous side of the CT are connected via an intersection (the line with C11 valve in Figure 4.2). The liquid side of the CT is connected with the flow preparation chamber. The system pressure is determined by the curvature of the meniscus in the compensation tube at the point where the intersection connects the CT with the FPC. The radius of the CT is $R'_{\mathrm{CT}} = 30$ mm and the resulting capillary pressure difference is $p' - p'_a = 2\sigma/R'_{\mathrm{CT}} = -1.07$ Pa. The CT also compensates the changing demand of the liquid in the loop. Flow rate changes induce liquid movements between the test channel inlet ($x = 0$) and the compensation tube. Depending on the flow regime (acceleration/deceleration) the liquid is withdrawn or displaced into the CT. Furthermore, the displaced liquid due to the gas volume added to the fluid loop during the gas breakthroughs in the test channel (choking) is accommodated by the compensation tube.

Phase Separation Chamber

Single-phase (gas free) liquid flow is required at the test channel inlet during the CCF operation. This is accomplished by the phase separation chamber located downstream from the test channel. The ingested gas (during choking) in the test channel is collected in the PSC and can be extracted through a needle which protrudes into its center. The PSC is located below the FPC, as shown in Figures 4.1(c) and 4.2. It consists of the vane structure, which ensures that gas is kept in the center of the PSC (Figure 4.3(a)). The porous screen located above the vanes disables gas from leaving the chamber. The size of the gas bubble is determined by three bubble sensors (thermistors) hosted within cannulae in the center of the PSC as shown in Figure 4.3(b). The principle of the gas bubble detection is based on the measuring of the thermal conductivity by measurement of the temperature of a heated surface. In this case the thermistor is used as a combined heater and temperature sensor, measuring its own temperature via its electrical resistance. Depending on the environment (low thermal conductivity - gas), the sensor indicates higher temperature when in contact with the gas phase.

During the CCF operation, the size of the gas bubble is adjusted with the gas plunger K3. The change in the gas bubble volume is indicated with the bubble sensors. The first sensor BS1 ($V_g^{BS1} = 87$ ml), the second sensor BS2 ($V_g^{BS2} = 150$ ml) and the third sensor BS3 (V_g^{BS3} = 200 ml) indicate the smallest, medium and largest measured gas volume, respectively. The intermediate volumes are determined with the displacement of the gas plunger K3 (gauging). The stroke of 1 % is equal to 2.73 ml of displaced (added or subtracted) volume of gas[1].

---

[1] Plunger K2 and K3 have same working volume and working stroke.

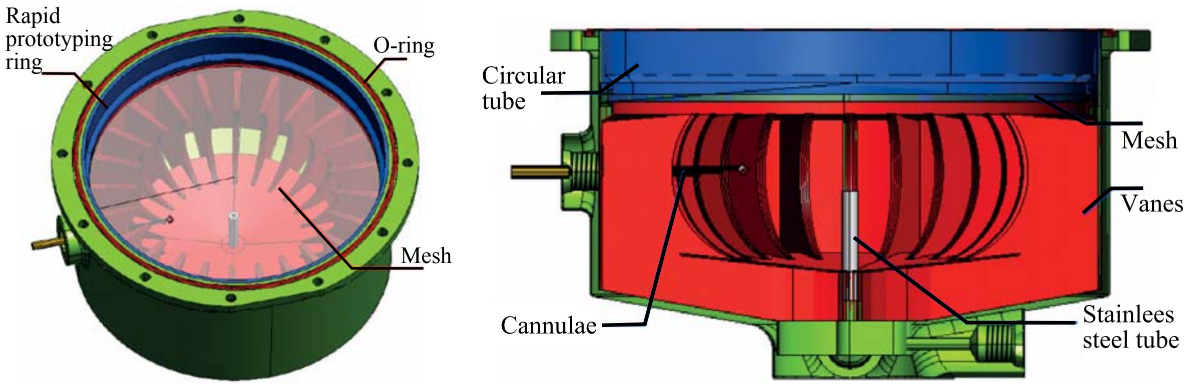

(a) PSC internal view. (b) PSC cross sectional view.

Figure 4.3: The CCF Phase Separation Chamber (3D rendering).

Test Fluids

The liquid used in the CCF experiment is the 3M$^{\text{TM}}$Novec$^{\text{TM}}$Engineered Fluid HFE-7500 with the properties listed in Table 4.1. This test liquid was chosen because of its wetting behavior (the static contact angle with glass is $\eta = 0°$) and very low overall toxicity (meets the MSG safety requirements).

Figure A.2(a) (Appendix A.1) shows the test liquid temperature evolution throughout the entire CCF experiment series EU#1. The liquid temperature is determined as

$$T_l = \frac{T_0 + T_1}{2} \quad , \tag{4.1}$$

where T_0 (`EUTemp5SW` temperature sensor) and T_1 (`EUTemp6SW` temperature sensor) are the temperatures at the channel inlet and outlet, respectively (Figure A.3 in Appendix A.2).

The linear fit in Figure A.2(a) (Appendix A.1) displays an increasing temperature evolution trend. During the experiment it was observed that the EU illumination has an influence (heating) on the CCF test liquid temperature. This explains the temperature increase towards the end of the operation. The time constant of the heating process, however, is in the order of hours. Since the time constant for a single measurement is in the order of minutes, isothermal conditions of the experiment can be assumed.

The minimum and maximum observed liquid temperatures are $T_l^{min} = 23.0$ °C and $T_l^{max} = 31.6$ °C, respectively. The average liquid temperature during the entire operation is $\overline{T_l} = 29.8$ °C, with the standard deviation $s_{\overline{T_l}} = 1.2$ °C. The dependency of the Ohnesorge number on the temperature is shown in Figure A.2(b) (Appendix A.1). The volume of the test liquid in the system is 1.68 liters.

The gaseous environment consists of nitrogen. During operations, the system pressure is typically in the range of 0.95×10^5 Pa to 1.15×10^5 Pa.

4.1.2 Image Acquisition and Evaluation

The CCF Optical Diagnostic Unit is equipped with the HSHR camera and the parallel light source. Both devices are mounted on the optical bench, as shown in Figure 4.1(d). The camera type is the Motion Blitz Cube 26H (Mikroton GmbH) together with the telemetric lens Invaritar$^{\mathrm{TM}}$ (Melles Griot). It can record up to 250 frames per second at a resolution of 1280 × 1024 pixels per frame. As a light source serves the illumination system consisting of the telecentric LED condenser (Correctal $^{\mathrm{TM}}$TC).

The camera is oriented perpendicular to the channel's glass walls. The channel inlet, outlet, both sliders and the free surface(s) can be easily identified (Figure 4.4(a)). During the CCF experiment series EU#1, an average of 100 to 600 HSHRC images at a resolution 1,280 × 888 per data point are recorded. Each image has a data volume of 1.08 MB. Due to the limited download capacities the recorded gray-scale images are processed on board the ISS and converted into binary images (data volume reduced by the factor of 7.7)(Figure 4.4(b)). The edge-detection software is based on the CANNY algorithm [9]. During the operation, the processed images, together with a few gray-scale images (usually 5 to 10), are systematically downloaded shortly after the collection of a single data point.

Downloaded images are further evaluated in order to find the interface contour k as a discrete function of the spatial coordinate x along the open capillary channel and time. The images are processed with an automated script [49] using MATLAB's Image Processing Toolbox. The interface is detected and written to a simple ASCII file for every single image.

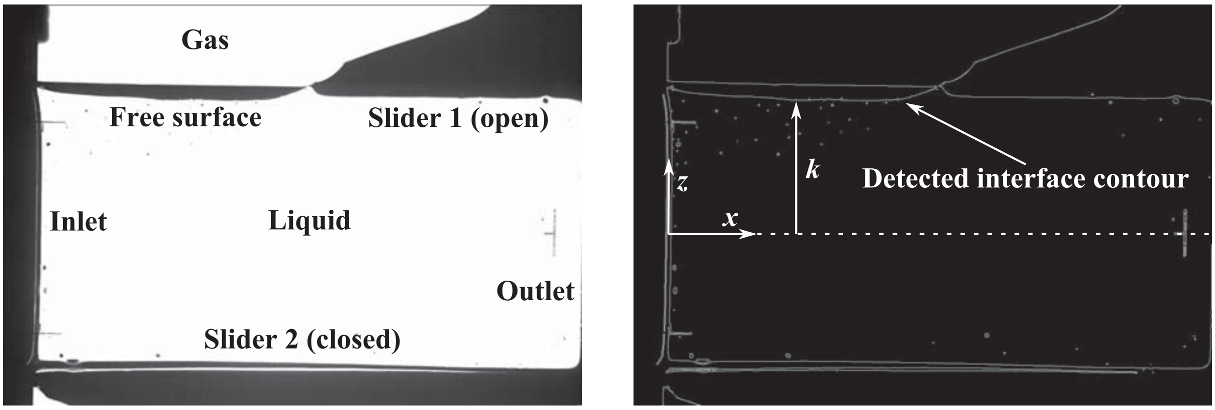

(a) Gray-scale original image.

(b) Processed binary image.

Figure 4.4: (a) Gray-scale HSHR camera image. The free liquid surface appears black due to the total reflection of the parallel light. (b) Corresponding processed binary image with the clearly visible free surface contour k. Contour k is defined as a distance between the channel's center and the lowermost points of the interface along the x axis.

At the end, the time averaged interface $\bar{k}$ is computed by averaging the individual interfaces k_i according to

$$\bar{k}'(x') = \frac{1}{n}\sum_{i=1}^{n} k_i'(x') \quad , \quad 0 \leq x' \leq l \quad , \tag{4.2}$$

where l is the length of the open section and n is the total number of images. Furthermore, the standard deviation $s_{\bar{k}'}$ is computed as

$$s_{\bar{k}'}(x') = \left[\frac{1}{n-1}\sum_{i=1}^{n}\left(k_i'(x') - \bar{k}'(x')\right)^2\right]^{1/2} \tag{4.3}$$

to get a first approximation of the error of the contour evaluation.

4.1.3 Software

During the CCF operation, the current state of the experimental hardware is monitored in two ways. Firstly, the MSG camera (live stream, Figure 4.5) is used for the visual inspection of the hardware. Secondly, the readings of the experiment sensors are plotted and monitored in real time on the display in the ground station (Figure A.3 in Appendix A.2).

The CCF experiment can be classified as real-time operation, since the average system response time (time it takes to observe the change in the MSG camera downlink after sending a command from the ground station) is approximately 5 seconds. The first series CCF EU#1 was operated 24 hours a day, 7 days a week, and time management was a very important part of the CCF operation. For the communication with the ISS the Tracking and Data Relay Satellite System (TDRSS) is used [85]. TDRSS routes two transmissions (radio links): the S band (used for audio) and Ku band (used for audio, video and data). The communication with the ISS is, however, not continuous and depends on the position of the TDRSS satellites. Commanding can be performed only during the Acquisition of Signal (AOS) phase. During the Loss of Signal (LOS) phase no data can be sent to the ISS or received from it.

Before every LOS, the experiments unit is set into the safe mode (sliders closed, pump running with low flow rate). The average AOS period for the CCF EU#1 experiment is 1.5 h, and the average LOS period is 15 min. During CCF operations, the Onboard Short Term Plan Viewer (OSTPV) was used for monitoring of the signal coverage [24]. OSTPV is used by NASA for scheduling of the ISS missions. During CCF operations the scientists are in continuous contact with the NASA Payload Operations Center at the Marshall Space Flight Center in Huntsville. CCF operation is monitored by the Payload Operations Director (POD) and the Payload Rack Officer (PRO). The DICES VoIP (voice over IP) client is used for communicating with NASA officers. The CCF experiment's progress is reported to the POD and PRO on a regular basis.

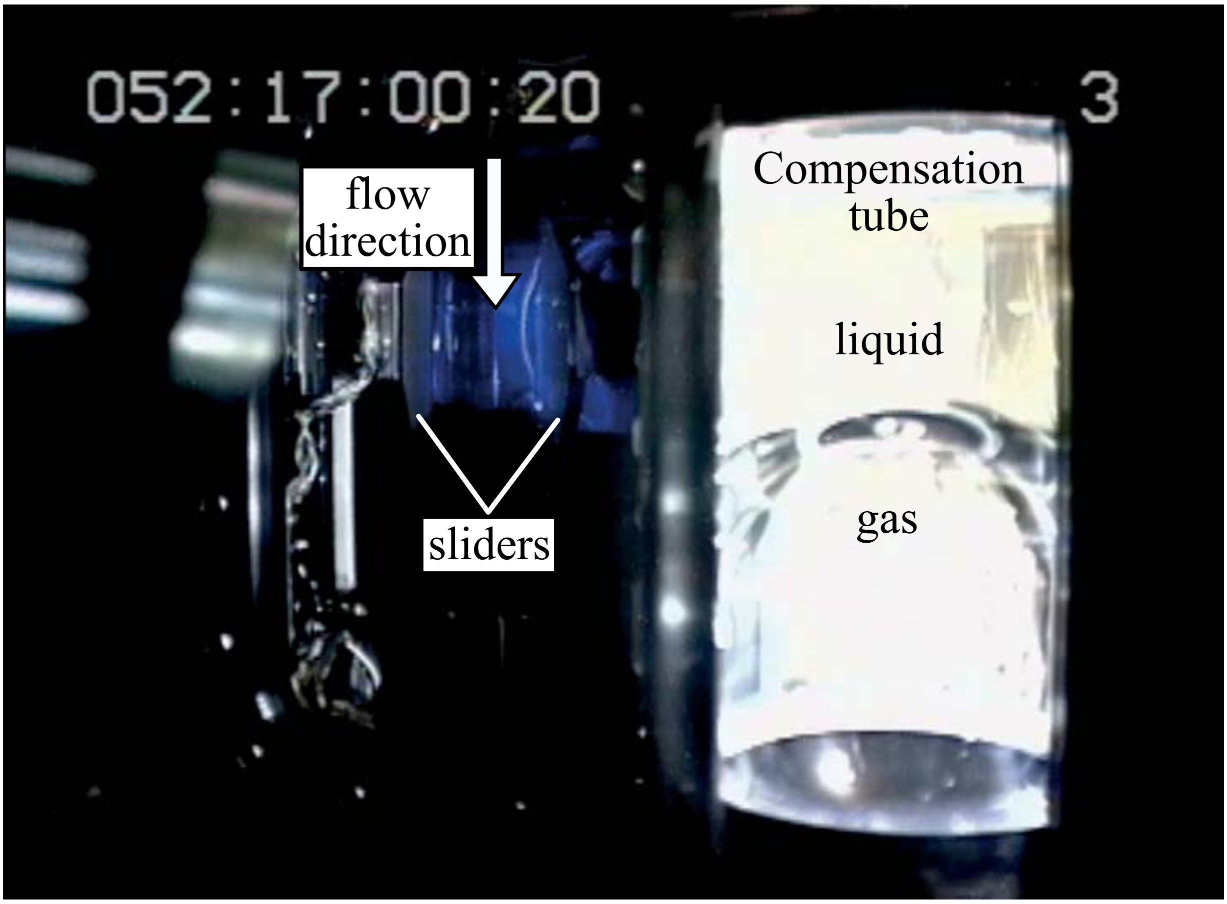

(a) MSG camera view.

Figure 4.5: MSG camera view used for monitoring and maintenance of the CCF experiment unit. The compensation tube can be seen on the right side of the image and the test channel on the left side.

The Experiment Ground Support Equipment (EGSE) software, specially developed for the CCF project, was used to control the experiments unit. EGSE allows the full control of the CCF hardware. It is designed firstly to command the experiments unit (commands are sent via telescience), and secondly to monitor the current state of the CCF hardware (update frequency 1 Hz).

4.2 Operational Scenarios

One of the main goals of the CCF experiment is the determination of the maximum forced flow rates that are possible before the free liquid surface becomes unstable and collapses. The critical flow rate Q_c is defined as the highest flow rate at which the flow is stable. Three approaches (steady, transient and oscillatory flow) of the critical flow rate are employed during the CCF experiment so the stability of the free surface is investigated in various flow regimes. It must be noted that only the steady and transient approaches are the subjects of this work. During the experiment, the test channel and compensation tube are observed with the MSG camera (Figure 4.5). Readings of the system sensors are monitored in real time, and the most important parameters listed in Table A.1 (Appendix A.2) are collected.

Steady Flow

In the steady flow regime, the flow rate is increased stepwise until choking is observed. The procedure of the steady flow experiment can be summarized in the following steps:

1. Start with a flow rate Q_0, far below the expected critical value Q_c.
2. Set the channel configuration and length by positioning of the sliders S_1 and S_2.
3. Set the HSHR camera parameters.
4. Increase the flow rate with small increments ΔQ until choking occurs.
5. Decrease the flow rate until stabilization.
6. Increase the flow rate with small increments until Q_c (determined in point 4) is reached.
7. Collect sensor data (listed in Table A.1 in Appendix A.2).
8. Trigger the HSHR camera at Q_c.
9. Decrease the flow rate until stabilization.
10. Activate image processing software.
11. Perform maintenance procedures (e.g., adjusting liquid level in the compensation tube).

Transient Flow

In the transient flow experiments, the flow rate is dynamically increased and the influence of the rate of flow rate increase $\delta = \Delta Q/\Delta t$ on the stability of the free surface is studied. During the experiments, $\Delta t = 1s$ is kept constant and ΔQ is varied. The critical flow rate increase δ_c is defined as a flow rate acceleration which leads to the instability of the flow (collapse of the free liquid surface). The procedure of the transient flow experiment can be summarized in the following steps:

1. Start with a flow rate Q_0, far below the expected critical value Q_c.
2. Set the channel configuration and length by positioning of the sliders S_1 and S_2.
3. Set the HSHR camera parameters.
4. Increase the flow rate with a pre-defined increment $\delta = \Delta Q/\Delta t$.
5. Decrease the flow rate back to Q_0.
6. Repeat cycle increasing δ until critical acceleration δ_c is determined.
7. Collect sensor data (listed in Table A.1).

Table 4.2: Accuracy of the quantities measured in the CCF experiment. Dimensionless values are given in brackets.

Device/Method	Measured quantity	Symbol	Accuracy ±
Slider set length	Length of the open section	l'	0.05 mm
Flow Meter	Flow rate	Q', Q'_c	0.1 ml/s (0.013)
Pixel detection (± 2-3 pixels)	Free surface contour	k'	0.12 mm (0.048)
PT1000 temperature detectors	Liquid/gas temperature	T_l, T_a	0.5 °C
PAA-33X pressure sensors	Liquid/gas pressure	p'_l, p'_a	10^2 Pa (15.4)
10K3MCD1 NTC thermistors	Gas bubble size in the PSC	-	0.2 °C

8. Trigger the HSHR camera during the increase of the flow rate with δ_c (determined in point 6).
9. Decrease the flow rate (stable flow).
10. Activate image processing software.
11. Perform maintenance procedures (e.g., adjusting liquid level in the compensation tube).

4.3 Experimental Uncertainties

The measurement errors can be divided into (i) systematic errors, due to the change in the measurement environment (changing conditions during the CCF operation), and (ii) statistic (random) errors, due to the senor inaccuracy, and random system fluctuations (e.g., capillary waves on the free surface in the test channel). The summary of the absolute measurement errors is given in Table 4.2. The error of the critical flow rate Q_c is determined by the accuracy of the flow rate meter, which is ±0.1 ml/s. The error of the free surface contour k measurement of ±0.12 mm is determined by the contour evaluation technique (on-board image processing and contour detection algorithm). On average, 100-600 HSHRC images are recorded per data point, which results in the statistic error expressed with the standard deviation in Equation (4.3). The statistic errors for Q and k for the multiple data points (repeated measurement during the course of CCF operation) are denoted with $\triangle$.

4.4 Experiment Summary

The CCF EU#1 installation into MSG took place on 26 December 2010 (Figure 4.6(a)). The hardware commissioning was performed remotely from the NASA Marshall Flight Center in Huntsville/Alabama by the CCF team from Bremen and the Astrium ST (now Airbus Defense and Space). After the successful hardware installation, the whole CCF operation was

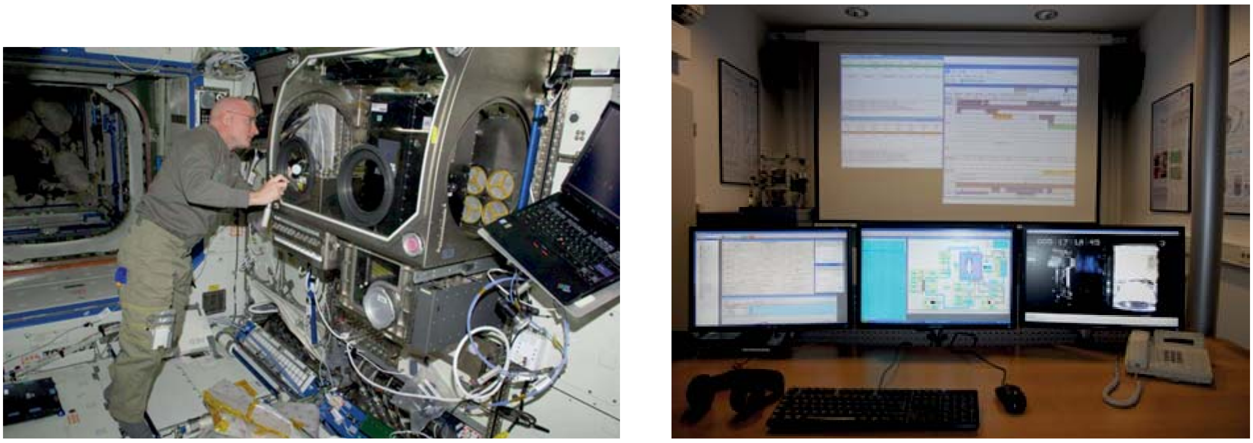

(a) CCF installation.

(b) CCF ground station at ZARM.

Figure 4.6: (a) Flight Commander Scott Kelly during the installation of the CCF experiment (EU#1) into the MSG (courtesy NASA). (b) CCF ground station at ZARM at the University of Bremen.

conducted around the clock from the ground station at ZARM (Figure 4.6(b)). The hardware de-installation and stowage took place on the 17 March 2011. A total number of 66 days of nominal operation (only science) was accomplished. A summary of the collected data points is shown in Table 4.3. The flow is divided into three groups (steady, transient and oscillatory) with the corresponding flow regimes. In case of the steady and oscillatory flows it can be distinguished between subcritical, critical and supercritical flow. In case of the transient flow, the results are divided into stable and unstable acceleration.

A total number of 2139 (PP: 187, GR: 1952) data points was achieved, therefore 846 (PP: 187, GR: 659) with the HSHR camera images. For the steady and oscillatory flow, the telemetry data, MSG camera video, and HSHRC images are recorded for every data point. For the transient flow, the HSHRC images are available only for 7.4 % of the gathered data points.

Table 4.3: Summary of the collected data points during the EU#1. The telemetry data are the CCF sensors data (Figure A.3 in Appendix A.2), which are automatically recorded during the entire CCF operation.

	Flow type	Flow regime	No. Data points	telemetry + MSG+ HSHRC	telemetry + MSG
Parallel plates	Steady	Subcritical	0	0	0
		Critical	83	83	0
		Supercritical	13	13	0
	Oscillatory	Subcritical + critical	91	91	0
		Sum:	187	187	0
Groove	Steady	Subcritical	5	5	0
		Critical	69	69	0
		Supercritical	102	102	0
	Transient	Stable + unstable acceleration	1403	110	1293
	Oscillatory	Subcritical + critical	373	373	0
		Sum:	1952	659	1283

Chapter 5

Numerical Tools

The flow in capillary channels is numerically simulated with two techniques: one-dimensional with ccFlow (code developed at ZARM), and three-dimensional with OpenFOAM (open-source CFD code). Both tools can be employed for steady and transient flow simulations in capillary channels. As will be shown later, both packages deliver very good results for the flow in the stable regime. ccFlow is a very fast tool (solution within minutes), whereas the simulations with OpenFOAM are much more time consuming (solution within days plus time required for the preparation of the computational mesh). OpenFOAM has some advantages in comparison to ccFlow (Table 5.1). Firstly, it can be applied to model the flow in the unstable regime (choking phenomenon). Furthermore, OpenFOAM can be employed for the general investigation of the flow conditions in the CCF setup, with a focus on the inlet section of the capillary channel. The knowledge of the flow behavior, in particular the pressure loss in the inlet nozzle, is crucial for the proper application of the boundary conditions required for the 1D model.

Table 5.1: Advantages and disadvantages of the numerical tools applied for the simulation of the flow in the capillary channels.

	ccFlow	OpenFOAM
Pros:	- Fast tool (solution within minutes) - Inexpensive in terms of hardware - Source code easy to modify	- Very good agreement with the experiment - Applicable for stable and unstable flow (choking) - Can be used to study the general flow behavior in the CCF setup
Cons:	- Applicable only for stable flow - Restricted to three geometries (PP, GR, WE) - Inaccurate results for channels with $l < 8$	- Time consuming - Expensive in terms of hardware

5.1 ccFlow (One-dimensional)

ccFlow is a one-dimensional numerical tool developed at ZARM [31]. It can be used for the prediction of the contour of the free surface and the critical flow rate for the flow in capillary channels under the condition of reduced gravity. ccFlow is based on the capillary channel flow mathematical model introduced in Section 3. In ccFlow, the system of coupled partial nonlinear differential equations describing the flow velocity, flow cross-sectional area, free surface curvature and the free surface contour is solved in non-dimensional form [28]. Steady and unsteady (time dependent) solutions can be obtained. Central differences or upwind methods can be chosen for the discretization of the differential equations. The parameters required to solve the flow equations are given in Table 5.2.

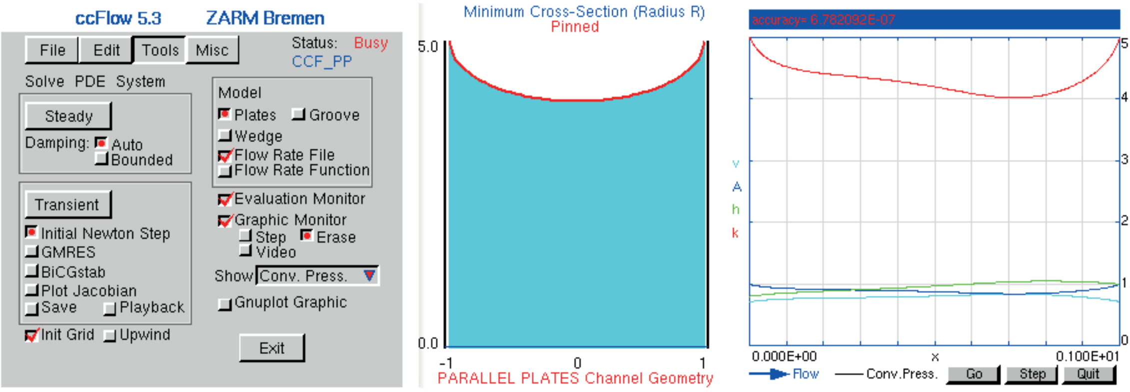
Status: Busy
CCF_PP
Damping: ☒ Auto ☐ Bounded
Model: ☒ Plates ☐ Groove ☐ Wedge ☑ Flow Rate File ☐ Flow Rate Function
☒ Initial Newton Step ☐ GMRES ☐ BiCGstab ☐ Plot Jacobian ☐ Save ☐ Playback
☑ Init Grid ☐ Upwind
☑ Evaluation Monitor
☑ Graphic Monitor ☐ Step ☒ Erase ☐ Video
Show Conv. Press.
☐ Gnuplot Graphic
accuracy= 6.782092E-07

Figure 5.1: Graphical user interface of the ccFlow tool. Left image: the control window through which the simulations are set up. Middle and right images show the evaluation monitors, where the solution is displayed in graphical form. Middle image: the flow cross section at the point of the minimum cross section (due to scaling the radius appears elliptical). Right image: the flow velocity v, the flow cross-sectional area A, the free surface curvature h and the free surface contour k as functions of the flow coordinate x.

In case of the steady flow computation, the critical flow rate is defined for the highest flow rate for which the solution converges. With this method the shape of the free interface can be determined for any flow rate $0 < Q \leq Q_c$. For the steady solution, the time dependent terms in the governing equations (3.49) and (3.50) are set to zero ($\partial v/\partial t = \partial A/\partial t = 0$). In such case a singularity occurs during the computation of the flow at the critical rate. This numerical behavior is employed for the critical flow prediction. The critical flow rate is defined as the highest computed flow rate value for which the singularity does not occur.

Table 5.2: Summary of the CCF experiment parameters. The liquid properties correspond to the HFE-7500 properties in Table 4.1.

Parameter	Value	Source	Equation
System pressure coefficient	$K_0 = 0.166$	$K_0 = a/R_{CT}$ †	(3.59)
Pressure loss coefficient 1	$K_1 = 527$	Section 9.2.2	(3.59)
Pressure loss coefficient 2	$K_2 = 1.68$	Section 9.2.2	(3.59)
Pressure loss coefficient 3	$K_3 = 442$	$K_3 = \mathrm{Oh}^{-1}$	(3.59)
Pressure loss factor for PP	$K_{Pf}^{\mathrm{PP}} = 96$	Section 3.3	(3.49)
Pressure loss factor for GR	$K_{Pf}^{\mathrm{GR}} = 86.4$	Section 3.3	(3.49)
Liquid column length	$l_0 = 155.2$	CAD model	(3.59)
Entrance factor 1	$L_0 = 0$ or 1 ‡	Section 3.3	(3.42)
Entrance factor 2	$L_1 = 0$	Section 3.3	(3.42)

† non-dimensional equation (3.60)

‡ 0 - developed, 1 - undeveloped flow assumption

It must be noted that the solution algorithm used in ccFlow cannot handle a non-unique function $k(x)$, which occurs when the slope of $k(x)$ is infinite at one or multiple locations other than the inlet or outlet of the channel. In other words, the free surface is not allowed to stretch out of the integral range $0 \leq x \leq l$. Free surfaces of that kind can be studied with a different tool, such as Surface Evolver [51].

Test Matrix for ccFlow

Two ideal scenarios are considered in this study: (i) fully developed flow with parabolic velocity profile ($\hat{x} = 0.24$ in equation (3.36)), and (ii) undeveloped flow with constant velocity ($\hat{x} = 0$). These cases represent two extremes of the inlet flow conditions bracketing all the intermediate scenarios of a developing flow. The test matrix for the ccFlow simulations is shown in Table 5.3.

Table 5.3: Test matrix for the ccFlow simulations of the steady flow in the capillary channels. Simulation parameters correspond to the ones depicted in Table 5.2.

Geometry	Flow condition	Channel length l	No. cases	Objectives	Results Figure / Chapter
				-	
PP	devel.	2.5 . . . 19.2	43	comparison with	6.4(a), 6.10, 6.12(a)
PP	undevel.	2.5 . . . 19.2	43	CCF Exp. (Q_c and k)	
GR	devel.	2.5 . . . 19.2	43	comparison with	6.4(b), 6.11
GR	undevel.	2.5 . . . 19.2	43	CCF Exp. (Q_c and k)	
PP	devel.	2.5 . . . 520	76	influence of $\tilde{l}$ on Q_c	6.6(a)
PP	devel.	2.5 . . . 19.2	90	influence of Oh on Q_c	6.6(b)
PP	devel.	5, 19.2	6	influence of Oh on k	6.13
PP	devel.	2.5 . . . 19.2	80	general free surface behavior	Chapter 7
		sum	424		

5.2 OpenFOAM (Three-dimensional)

OpenFOAM (Open source Field Operation And Manipulation) is a C++ written CFD toolbox. The code is released as free and open source software under the GNU General Public License. OpenFOAM (version 2.0.x) contains several solvers classified into the thematic groups: "basic" CFD codes, incompressible flow, compressible flow, multiphase flow, DNS (Direct Numerical Simulation) and LES (Large Eddy Simulation), combustion, particle-tracking, heat transfer and buoyancy-driven flow and molecular dynamics solver.

For the modeling of the free surface flow in the capillary channel, the interFOAM solver is employed. interFOAM is a two-phase, laminar, transient solver for incompressible fluids. The free surface is modeled with the Volume Of Fluid (VOF) method, in which the same transport equations are solved for both phases [40]. The momentum (NAVIER-STOKES) and continuity equations take the form [72]

$$\frac{\partial(\rho\vec{U})}{\partial t} + \nabla\cdot(\rho\vec{U}\vec{U}) = -\nabla p' + \nabla\cdot\tau + \rho\vec{g'} + \vec{F'}_\sigma \;, \tag{5.1}$$

$$\nabla\cdot\vec{U} = 0 \;, \tag{5.2}$$

where $\vec{U}$ represents the velocity field of the artificial fluid mixture $\vec{U} = \vec{U}_l + \vec{U}_g$, p' is the pressure field, τ is the viscous stress tensor (Newtonian fluid model), and $\vec{F'}_\sigma$ is the surface tension force. The phase fraction α^{OF} (scalar function) is computed from the separate passive transport equation

$$\frac{\partial\alpha^{OF}}{\partial t} + \nabla\cdot(\alpha^{OF}\vec{U}) = 0 \;. \tag{5.3}$$

The volume of fluid in a cell is computed as $V'_{vol} = \alpha^{OF}V'_{cell}$, where V'_{cell} is the volume of a computational cell. The value of α^{OF} ranges between 0 (cell completely filled with the void phase) and 1 (cell completely filled with the liquid). At the interface, the value of α^{OF} is between 0 and 1. The physical properties of the fluid mixture (ρ and μ) are calculated as weighted averages based on the volume fraction α^{OF}

$$\rho = \rho_1\alpha^{OF} + \rho_g(1-\alpha^{OF}) \;, \tag{5.4}$$

$$\mu = \mu_1\alpha^{OF} + \mu_g(1-\alpha^{OF}) \;, \tag{5.5}$$

where ρ_l, μ_1 and ρ_g, μ_g are densities and dynamic viscosities of liquid and gas, respectively. The surface tension force F_σ is modeled according to the Continuum Surface Force (CSF) model [4] as

$$\vec{F'}_\sigma = \sigma h'\nabla\alpha^{OF} \;, \tag{5.6}$$

where σ is the surface tension and h the interface mean curvature computed as

$$h = -\nabla\cdot\left(\frac{\nabla\alpha^{OF}}{\mid\nabla\alpha^{OF}\mid}\right) \;. \tag{5.7}$$

The surface tension force F_σ is only active in the interfacial region where $0 < \alpha^{OF} < 1$. Equation (5.6) is valid only for the cases with constant surface tension, as considered in this work due to the isothermal environment and the pure liquid.

The pressure coupling of the governing equations is solved by the PIMPLE (Pressure Implicit Method for Pressure Linked Equations) algorithm which results from combining the SIMPLE (Semi-Implicit Method for Pressure Linked Equations) and PISO (Pressure Implicit with Splitting of Operators) methods. The pressure is calculated with the SIMPLE algorithm from the velocity components by applying an iterative procedure coupled with the NAVIER-STOKES equations [23]. The PISO algorithm is implemented to rectify the second pressure correction and correct both velocities and pressure explicitly. A detailed description of the solution procedure of the used algorithm can be found in [72].

For the spatial discretization, the computational domain is divided into a finite number of volumes, where the solution is calculated. The computational mesh is specified through cells with an arbitrary number of faces, which are defined by a number of vertices (points).

For the single-phase simulations, the steady-state solver simpleFOAM is employed.

Test Matrix for OpenFOAM

A set of OpenFOAM simulations are carried out to study the flow in the capillary channels under microgravity conditions. The simulations performance and results will be discussed in Chapter 9. In total, 189 simulations are performed. In Table 5.4 the corresponding test matrix is given. The openFOAM capabilities are validated with the simpleFOAM solver for a flow in the tube with circular cross section. The numerical results are compared with the analytical solution. The flow simulations in the CCF setup can be divided into two groups: (i) single-phase flow in the channel with closed sliders to investigate the general flow behavior in the CCF inlet section, and (ii) two-phase simulation of the flow in the open channel with free surface(s), aiming at a comparison with the experimental results. The details of the numerical setup and the numerical performance are given in Chapter 9.

Table 5.4: Generic test matrix of the OpenFOAM simulations. ’sF’ - simpleFOAM; ’iF’ - interFOAM; ’Fixed’ - constant flow rate; ’Ramp’ - dynamically increased flow rate; ’BC’ - Boundary Conditions; ’IN’ - flow rate applied at the domain’s inlet; ’OUT’ - flow rate applied at the domain’s outlet; ’Str.’- structured mesh; ’Unstr.’- unstructured mesh. The performance of the simulations will be discussed in Chapter 9.

Geometry	Flow	Solver	Channel length l' / mm	Flow rate Q'/ml s^{-1}		BC	Mesh type	Objectives	No. Cases
				Fixed	Ramp				
Cylindric. tube	steady	sF	-	1 ... 10 with $\Delta Q' = 1$	-	IN	Str.	Solver validation	10
						OUT	Unstr.		10
						IN	Unstr.		10
						OUT	Struct.		10
CCF inlet	steady	sF	-	1 ... 15 with $\Delta Q' = 1$ml s^{-1}, and Q = 1.5	-	IN	Str.	Pressure loss Flow development	16
PP	quasi-steady	iF	5 ... 45 with $\Delta l' = 5$, and 6; 7; 8; 9; 12; 18; 48	-	$Q'_0 = 0$; $Q'_{end} = 10$ t’ = 100 s	OUT	Str.	Q'_c coarse estimation ($\pm$1ml s^{-1})	16
PP	steady	iF	5 ... 45 with $\Delta l' = 5$, and 6; 7; 8; 9; 12; 18; 48	Q' variation	-	OUT	Str.	Q'_c fine estimation ($\pm$0.1ml s^{-1})	51
GR	quasi-steady	iF	5 ... 45 with $\Delta l' = 5$, and 8; 48	-	$Q'_0 = 0$; $Q'_{end} = 10$ t’ = 100 s	OUT	Str.	Q'_c coarse estimation ($\pm$1ml s^{-1})	11
GR	steady	iF	5 ... 45 with $\Delta l' = 5$, and 8; 48	Q' variation	-	OUT	Str.	Q'_c fine estimation ($\pm$0.1ml s^{-1})	46
GR	steady	iF	25	-	$Q'_0 = 0$; $Q'_{end} = 0.5$ t’ = 5 s	OUT	Str.	Parallel performance	9
								sum	189

Chapter 6

Steady Flow Results

In this chapter, the results of the CCF steady flow experiments are evaluated and compared to the results of numerical simulations (1D and 3D). Some first results were recently published by Conrath et al. [13]. An overall number of 272 data points (PP: 96, GR: 176) for steady flow (subcritical and supercritical regime) were achieved during the CCF EU#1 series. An essential goal of the CCF experiment is to investigate the stability of the free surface flow in the capillary channels. The instability is defined by gas ingestion into the flow path, resulting in two-phase flow. In case of the steady flow, the instability occurs due to the choking effect. In the following, the experimental results will be used to verify the mathematical models introduced in Chapter 3. The evaluation focuses on the determination of the maximum flow rates resulting in the stable flow and the corresponding contours of the free surfaces.

A realization of at least one data point (critical flow rate determination) for the representative lengths in the range $2 \leq l \leq 19.2$ for both geometries was the initial goal of the CCF experiment. As shown in a histogram in Figure 6.1, not only this goal was achieved, but also for the the sake of statistic (reproducibility) several repetitions were carried out.

6.1 Stable and Unstable Flow

During the steady flow experiments the flow rate Q is increased stepwise (as described in Section 4.2), and the influence of the flow rate variation on the gas-liquid interface behavior is inspected visually. With increasing flow velocity in the capillary channel, the liquid pressure decreases. As a consequence, the deformation of the free surface increases. The flow remains stable as long as the curvature of the free surface balances the pressure difference between the liquid and the surrounding gas. For a given channel length, the stability limit is achieved for the last flow rate resulting in a stable free surface. Collapse of the free surface and gas ingestion (choking) indicate an unstable flow.

(a) parallel plates

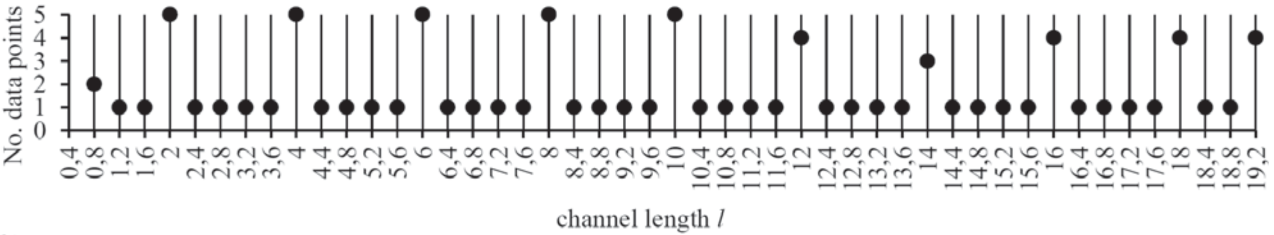

b) groove

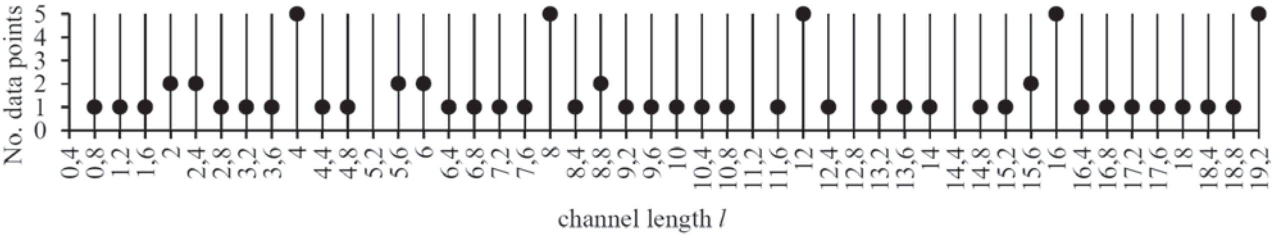

Figure 6.1: Number of data points (critical flow rate determined and last stable interface recorded with the HSHRC) realized per channel length l. The total of data points is 83 for parallel plates, and 69 for the groove channel (steady flow, critical regime).

In the CCF experiment, the last stable interfaces are recorded with a HSHR camera. Examples of unprocessed images for both geometries are shown in Figure 6.2. The corresponding experimental data are summarized in Table 6.1. The lengths $l = 2$ and $l = 19.2$ are the shortest and longest realized in the experiment, respectively. The presented images are randomly chosen single frames. The time evolution of the free surfaces during the stable flow is shown in Figure B.1 (Appendix B.2). It can be clearly seen that the free surfaces remain stable throughout the entire duration of the experiment. In the presented cases (Figure B.1 in Appendix B.2), the duration of the HSHRC video material is 1.62 s with 62 Fps (for each data point). In the experiment, the free surfaces were monitored with the MSG camera for at least 30 s, which is assumed sufficient to determine the flow condition (stable or unstable). Minor oscillations can be observed on the free surfaces shown in Figure B.1 (Appendix B.2). These oscillations possess features of standing capillary waves. Nodes between waves can be identified when the standard deviations of the time averaged free surface contours $k(x)$ are examined. It is found [91] that said waves originate from the vibrations caused by the gear pump generating the flow.

The unstable flow regime is defined for the supercritical flow for which $Q = Q_c + \Delta Q$. It must be noted that the mathematical model introduced in Chapter 3 does not apply for the flow in the supercritical regime. During unstable flow, the free surface curvature fails to balance the pressure gradient $p - p_a$. As a consequence, the free surface looses its stability and gas ingestion into the flow path occurs. Figure 6.3(a) shows an example of the recorded unstable flow in the groove, where the gas bubble formation can be clearly observed. After exceeding

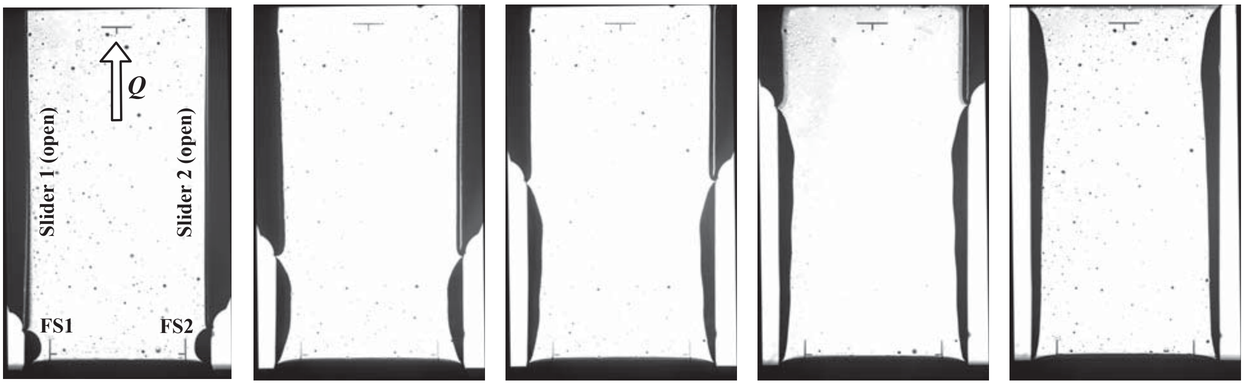

(a) PP, $l = 2$ (b) PP, $l = 6$ (c) PP, $l = 10$ (d) PP, $l = 14$ (e) PP, $l = 19.2$

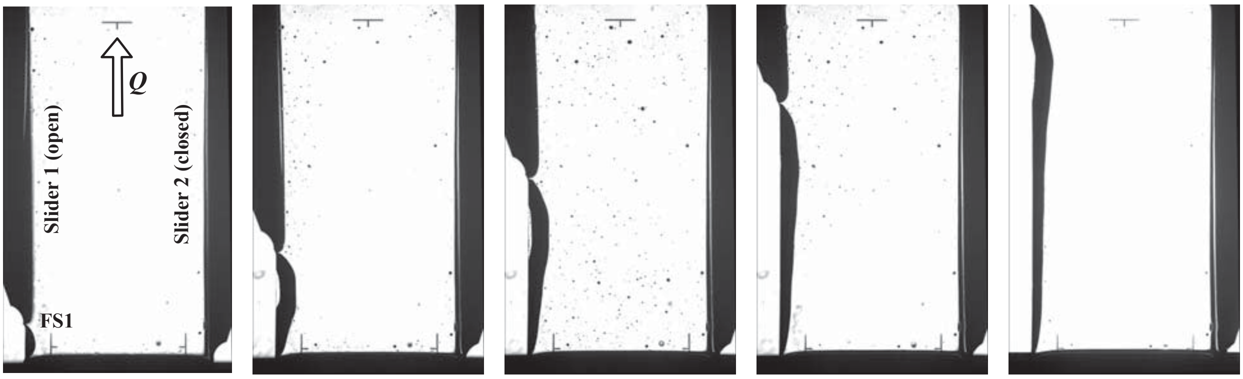

(f) GR, $l = 2$ (g) GR, $l = 6$ (h) GR, $l = 10$ (i) GR, $l = 14$ (j) GR, $l = 19.2$

Figure 6.2: HSHRC images showing the test channel during stable steady flow. (a-e): parallel plates (both sliders open); (f-j): groove channel (one slider open). Flow is from bottom to top. Last stable free surfaces (visible as a black area bending into the channel) are recorded. Corresponding result data are summarized in Table 6.1.

the limiting value Q_c, the free surface bends into the channel ($t' = 5.8$ s) and collapses after the gas bubble is formed ($t' = 6.3$ s). The gas bubble enters the flow path and moves towards the channel outlet. This periodic gas ingestion (choking) repeats itself until the flow rate is reduced sufficiently. For parallel plates, choking is possible on both sides of the channel (Figure 6.3(b)). Both free surfaces bend almost identically into the channel during the flow with supercritical flow rate (0 - 2.0 s). However, only one free surface looses the stability and the opposite free surface retracts significantly at the time when the gas bubble is formed. For the time being, there is no explanation which side is favored.

It is found that the volume of the ingested gas bubbles is independent of the flow rate Q [8]. In other words, with increasing supercritical flow rate, the gas bubble volume[1] remains

---

[1] The gas bubble volume is in fact a function of the channel length l (length of the open channel section through which the surrounding gas enters the flow path).

Table 6.1: Experimental data corresponding to the HSHR camera images depicted in Figure 6.2, where Q_c - evaluated critical flow rate; T_l - liquid temperature; p' - the liquid pressure; p'_a - ambient pressure; $\Delta p' = p' - p'_a$ is the differential pressure. Fps and duration are the frame rate and length of the HSHR camera video material, respectively.

Geometry	l'	l	ID	Q'_c	Q_c	T_l	p' †	p'_a ‡	$\Delta p'$	Fps	Duration	Figure
-	mm	-	-	ml s^{-1}	-	°C	Pa	Pa	Pa	1/s	s	-
PP	5	2	00642	7.88	0.995	28.5	1029.8	1027.4	2.4	62	1.62	6.2(a)
	15	6	00728	6.14	0.775	29.9	1039.7	1040.0	-0.3	250	1.00	6.2(b)
	25	10	00730	5.62	0.710	30.1	1041.1	1041.2	-0.1	250	1.00	6.2(c)
	35	14	00742	5.67	0.716	30.5	1043.3	1043.6	-0.3	62	1.62	6.2(d)
	48	19.2	00652	5.27	0.666	30.1	1028.8	1028.5	0.3	62	1.62	6.2(e)
GR	5	2	00028	7.86	0.992	28.4	1025.2	1014.0	11.2	62	1.62	6.2(f)
	15	6	00042	6.29	0.794	29.8	1039.0	1040.2	-1.2	62	1.62	6.2(g)
	25	10	00055	5.93	0.748	28.4	1031.8	1033.2	-1.4	62	3.24	6.2(h)
	35	14	00066	5.65	0.714	29.9	1039.0	1040.3	-1.3	62	3.24	6.2(i)
	48	19.2	00110	5.41	0.683	28.7	1040.5	1041.6	-1.1	62	3.24	6.2(j)

† PressureC9 sensor (Figure A.3 in Appendix A.2)
‡ Pressure1TU sensor (Figure A.3 in Appendix A.2)

constant. The ingestion frequency (number of gas bubbles ingested per time unit), however, strongly depends on the flow rate. It increases linearly when the flow rate is increased. The gas bubbles recorded on the HSHRC images tend to have an almost spherical shape (in the xz-plane). However, the bubbles are confined between the channel walls and their diameters are larger than the channel's plate distance a. This means that the ingested gas bubbles are not spheres, but they resemble a "cheese wheel" (closed toroidal bubble). The three-dimensional flow simulations confirm this observation.

During unstable flow experiments, the MSG camera (live stream) was used for monitoring the liquid fill level in the compensation tube. An example of the unstable flow recorded with the MSG camera is shown in Figure B.2 (Appendix B.3). The gas that enters the flow path in the test channel (during choking) is caught in the phase separation chamber. The meniscus in the compensation tube rises with increasing volume of the gas bubble in the PSC. The fill level difference Δh_{CT} is used to evaluate the amount of gas ingested during the choking process.

More examples of the recorded HSHRC images can be found in the CCF internet database `http://ccf.zarm.uni-bremen.de/`.

(a) groove (ID 00059)

$t' = 0$ $t' = 2.7$ s $t' = 5.8$ s $t' = 6.3$ s $t' = 6.5$ s

(b) parallel plates (ID 00715)

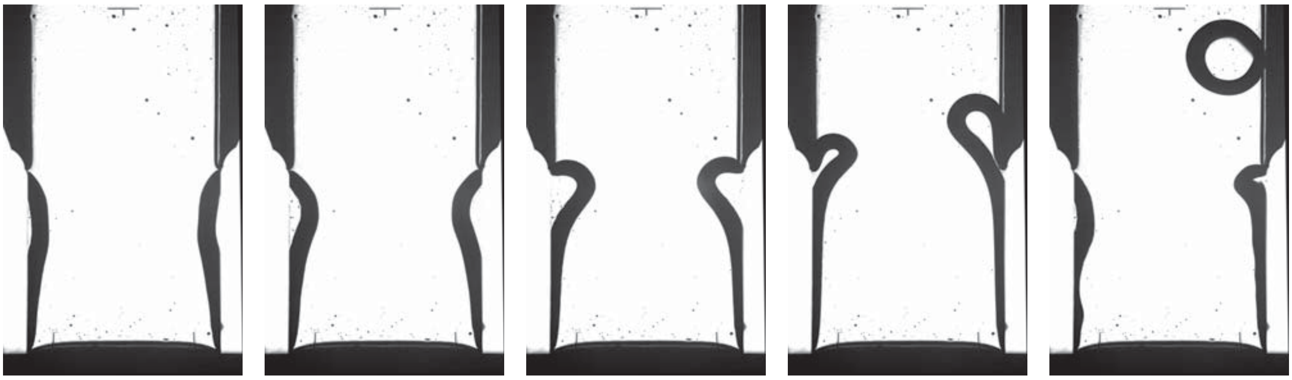

$t' = 0$ $t' = 0.8$ s $t' = 2.0$ s $t' = 2.8$ s $t' = 3.2$ s

Figure 6.3: HSHR camera images showing unstable choked flow. Flow is from bottom to top. (a) groove channel with $l = 11.6$ and $Q/Q_c = 1.01$. (b) parallel plates with $l = 10$ and $Q/Q_c = 1.01$.

6.2 Critical Flow Rate

An essential goal of the CCF experiment is to determine the maximum forced flow rates which are possible for given channel lengths before the free surface(s) of the flowing liquid become(s) unstable. This is accomplished by increasing the flow rate in small steps (quasi steady). The critical flow rate Q_c is defined as the maximum measured flow rate at which stable interfaces are observed. Exceeding the flow rate beyond the critical rate leads to the instability due to the choking effect. Values of the critical flow rate for different channel lengths for both geometries are determined experimentally and compared with the results from numerical simulations (Figure 6.4). The characteristic experimental data are summarized in Table 6.2.

The critical flow rate is a function of the channel length for both geometries, and it decreases with increasing channel length. This decrease appears hyperbolic for channels with $l \leq 8$ and almost linear for channels with $l > 8$. For sufficiently short channels, the reversible convective

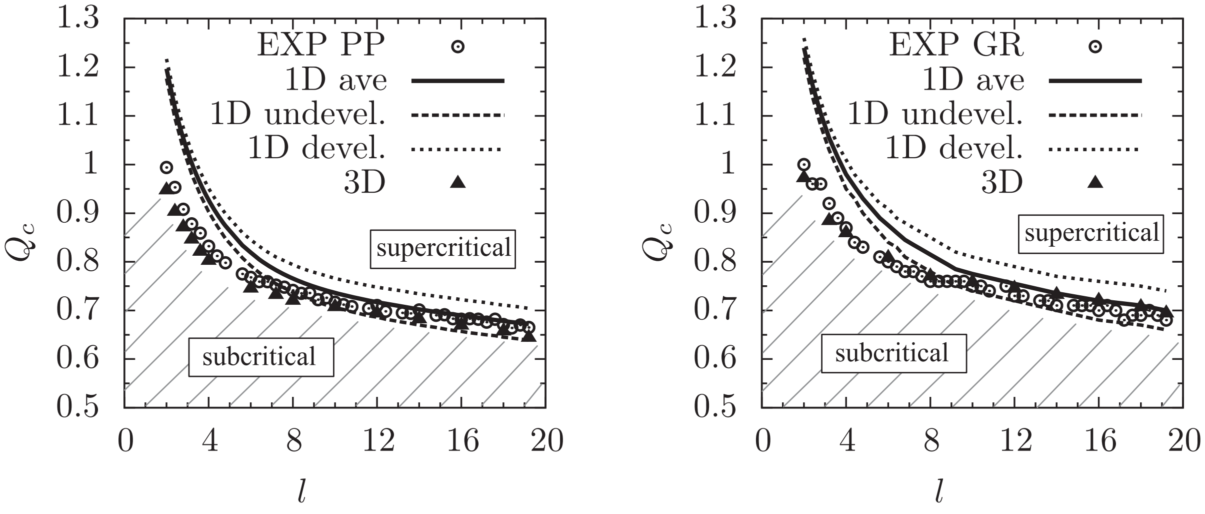

(a) Parallel plates (b) Groove

Figure 6.4: Critical flow rate versus the channel length for the parallel plates (PP) and groove channel (GR). Hatched lines depict the stable flow region where the mathematical model applies. The maximal experiment error is less than ±0.02. EXP - experiment; 1D - `ccFlow` simulations; 3D - `OpenFOAM` simulations.

pressure dominates over the irreversible viscous pressure losses (will be discussed later in section 7.3). Smaller pressure losses result in higher values of the critical flow rate.

A comparison between the experimental and 1D computational results shows very good agreement for channels $l > 7.2$ with a deviation less than 5%. The average critical flow rate determined with 1D simulations is defined as

$$Q_c^{1D} = \frac{Q_{c,undevel.}^{1D} + Q_{c,devel.}^{1D}}{2} \quad , \tag{6.1}$$

where $Q_{c,undevel.}^{1D}$ and $Q_{c,devel.}^{1D}$ are critical flow rates computed for the undeveloped and fully developed flow conditions at the channel inlet, respectively. The discrepancy between the experiment and 1D model increases for short channels. This behavior is related to the additional flow effects which are not included in the mathematical model (will be discussed in Section 6.4). A comparison between the experimental and 3D results shows very good agreement (deviation less than 5 %) for the entire range of lengths l. The 3D solver `OpenFOAM` solves the full NAVIER-STOKES equations in the three-dimensional domain. Not only the numerical method but also the computational domain (geometry) used in the 3D simulations better resemble the CCF experimental setup. This could explain the better performance of the 3D solver for short channels.

The values of the critical flow rate for the groove are higher than for the parallel plates geometry. This is a consequence of the smaller flow cross-section area between the parallel plates

Table 6.2: The critical flow rate Q_c for the parallel plates and the groove channel. Representative channel lengths are chosen for comparison. For 1D results, the average values between the developed and undeveloped flow assumptions are listed (Equation (6.1)). EXP - experiment, 1D - ccFlow, 3D - OpenFOAM, n - number of gathered data points, $s_{Q^{EXP}_{c,PP,GR}}$ - standard deviation. The complete list for the lengths realized in the CCF experiment can be found in Tables B.1, B.2 (Appendix B.1). The corresponding values of the Q_c determined with ccFlow can be found in Tables C.1 and C.2 (Appendix C.1). The relative error is defined as $\Delta Q_c = \mid (Q_c^{EXP} - Q_c^{1D,3D})/Q_c^{1D,3D} \mid \times 100$.

	Parallel plates							Groove						
l	$Q^{EXP}_{c,PP}$	n	$s_{Q^{EXP}_{c,PP}}$	$Q^{1D}_{c,PP}$	ΔQ_c	$Q^{3D}_{c,PP}$	ΔQ_c	$Q^{EXP}_{c,GR}$	n	$s_{Q^{EXP}_{c,GR}}$	$Q^{1D}_{c,GR}$	ΔQ_c	$Q^{3D}_{c,GR}$	ΔQ_c
-	-	-	-	-	%	-	%	-	-	-	-	%	-	%
2.0	0.994	5	0.007	1.197	16.9	0.947	5.0	1.000	2	0.012	1.239	19.2	0.972	2.9
4.0	0.832	5	0.017	0.928	10.3	0.802	3.8	0.868	5	0.005	0.984	11.7	0.859	1.1
6.0	0.768	5	0.006	0.819	6.2	0.745	3.1	0.796	2	0.003	0.874	8.9	0.808	1.5
8.0	0.741	5	0.007	0.766	3.3	0.720	2.9	0.763	5	0.003	0.814	6.2	0.770	0.9
10.0	0.717	5	0.006	0.736	2.6	0.707	1.4	0.748	1	-	0.776	3.6	0.758	1.2
12.0	0.710	4	0.007	0.717	1.0	0.694	2.2	0.732	5	0.006	0.753	2.7	0.745	1.7
14.0	0.701	4	0.011	0.703	0.3	0.682	2.7	0.714	1	-	0.736	3.0	0.732	2.6
16.0	0.682	4	0.009	0.690	1.1	0.669	1.9	0.703	5	0.006	0.723	2.6	0.720	2.3
18.0	0.671	4	0.005	0.678	1.0	0.657	2.2	0.692	1	-	0.711	2.6	0.707	2.1
19.2	0.665	4	0.007	0.672	1.0	0.644	3.3	0.678	5	0.019	0.705	3.8	0.694	2.4

due to the two-sided indentation of the surfaces. Smaller cross-section area in the parallel plates channel requires higher flow velocities (flow continuity is preserved) leading to larger pressure gradients than in the groove geometry (larger cross-section). Thus, higher flow rates can be achieved for the groove channel before the curvature fails to balance the pressure difference $p - p_a$ and the free surface collapses.

As shown in Figure 6.4, a clear limit between the stable and unstable flows for both geometries is identified experimentally and numerically. For any flow rate $Q \leq Q_c$ (subcritical and critical regime), the mathematical model is applicable. To study the flow with $Q > Q_c$ (supercritical regime), an experiment or 3D unsteady simulations are required.

The complete list of the critical flow rates Q_c for all lengths l realized in the CCF experiment can be found in Tables B.1 and B.2 (Appendix B.1) with the corresponding 1D simulation results in Tables C.1 and C.2 (Appendix C.1).

6.2.1 Influence of the Flow Development State

The tool ccFlow is used to show the dependency of the flow condition at the channel inlet on the critical flow rate. The flow development is defined with the parameter β, which is controlled with the factors L_0 and L_1 as described in Section 3.3. A parametric study is performed for parallel plates with $l = 2$ and $l = 19.2$. The model parameters are summarized in Table 5.2. Three cases are distinguished in terms of the flow condition at the capillary channel inlet ($x = 0$): (i) undeveloped flow (constant velocity profile), where $L_0 = 1$ and $L_1 = 0$; (ii) developing flow: $L_0 = 1$ and $L_1 < 0$; and developed flow (parabolic velocity profile), where $L_0 = 0$ and $L_1 = 0$. For the developing flow, the parameter L_1 is varied between the $-1000 < L_1 < 0$. As shown in Figure 6.5, the lowest flow rates are obtained for the undeveloped flow assumption, and the highest for the developed flow assumption. Both cases are depicted with solid lines. For the developing flow, the lowest values of the critical flow rate are computed for $L_1 \to 0$. Decreasing the parameter L_1 below the value of zero leads to an asymptotic increase of the critical flow rate.

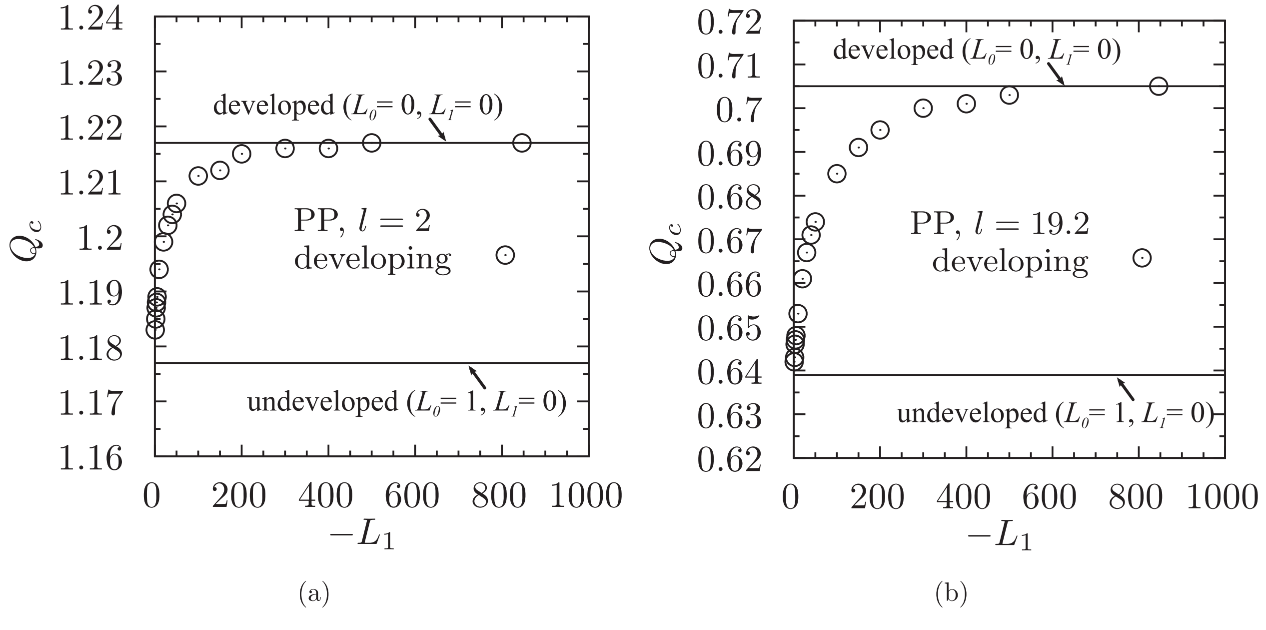

(a)

(b)

Figure 6.5: The critical flow rate Q_c computed with ccFlow as a function of the parameter L_1 for parallel plates. Empty circles depict the critical flow rate computed for different values of parameter L_1 ($L_0 = 1$). (a) "short" channel $l = 2$, where $Q^{1D}_{c,undevel.} = 1.177$ and $Q^{1D}_{c,devel.} = 1.217$; (b) "long" channel $l = 19.2$ where $Q^{1D}_{c,undevel.} = 0.639$ and $Q^{1D}_{c,devel.} = 0.705$.

6.2.2 Influence of the Characteristic Numbers

The parameters chosen for the parametric study are the Ohnesorge number Oh and the dimensionless length $\tilde{l}$. The study is performed with the tool ccFlow. The model parameters are summarized in Table 5.2. A fully developed flow between parallel plates is assumed.

Capillary channels with the open sections longer than investigated in the CCF experiment ($l > 19.2$) might be required for technical applications. In the parametric study, the channel length l is varied between the $2 \leq l \leq 520$ ($5.64 \times 10^{-4} \leq \tilde{l} \leq 1.46 \times 10^{-1}$) and the resulting critical flow rates are computed. The results are shown in Figure 6.6(a). As expected, with increasing the flow lengths (above the range investigated in the CCF), the critical flow rate further decreases. In Figure 6.6(a), v^* and A^* are the velocity and the flow cross section at the point $x = x^*$ (channel's throat), respectively.

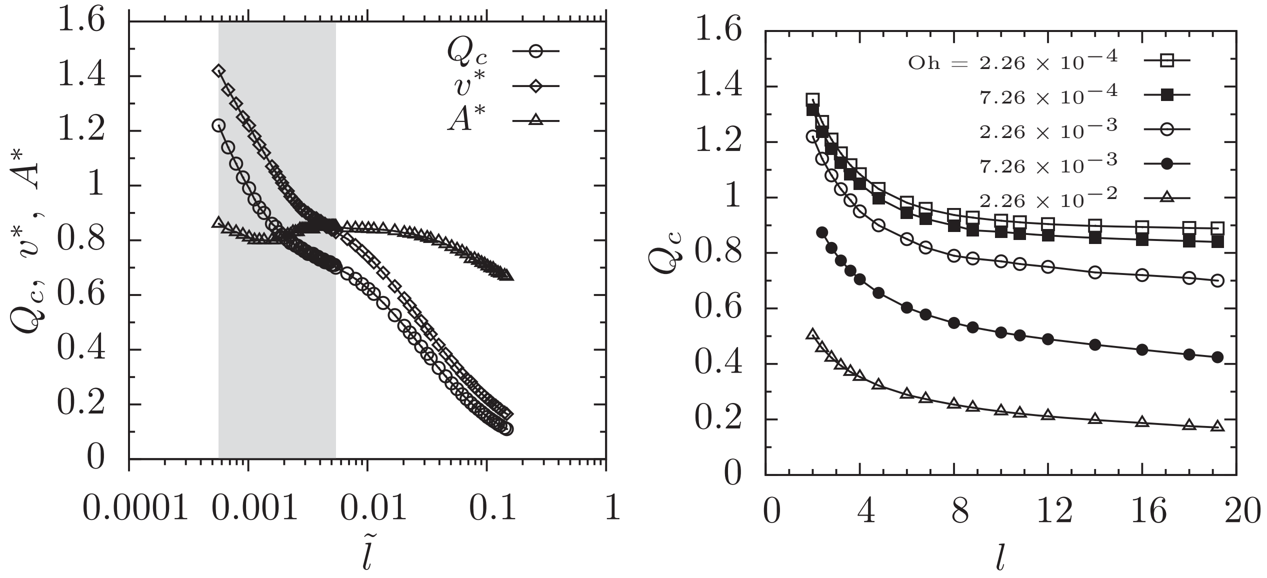

(a) (b)

Figure 6.6: The parametric study with ccFlow for parallel plates. (a) variation of the flow length $\tilde{l}$ with constant Oh number Oh $= 2.26 \times 10^{-3}$ (as in the CCF experiment). Parameters v^* and A^* are the corresponding flow velocity and cross-section area at the point of the minimum cross-section (k_{min} point). Grey region corresponds to the CCF experiment range. (b) Variation of Oh number and length l.

As already mentioned, the test liquid temperature increased towards the end of the experiment operation on the ISS (EU#1), resulting in a variation of the test liquid properties (density, viscosity, and surface tension). As shown in Figure A.2(a) (Appendix A.1), the lowest liquid temperature monitored in the CCF EU#1 is $T_{min} = 23$ °C (corresponding to $\mathrm{Oh}_{\mathrm{min}} = 2.48 \times 10^{-3}$) and the highest $T_{max} = 31.6$ °C ($\mathrm{Oh}_{\mathrm{max}} = 2.21 \times 10^{-3}$). The difference of 2.7×10^{-4} in the Oh number results in the 3.7 % and 1.4 % difference in the critical flow rate for the shortest ($l = 2$), and longest ($l = 19.2$) channel realized in the CCF experiment, respectively.

In the parametric study, the Oh number Oh = 2.26 $\times 10^{-3}$ (corresponding to the average liquid temperature in the CCF experiment T = 30 °C) is increased and decreased by a factor of 10. The influence of the Oh number on the critical flow rate is shown in Figure 6.6(b). For constant Oh, the critical flow rate decreases exponentially with l. The highest values of Q_c are achieved for the lowest Oh numbers Oh = 2.26×10^{-2}. With increasing Oh number the flow becomes more viscous. Due to the irreversible frictional pressure losses, lower values of Q_c can be achieved in the viscous region. In other words, for the flow with high OHNESORGE number (viscous flow), the free surface collapses sooner than with the flow with low OHNESORGE number (convective/inertia flow).

6.3 Free Surface Contours

The HSHR camera images are evaluated in the manner described in Section 4.1.2. The goal of the image processing is the determination of the time averaged free surface contours k along the channel x-axis. The contours of the last stable interfaces are employed (in addition to the critical flow rates) for validation of the mathematical model (comparison with the results of ccFlow simulations).

During the CCF experiments with the parallel plates channel it was observed that both free surfaces behave identically during subcritical flow with $Q \leq Q_c$ (Figure B.3, Appendix B.4). Based on this observation, a symmetry within the channel with respect to the x, y-plane ($z = 0$) is assumed. In the following discussion the contour data of the upper free surface (z positive) are presented.

Experimentally determined free surface contours for both channel configurations are shown in Figure 6.7. The corresponding experimental data are summarized in Table 6.3. The lengths $l = 2$ and $l = 19.2$ are shortest and longest from realized in the CCF experiment, respectively. The inspection of the evaluated free surface contours shows that the shape of the free surface profiles depends on the length of the channel. For channels with $l = 2$ (for both PP and GR channel), the contours of the free surface are almost symmetrical with respect to the channel center $x = 0.5$ (Figures 6.7(a) and 6.7(b)). For channels with $l = 19.2$, the contours are highly asymmetrical. For the lengths $l = 10$ and $l = 19.2$ of the groove channel, the free surface profiles are more deformed than for parallel plates channel (lower values of k). These differences will be discussed later.

The influence of the length l on the free surface contour is shown in Figures 6.7(c) and 6.7(d). The displacement of the free surface increases with increasing channel length. For short channels ($l \leq 4$), the contours remain quasi symmetrical but k lowers. For the channels with

$l > 4$, k rises and the profiles become more asymmetric in the vicinity of the channel exit ($x = 1$) (Figure 6.7(d)). The changing shape of the free surface with increasing channel length is a consequence of different physical regimes influencing the flow (will be discussed in Section 7.3).

Table 6.3: Experiment data corresponding to the free surface profiles depicted in Figure 6.7.

Geometry	l'/mm	l	ID	$\tilde{l}$	Q_c	Figure
PP	5	2	00746	5.64×10^{-4}	1.003	6.7(a),6.7(c)
	7	2.8	00659	7.90×10^{-4}	0.908	6.7(c)
	8	3.2	00660	9.03×10^{-4}	0.878	6.7(c)
	9	3.6	00661	1.02×10^{-3}	0.859	6.7(c)
	10	4	00747	1.13×10^{-3}	0.832	6.7(c)
	15	6	00645	1.69×10^{-3}	0.762	6.7(d)
	25	10	00754	2.82×10^{-3}	0.719	6.7(a)
	35	14	00649	3.95×10^{-3}	0.696	6.7(d)
	48	19.2	00703	5.42×10^{-3}	0.675	6.7(a)
	48	19.2	00652	5.42×10^{-3}	0.666	6.7(d)
GR	5	2	00028	6.21×10^{-4}	0.992	6.7(b)
	25	10	00055	3.10×10^{-3}	0.748	6.7(b)
	48	19.2	00110	5.96×10^{-3}	0.683	6.7(b)

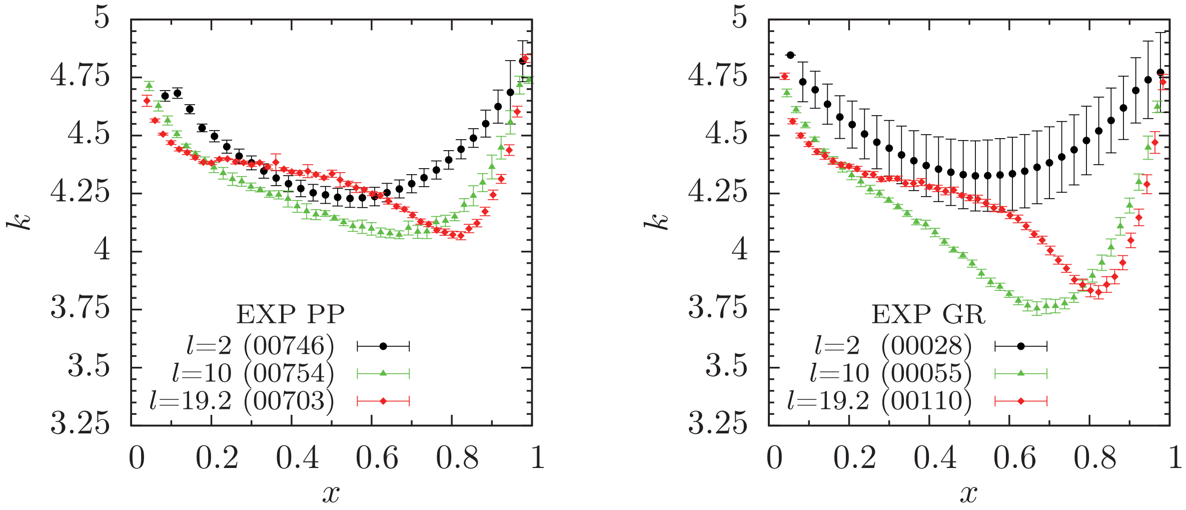

(a) parallel plates (b) groove

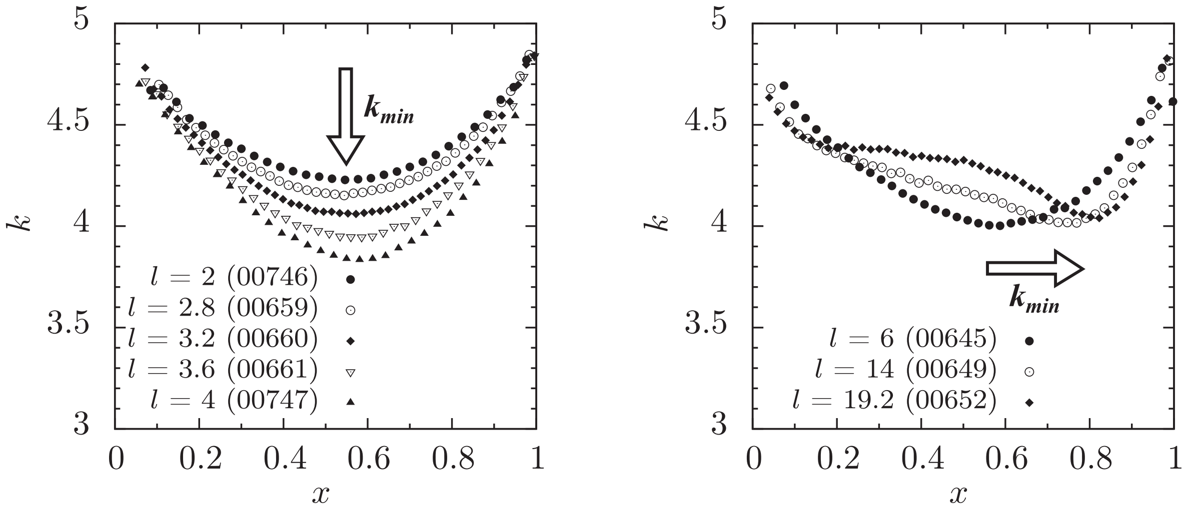

(c) parallel plates (d) parallel plates

Figure 6.7: Experimentally determined free surface contour k along the channel x-axis. Maximum stable (critical flow) interfaces are depicted. In (a) and (b) , data for three characteristic channel lengths ($l = 2$ - “short”, $l = 10$ - “medium” and $l = 19.2$ - “long” channel) are shown for both geometries. Different shapes of the free surface profiles represent different flow regimes. Bars represent the average standard deviation (Equation (4.3)). In (c) and (d), the influence of the length l on the free surface profiles is shown. The point k_{min} lowers for short channels (c) and moves towards the channel exit for channels $l > 4$ (d). The error bars are dropped for the sake of comparison.

6.3.1 Reproducibility

An essential part of the CCF experiment was the determination of the shape of the free surface profiles for the flow at the critical rate (last stable interfaces). For the representative channel lengths (Figure 6.1), multiple experiments were performed in order to study the reproducibility of the obtained results. Providing constant experimental conditions is intended throughout the entire operation on the ISS. There were, however, some fluctuations of the experimental parameters during the experiment. This has to be taken into account during a long-time experiment. Presumably, due to the external heat sources, the liquid temperature increased towards the end of the operation (Figure A.2(a) in Appendix A.1). Other parameters, such as the differential pressure (gas-liquid) or the size of the gas bubble in the flow preparation chamber, might also influence the measurements. For a single measurement (order of minutes), however, a constant experimental conditions are assured. Multiple data points are evaluated, and the comparison of the free surface contour k is shown in Figures 6.8 and 6.9. Corresponding experimental data are summarized in Tables 6.4 and 6.5. In general, a good reproducibility of the free surface profiles is obtained. A vertical offset between the k curves in the vicinity of the channel's throat (minimum cross-section area) can be identified for some cases. The relative difference between the maximum and minimum measured contour k is defined as

$$\Delta k = \left| \frac{k_{max} - k_{min}}{k_{min}} \right| \times 100 \quad . \tag{6.2}$$

The maximum relative difference Δk_{max} among all multiple data points is 9 % and 17.2 % for the parallel plates and the groove channel, respectively. The average relative difference $\Delta \bar{k}_{max}$ is 4.3 % (with $s_{\Delta \bar{k}_{max}} = 2.7$ %) and 6.5 % (with $S_{\Delta \bar{k}_{max}} = 5.6$ %) for the parallel plates and the groove channel, respectively. As shown in Tables 6.4 and 6.5, the liquid temperature T_l differs between the multiple data points realized for a particular channel length. Consequently, the liquid properties vary slightly among the collected data points, which might cause the differences in the shape of the measurement contours.

Furthermore, a discrepancy in the measured values of Q_c for a particular channel length can be observed. The highest standard deviation is $s_{Q_c} = 0.02$ for the parallel plates channel with $l = 4$. The average standard deviation among all multiple measurements is $\bar{s}_{Q_c} = 0.01$, which is equal to 2 % and 3 % for the highest and lowest determined flow rates. It will be shown in Section 7.2.1 that a small change (even below 2 %) in the value of the flow rate leads a significant change of the shape of the free surface profiles for the flow in the critical regime. In other words, small fluctuations of the flow rate in the vicinity of the stability limit result in the significant differences in the $k = f(x)$ plot. This (together with the experimental conditions fluctuations) could also explain the offset between the contours determined in the CCF experiment (Figures 6.8 and 6.9).

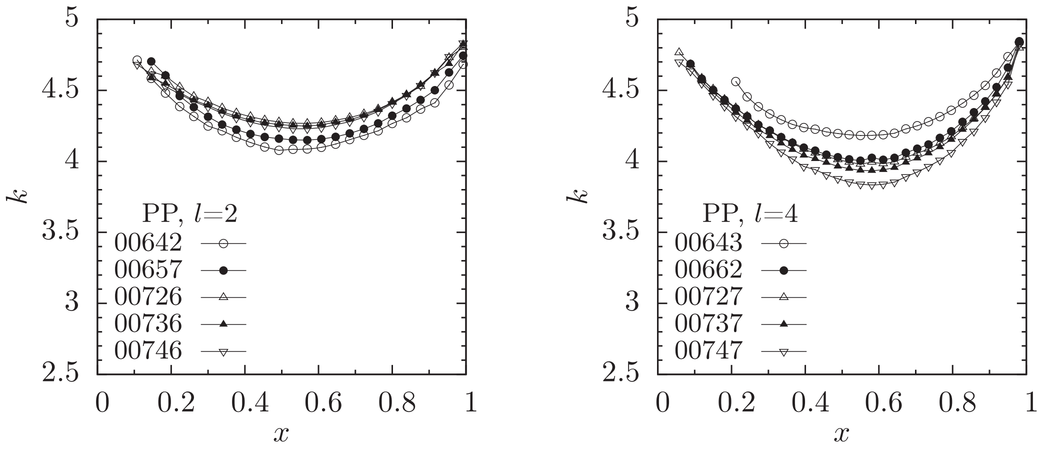

(a) $\Delta k = 4.9$ % (b) $\Delta k = 9$ %

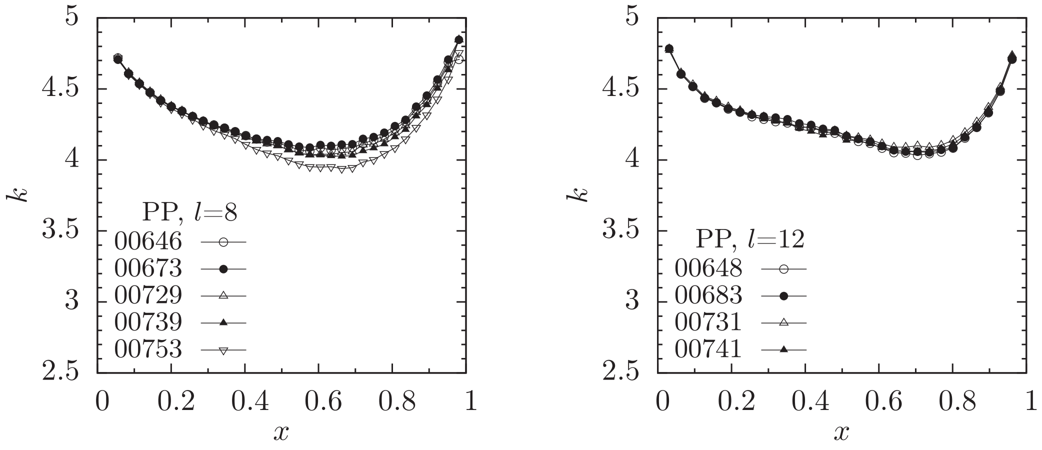

(c) $\Delta k = 3.8$ % (d) $\Delta k = 1.1$ %

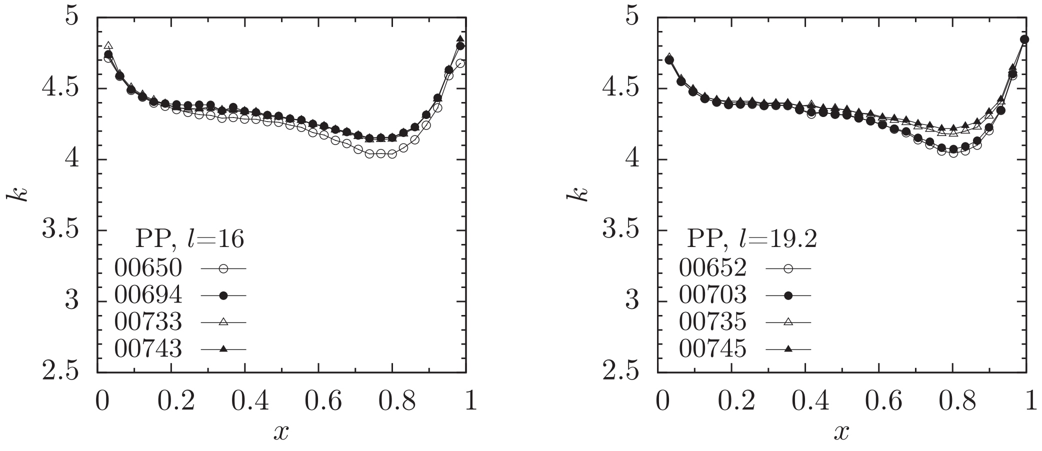

(e) $\Delta k = 2.9$ % (f) $\Delta k = 4.3$ %

Figure 6.8: Multiple data point results for the **parallel plates** channel. Time averaged (Equation (4.3)) free surface contours k along the channel x-axis. Maximum stable (critical flow) interfaces are depicted. The error bars are dropped for the sake of comparison.

Table 6.4: Experiment data from the multiple measurements of the free surface contours between **parallel plates** channel. Presented cases correspond to the plots in Figure 6.8. T_l - liquid temperature, p_l' - liquid pressure, p_g' - ambient gas pressure.

l	ID	Q_c	T_l	p_l' †	p_g' ‡	Frames	Duration	Fps	Figure
-	-	-	°C	Pa	Pa	-	s	s^{-1}	-
2	00642	0.995	28.5	1029.8	1027.4	100	1.62	61.8	6.8(a)
	00657	0.985	30.7	1030.4	1029.6	100	1.63	61.5	
	00726	0.991	29.4	1035.1	1035.3	250	1.00	251.0	
	00736	0.999	30.5	1042.4	1042.6	100	1.63	61.5	
	00746	1.003	30.7	1042.7	1043.0	100	1.63	61.5	
4	00643	0.804	29.6	1033.0	1032.7	100	1.63	61.5	6.8(b)
	00662	0.831	30.4	1032.2	1031.3	100	1.63	61.5	
	00727	0.844	29.8	1039.1	1039.3	250	1.00	251.0	
	00737	0.848	30.5	1042.3	1042.5	100	1.63	61.5	
	00747	0.832	30.7	1042.1	1042.2	100	1.63	61.5	
8	00646	0.735	29.9	1040.0	1040.0	100	1.63	61.5	6.8(c)
	00673	0.739	30.3	1037.8	1037.5	100	1.63	61.5	
	00729	0.743	30.0	1040.5	1040.9	250	1.00	251.0	
	00739	0.735	30.5	1043.0	1043.3	100	1.63	61.5	
	00753	0.751	28.7	1031.2	1032.0	100	1.62	61.7	
12	00648	0.707	30.0	1012.8	1014.0	100	1.63	61.5	6.8(d)
	00683	0.702	30.2	1038.2	1037.8	100	1.63	61.5	
	00731	0.718	30.1	1040.7	1040.8	250	1.00	251.0	
	00741	0.712	30.5	1043.9	1044.1	100	1.63	61.5	
16	00650	0.692	29.5	1027.0	1027.0	100	1.63	61.5	6.8(e)
	00694	0.687	30.4	1033.7	1034.2	100	1.63	61.5	
	00733	0.679	30.2	1041.4	1041.7	250	1.00	251.0	
	00743	0.671	30.5	1043.0	1043.3	100	1.63	61.5	
19.2	00652	0.666	30.1	1028.8	1028.5	100	1.63	61.5	6.8(f)
	00703	0.675	28.9	1037.3	1037.6	100	1.62	61.6	
	00735	0.659	30.3	1041.4	1041.5	250	1.00	251.0	
	00745	0.662	30.4	1043.1	1043.2	100	1.63	61.5	

† PressureC9 sensor (Figure A.3 in Appendix A.2)

‡ Pressure1TU sensor (Figure A.3 in Appendix A.2)

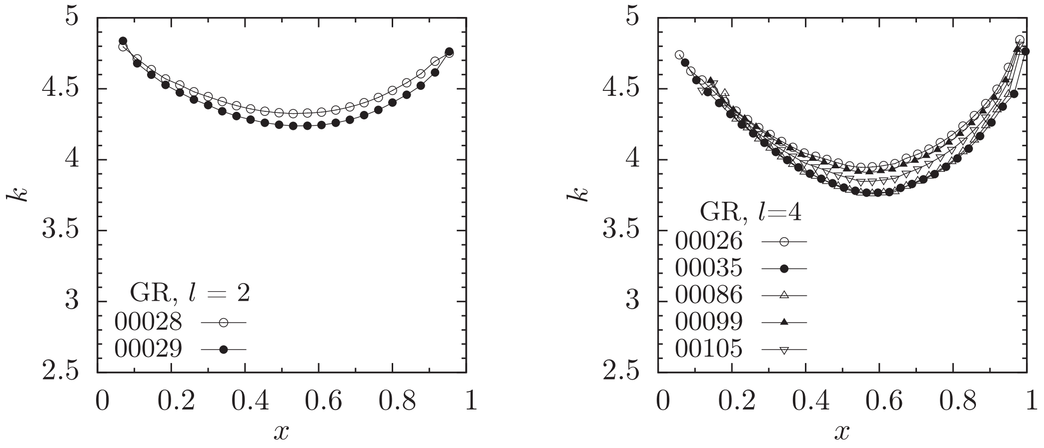

(a) $\Delta k = 2.1$ % (b) $\Delta k = 5.0$ %

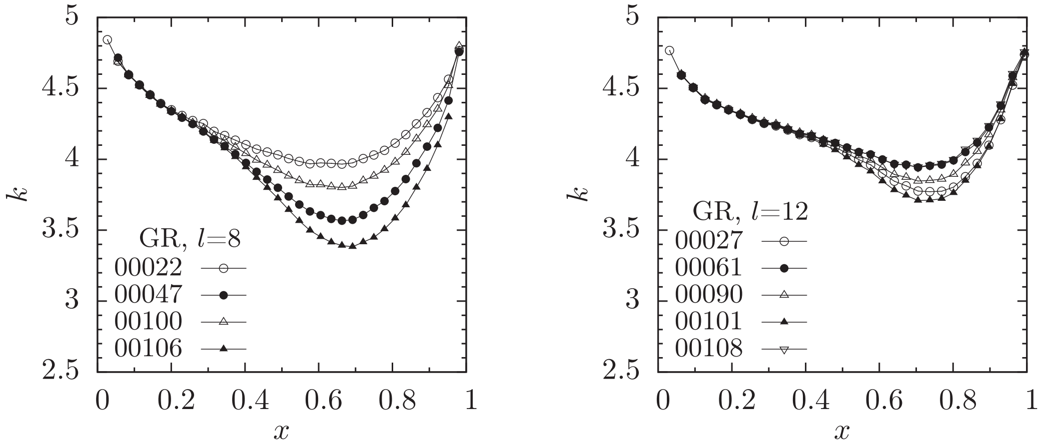

(c) $\Delta k = 17.2$ % (d) $\Delta k = 6.7$ %

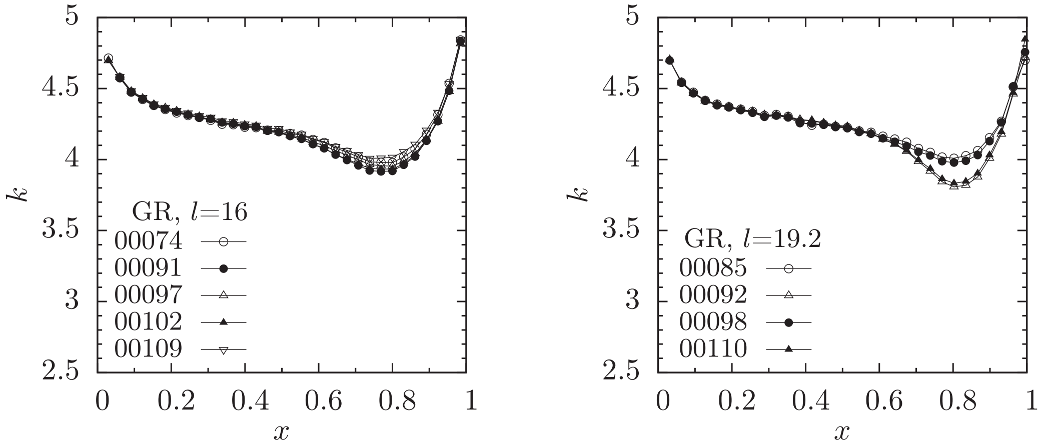

(e) $\Delta k = 2.4$ % (f) $\Delta k = 5.5$ %

Figure 6.9: Multiple data point results for the **groove** channel. Time averaged (Equation (4.3)) free surface contours k along the channel x-axis. Maximum stable (critical flow) interfaces are depicted. The error bars are dropped for the sake of comparison.

Table 6.5: Experiment data from the multiple measurements of the free surface contours in the **groove** channel. Presented cases correspond to the plots in Figure 6.9. T_l - average liquid temperature, p'_l - liquid pressure, p'_g - ambient gas pressure.

l -	ID -	Q_c -	T_l °C	p'_l † Pa	p'_g ‡ Pa	Frames -	Duration s	Fps 1/s	Figure -
2	00028	0.992	28.4	1025.2	1014	100	1.62	62.0	6.9(a)
	00029	1.009	27.2	1016.4	1017.5	100	1.62	61.7	
4	00026	0.866	28.1	1026.5	1025.3	100	1.62	61.8	6.9(b)
	00035	0.866	29.1	1016.6	1017.7	200	3.26	61.4	
	00086	0.875	25.6	1038.6	1039.9	200	3.25	61.5	
	00099	0.862	30.1	1047.3	1048.5	100	1.63	61.5	
	00105	0.870	23.0	1017.3	1018.3	200	3.24	61.7	
8	00022	0.767	25.3	1003.3	1004	800	13.05	61.3	6.9(c)
	00047	0.760	29.9	1038.9	1040.3	100	1.62	61.6	
	00100	0.763	30.2	1047.3	1048.5	100	1.63	61.5	
	00106	0.763	25.8	1027.2	1028.2	200	3.25	61.5	
12	00027	0.739	28.2	1028.2	1027.2	100	1.62	61.8	6.9(d)
	00061	0.730	29.6	1037.3	1038.6	200	3.26	61.3	
	00090	0.738	28.5	1052.2	1053.5	200	3.26	61.3	
	00101	0.727	30.2	1047.5	1048.5	100	1.63	61.6	
	00108	0.724	27.1	1033.4	1034.4	200	3.25	61.5	
16	00074	0.712	27.1	1032.4	1033.8	200	3.26	61.4	6.9(e)
	00091	0.704	28.7	1053.5	1054.8	200	3.26	61.3	
	00097	0.700	30.0	1046.8	1048.1	100	1.63	61.5	
	00102	0.698	30.3	1047.7	1048.8	100	1.62	61.6	
	00109	0.698	28.2	1038.5	1039.4	200	3.26	61.3	
19.2	00085	0.682	24.2	1032.1	1033.3	200	3.24	61.7	6.9(f)
	00092	0.690	28.9	1054.2	1055.5	200	3.26	61.3	
	00098	0.686	30.1	1047.2	1084.6	100	1.63	61.6	
	00103	0.683	28.7	1040.5	1041.6	100	1.63	61.5	

† PressureC9 sensor (Figure A.3 in Appendix A.2)

‡ Pressure1TU sensor (Figure A.3 in Appendix A.2)

6.3.2 Comparison with the Mathematical Model

As already mentioned, for each single data point the contour k is averaged over time and a standard deviation is computed (Equations (4.2) and (4.3)). The experimental contour data depicted in Figures 6.8 and 6.9 are used for the comparison with the results of the ccFlow simulation. The value of time averaged contours k for each channel length is built. As shown in Tables 6.4 and 6.5, the number of recorded HSHRC images differs for each measurement. Therefore, the weighted averages of standard deviations are computed according to

$$\bar{s}_{\bar{k}}(x) = \sqrt{\frac{(n_1-1)(s_{\bar{k}1})^2 + (n_2-1)(s_{\bar{k}2})^2 + \ldots + (n_i-1)(s_{\bar{k}n})^2}{n_1 + n_2 + \ldots + n_i - N}}, \tag{6.3}$$

where $s_{\bar{k}n}$ is the standard deviation for a single data point according to Equation (4.3), n is the sample size (number of HSHRC frames for given data point) and N is the population size (number of data points for a given channel length).

The comparison is shown in Figures 6.10 and 6.11, with the corresponding data summarized in Table 6.6. Representative short ($l = 2,\ l = 4$), medium ($l = 8,\ l = 12$), and long channels ($l = 16,\ l = 19.2$) are chosen for comparison. For the 1D model (ccFlow simulation), two flow assumptions at the channel inlet are considered: developed (solid lines) and undeveloped (dashed lines) flow.

Table 6.6: Free surface contour data corresponding to the results shown in Figures 6.10 and 6.11. Results of the 1D simulations (k^*_{1D} and x^*_{1D}) are the average values computed for the developed and undeveloped flow assumptions.

Geometry	l' / mm	l	k^*_{exp}	k^*_{1D}	Δk^* /%	x^*_{exp}	x^*_{1D}	Δx^*/ %
PP	5	2	4.19	4.08	2.9	0.61	0.51	19.7
	10	4	3.99	3.81	4.8	0.55	0.52	7.0
	20	8	4.03	3.89	3.8	0.58	0.55	4.6
	30	12	4.05	3.99	1.5	0.73	0.62	16.4
	40	16	4.12	4.00	3.0	0.74	0.69	6.6
	48	19.2	4.13	4.00	3.1	0.82	0.74	11.3
GR	5	2	4.28	4.05	5.8	0.54	0.51	5.1
	10	4	3.86	3.51	10.2	0.56	0.52	7.4
	20	8	3.68	3.29	12.0	0.67	0.55	22.8
	30	12	3.83	3.60	6.7	0.73	0.60	20.9
	40	16	3.96	3.73	6.0	0.79	0.67	16.8
	48	19.2	3.90	3.75	4.1	0.82	0.72	14.6

In general, good agreement between experiment and numerical predictions is obtained. 1D profiles, however, are slightly shifted towards the channel inlet $x = 0$ (the deformation of the free surface is underestimated). For the groove channel, also lower values of k are obtained than in the experiment. The differences in the examined contour plots can be evaluated in the vicinity of the minimum cross-section point. The relative difference between the measured values of k^* and the corresponding x^* at the point of the minimum cross section is defined as

$$\Delta k^* = \left| \frac{k^*_{EXP} - k^*_{1D}}{k^*_{1D}} \right| \times 100 \quad \text{, where} \quad k^*_{1D} = \frac{k^*_{1D,devel.} + k^*_{1D,undevel.}}{2} \quad , \tag{6.4}$$

and

$$\Delta x^* = \left| \frac{x^*_{EXP} - x^*_{1D}}{x^*_{1D}} \right| \times 100 \quad \text{, where} \quad x^*_{1D} = \frac{x^*_{1D,devel.} + x^*_{1D,undevel.}}{2} \quad . \tag{6.5}$$

As shown in Table 6.7, the maximum relative difference Δx^*_{max} is 19.7 % and 22.8 % for the parallel plates and the groove channel, respectively. The average difference $\bar{\Delta}x^*$ is 10.9 % (with $S_{\bar{\Delta}x^*} = 6.0$ %) and 14.6 % (with $S_{\bar{\Delta}x^*} = 7.1$ %) for the parallel plates and the groove channel, respectively. The average difference in the value of x^* is however less than 15 % for both geometries.

The maximum relative difference Δk^*_{max} is 4.08 % and 12 % for the parallel plates and the groove channel, respectively. For both geometries, the displacement of the predicted contours is slightly overestimated. The average difference $\bar{\Delta}k^*$ is 3.2 % (with $S_{\bar{\Delta}k^*} = 1.1$ %) and 7.4 % (with $S_{\bar{\Delta}k^*} = 3.0$ %) for the parallel plates and groove channel, respectively.

Table 6.7: Maximum differences in the values of x^* and k^* determined experimentally and numerically. Δx^*_{max} - maximum difference in x^*; $\bar{\Delta}x^*$ - average difference in x^*; $S_{\bar{\Delta}x^*}$ - standard deviation; Δk^*_{max} - maximum difference in k^*; $\bar{\Delta}k^*$ - average difference in k^*; $S_{\bar{\Delta}k^*}$ - standard deviation.

Geometry	Δx^*_{max} /%	$\bar{\Delta}x^*$ /%	$S_{\bar{\Delta}x^*}$ /%	Δk^*_{max} /%	$\bar{\Delta}k^*$ /%	$S_{\bar{\Delta}k^*}$ /%
PP	19.7	10.9	6.0	4.08	3.2	1.1
GR	22.8	14.6	7.1	12	7.4	3.0

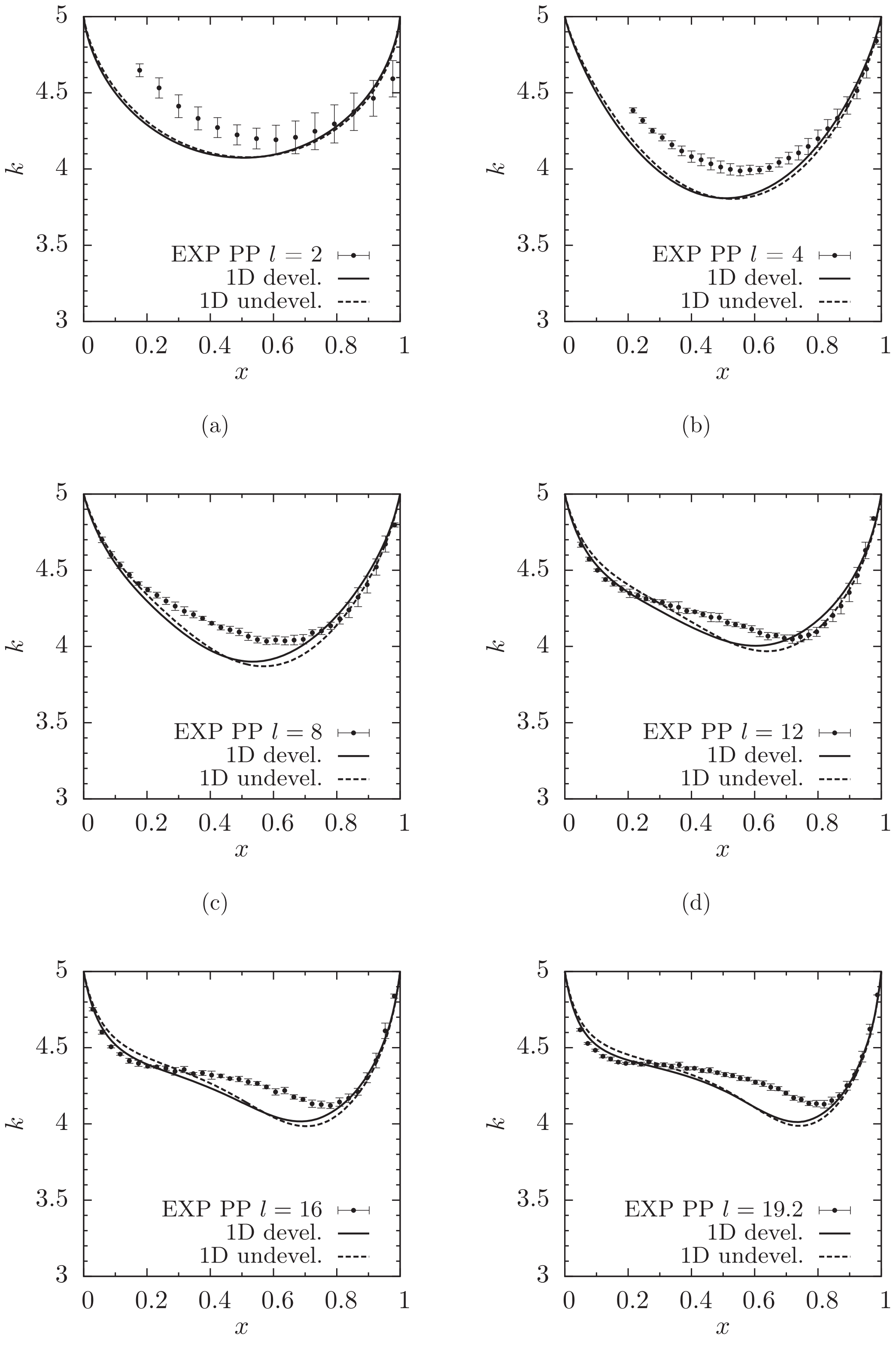

(a) (b) (c) (d) (e) (f)

Figure 6.10: Comparison of the maximum stable free surface contours k along the channel x-axis in the **parallel plates** channel. Points depict the experiment (average values of the multiple data points), where the error bars are the weighted averages of standard deviations (Equation (6.3)).

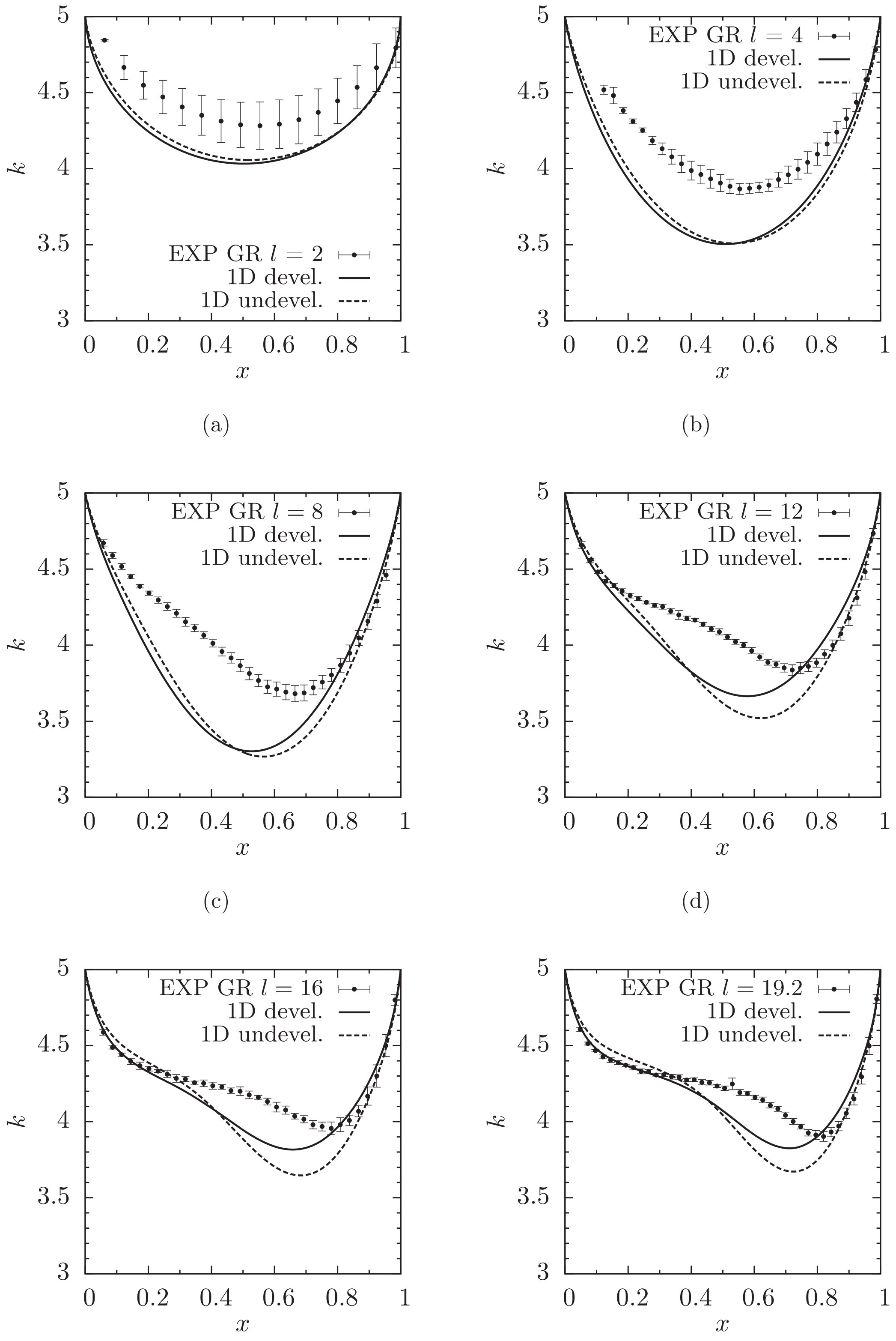

(a) (b)

(c) (d)

(e) (f)

Figure 6.11: Comparison of the maximum stable free surface contours k along the channel x-axis in the **groove** channel. Points depict the experiment (average values of the multiple data points), where the error bars are the weighted averages of standard deviations (Equation (6.3)).

6.3.3 Minimum Contour Point

To aid further examination of the free surface contour, the minimum contour point $k_{min}(x^*, k^*)$ is evaluated. A comparison of the position of the spatial coordinates of k_{min} between the experiment and the mathematical model (ccFlow) is shown in Figure 6.12(a), with the corresponding data summarized in Table 6.8 . The point k_{min} is located in the vicinity of $x = 0.5$ for short channels and is typical for convective dominated, symmetrical profiles. As the channel length is increased, the coordinate x^* of k_{min} shifts towards the channel outlet. As the channel length increases, the deformation of the free surface also increases due to the shifting of k_{min} towards the channel outlet. In the experiments (EXP), k^* increases with l for channels with $l > 3.6$. The same trend is observed for results of the 1D model, albeit for channels with $l > 4.8$. In both cases, k^* seems to tend towards a value of 4. It will be shown later that, for sufficiently long channels, $k^* = 4$ is a minimum value that is based on the channel geometry. As shown in Figure 6.12(b) the values of the experimentally determined coordinate x^* agree for parallel plates and the groove channel. Examination of k^* shows that lower values are obtained for the groove than for the parallel plates channel.

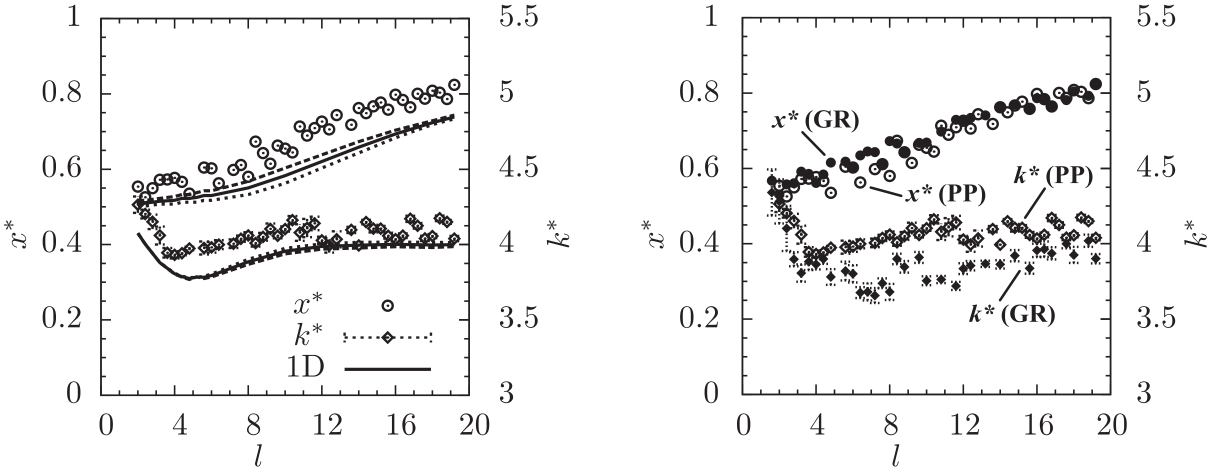

(a) Parallel plates.

(b) Parallel plates and Groove.

Figure 6.12: Position of the spatial coordinates of the minimum contour point $k_{min}(x^*, k^*)$ as a function of the channel length. Points $x^* = 0$ and $x^* = 1$ on the left ordinate axis correspond to the channel entrance and exit, respectively. The right ordinate axis represents the corresponding k^*. The flow is at the critical rate. (a) Solid lines are results of numerical simulations, whereas dotted and dashed lines represent the developed and undeveloped flow velocity profile assumption, respectively. (b) Comparison between the parallel plates and the groove channel (experimental results).

Table 6.8: Experimental (EXP) and numerical (1D) data corresponding to the k_{min} point (minimum contour point). The $\triangle$ depicts the difference between the measured and numerically computed values. Characteristic values A^*_{1D}, and h^*_{1D} at the k_{min} point v^*_{1D} are the flow velocity, flow cross-section area, and the mean curvature, respectively.

	l	x^*_{EXP}	x^*_{1D}	$\Delta x^*/\%$	k^*_{EXP}	k^*_{1D}	$\Delta k^*/\%$	v^*_{1D}	A^*_{1D}	h^*_{1D}
PP	2	0.554	0.503	9.3	4.264	4.074	4.5	1.42	0.86	2.06
	4	0.577	0.508	12.0	3.932	3.809	3.1	1.18	0.80	1.49
	6	0.603	0.518	14.1	3.982	3.804	4.5	1.05	0.80	1.25
	8	0.580	0.533	8.2	4.061	3.902	3.9	0.96	0.82	1.13
	10	0.655	0.563	14.1	4.103	3.975	3.1	0.91	0.84	1.08
	12	0.727	0.603	17.0	4.028	4.005	0.6	0.89	0.84	1.05
	14	0.762	0.643	15.6	3.994	4.015	0.5	0.87	0.85	1.05
	16	0.798	0.683	14.3	4.036	4.017	0.5	0.85	0.85	1.04
	18	0.808	0.719	11.1	4.056	4.015	1.0	0.84	0.85	1.04
	19.2	0.824	0.734	11.0	4.040	4.013	0.7	0.83	0.85	1.04
GR	2	0.531	0.5025	5.3	4.281	4.033	5.8	1.36	0.92	2.03
	4	0.562	0.508	9.6	3.863	3.504	9.3	1.16	0.87	1.52
	6	0.6	0.518	13.7	3.801	3.280	13.7	1.07	0.85	1.32
	8	0.672	0.528	21.5	3.68	3.302	10.3	1.00	0.85	1.21
	10	0.669	0.548	18.1	3.755	3.475	7.5	0.94	0.87	1.13
	12	0.729	0.578	20.7	3.835	3.664	4.4	0.89	0.89	1.08
	14	0.765	0.618	19.2	3.863	3.778	2.2	0.86	0.9	1.06
	16	0.786	0.658	16.3	3.956	3.816	3.5	0.84	0.9	1.05
	18	0.804	0.693	13.8	3.926	3.827	2.5	0.83	0.9	1.05
	19.2	0.823	0.709	13.9	3.901	3.825	1.9	0.82	0.9	1.05

6.3.4 Parametric Study

A parametric study with `ccFlow` is performed to demonstrate the influence of the OHNESORGE number on the shape of the free surface profiles. The model parameters are summarized in Table 5.2. A fully developed flow at the channel inlet is assumed. The OHNESORGE number $\mathrm{Oh} = 2.26 \times 10^{-3}$ (from CCF experiment) is increased and decreased by a factor of 1000. For $\mathrm{Oh} = 2.26 \times 10^{-3}$, the profiles are almost symmetrical with respect to $x = 0.5$ (Figure 6.13), which is typical for inertia dominated flows. With increasing Oh number, the displacement and the deformation of the free surface profile increase. It is interesting to see that, for the short channel $l = 4$, the contour k is quasi-symmetrical even for the large value of $\mathrm{Oh} = 2.26$, whereas for $l = 19.2$, the contour is highly non-symmetrical. This justifies the choice of the dimensionless channel length $\tilde{l}$ as a parameter characterizing the flow regimes in the capillary channels (will be discussed in Chapter 7).

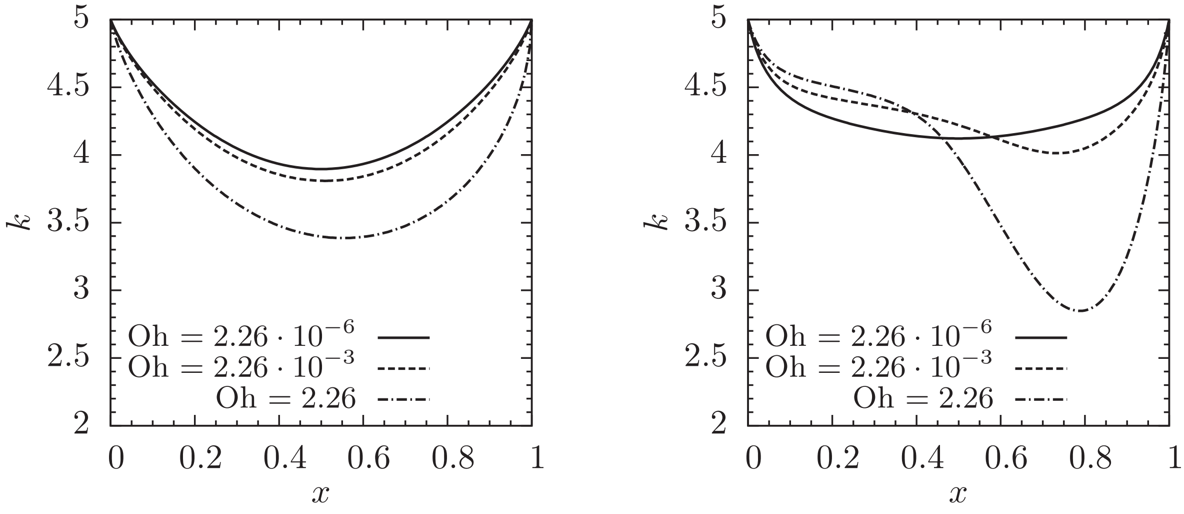

(a) $l = 4$ (b) $l = 19.2$

Figure 6.13: Free surface contour k depending on the Oh number in the parallel plates channel. Short channels $l = 4$ (a) and long channels $l = 19.2$ (b) are chosen for comparison. Last stable interfaces are depicted (flow at the critical flow rate). The value $\mathrm{Oh} = 2.26 \times 10^{-3}$ corresponds to the CCF experiment.

6.4 Weaknesses of the Mathematical Model

As shown above, the 1D model generally predicts well the shape of free surface profiles and values of the critical flow rate for the flow between parallel plates and in the groove channel under microgravity conditions. It does, however, overestimate the critical flow rate for short channels $l < 7.2$ (Figure 6.4). Furthermore, the predicted contours of the free surface profiles are slightly shifted towards the channel entrance (Figures 6.10 and 6.11). These differences reveal the weaknesses of the 1D model and its assumptions. These are shortly addressed in the following. During the experiments performed on the research rocket TEXUS the flow separation phenomenon was observed for the flow between parallel plates [69]. Tracer particles were used to study the behavior of the flow. For internal flows, such as CCF, the separation of the boundary layer (in the vicinity of the downstream part of the interface) causes an increase of the pressure loss [78]. The 1D model does not account for such a pressure loss. The flow separation is confirmed with the 3D simulations of the flow in the capillary channel (resembling the CCF test channel) with variable cross-sectional area [52]. This could explain the overestimation of the critical flow rate for short channels. In addition, at the channel inlet, the wall boundary condition changes from no-slip to slip, due to the presence of the free surface. Therefore, it takes a certain channel length for the flow to adjust to the new boundary conditions. The existence of such an adjustment region [37] adds more complexity to the entire flow, especially when the channel is short.

Chapter 7

General Behavior of Free Surfaces

The present chapter is based on the publication "Free surfaces in open capillary channels - Parallel plates" by P. Bronowicki, P. Canfield, A. Grah and M. Dreyer [5]. The validation of the mathematical model used for the prediction of the behavior of the gas-liquid interface in capillary channels in forced flow under microgravity conditions was provided in Chapter 6. It is demonstrated that the critical flow rate and free surface contours can be predicted with the 1D model. In general, the shape of the interface is influenced by geometrical constraints, the system pressure, and flow conditions. A number of numerical computations are performed in order to study the effects of the influencing parameters and to exploit the mathematical model. In the following developed flow at the channel entrance and pinned free surfaces are assumed. Three scenarios are considered: (i) static solution, no flow; (ii) dynamic solution, flow rate variation; (iii) dynamic solution, channel length variation. Steady flow between parallel plates is considered. Liquid properties and simulation parameters correspond to the CCF experiment (unless otherwise specified).

7.1 Static Solution

Reducing the flow in the channel to the static problem presents a possibility to study the influence of geometrical constraints and boundary conditions on the behavior of the gas-liquid interface. Since there is no flow, pressure is constant over the length of the channel and the free surface has a constant mean curvature along x. For zero flow, the momentum Equation (3.49) reduces to

$$\frac{\mathrm{d}h}{\mathrm{d}x} = 0 \, , \tag{7.1}$$

which means that the mean curvature h along the channel is dictated by the pressure boundary condition h_0

$$p_a - p = h = h_0 = \left(\frac{1}{R_1} + \frac{1}{R_2}\right) = const \, . \tag{7.2}$$

For the static solution, this equation applies everywhere along the free surface. Furthermore, Equation (3.59) reduces to $h_0 = h(x = 0) = K_0$. Therefore, the surface curvature in the channel is only a function of the system pressure induced by the meniscus in the compensation tube. Figure 7.1 shows static free surface contours for different channel lengths, where $K_0 = 0.166$ and $\Lambda = 5$, as in the CCF experiment. For the sake of comparison, both non-dimensional and dimensional quantities are depicted. The indentation of the free surface increases with increasing channel length. For channels with $l > 7.2$, the minimum contour height k maintains the same level in the middle part of the profile (Figure 7.1(b)). Here, the flat part of the profile in the vicinity of the channel center can be identified. Another feature that can be identified when dimensional values of the free surface contour are considered (Figure 7.1(a)) is the free surface contour slope $d_x k'$ at the channel entrance. The slope is dictated by the pressure (Equation (3.59)) at the channel entrance and appears identical for all channel lengths. Further increase of the length of the open section above $l = 7.2$ ($l' = 18$ mm) leads to the extension of the middle flat part of the profile.

There are, however, some limits to the mean curvature at the channel inlet, beyond which a stable, pinned free surface fails to exist, even for zero flow conditions. The externally applied pressure difference K_0 is limited by the physical conditions of the interface in the channel.

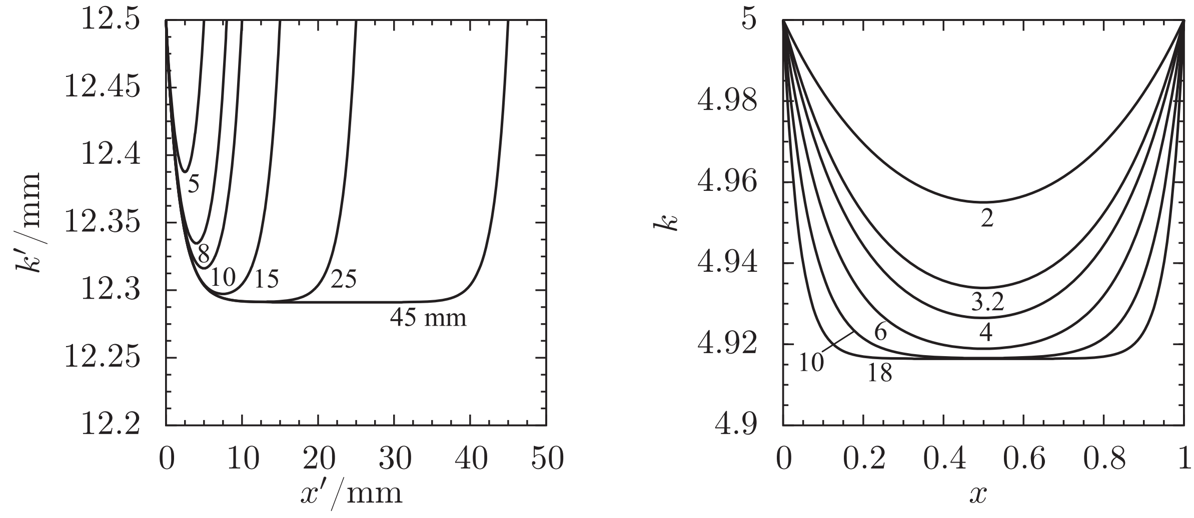

(a) (b)

Figure 7.1: Free surface contours along the channel axis x for different channel lengths (l' and l) and zero flow. The inlet boundary conditions correspond to the CCF experiment. Indentation of the free surface is dictated by the pressure boundary condition at the channel entrance and geometric constraints. Different characteristics can be observed depending on whether dimensional (a) or non-dimensional (b) quantities are observed.

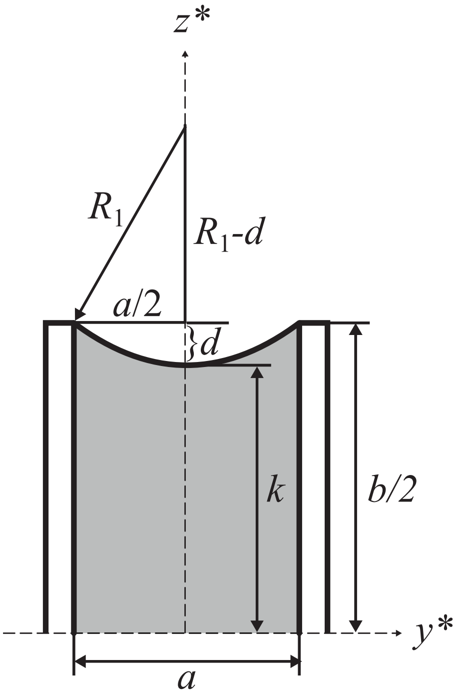

Figure 7.2: Channel cross-section at the lowest point of the free surface indentation ($k = k^*$). Grey color represents the liquid in the channel. Free surface displacement is depicted with d. R_1 is the first principal radius of curvature.

The free surface curvature is related to the free surface displacement $d = b/2 - k$ as shown in Figure 7.2. Both principal radii curvature can then be expressed as geometrical relations in dimensional form

$$R_1' = \frac{\left(\frac{a}{2}\right)^2 + d'^2}{2d'} \qquad \text{and} \qquad R_2' = \frac{\left(\frac{l'}{2}\right)^2 + d'^2}{2d'} \,. \tag{7.3}$$

Inserting Equation (7.3) into the dimensional YOUNG-LAPLACE Equation (3.3) and subsequent scaling yields

$$p - p_a = -2d \left(\frac{1}{1+d^2} + \frac{1}{\frac{1}{4}\left(\frac{1}{\Gamma}\right)^2 + d^2} \right), \tag{7.4}$$

where $1/\Gamma = l$. Equation (7.4) can be used to calculate the maximum pressure for given a, l, and d (Figure 7.3). The maximum free surface displacement for the channel with a gap distance $a = 5$ mm, resulting in a pinned free surface, is $d_{max} = R_{1max} = 1$, where $R'_{1max} = a/2 = 2.5$ mm. The dimensionless parameter Γ is used to quantify the obtained results. The uppermost curve in Figure 7.3 represents “long” channels with $\Gamma \to 0$, for which the maximum mean curvature is $h_{max} = -p_{max} = 1$. In the case of the CCF setup for channels

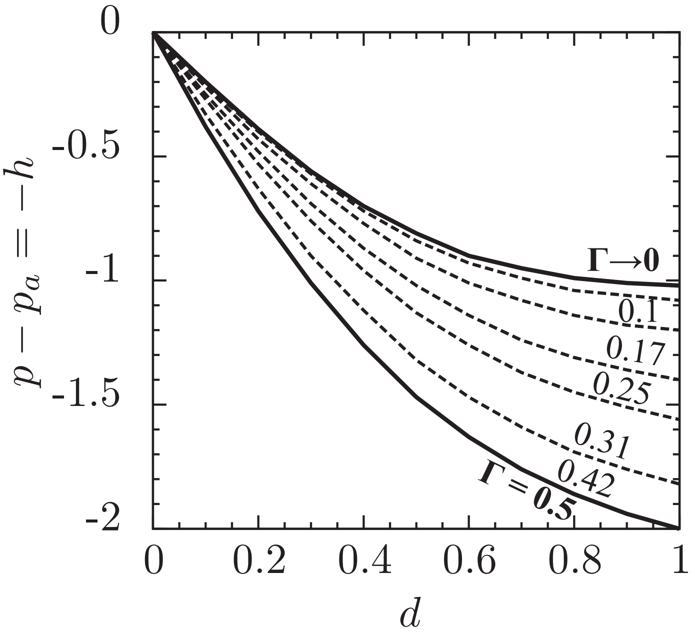

Figure 7.3: Pressure difference $p - p_a$ as a function of the surface displacement d. Maximum value of $d_{max} = R_{1max} = 1$ is a pure geometrical property.

with $l > 10$ ($\Gamma > 0.1$) the maximum mean curvature $h_{max} < 1.08$, and the second term on the right hand side of Equation (7.4) can be neglected. With increasing Γ (channel length decreases), the second curvature component becomes more significant and consequently the pressure difference in Figure 7.3 decreases. The lowermost curve in Figure 7.3 represents the shortest channel examined here, for which $l' = a$ and $\Gamma = 0.5$. In this case both mean curvature components contribute equally, and $h_{max} = 2$.

Furthermore, the minimum value k^* can be calculated as $k^*_{min} = k_{max} - d_{max}$. The maximum value k_{max} is a geometrical property that is defined by the channel wall's width b, where $k'_{max} = b/2 = 12.5$ mm (for CCF setup). The maximum displacement for the pinned free surface is $d_{max} = 1$. Assuming $d_{max} = 1$ and $k_{max} = 5$, the minimum value of k^* is $k^*_{min} = 4$. This value corresponds to the CCF experiment results shown in Figure 6.12(a), where for long channels the vertical coordinate of the k_{min} point $k^* \sim 4$. It confirms the assumption that the minimal contour point of the free surface is a geometric quantity. At $d_{max} = 1$, the interface reaches its maximum curvature for a pinned free surface.

Furthermore, the individual components of the mean curvature are evaluated. At the channel entrance and exit, the free surface is pinned at the edges of the slider and the channel. Thus, the first principal radius $R_1 \to \infty$ and, as a consequence the component $1/R_1 = 0$ at $x = 0$ and $x = 1$ (Figure 7.4). To satisfy Equation (7.2), the second curvature term must balance the pressure boundary condition, thus $1/R_2 \to 0.166 = h_0$ at the channel entrance and exit. For the channel length $l = 2$, the curvature is supported by both radii at any point $0 < x < 1$. For the channel length $l = 18$, the flat, middle profile part can be identified, where $R_2 \to \infty$. Thus, $1/R_2 \to 0$ between $x \approx 0.2$ and $x \approx 0.8$. Here, only the radius perpendicular to the flow forms the free surface. Consequently, for a long channel, between $x \approx 0.2$ and $x \approx 0.8$ the first curvature component adjusts to a fixed boundary condition so $1/R_1 \to 0.166 = h_0$.

Expanding the study to the whole range of channel lengths (corresponding to the CCF experiment) it is observed that, for channels with $l < 7.2$ both principal radii contribute to the mean curvature. In this case the free surface is supported by both radii. For long channels with $l > 7.2$, the flat profile part in the middle section can be identified, where only the first principal radius R_1 contributes to the curvature. In this case, the free surface is supported by only one radius ($1/R_2 \leq 0.01$ at $x = 0.5$). It must be noted that the length $l = 7.2$ corresponds to the previously determined length above which the minimum contour height k maintains the same level in the middle part of the profile (Figure 7.1(b)).

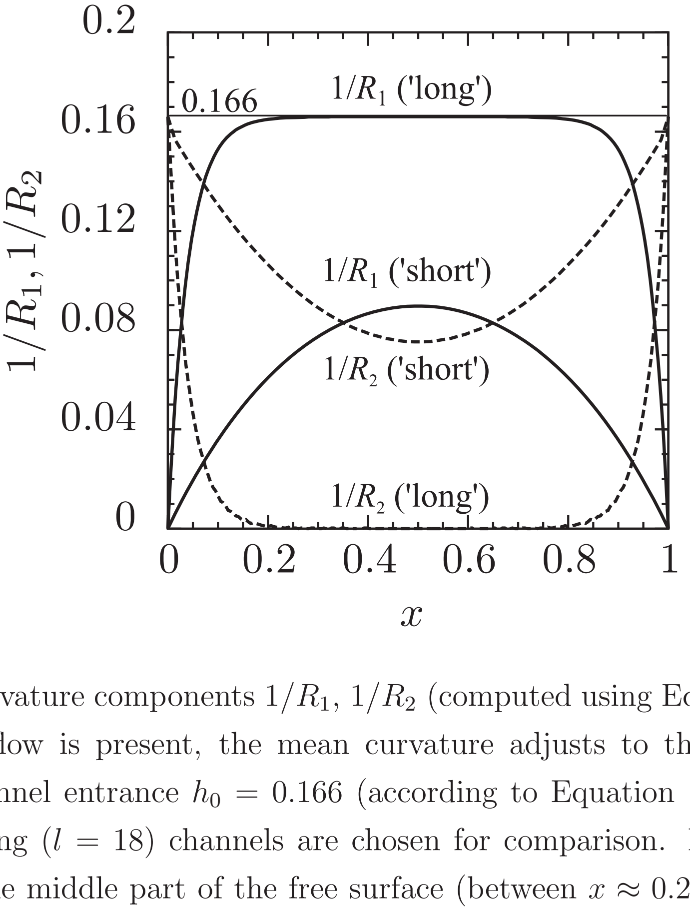

Figure 7.4: Mean curvature components $1/R_1$, $1/R_2$ (computed using Equations (3.54), (3.55)) along x. Since no flow is present, the mean curvature adjusts to the curvature boundary condition at the channel entrance $h_0 = 0.166$ (according to Equation (7.2)). Characteristic short ($l = 2$) and long ($l = 18$) channels are chosen for comparison. For long channels, the term $1/R_2 \to 0$ in the middle part of the free surface (between $x \approx 0.2$ and $x \approx 0.8$). This is the indicator of the flat profile section where $\mathrm{d}_{xx}k \to 0$.

7.2 Dynamic Solution

The influence of various flow effects on the shape of the free surface can be studied by variation of the flow conditions (flow rate and channel length). The CCF experiment mainly focuses on the investigation of free surfaces at the critical point where last stable contours were recorded with a high speed camera. In the following, the mathematical model is employed in order to examine the behavior of free surfaces in the stable, subcritical flow regime. A parametric study is performed for representative channel lengths. Geometrical and liquid properties correspond to the CCF experiment (Table 4.1), except for the system pressure boundary condition, which is set to $K_0 = 0$ for the sake of convenience.

7.2.1 Flow Rate Variation

The flow rate is varied between 0 (no flow) and the critical value Q_c. Representative short ($l = 2$) and long ($l = 18$) channels are presented. For the short channel, free surface profiles are almost, symmetrical with respect to the plane $x = 0.5$ (Figure 7.5(a)). For the long channel, the profiles are asymmetric, and the minimum contour point is shifted towards the channel exit (Figure 7.5(b)). In general, the asymmetry of the free surface increases with increasing flow rate. During the CCF experiment, however, it was observed that a given, constant change of the flow rate $\triangle Q$ leads to a different change of the free surface displacement, depending on the flow conditions (moderate or high flow velocities). Results of numerical simulations confirm this behavior. As can be seen in Figures 7.5(a) and 7.5(b) a 1% increase of the flow rate, from $Q/Q_c = 0.99$ to Q_c (critical regime), leads to a higher increase of the free surface displacement than an increase by 10% in the moderate, subcritical flow regime ($Q/Q_c < 0.95$). This illustrates the sensitivity of the free surface in the vicinity of Q_c, where a small change of the flow rate leads to a significant change of the free surface profile.

Furthermore, for stable flow, the mean free surface curvature h along the channel must balance the pressure difference between the flowing liquid and the surrounding gas at any point of the interface according to the YOUNG-LAPLACE Equation (3.3). As shown in Figures 7.5(c) and 7.5(d), the mean curvature increases with the free surface displacement along x. For the short channel, the curvature h has the same value at the inlet and at the outlet, which is typical for convective dominated flows, where the reversible pressure loss dominates the momentum balance. Convective acceleration leads to a pressure decrease between $x = 0$ and $x = x^*$, which is then recovered between $x = x^*$ and $x = 1$. For the long channel, the curvature h reaches higher values at the channel exit than at the channel entrance, which is, as a consequence of the pressure loss, attributed to viscous effects (Figure 7.5(d)). This behavior will be discussed in Section 7.3.

Furthermore, the components of the mean curvature along x are examined. Figures 7.6(a) and 7.6(b) show the first curvature component $1/R_1$. For the short channel, plots are symmetric with respect to the plane $x = 0.5$. $1/R_1$ reaches its maximum value of 1 in the middle part of the profile at the critical flow rate. This geometric property was discussed in Section 7.1. Plots of the second curvature component $1/R_2$ are shown in Figures 7.6(c) and 7.6(d). Also in this case curves are symmetric for the short channel. It is worth noting that, for the long channel, the term $1/R_2 \to 0$ in the middle part of the profiles for all considered flow rates. Even for the low flow rates $Q/Q_c < 0.1$, the free surface profile has a flat middle part where $1/R_2 \to 0$.

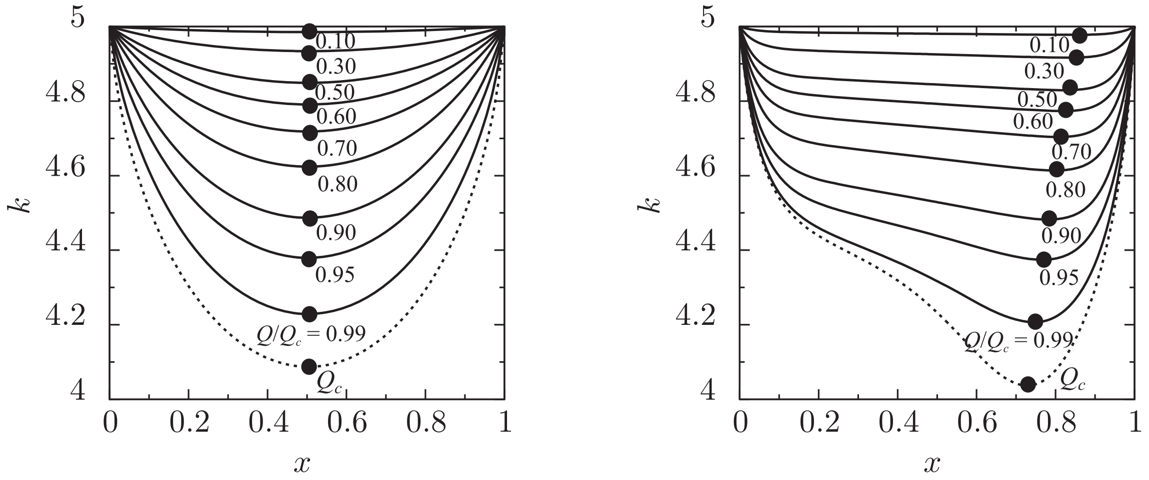

(a) $l = 2$ (b) $l = 18$

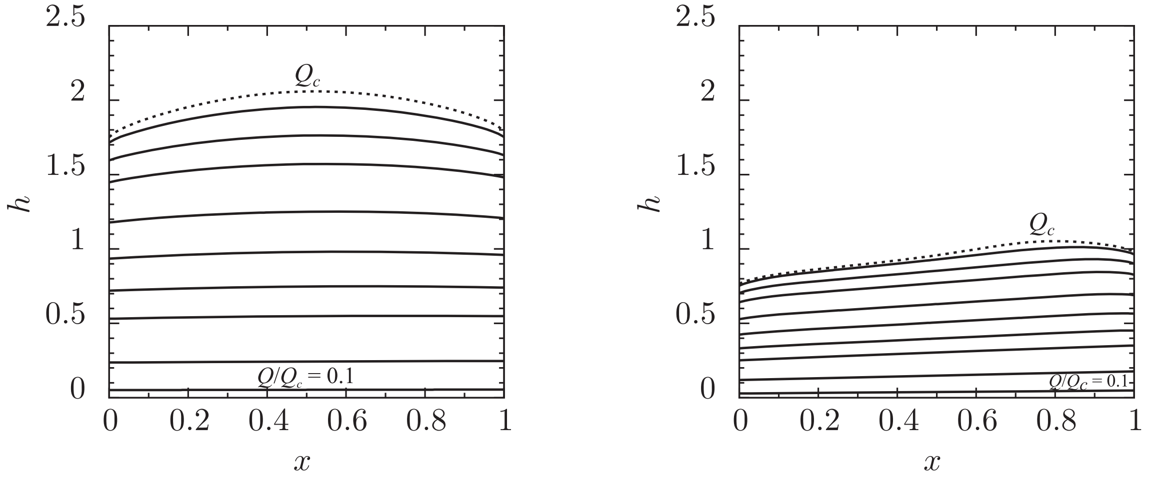

(c) $l = 2$ (d) $l = 18$

Figure 7.5: Typical results of numerical computations of flow between parallel plates. The left column shows results for the representative short channel ($l = 2$, $Q_c = 1.27$) and the right column for the long channel ($l = 18$, $Q_c = 0.79$). Depicted are: (a), (b) - free surface contour k, where circles depict the k_{min} point at position x^*; (c), (d) - mean curvature h, where Q/Q_c from bottom to top are 0.1, 0.3, 0.5, 0.6, 0.7, 0.8, 0.9, 0.95, 0.99, 1.

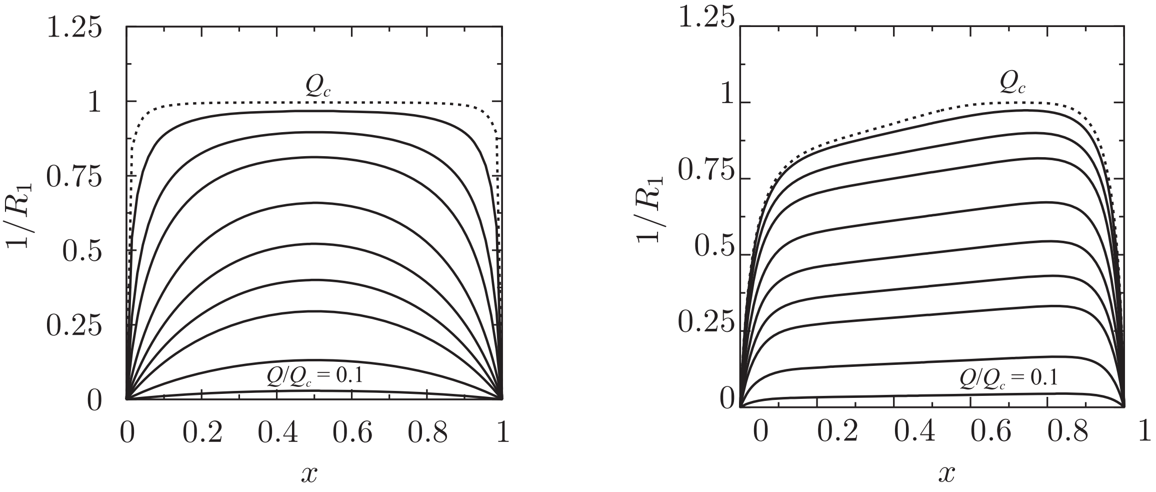

(a) $l = 2$ (b) $l = 18$

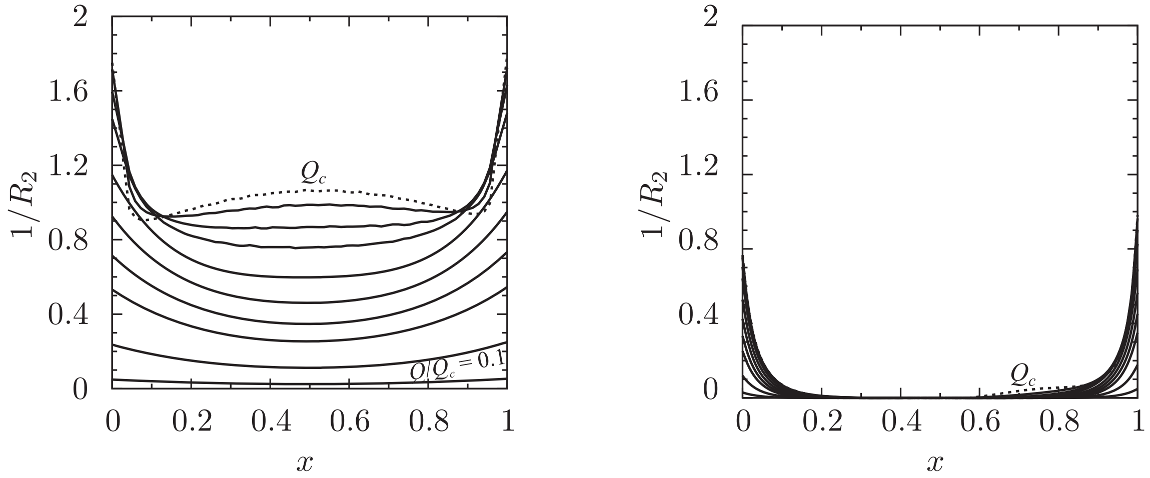

(c) $l = 2$ (d) $l = 18$

Figure 7.6: Typical results of numerical computations of flow between parallel plates. The left column shows results for the representative short channel ($l = 2$, $Q_c = 1.27$) and the right column for the long channel ($l = 18$, $Q_c = 0.79$). Depicted are: (a), (b) - first curvature component $1/R_1$; (c), (d) - second curvature component $1/R_2$. From from bottom to top Q/Q_c are 0.1, 0.3, 0.5, 0.6, 0.7, 0.8, 0.9, 0.95, 0.99, 1.

7.2.2 Channel Length Variation

In the following, the steady flow with a constant flow rate $Q = 0.63$ (subcritical flow) is considered in order to distinguish between effects that are typical for subcritical and critical flow. The channel length l is varied in a range $2 \leq l \leq 19.2$. Figure 7.7(a) shows plots of the contour k. The clear difference between the quasi-symmetric profiles for short channels and the asymmetric profiles for long channels can be seen. With increasing channel length the free surface displacement also increases. The minimum contour point k_{min} decreases and is shifted towards the channel exit. For channels $l > 4.8$, the longitudinal shift of the minimum contour point becomes significant ($x^* > 0.5 \pm 2.5$ %). The mean curvature adjusts to the free surface deformation, as depicted in Figure 7.7(b). The curvature difference between the channel inlet and outlet increases with the channel length. The first and second curvature components are shown in Figures 7.7(c) and 7.7(d), respectively. It is worth noting that all plots of $1/R_2$ are quasi-symmetric with respect to the plane $x = 0.5$ for all considered channel lengths. For channels $l > 7.2$, the second curvature component $1/R_2 \leq 0.01$ in the middle part of the profile. This indicates the presence of the flat profile part in the middle of the channel. $l > 7.2$ corresponds to the characteristic length identified using the static solution (Section 7.1), where for channels $l > 7.2$ the flat part of the profile is also present. Regarding the first curvature component, plots are quasi-symmetric for channels with $l < 4.8$. For longer channels, the asymmetry of $1/R_1$ increases towards the channel exit.

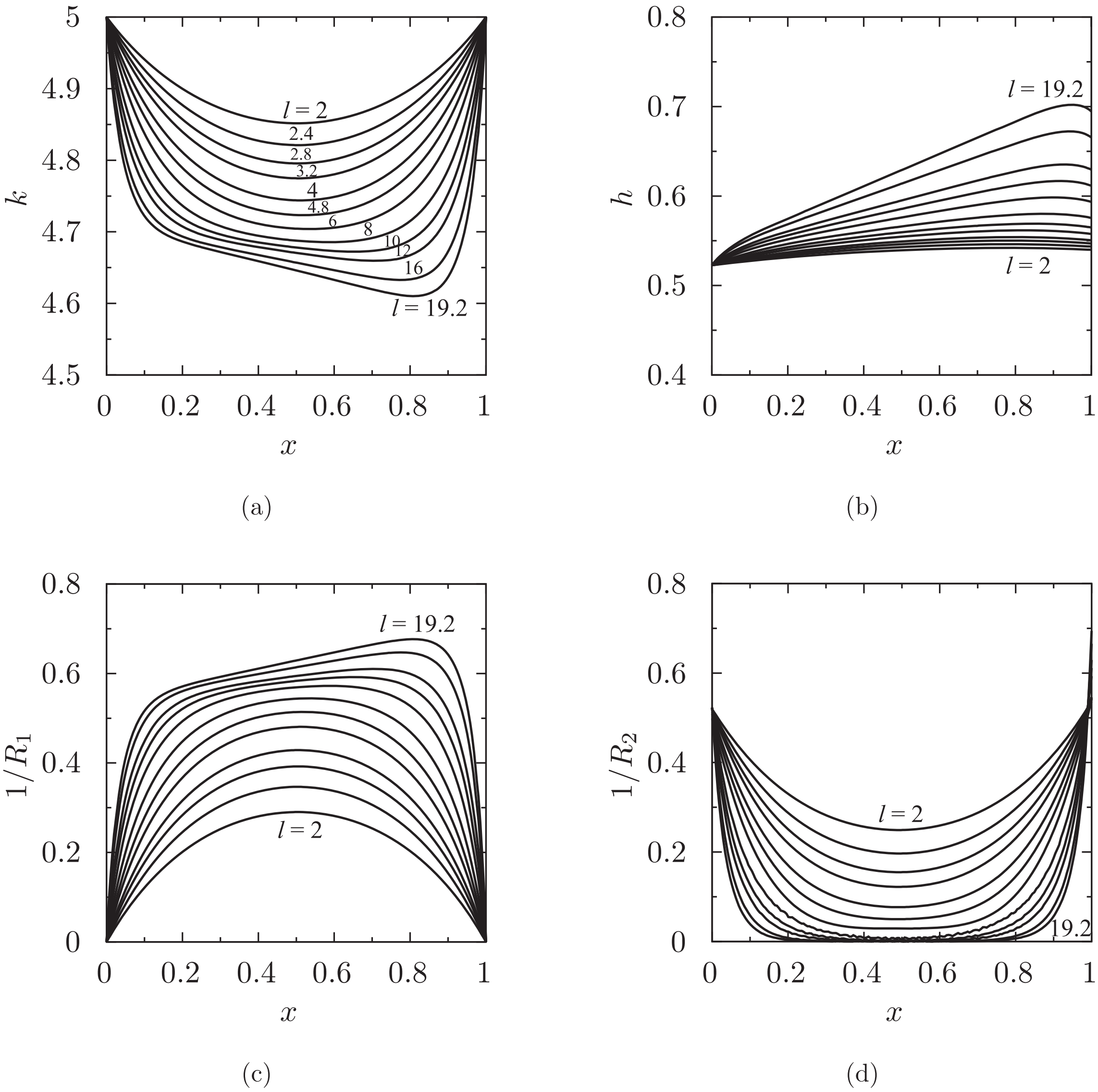

(a) (b)

(c) (d)

Figure 7.7: Typical results of numerical computations of the flow between parallel plates with a fixed flow rate $Q = 0.63$. The channel length is varied in the range $2 \leq l \leq 19.2$, which corresponds to the range of lengths investigated in the CCF experiment. (a) - free surface contour k; (b) - mean curvature h; (c) - first curvature component $1/R_1$; (d) - second curvature component $1/R_2$. In (b) and (c), from bottom to top, the values of l are 2, 2.4, 2.8, 3.2, 4, 4.8, 6, 8, 10, 12, 16, 19.2. In (d) from top to bottom, the values of l are 2, 2.4, 2.8, 3.2, 4, 4.8, 6, 8, 10, 12, 16, 19.2.

7.3 Physical Flow Regimes

In the following, the influences of two major flow effects, convective acceleration and viscous pressure loss, on the behavior of the free surface is studied. The flow is assumed to be at its critical rate, and the model parameters correspond to the CCF experiment shown in Table 4.1. A fully developed velocity profile ate the channel entrance is assumed. The numerical code provides the steady flow solution of the free surface contour k, flow velocity v, flow cross-section area A, and the mean curvature h along the x-axis (Figure 7.8). For the channel with $l = 2$, the plot of the free surface contour k is symmetrical with respect to the plane $x = 0.5$ (Figure 7.8(a)). For the channel with $l = 18$, the contour is non-symmetric (Figure 7.8(b)), and the minimum contour point is shifted towards the channel exit. In both cases, the flow velocity v reaches its maximum value at the channel throat (minimum contour point), where the flow cross-section area A reaches its minimum. In both cases the mean curvature h increases between $x = 0$ and $x = x^*$ due to the pressure decrease (consequence of the convective flow acceleration). For the channel with $l = 2$, the curvature h has almost the same value at the channel inlet and outlet. The pressure is almost fully recovered between $x = x^*$ and $x = 1$. For the channel with $l = 18$, the curvature h has a higher value at the channel exit than at the channel inlet.

In the following, the contributions of the individual terms of the momentum equation to the balance are investigated. In Equation (3.49), the reversible pressure loss due to the convective acceleration is represented by the convective term. The irreversible frictional pressure loss

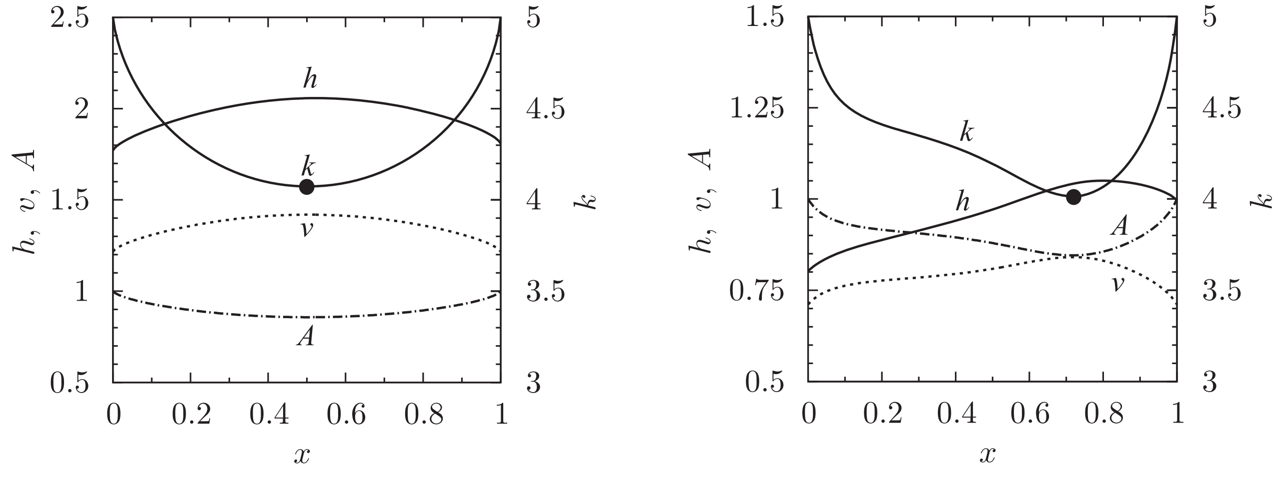

(a) $l = 2$ (b) $l = 18$

Figure 7.8: Typical results of the 1D simulation of the flow between the parallel plates with the critical flow rate. The value of the mean curvature h at the channel entrance $x = 0$ is defined by Equation (3.59). The value of the coordinate x^* (●) of the minimum contour point is $x^* = 0.50$ for the channel with $l = 2$ and $x^* = 0.68$ for the channel with $l = 18$.

is described by the viscous term. The observation was made that the relative proportion of both terms differs with the flow length. This is addressed in the following. Integration of the momentum Equation (3.49) yields

$$\underbrace{\frac{1}{2}\left(v^2 - v_0^2\right)}_{\chi} = \underbrace{h - h_0}_{\mathcal{H}} - \underbrace{\frac{K_f\,\tilde{l}}{2}\int_0^x v dx}_{\Psi} \,, \tag{7.5}$$

where the terms from left to right represent the convective, curvature, and viscous contribution, respectively. The unsteady term is skipped since steady flow is considered.

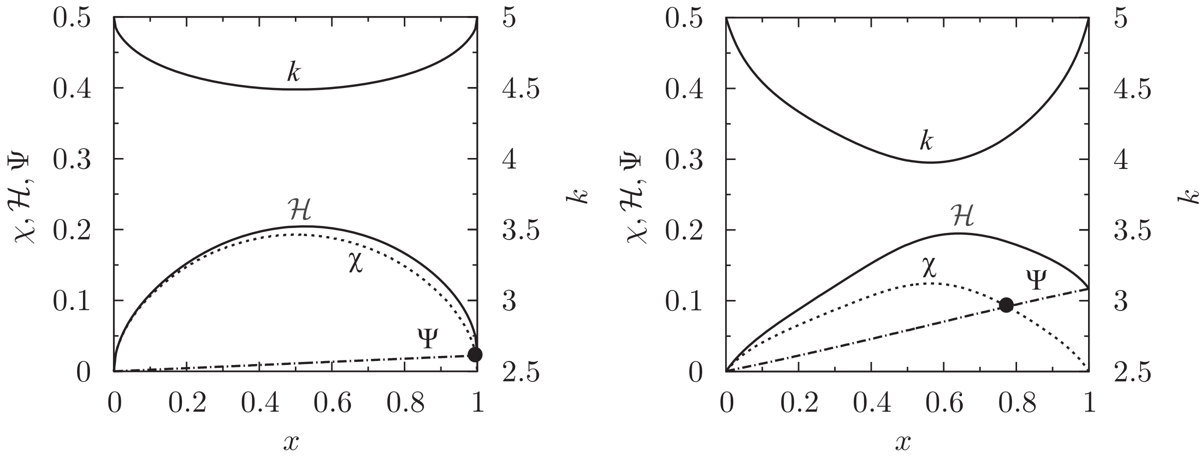

(a) $l = 1$ (b) $l = 10$

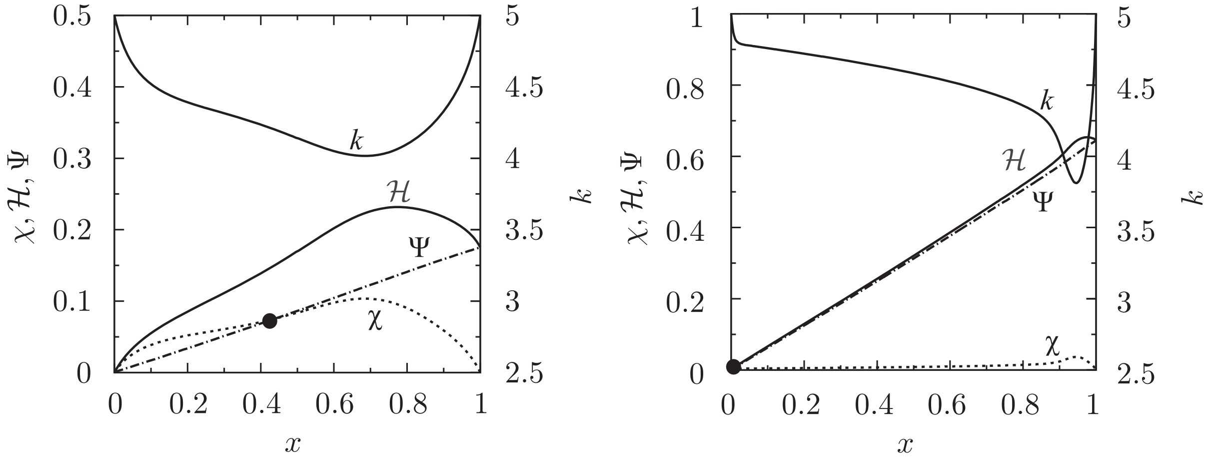

(c) $l = 16$ (d) $l = 120$

Figure 7.9: Contributions to the momentum balance for the flow at the critical rate. Curves χ, $\mathcal{H}$, Ψ represent the convective, curvature, and viscous terms, respectively. Dots depict the point x^+ where $\chi = \Psi$.

Results of 1D simulations are analyzed to determine the magnitude of the said terms, which are then plotted along the channel axis x (Figure 7.9). The term $\mathcal{H}$ (curvature) reflects the capillary pressure evolution along the channel and reaches higher values at the channel outlet than at the channel inlet. In general, with increasing channel length, the viscous effects become more significant. The irreversible frictional pressure loss causes the curvature difference between the channel outlet and inlet. The term χ (representing the convective term) is a function of the local flow velocity. It reaches maximum values at the point of the minimum cross-section (where the flow velocity reaches ist maximum values). The term Ψ (viscous term) increases linearly along the channel and reaches the highest value at the channel outlet. For sufficiently short channels (Figure 7.9(a)), the term χ dominates over Ψ along the entire channel. Conversely, for sufficiently long channels (Figure 7.9(d)), the term Ψ is dominant. A characteristic point is x^+, where the convective and viscous terms are equal in magnitude ($\chi = \Psi$).

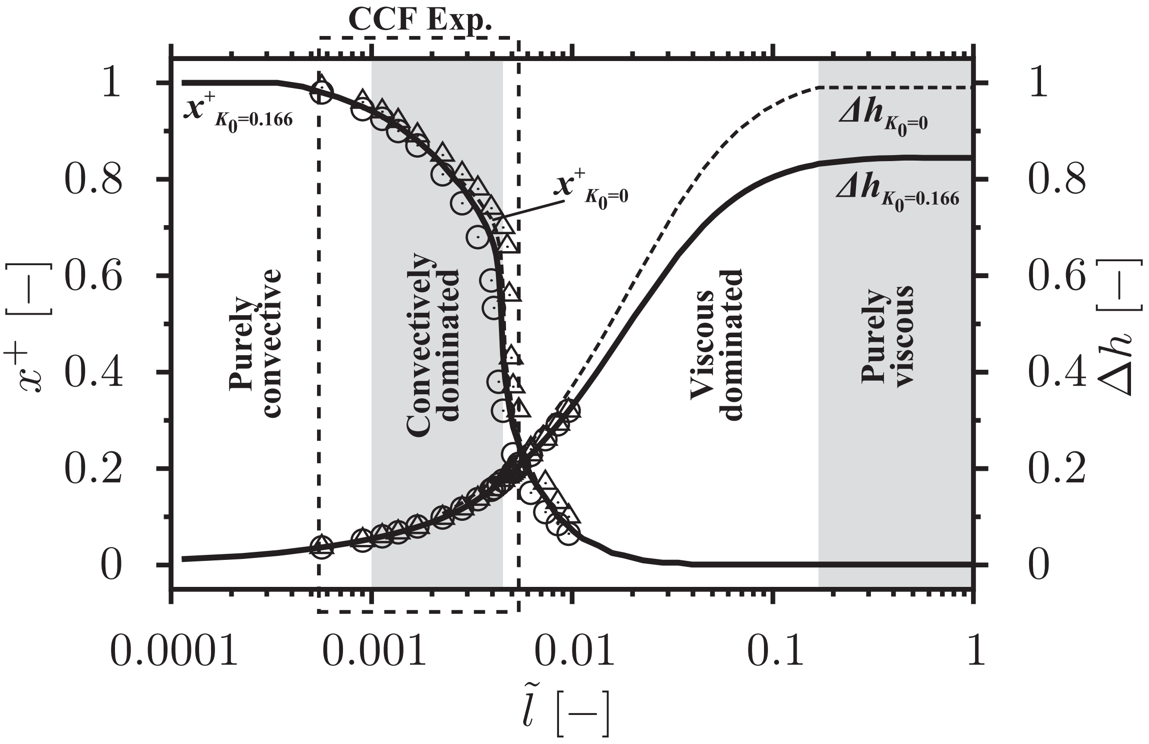

Figure 7.10: Location of x^+ (left ordinate axis) and the irreversible pressure loss $\triangle h$ (secondary axis) as functions of the dimensionless flow length $\tilde{l}$ at the critical flow rate. Solid lines represent results for $\Lambda = 5$ and the system pressure $K_0 = 0.166$ (as in the CCF experiment). Dashed lines are for $\Lambda = 5$ and $K_0 = 0$. The curvature difference $\triangle h$ is depicted with triangles for $\Lambda = 4$, and circles for $\Lambda = 6$. The dashed box depicts the range of $\tilde{l}$ which was investigated in the CCF experiment. Shaded areas indicate the convectively dominated and purely viscous regimes.

The location of x^+ is a function of the channel length (Figure 7.10, left ordinate axis) and can be used to characterize the transition between different flow regimes. For flow lengths $\tilde{l} < 4 \times 10^{-4}$, x^+ is located in the vicinity of the channel outlet ($x^+ \rightarrow 1$), and for flow lengths $\tilde{l} > 3 \times 10^{-2}$ in the vicinity of the channel inlet ($x^+ \rightarrow 0$). With increasing flow length, x^+ shifts towards the channel inlet ($x = 0$). A sudden drop of the curve x^+ occurs at $\tilde{l} \approx 4.5 \times 10^{-3}$. The transition between the convective and viscous dominated flow domains is begins here.

It must be noted that, in the case of convective dominated flow, both flow effects (convective and viscous) exist and influence the free surface curvature. The same applies for viscous dominated flows. The terms "viscous" and "convective" dominated imply the dominance of the particular term. For a further classification of the physical flow regimes, the curvature difference between the channel outlet and inlet $\triangle h = h(x = 1) - h(x = 0)$ is inspected. The reversible convective momentum transport does not affect the pressure difference between inlet and outlet of the channel. Therefore, $\triangle h$ is an indicator of the presence of the irreversible, frictional pressure loss. Figure 7.10 (secondary axis) shows $\triangle h$ as a function of the dimensionless flow length $\tilde{l}$. In general, the curvature difference increases with increasing channel length. It is worth noting that the results for different aspect ratios Λ overlap. For sufficiently short channels $\tilde{l} \leq 3 \times 10^{-4}$, the curvature difference tends to zero (negligible viscous pressure loss). For channel lengths $\tilde{l} \geq 1.7 \times 10^{-1}$, the curvature difference tends to unity (convective effects can be assumed negligible). Therefore, for lengths $\tilde{l} \geq 1.7 \times 10^{-1}$, the flow is classified to be in the purely viscous regime (criterion is $\triangle h > 0.99$). The curvature difference $\triangle h$ is equivalent to the net pressure loss in the channel. If the system pressure K_0 is greater than zero, then $\triangle h \rightarrow (1 - K_0)$ in the purely viscous regime (solid line for $\triangle h$ in Figure 7.10).

Finally, the purely convective flow domain can be identified for sufficiently short channels. The criteria are the curvature difference ($\triangle h < 0.05$) and the free surface symmetry. Besides the curvature difference between the channel inlet and outlet, the free surface asymmetry also indicates the presence of the irreversible pressure loss. Evaluation of the CCF experiment and the numerical study show that, for short channels $l < 4.8$ (1D model) the minimum contour point is located almost in the symmetry plane ($x^* = 0.5 \pm 0.012$), as displayed in Figure 6.12(b). It can also be seen in Figure 6.12(b) that the length $l = 4.8$ (1D) is a characteristic length where k^* reaches its minimum value. Free surface profiles are symmetric for $l < 4.8$. Increasing the channel length above $l = 4.8$ leads to the profile asymmetry due to the irreversible frictional pressure loss. The influence of the viscous term is negligible for flow lengths $\tilde{l} < 10^{-3}$ (symmetric free surface contours). Therefore, flow lengths $\tilde{l} < 10^{-3}$ are classified to be in the purely convective regime. A summary of the identified flow regimes is shown in Table 7.1.

The non-dimensional flow length $\tilde{l}$ is a function of two non-dimensional numbers, the Ohnesorge number Oh and the length aspect ratio Γ (Section 3.4). As shown before, $\tilde{l}$ can be used to characterize the physical flow regimes for the capillary channel flow. For sufficiently

Table 7.1: Physical flow regimes as a function of the dimensionless channel length $\tilde{l}$. Non-dimensional parameter space is given in the Table 4.1. Presented domains correspond to the ones depicted in Figure 7.10.

Flow regime	$\tilde{l}$	Criterion
purely convective	$\tilde{l} < 10^{-3}$	- symmetrical profiles ($x^+ \approx x^*$) - $\triangle h < 0.05$
convective dominated	$10^{-3} \leq \tilde{l} < 4.5 \times 10^{-3}$	- $\triangle h$ increases - x^+ shifts towards the channel inlet
transition regime	$\tilde{l} \approx 4.5 \times 10^{-3}$	- sudden drop in the x^+ curve
viscous dominated	$4.5 \times 10^{-3} < \tilde{l} < 1.7 \times 10^{-1}$	- $\triangle h$ increases
purely viscous	$\tilde{l} \geq 1.7 \times 10^{-1}$	- $\triangle h > 0.99$

small $\tilde{l}$, the frictional pressure loss can be neglected, and the behavior of the free surface is essentially affected by the convective term. With increasing $\tilde{l}$, the dominance of the convective term reduces and viscous effects become more significant. For channel lengths $\tilde{l} \geq 4.5 \times 10^{-3}$ (transition regime), the contribution of the viscous momentum transport is at least equal to the convective contribution (or greater). For sufficiently large $\tilde{l}$, the curvature (pressure) gradient is only related to the irreversible frictional pressure loss. The analytical formulation of the critical flow rate Q_c^{an} in the purely viscous regime was given in Equation (2.5). For flow lengths $\tilde{l} < 1.7 \times 10^{-1}$, no analytical solution exists, and numerical methods are used to predict the value of the critical flow rate and the shape of the free surface contour. Characteristic results for two representative flow lengths $\tilde{l} = 1.13 \times 10^{-3}$ (left boundary, purely convective flow) and $\tilde{l} = 2.82 \times 10^{-1}$ (right boundary, purely viscous flow) are given in Table 7.2. The presented values are valid for the following parameters: $\Lambda = 5$, $\mathrm{Oh} = 2.26 \times 10^{-3}$, $K_0 = 0$.

Table 7.2: Results of the 1D simulation for two representative flow lengths corresponding to the ones depicted in Figure 7.10. The critical flow rate and the properties at the point of the minimum cross-section (flow velocity v^* and flow cross-section area A^*) are listed.

Flow regime	$\tilde{l}$	Q_c^{1D}	Q_c^{an}	v^*	A^*	Comments
purely convective	1.13×10^{-4}	2.32	does not apply	2.39	0.97	$v^{*'} = 2.39 v_c$
purely viscous	2.82×10^{-1}	0.07	0.07	0.11	0.62	$v^{*'} = 0.11 v_c$

Chapter 8

Transient Flow Results

In the following, the results of the transient flow experiments in the groove channel are evaluated. The total number of 1403 transient data points (thereof, 110 with HSHR camera images) was achieved during the CCF EU#1 series.

In the experiment, the test channel was observed in real time with the MSG camera. It was determined during the visual inspection whether the flow remains stable under certain flow conditions or not (well defined acceleration δ). For each of the considered channel lengths, the acceleration $\delta = \Delta Q/\Delta t$ is varied (beginning with low flow rates) until a clear limit between stable and unstable accelerations is resolved. Three parameters are required to define the transition: the increase of the flow rate at the channel outlet ΔQ, the period of time Δt, and the final steady flow rate Q. The Δt has to be in the magnitude of a natural time constant of the system. A too large time period could lead to the undesired quasi-steady behavior of the flow. A too small time period could spoil the results due to incapability of the system to adapt to the new conditions. The natural time constant $\Delta t = 1$ s of the CCF system was determined experimentally. In order to reduce the number of parameters required for the definition of the transition a constant time period Δt was assumed. The main goal of the transient experiments was to determine transient stability diagrams as shown in Figure 3.8(b) for all considered channel lengths.

As discussed in Section 3.5, the liquid pressure in the test channel decreases with increasing flow rate at the channel outlet. As a consequence, the free surface bends inwards into the channel. During an stable acceleration, the free surface remains stable after the transition. During an unstable acceleration, the free surface loses its stability, leading to a collapse and gas ingestion into the flow path occurs. In terms of the flow regime two cases can be distinguished : (i) the flow after the transition is supercritical ($Q > Q_c$), or (ii) the flow after the transition is subcritical or critical ($Q \leq Q_c$). In the first case, the stable acceleration δ cannot be determined, because the stability limit of the steady flow (after the transition) is exceeded. In the second case, the stability of the free surface after the transition depends on the acceleration and the flow regime at which the transition takes place (subcritical or critical). Figure 8.1 shows the typical behavior of the free surface during (a) a stable and (b) an unstable acceleration in the groove channel with $l' = 30$ mm. In the first example (Figure 8.1(a)), the flow rate is increased by $\delta' = 2$ ml/s^2 from $Q'_0 = 3.0$ ml/s to $Q' = 5.0$ ml/s. In the second example (Figure 8.1(b)), the flow rate is increased by $\delta' = 3$ ml/s^2 from $Q'_0 = 2.0$ ml/s to $Q' = 5.0$ ml/s. The corresponding critical flow rate is $Q'_c = 5.8$ ml/s. In both cases the flow is under steady flow conditions at the beginning of the transition ($t' = 0$). The free surface bends inwards into the channel when flow rate is increased. At time $t' = 1.6$ s the flow rate at $x = l = 1$ in both cases is equal to the set value after the transition $Q' = 5.0$ ml/s.

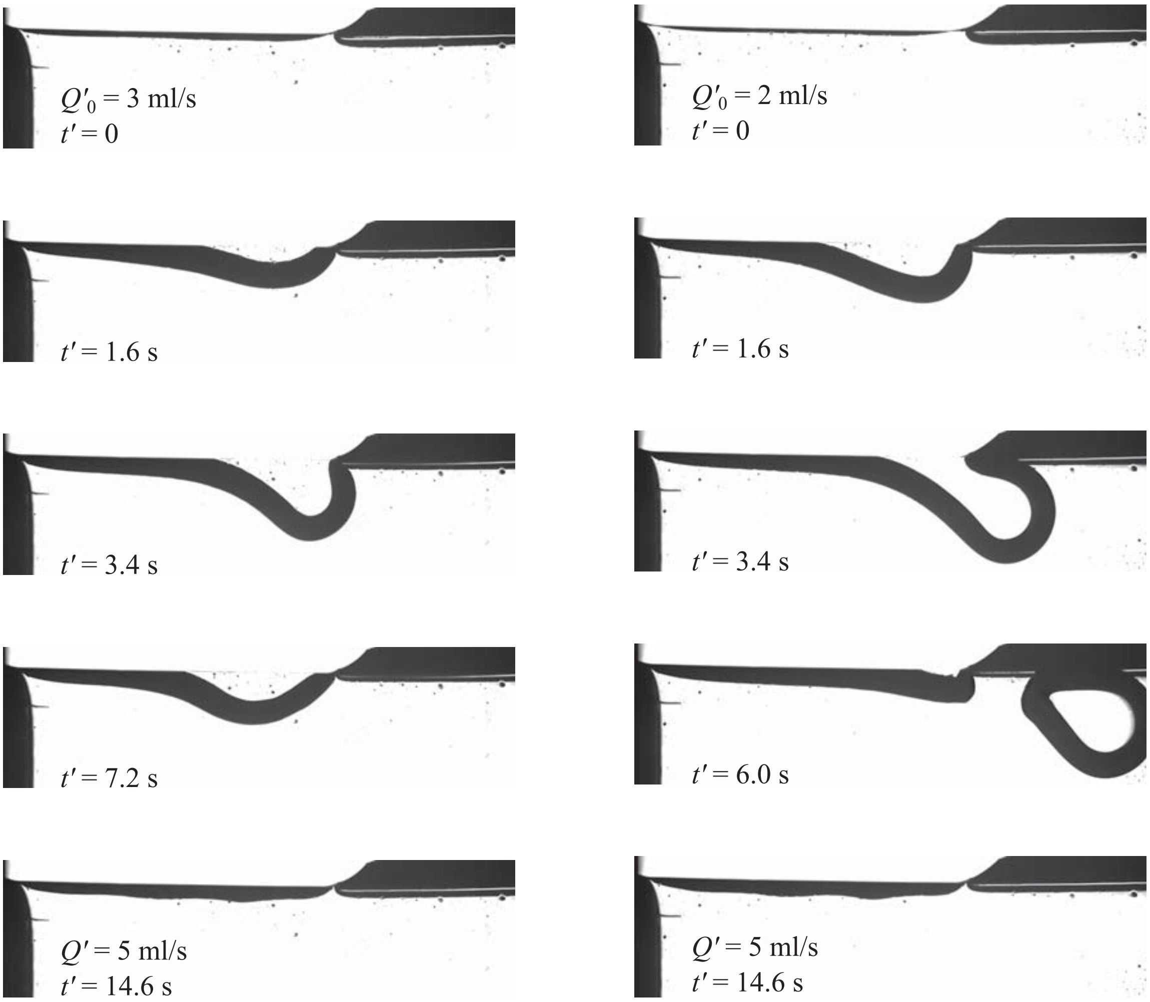

(a) Stable acceleration, $\delta' = 2$ ml/s^2 (ID 00526).

(b) Unstable acceleration, $\delta' = 3$ ml/s^2 (ID 00529).

Figure 8.1: HSHRC images illustrating the free surface behavior during a stable (a) and an unstable (b) flow acceleration in the groove channel with $l' = 30$ mm. The flow is from left to right.

The dynamic effects (inertia of the accelerated liquid) drive the further displacement and deformation of the free surfaces. The free surface reaches its maximum indentation at $t' = 3.4$ s for the stable acceleration. After $t' = 3.4$ s the free surface is being pulled back and adjusts to the "new" steady flow conditions ($Q' > Q'_0$).

In case of the unstable acceleration (Figure 8.1(b)), the free surface curvature fails to balance the pressure difference across the interface. As a consequence, the free surface loses its stability, leading to a collapse and gas ingestion ($t' = 3.4$ and 6.0 s) into the flow path (choking). After the gas bubble detaches, the free surface stabilizes and is being pulled back, as for the steady acceleration. The ingestion would repeat periodically if the flow rate after the transition was above the critical value ($Q' > Q'_c$).

The transient flow measurements were performed in different series through the entire CCF experiments course. The amount of gas in the PSC is varied between the series in order to verify the transient stability model (Section 3.5). Table 8.1 gives an overview of the performed transient flow experiments.

Table 8.1: Summary of the performed transient flow experiments. The amount of gas V'_g in the phase separation chamber was determined during the experiment. r is the corresponding feedback ratio according to Equation (3.68).

Sequence	V'_g/ ml	r	No. Data Points
1a	125	4.57	718
1b	200	3.54	
2a	51	6.95	174
2b	80	5.71	
2c	125	4.57	
2d	190	3.64	
3a	59	6.55	300
3b	74	5.93	
3c	100	5.13	
4	$\rightarrow 0$	12.00	151
5	$\rightarrow \infty$	1.00	60

8.1 Stability Diagrams

In the following, the results from the CCF transient flow experiments are compared with the flow stability model introduced in Section 3.5. Figures 8.2 and 8.3 show the evaluated stability diagrams for the characteristic channel lengths (measurement sequence 1a and 1b). The acceleration is normalized with the transients stability constant $\delta_0 = (h^* - K_0)/l_0 = 0.0118$, where $h^* = 2$ is the scaled capillary pressure at the point of the minimum cross-section (as discussed in Section 3.5.1), $K_0 = a/R'_{CT} = 0.166$ is the scaled system pressure (Equation (3.60)), and $l_0 = 155.2$ (scaled with $a/2$) is the effective length of the accelerated liquid column between the compensation tube and the channel inlet. The flow rate Q is the final flow rate after the transition. Filled and empty circles (one circle is one data point) represent stable and unstable acceleration, respectively. The solid lines represent the stability limits determined with Equation (3.75). The dependency of the flexibility function f (Equation (3.67)) on the channel length is shown in Figure B.4 (Appendix B.5). Arrows in Figure 8.2(a) present the way the stability diagrams should be interpreted. And so, for the channel with $l = 2$ the maximum stable acceleration is $\delta/\delta_0 = 1.1$ if the final flow rate after the transition is $Q/Q_c = 0.7$.

As expected, the lower the flow rate at which the transition ends, the higher the maximum stable acceleration is. The acceleration stability limit decreases with increasing flow rate. This is a consequence of the two effects causing the instability, the steady flow pressure due to convective acceleration and the transient pressure due to temporal acceleration.

To solve Equation (3.75), the value of the critical flow rate for the given channel length is required. For channels with $l \geq 8$, the tool ccFlow can be used for determining the critical flow rates. As shown in Figure 6.4, there is a discrepancy between the experimental results and the 1D model for channels with $l < 8$. In this case, the experimentally obtained values of Q_c (if available) should be applied.

Furthermore, the CCF experimental results confirm that the flexibility effect (introduced in Section 3.5.2) is well modeled. The stability enhancement, indicated by red vertical lines on the secondary axes in Figures 8.2 and 8.3, is determined for the channels with $l > l_f0$ $(l > 3)$.

There are, however, some minor discrepancies between the experimental and theoretical results. The slope of the TSM lines deviates slightly from the slope of the experimentally determined stability limit (Figures 8.2 and 8.3). This indicates some weaknesses of the transient stability model in Equation (3.75) and will be further elaborated in Section 8.2.

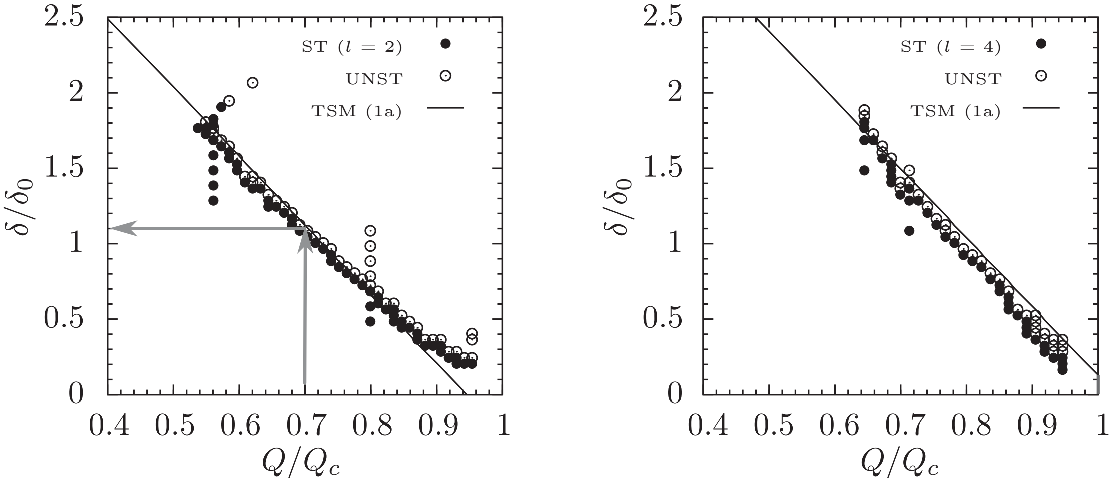

(a) No. data points: 105.

(b) No. data points: 75.

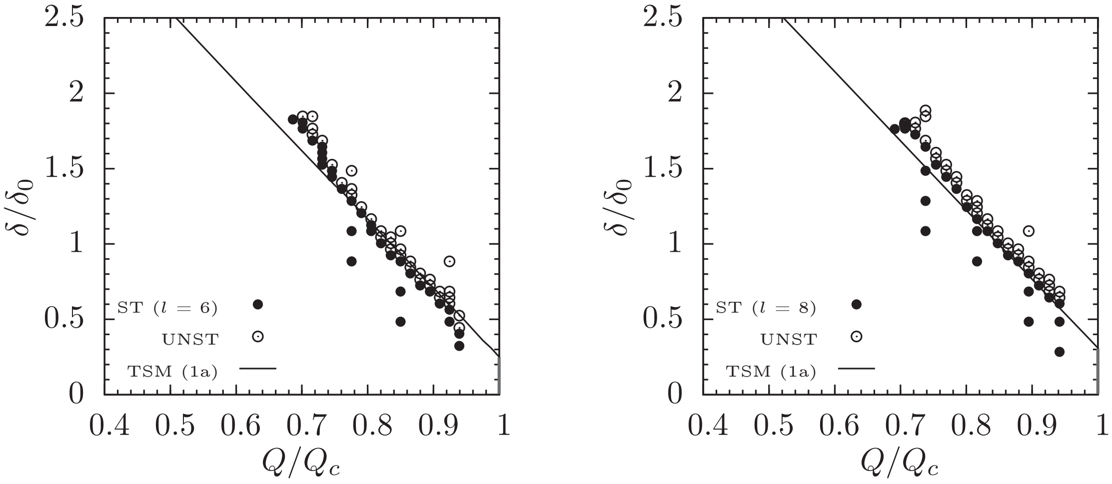

(c) No. data points: 64.

(d) No. data points: 65.

Figure 8.2: Stability diagrams for measurement sequence 1. Experimental data for stable (ST) and unstable (UNST) acceleration in comparison to the Transient Stability Model (solid lines) in Equation (3.75).

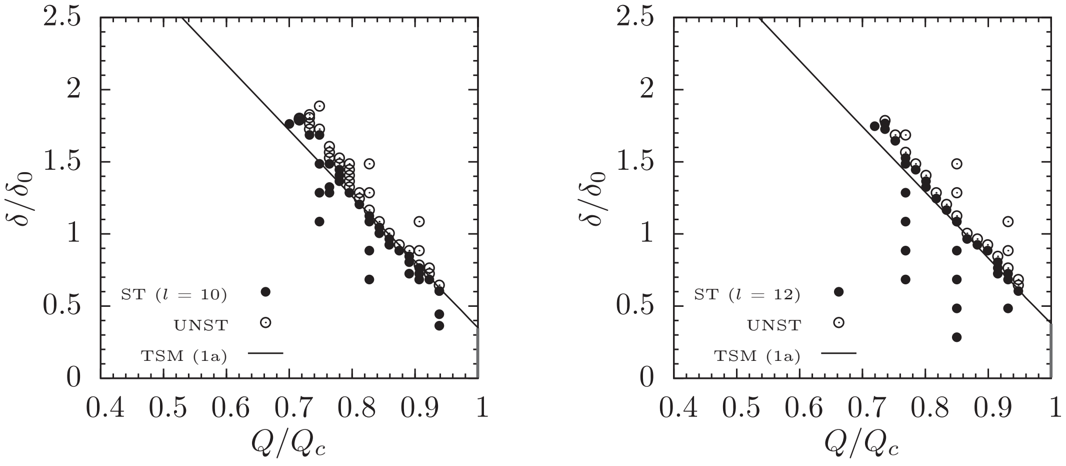

(a) No. data points: 70.

(b) No. data points: 51.

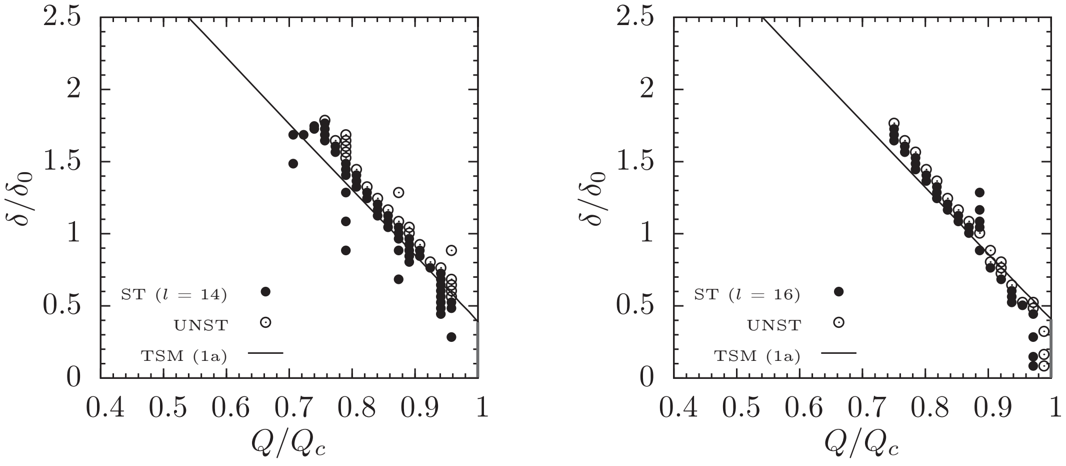

(c) No. data points: 75.

(d) No. data points: 55.

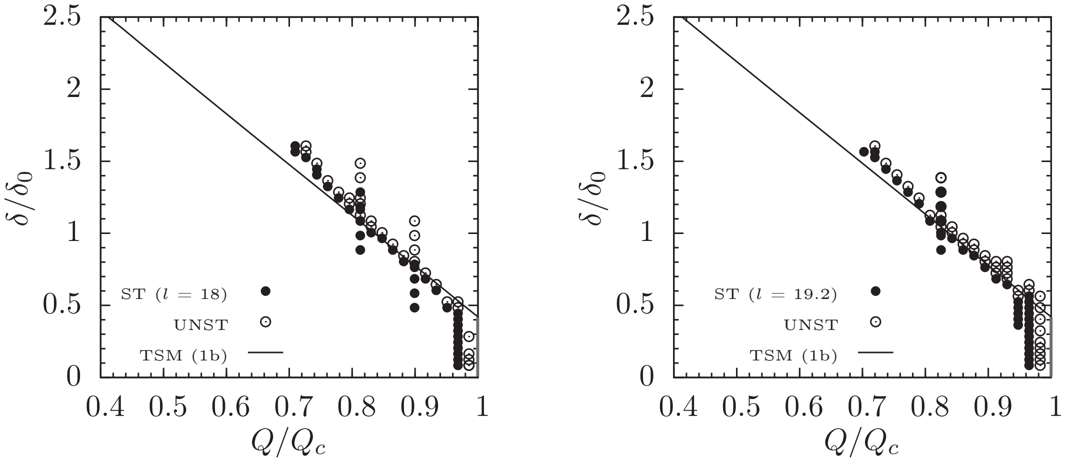

(e) No. data points: 68.

(f) No. data points: 90.

Figure 8.3: Stability diagrams for measurement sequence 1. Experimental data for stable (ST) and unstable (UNST) acceleration in comparison to the Transient Stability Model (solid lines) in Equation (3.75).

8.1.1 Scaling of the Stability Diagrams

The purpose of the scaling of the stability diagrams is to provide a universal description of the stability limits determined in the CCF experiments. A clear limit between stable and unstable accelerations can be identified in the stability diagrams presented in Figures 8.2 and 8.3. The amount of collected data points can be reduced by averaging of measured accelerations in the vicinity of the stability limit. For all data points summarized in Table 8.1, an average value between the maximum stable and minimum unstable acceleration δ for a given flow rate Q is built. Furthermore, the previously introduced scaling (Equation (3.75)) is applied. The proposed scaling presents a possibility to eliminate the flexibility (enhanced stability for long channels) and feedback (CCF setup specific) effects. As shown in Figure 8.4, all data points coincide into one single diagram. Results can be sorted either by the channel length l (Figure 8.4(a)) or by the feedback ratio r (Figure 8.4(b)).

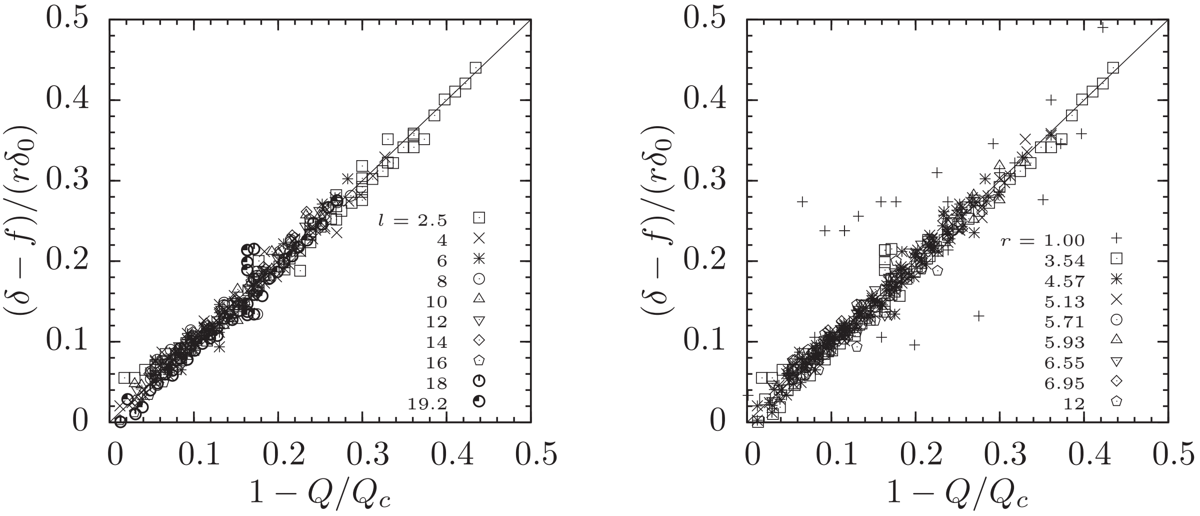

(a)

(b)

Figure 8.4: Transient stability diagrams scaled according to Equation (3.75). (a) sorted by the channel length l; (b) sorted by the feedback ratio r. Each point represents an average of two measurements for a given flow rate Q, the maximum stable and minimum unstable accelerations δ.

8.2 Parametric study

As already mentioned, some discrepancies between the experimentally and theoretically determined stability limits can be identified in the stability diagrams (Figures 8.2 and 8.3). In the following, it will be shown that the accuracy in the determination of the feedback ratio r and the critical flow rate Q_c is essential for the proper evaluation of the transient stability model (Equation (3.75)).

The feedback ratio r is estimated according to Equation (3.68). It depends on the gas volume V_g in the phase separation chamber and is determined experimentally as described in Section 4.1.1. The critical flow rate Q_c can be predicted with the numerical tolls ccFlow and OpenFOAM, or, for the channels with $7.2 \leq l \leq 19.2$, the experimentally determined values can be used. The parametric study is carried out for the groove channel with $l = 4$. The parameters r and Q_c are varied independently. It is found that the slope of the TSM lines in the stability diagrams is determined by the feedback ratio r as shown in Figure 8.5(a). The feedback ratio r is varied between the minimum value of 1 (no feedback) and maximum value of 12 (full feedback). During the experiment, the gas bubble volume in the phase separation chamber is set as a boundary condition prior to every measurement. The gas bubble senors and gauging with the gas plunger `K3` are used to control the volume of gas (discussed in Section 4.1.1). The lines for $r = 5.4$, and $r = 4.14$ in Figure 8.5(a), represent the smallest ($V_g^{\prime BS1} = 87$ ml) and medium ($V_g^{\prime BS3} = 200$ ml) gas bubble volume detectable with the temperature sensors, respectively. The line $r = 4.57$ corresponds to the CCF experiment (1a series), where the set bubble volume is $V_g^{\prime} = 125$ ml.

Furthermore, as shown in Figure 8.5(b), Q_c defines the limit at the abscissa axis. Thus, the inaccurate prediction of the Q_c might cause an offset of the TSM lines in the stability diagrams. A variation of the critical flow rate Q_c^{var} is shown in Figure 8.5(b). The line $Q_c^{var}/Q_c^{EXP} = 1$ corresponds to the experimentally obtained value of the critical flow rate. The lines $Q_c^{var}/Q_c^{EXP} = 0.90, 0.95, 1.05$, and 1.10 represent a 10% decrease, 5% decrease, 5% increase, and 10% increase of the Q_c, respectively. As shown in Figure 8.5(b) the difference of 5% in the value of Q_c significantly changes the position of the TSM. Therefore, for the channels with $l < 8$ (for which the ccFlow overestimates Q_c, Figure 6.4) the experimentally determined values of the critical flow rate (if available), or computed with OpenFOAM should be applied to solve the model Equation (3.75).

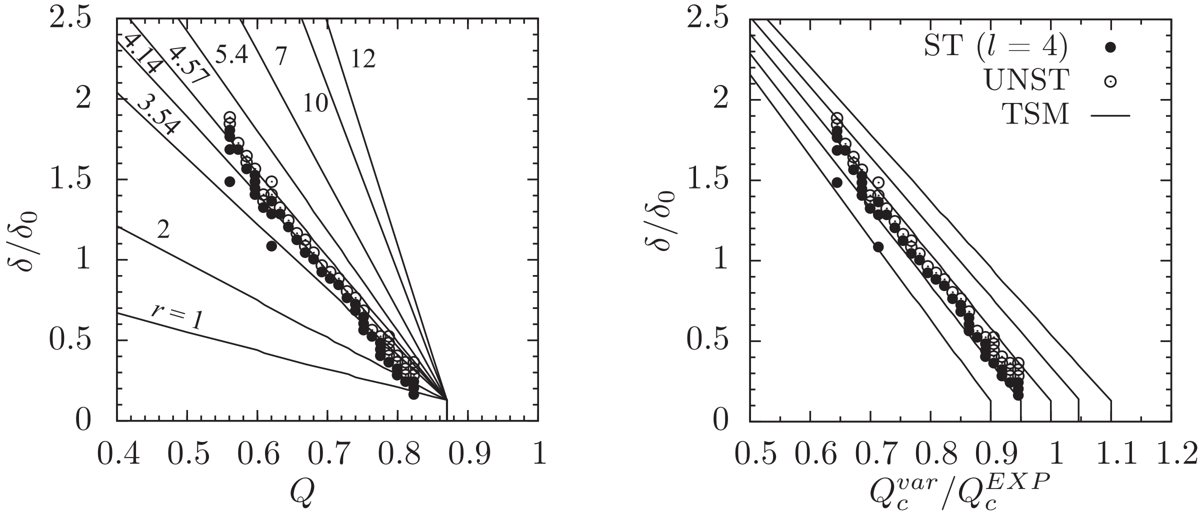

(a) r variation (b) Q_c variation

Figure 8.5: Results of the parametric study. Normalized acceleration δ/δ_0 versus the flow rate Q. Groove channel with $l = 4$ is considered. The experimental results (filled circles - stable and empty circles - unstable acceleration) in comparison with the transient stability model (Equation (3.75)). (a) feedback ratio r variation. The solid line $r = 4.57$ correspond to the CCF experiment (sequence 1a). (b) critical flow rate Q_c variation. The solid line $Q_c^{var}/Q_c^{EXP} = 1$ corresponds to the experimentally obtained value of the critical flow rate.

Chapter 9

Three-Dimensional Computations

The knowledge of flow behavior in the inlet section of the CCF experiment setup is essential for the proper application of boundary conditions required for the 1D model (as discussed in Section 3.4). Due to the complexity of the setup, there is no analytical formulation of the pressure losses in the inlet part of the channel. Furthermore, there is no experimental apparatus enabling the observation of the flow development upstream from the channel entrance and the flow conditions at the channel entrance $x = 0$. Therewith, the numerical tool OpenFOAM is employed and a series of three-dimensional simulations of the flow in a geometry resembling the CCF geometry is carried out.

Two channel configurations are investigated: (i) closed channel with single-phase (liquid), and (ii) open channel with two phases (liquid and gas). The main goal of the single-phase simulations is to study the flow behavior in the inlet section of the test channel $x \leq 0$ (Table 9.1). With the two-phase simulations, the flow behavior in the open section of the test channel ($x > 0$) (free surface stability) is investigated. The OpenFOAM code is validated with the computations of the flow in a straight tube with circular cross section. The liquid properties applied in the numerical model correspond to those of CCF test liquid in Table 4.1.

Table 9.1: Summary of the OpenFOAM solvers and objectives of the numerical simulations of the flow in the CCF setup

solver	type	slider position	objectives
simpleFOAM	steady	closed	Flow behavior upstream from the channel - pressure loss - flow development
interFOAM	transient	open	Flow behavior in the channel - free surface behavior

9.1 Flow In Straight Tube - Solver Validation

Single-phase, steady flow simulations in a straight cylindrical tube were carried out with the simpleFOAM solver. The flow is assumed to be incompressible and laminar. In the following, the results of the solver validation (comparison with the analytical solution) are presented. Besides the validation, proper boundary conditions for further flow simulations in the CCF setup and the influence of the grid topology on the numerical results are studied.

9.1.1 Computational Domain

A circular tube with the cross-sectional area $A'_t = 1.25$ cm^2 (same as the cross-section area of the CCF channel) is considered. The length of the tube is determined as $l'_t = 1.5 L'_{e,t}$ which is assumed to be sufficient for flow to fully develop. The hydraulic length $L'_{e,t}$ is defined as [22]

$$L'_{e,t} = 0.06 \; \mathrm{Re_t} \; D'_t \quad , \tag{9.1}$$

where $\mathrm{Re_t}$ is the Reynolds number and $D'_t = 1.26$ cm the diameter of the tube. The Reynolds number is defined as $\mathrm{Re_t} = (\bar{v}'_x D^t_h)/\nu$, where $\bar{v}'_x$ is the area average velocity in flow direction. D^t_h is the hydraulic diameter (for the circular tube $D^t_h = D'_t$) and ν is the kinematic viscosity (Table 4.1). The flow rate Q' is varied between 1 ml/s and 10 ml/s, which corresponds to the flow rates range in the CCF experiment. The simulation parameters are summarized in Table 9.2. The maximum Reynolds number is $\mathrm{Re_t} < 1500$, therefore laminar flow is assumed.

Table 9.2: Simulation parameters for the flow in the circular cylindrical tube. l'_t is the length of the tube (computational domain).

Q'	ml/s	1	2	3	4	5	6	7	8	9	10
$\bar{v}'_x$	cm/s	0.8	1.6	2.4	3.2	4.0	4.8	5.6	6.4	7.2	8.0
$\mathrm{Re_t}$	-	141	282	423	564	705	846	987	1128	1269	1410
l'_t	cm	16	32	48	64	80	96	112	128	144	160

Two mesh types, structured and unstructured, are considered in this study (Figure 9.1). Ten different grids (different domain lengths) were generated for each mesh type according to the length details given in Table 9.2. Structured grids were generated with blockMesh, which is a standard OpenFOAM utility [59]. The inlet of the tube (Figure 9.1(a)) is divided into 5 sections for which the number of hexahedral elements is specified. The inlet patch with the defined mesh resolution is extruded along the flow axis for the desired tube length l'_t. Unstructured grids were created with the software Gmsh [26]. The number of grid elements depends on the length of the computational domain.

The physical boundary conditions are inlet, outlet, and wall. Two different variants of boundary conditions are considered: (i) the velocity condition is applied at the channel inlet

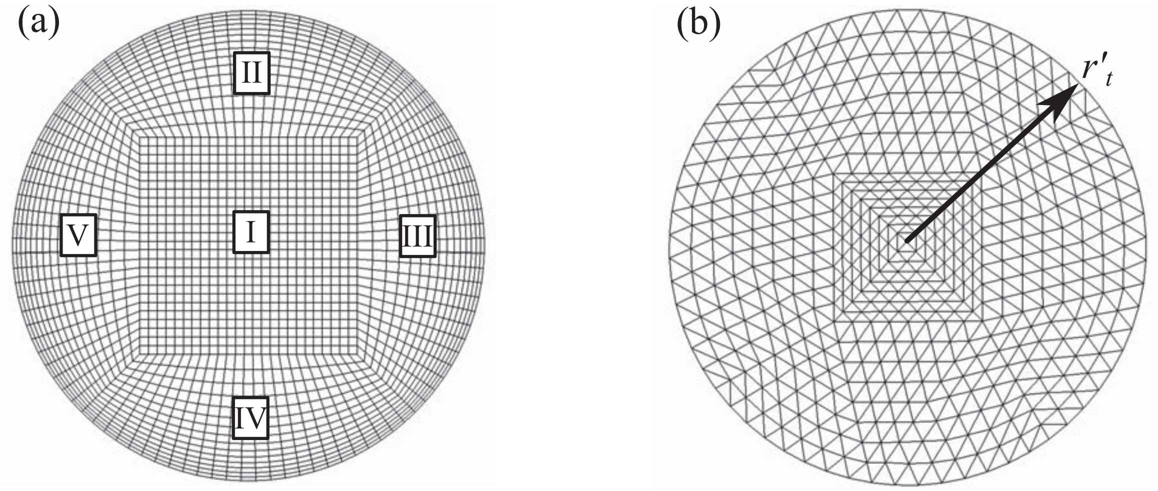

Figure 9.1: Tube inlet area for both numerical grids used for simulations with the simpleFOAM solver. (a) structured mesh generated with blockMesh. (b) coarse variant of the unstructured mesh generated with Gmsh. The mesh sensitivity study for unstructured grids shows a minor influence of grid resolution on the numerical results.

(IN), and (ii) the velocity condition is applied at the outlet (OUT). These are summarized in Table 9.3. The pressure boundary condition zeroGradient (Neumann boundary condition [92]) is applied at the channel outlet if the velocity is applied at the inlet. Analogously, if the velocity is set at the outlet then zeroGradient for pressure is set at the inlet. Undeveloped (uniform) velocity profile at the channel inlet is assumed. To assure the no-slip condition, the velocity is set to zero at the wall.

Table 9.3: Summary of the boundary conditions applied. IN: velocity is applied at the channel inlet; OUT: velocity is set at the channel outlet. Fixed value is a Dirichlet boundary condition type. A fixed value for v' was set according to Table 9.2. The pressure $p' = 0$ was kept constant.

	inlet	outlet	wall
IN	v' = fixed value p' = zeroGradient	v' = zeroGradient p' = fixed value	no-slip
OUT	v' = zeroGradient p' = fixed value	v' = fixed value p' = zeroGradient	no-slip

Ten flow velocities for both variants of boundary conditions and two mesh types are considered, which results in a total number of 40 simulations.

9.1.2 Results

The simulation results are nondimensionalized in the following way:

$$p = \frac{p'}{0.5\rho\bar{v}_x'^2} \quad , \quad x = \frac{x'}{D_h^t \mathrm{Re}_\mathrm{t}} \quad , \quad v_x = \frac{v_x'}{\bar{v}_x'} \;, \quad r_t = \frac{r_t'}{D_h^t}. \tag{9.2}$$

In general, the pressure loss of developed flow in a circular tube can be estimated with the Hagen-Poiseuille law [99]

$$\triangle\, p = f_D \frac{l_t}{D_t} \frac{\rho\bar{v}_x^2}{2}, \tag{9.3}$$

where $\rho\bar{v}_x^2/2$ is the dynamic pressure. f_D is the friction factor (e.g. Darcy friction factor), which for fully developed flow writes

$$f_D = \frac{64}{\mathrm{Re}_\mathrm{t}}. \tag{9.4}$$

The friction factor is a function of the flow Reynolds number only and, for laminar flow, is independent of the roughness of the tube surface.

Figure 9.2 shows the pressure evolution along the flow axis x for both considered mesh types. Good agreement between the simulation results and the analytical solution is obtained for structured grids (Figure 9.2(a)). The pressure decrease is hyperbolic in the entrance region ($x < 0.06$), which is typical for developing flows. A linear decrease is achieved from $x \approx 0.06$ on,

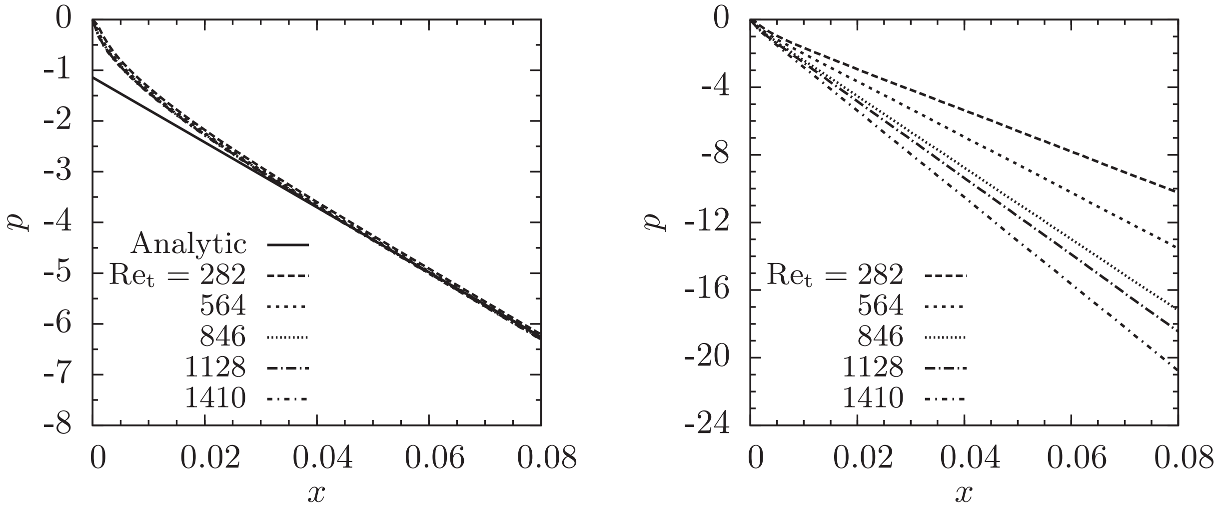

(a) (b)

Figure 9.2: Pressure evolution along the flow axis in the circular tube (IN boundary condition variant) as a function of the Reynolds number. The pressure p at $x = 0$ is set to zero for the sake of comparison. The entrance length is $L_{e,t} = 0.06$. (a) structured mesh, where the solid line represents the Hagen-Poiseuille (Equation (9.3)) solution, (b) unstructured mesh.

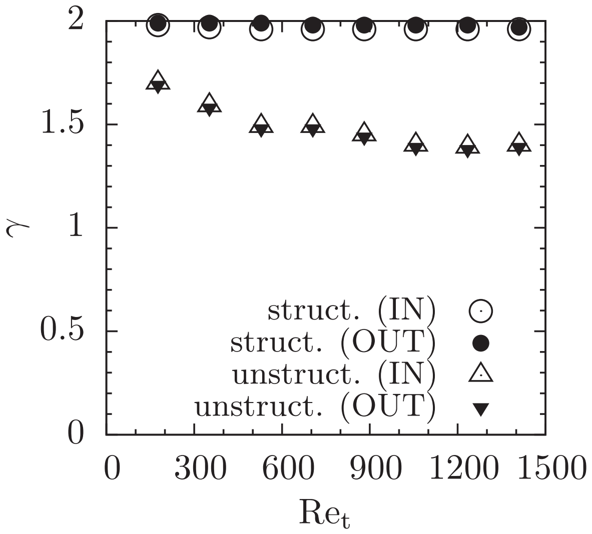

Figure 9.3: Flow development parameter γ at the hydraulic length ($x = 0.06$) of the circular cylindrical channel as a function of the REYNOLDS number. Circles and triangles represent the structured and unstructured grids, respectively. The theoretical value of γ is 2 for the developed laminar flow in the circular tubes. Both boundary conditions variants are chosen for comparison.

which corresponds well to the hydraulic entrance length $L_{e,t} = 0.06$. In the case of unstructured grids, the pressure curves do not collapse into one curve (Figure 9.2(b)). This behavior does not obey the scaling assumptions and is assumed to be incorrect.

Furthermore, the flow development along the tube is examined with the flow development parameter γ defined according to Equation (3.40). This parameter measures the degree of development of the velocity profile and is defined as a ratio of the local maximum velocity over the average velocity. For the developed laminar flow in the circular cylindrical tube, γ reaches the value of 2. Figure 9.3 shows the flow development parameter γ evaluated at $x = 0.06$. This position corresponds to the end of the development region. It can be clearly seen that for the structured grids, the flow is fully developed ($\gamma \sim 2$) for all considered flow Reynolds numbers (deviation from theory less than 3 %). It is worth noting that the same results are obtained for both boundary condition variants (IN and OUT). In case of unstructured grids, the flow is not fully developed at the end of the entrance length, γ decrease with increasing REYNOLDS number. For the laminar flow in the cylindrical tube, the velocity profile of fully developed flow can be described as

$$v(r) = 2\bar{v}_x \left(1 - \frac{r^2}{r_t^2}\right), \tag{9.5}$$

where r_t is tube radius and r is the radial coordinate. Figure 9.4 shows the evaluated velocity profiles at the position $x = 0.06$. For the structured grids a fully developed flow is achieved in

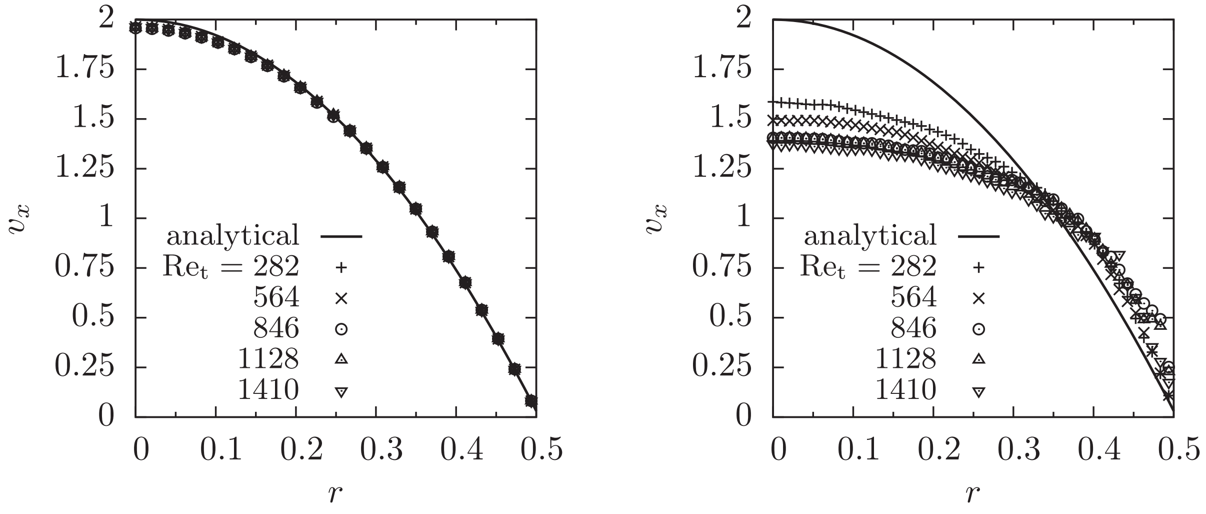

(a)

(b)

Figure 9.4: Velocity profiles (velocity as a function of the radial coordinate) at the end of the length ($x = 0.06$) of the cylindrical tube for different Reynolds numbers. IN boundary condition variant is shown. The solid line represents the solution of Equation 9.5. (a) structured mesh; (b) unstructured mesh.

the whole range of flow velocities. Obtained parabolic profiles agree well with the theory. In case of the unstructured grids, the flow is not fully developed, and the depicted profiles do not coincide with the analytical solution.

9.1.3 Conclusions

As shown above the OpenFOAM code (solver simpleFOAM) is a suitable tool for simulating the flow in closed ducts. In the above presented case, the unstructured grids fail in every respect. The numerical results of pressure loss and flow development do not coincide with the analytical solutions. In contrast to unstructured grids, the simulation with structured meshes deliver results which agree well with the theory. Two main aspects, pressure loss and flow development, are predicted accurately. Both boundary condition variants (IN and OUT) deliver satisfactory results.

It must be noted that the above presented results and statements are valid for this specific flow problem and the solver simpleFOAM (OpenFOAM ver. 2.0.x) only, with its settings listed in Appendix D.1.

9.2 Flow in the CCF Setup

9.2.1 Computational Domain

The CCF inlet section consists of the flow preparation chamber, the entrance nozzle, and the entrance duct (Figures 3.5(a) and 9.5). Plug flow (constant velocity profile) is assumed at the inlet into the considered domain through the perforated sheet on the upstream side of the FPC. Along the flow path, the flow cross-sectional area changes from circular in the FPC to rectangular in the entrance duct (area decreases by a factor of 32). A partially developed flow leaves the nozzle at $x_{n,e}$ and develops further in the entrance duct upstream from the channel entrance. The flow condition at the channel inlet ($x = 0$) depends on the flow velocity and flow development in the said section. In the CCF setup, the FPC is connected to the compensation tube via a circular tube (Figure 4.2). This intersection is not included in the numerical domain. It will be shown that such a simplification does not influence the results of the quasi-steady simulations. Instead of modeling the CT with its meniscus, the pressure boundary condition can be applied at the inlet to the FPC (perforated sheet). Another simplification is the shape

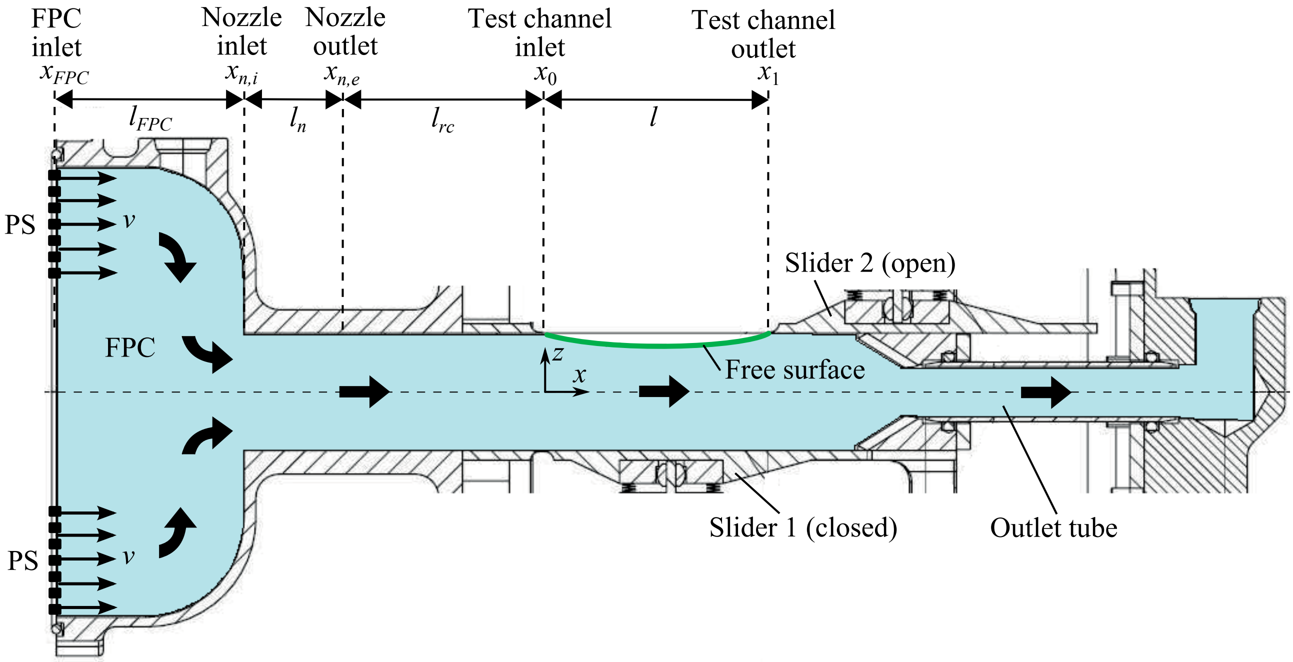

Figure 9.5: Inlet section, test channel, and outlet section of the CCF experimental setup (meridional section at $y = 0$). Cyan color depicts the liquid flowing from left to right, as indicated by the arrows. The liquid enters the flow preparation chamber (FPC) through the perforated sheet (PS). Lengths l_{FPC}, l_n, l_{rc} and l are the lengths of the FPC, entrance nozzle, entrance duct (rectangular channel), and test channel, respectively. The x coordinates of the characteristic points are: x'_{FPC} = -8.45 cm ; $x'_{n,i}$ = -6.35 cm ; $x'_{n,e}$ = -3.35 cm ; $x_0 = 0$; $x_1 = l$, where l is determined with the slider.

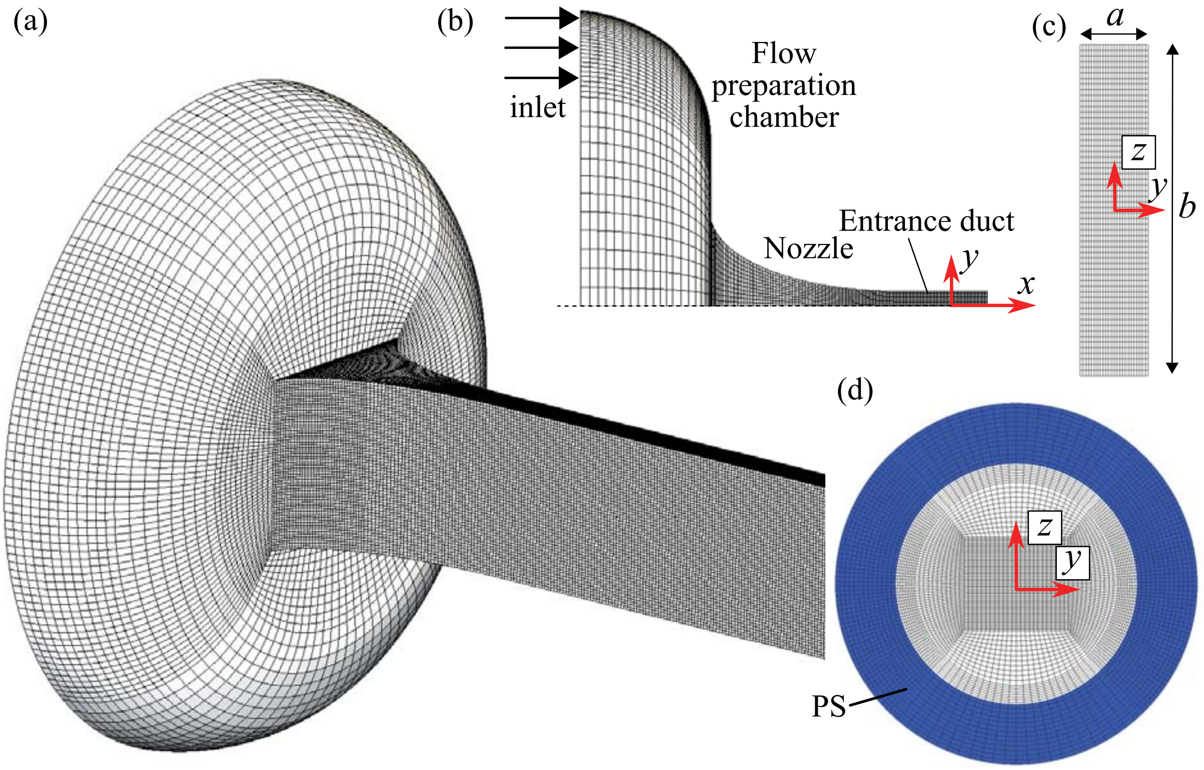

Figure 9.6: Fine variant of the numerical grid used for the single-phase flow simulations with simpleFOAM. (a) isometric view, (b) close-up view in the vicinity of the entrance nozzle. Due to symmetry in the xz-plane, only the half of the domain with positive y is depicted. (c) grid elements on the outlet patch (a and b correspond to the CCF experiment). (d) inlet patch (colored with blue) with the inflow area corresponding to the area of the Perforated Sheet (PS) at the inlet of the FPC in the CCF setup.

of the outlet section of the channel. In the CCF setup, the rectangular channel converts into a circular tube (Figure 9.5). In this study, the outlet part is of rectangular cross-section (the channel is extended by the length of the outlet tube).

The numerical grids were generated with Gmsh. Two variants of grids are considered: (i) fine mesh for single-phase simulations (Figure 9.6), and coarse mesh for two-phase simulations (Figure 9.7). The main difference between these two configurations is the surrounding gas volume, which is dropped for single-phase modeling (closed channel, no liquid-gas interface). The mesh quality is controlled with the checkMesh tool [60]. The fine mesh contains 804×10^3 grid elements. For the coarse variant, the mesh size depends on the channel geometry (PP or GR) and the length of the open section. The largest grids for channels with $l' = 48$ mm contain 242×10^3 and 386×10^3 grid elements for the GR and the PP channel, respectively.

As shown in Figure 9.6, the liquid flows from the FPC via a nozzle into the rectangular channel. For the single-phase simulations, the length of the channel is determined as $l_{rc} =$

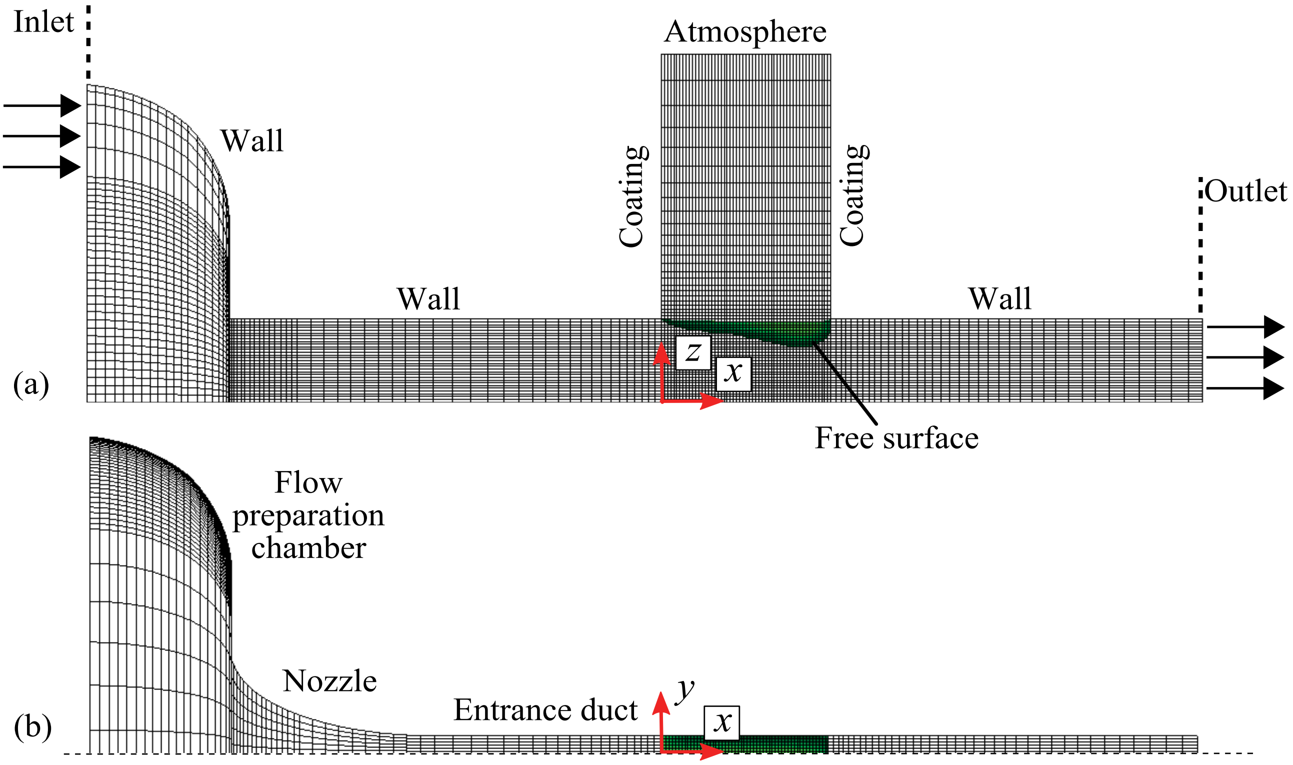

Figure 9.7: Coarse numerical grid used for the two-phase flow simulations with interFOAM. Flow direction is from left to right. The free surface is depicted for the sake of clarity (green). (a) side view (due to symmetry in the xy-plane for parallel plates, only the z-positive half of the domain is depicted). (b) top view (due to symmetry in the xz-plane, only the y-positive half of the domain is depicted).

$1.5L_{e,rc}$, which is assumed to be sufficient to achieve developed flow conditions. The hydraulic entrance length for rectangular channels with an aspect ratio of 5:1 is [80]

$$L_{e,rc} = 0.0138\ D_h^{rc}\ \mathrm{Re}_{\mathrm{rc}}. \tag{9.6}$$

The hydraulic diameter is defined as

$$D_h^{rc} = \frac{2ab}{a+b}, \tag{9.7}$$

where a and b are the channel width and height, respectively. The Reynolds number is defined as $\mathrm{Re}_{\mathrm{rc}} = \bar{v}'_x D_h^{rc}/\nu$. For the highest considered flow rate ($Q' = 15$ ml/s), the entrance length required for the flow to fully develop is $L'_{e,rc} = 16.8$ cm, so the corresponding numerical domain length is $l'_{rc} = 25.2$ cm.

Boundary Conditions

For the single-phase simulations (simpleFOAM) the flow rate (varied between 1 and 15 ml/s) is imposed at the channel inlet, and a constant pressure ($p' = 0$) at the outlet. The characteristic parameters are summarized in Table 9.4.

Table 9.4: Parameters for the single-flow simulations in the CCF setup. The average velocity refers to the point $x = 0$ and is calculated as $\bar{v}'_x = Q'/A'$.

Q'	ml/s	1	1.5	2	3	4	5	6	7	8	9	10	11	12	13	14	15
$\bar{v}'_x$	cm/s	0.8	1.2	1.6	2.4	3.2	4.0	4.8	5.6	6.4	7.2	8.0	8.8	9.6	10.4	11.2	12.0
$\mathrm{Re}_{\mathrm{rc}}$	-	93	140	186	280	373	466	559	653	746	839	932	1026	1119	1212	1305	1399

For the two-phase simulations (interFOAM), the velocity boundary condition is applied at the domain's outlet and the constant pressure condition at the inlet. Such a setting resembles the real CCF setup, where the flow is driven by the pump located downstream from the channel outlet and the system pressure is determined by the meniscus in the CT at the point where it connects to FPC (upstream from the channel inlet). The velocity is quasi-steadily increased over a time period of 100 s from 0 to 0.08 m/s (corresponds to flow rate range $0 \dots 10$ ml/s). The pressure at the inlet is set to $p_{FPC} = -1.07$ Pa, which corresponds to the differential pressure $p' = 2\sigma/R'_{CT}$ induced by the meniscus in the compensation tube.

A no-slip boundary condition and a contact angle of zero are set at the walls of the domain. In the experiment, the free surface(s) in the open channel is (are) pinned along the channel's edge at the inlet and at the slider's edge at the outlet (points x_0 and x_1 in Figure 9.5). The free surface is exposed to the ambient gas. For the two-phase flow simulations, a simplification is made and the pinning edges are modeled as 90° edges (corners) (Figure 9.7). In order to avoid capillary rise up the vertical walls (denoted with coating in Figure 9.7), a contact angle of 180° is imposed there.

The liquid properties correspond to the CCF test liquid HFE-7500 (its properties are listed in Table 4.1). The properties for the gaseous phase are as for nitrogen: $\rho = 1.165$ kg/m^3, $\nu = 1.56 \times 10^{-5}$ m^2/s. Two-phase flow simulations are initialized with the liquid occupying the flow preparation chamber, the nozzle and the entire channel. 16 single-phase simulations with simpleFOAM and 133 two-phase simulations with interFOAM were conducted.

Parallel performance

A series of two-phase flow test simulations were performed in order to explore the parallel performance of the interFOAM solver for the considered computational domain. The test grid contains 410×10^3 hexahedral elements (mesh type as shown in Figure 9.7, but with finer resolution). The groove channel with $l' = 25$ mm is considered. The simulation is run for 5 s (real time) with a constant time step. The computational domain is decomposed into subdomains in a range $i = 4 \leq i + n, i + 2n, \dots, \leq 36$, where $n = 4$, with a METIS/SCOTCH [60] decomposition method. Simulations are carried on the linux infiniband cluster with 8 nodes and 16 cores per node (technical specification given in Appendix D.2). As expected, with increasing number of CPUs, the execution time for a single run decreases. The speed up is

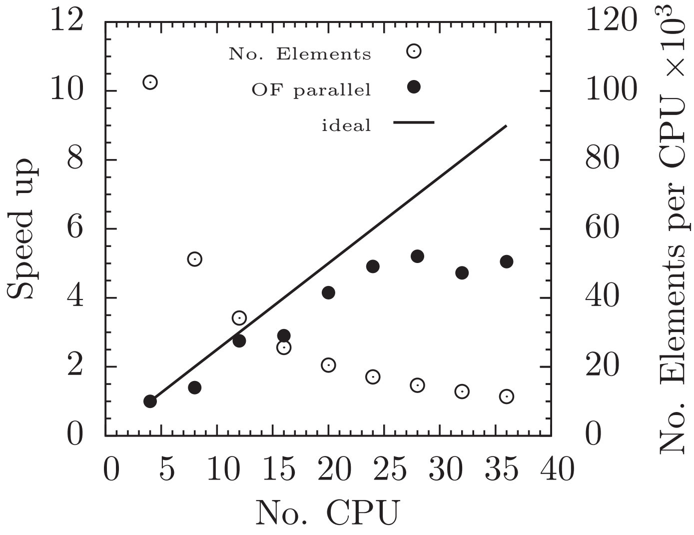

Figure 9.8: Parallel performance of the interFOAM solver on the infiniband cluster. Solid line represents the ideal speed up.

approximately linear up to 28 CPUs (Figure 9.8), which corresponds to a number of 14600 grid elements per CPU. Further increase of the number of CPUs (above 28) does not improve the speed up ratio. The speed up ratio is defined as the execution time of the simulation divided by the execution time for the simulation with 4 CPUs).

9.2.2 Results

Pressure Loss in the Inlet Section

The results of the three-dimensional flow simulations are evaluated to determine the pressure loss in the inlet section of the CCF experiment (Figure 9.5). This is essential for the proper application of the boundary conditions required for the numerical solution of the mathematical model (as discussed in Section 3.4). The pressure loss p'_n is defined as the pressure difference in the liquid volume between the inlet of the Flow Preparation Chamber (p'_{FPC}) and the test channel inlet (p'_0)

$$p'_n = p'_{FPC} - p'_0 = K_\tau \mu \frac{v'_0}{D_h^{rc}} + K_c \rho v_0'^2 \quad , \tag{9.8}$$

where terms on the right side represent the viscous (shear in the boundary layer) and convective effects (acceleration of the core flow). The hydraulic diameter for the closed duct is defined according to Equation (9.7). In the experimental setup, the pressure at the inlet of the FPC can be estimated as

$$p'_{FPC} = p'_a - \frac{2\sigma}{R'_{\mathrm{CT}}} \quad , \tag{9.9}$$

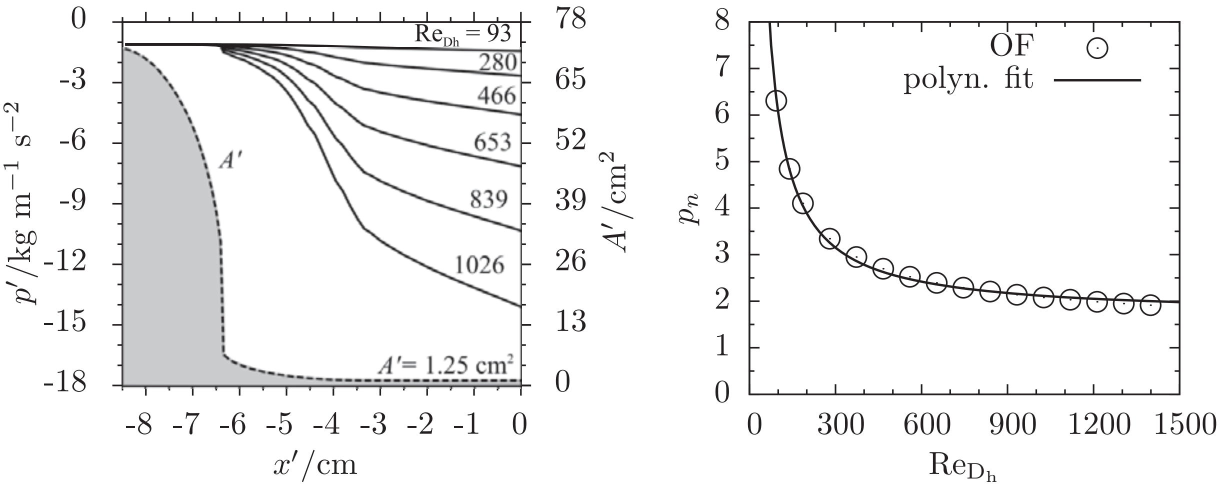

(a) (b)

Figure 9.9: (a) pressure evolutions along the x' axis for different Reynolds numbers. The pressure at the left boundary is constant. It corresponds to the pressure induced by the meniscus in the compensation tube $p' = -1.07$ Pa. A' is the flow cross-sectional area. Point $x' = 0$ corresponds to the CCF channel entrance. (b) non-dimensional pressure loss $p_n = p'_n/(0.5\rho v_0'^2)$ fitted to a polynomial function of the first order. The polynomial coefficients are $C_1 = 439.5$ and $C_2 = 1.68$.

where p'_a is the ambient pressure and $2\sigma/R'_{\mathrm{CT}}$ is the pressure induced by the meniscus in the compensation tube. Rearranging Equation (9.8) and scaling with $\rho v_0'^2/2$ yields

$$\frac{p'_{FPC} - p'_0}{0.5\rho v_0'^2} = \frac{2K_\tau}{\mathrm{Re_{D_h}}} + 2K_c\ . \tag{9.10}$$

The numerically determined pressure evolutions along the channel for different Reynolds numbers are shown in Figure 9.9(a). Area averaged values of pressure are considered. As expected, with increasing the flow velocity, the pressure drop increases. Evaluating the pressure at the point $x = 0$ (channel inlet) yields the pressure loss shown in Figure 9.9(b), where the dimensionless values of p_n are plotted versus the Reynolds number. The numerical data are fitted with the polynomial function of first order

$$\frac{p'_{FPC} - p'_0}{0.5\rho v_0'^2} = \frac{C_1}{\mathrm{Re_{D_h}}} + C_2 \quad , \tag{9.11}$$

where C_1 and C_2 are fit coefficients and $\mathrm{Re_{D_h}}$ is the Reynolds number based on the hydraulic diameter of the closed duct. Comparing the theoretical pressure loss $(p'_{FPC} - p'_0)/0.5\rho v_0'^2$ from Equation (9.10) with the numerical fit (9.11) yields

$$\frac{2K_\tau}{\mathrm{Re_{D_h}}} + 2K_c = \frac{C_1}{\mathrm{Re_{D_h}}} + C_2 \tag{9.12}$$

and ,consequently,

$$C_1 = 2K_\tau \ , \tag{9.13}$$

$$C_2 = 2K_c \ . \tag{9.14}$$

Combining the Equations (9.8) and (9.9) yields the pressure difference with respect to the channel inlet ($x = 0$)

$$p'_a - p'_0 = \frac{2\sigma}{R'_{\mathrm{CT}}} + K_\tau \mu \frac{v'_0}{D_h^{rc}} + K_c \rho v_0'^2 \ , \tag{9.15}$$

in which the viscous and convective effects upstream from the channel inlet ($x = 0$) are accounted for. Adapting Equation (9.15) to the ccFlow scaling (Section 3.4) yields

$$\begin{aligned} \frac{p'_a - p'_0}{2\sigma/a} &= \frac{a}{R'_{CT}} + K_\tau \frac{2a}{D_h^{rc}} \frac{\rho\nu}{\sigma} \frac{v'_0}{4} + K_c 2a \frac{\rho}{2\sigma} \frac{{v'_0}^2}{2} && (9.16) \\ &= \frac{a}{R'_{CT}} + 2K_\tau \frac{2a}{D_h^{rc}} \mathrm{Oh} \frac{v_0}{4} + 2K_c \frac{{v_0}^2}{2} && (9.17) \\ &= K_0 + K_1 \mathrm{Oh} \frac{v_0}{4} + K_2 \frac{{v_0}^2}{2} \ , && (9.18) \end{aligned}$$

where

$$\begin{aligned} K_0 &= \frac{a}{R'_{CT}} \ , && (9.19) \\ K_1 &= 2K_\tau \frac{2a}{D_h^{rc}} \ , && (9.20) \\ K_2 &= 2K_c \ . && (9.21) \end{aligned}$$

Combining Equations (9.12), (9.20), and (9.21) yields

$$\frac{K_1 \dfrac{b}{a+b}}{\mathrm{Re}_{\mathrm{D_h}}} + K_2 = \frac{C_1}{\mathrm{Re}_{\mathrm{D_h}}} + C_2 \ , \tag{9.22}$$

and consequently

$$\begin{aligned} K_1 &= C_1 \frac{a+b}{b} = \frac{6}{5} C_1 = 527.4 \ , && (9.23) \\ K_2 &= C_2 = 1.68 \ , && (9.24) \end{aligned}$$

where K_1 and K_2 are the pressure coefficients describing the pressure loss in the inlet section of the CCF setup. They are required for the definition of the pressure boundary condition (Equation (3.60) in the one-dimensional flow model).

The coefficients K_1 and K_2 are valid for both the parallel plates and the groove channel (contrarily to previous publications). This is due to the scaling and the definitions of the characteristic numbers considered in this work: (i) the same definition of the Ohnesorge number Oh in Equation (9.18) for both geometries; (ii) same pressure scale $2\sigma/a$ in Equation (9.16); (iii) the hydraulic diameter D_h in Equations (9.8), (9.15), and (9.20) is defined for the duct, because the pressure loss downstream from the plane $x = 0$ is of interest here; (iv) the same definition of the velocity scale in Equation (9.16) for both geometries.

Development of the Velocity Field

In the CCF experiment, liquid with a constant velocity profile enters the flow preparation chamber, as shown in Figure 9.5. A boundary layer develops along the walls of the FPC, in the nozzle, and in the entrance duct such that the flow at the test channel inlet ($x = 0$) does not possess an uniform velocity profile. The flow condition at $x = 0$ depends strongly on the flow velocity. The flow development in the CCF inlet section is examined with the parameter $\gamma = v_x/\bar{v}_x$. For the developed laminar flow in the duct of aspect ratio 5:1 (as in CCF), the parameter γ reaches a value of 1.7 [79]. Figure 9.10 shows the flow development parameter γ evaluated at the nozzle exit ($x_{n,e}$) and at the channel inlet ($x = 0$). It can be clearly seen that at the nozzle exit the flow is not fully developed. At the test channel inlet, γ reaches the value of 1.7 for the lowest flow rate ($Q' = 1$ ml/s, $\mathrm{Re_{Dh}} = 93$). With increasing REYNOLDS number, γ decreases. The corresponding velocity profiles at the two characteristic locations (nozzle exit and test channel inlet) are shown in Figure 9.11. It is clear that the length of the entrance duct located between the nozzle exit and the channel inlet is not sufficient to assure fully developed flow. This has to be taken into account in the one-dimensional modeling. Plots of the velocity distribution in the CCF inlet section are shown in Figure D.1 (Appendix D.3).

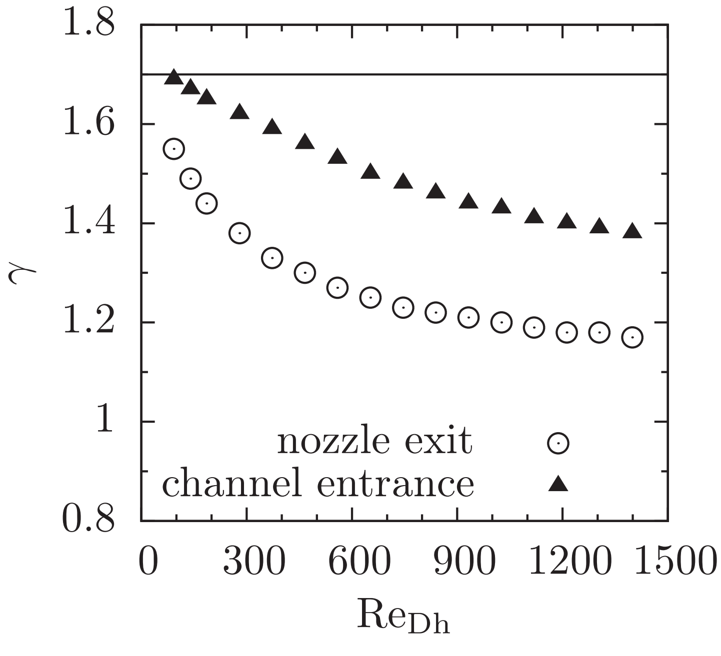

Figure 9.10: Flow development parameter γ as a function of the REYNOLDS number evaluated at the nozzle exit and at the test channel inlet. The solid lines represents the theoretical value of $\gamma = 1.7$ for fully developed flow. $\mathrm{Re_{Dh}}$ is based on the hydraulic diameter of the closed duct with an aspect ratio of 5:1.

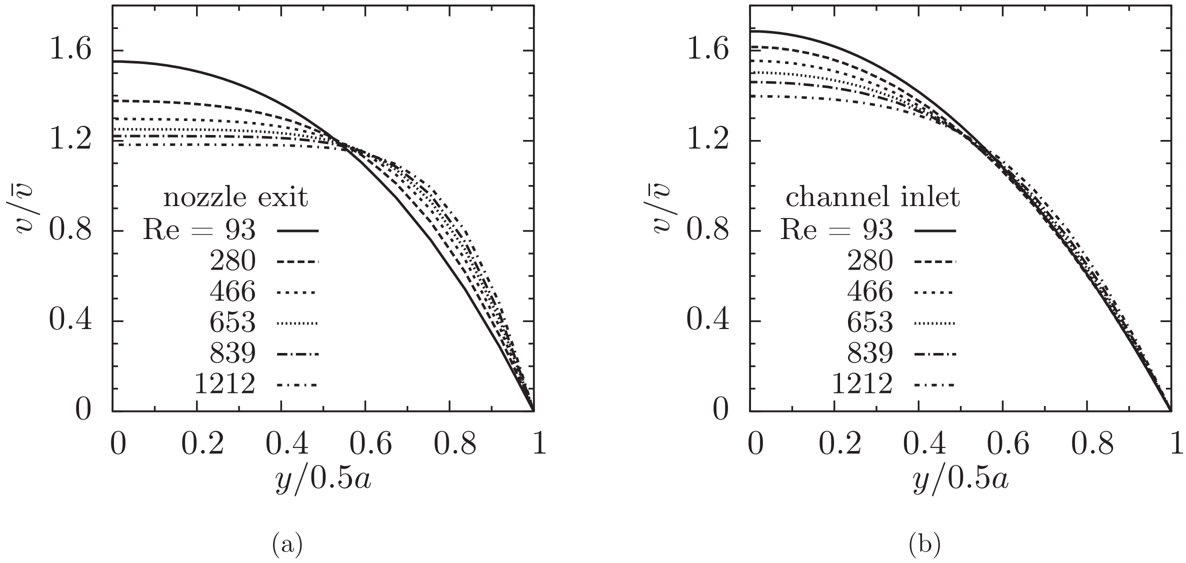

Figure 9.11: Velocity profiles across the duct dimension a (Figure 9.6(c)) with the REYNOLDS number as a parameter.

Determination of the Critical Flow Rate

An essential goal of the two-phase flow simulations with interFOAM is to determine the critical flow rates for the flow between the parallel plates and in the groove channel. Two approaches to the critical flow rate are defined as: (i) coarse approach, in which the flow rate is increased with a ramp function (quasi-steady flow), and (ii) fine approach, in which a constant flow rate is applied (steady flow). These approaches correspond to the experimental procedures for the critical flow rate determination.

The liquid enters the domain through the flow preparation chamber (Figure 9.7). The flow is initialized such as liquid occupies the FPC, nozzle, and the test channel. The capillary pressure across the gas-liquid interface is assumed to be zero, so the free surface possesses a "flat" profile (line denoted with Q_0 in Figure 9.12(a)). The flow rate at the outlet is quasi-steadily increased over a time period of 100 s from $Q'_0 = 0$ to $Q'_{end} = 10$ ml s^{-1} (simulating a pump). This corresponds to the flow rate ranges investigated in the CCF experiment. With increasing flow rate, the indentation and deformation of the free surface increase. The obtained results are visually inspected with the post-processing software paraView [46] and the time instant when the free surface loses its stability is estimated. Furthermore, the pressure p'_0 at the test channel inlet ($x = 0$) is monitored through the entire simulation. The definition of the critical flow rate (coarse estimation) is shown in Figure 9.12(b), where the pressure p'_0 versus the flow rate Q' for different channel lengths is depicted. The pressure for $Q' = 0$ corresponds to the boundary condition at the domain inlet. With increasing flow rate at the channel outlet,

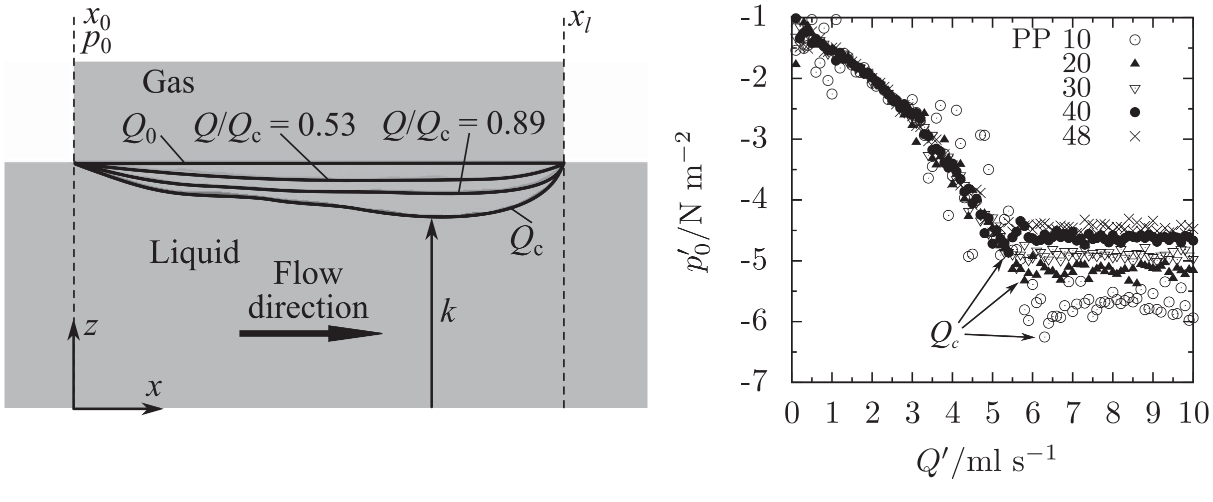

(a) (b)

Figure 9.12: (a) Free surface contours in the symmetry x, z-plane (at $y = 0$) determined with interFOAM for different flow rates. The last stable interface is noted with Q_c. (b) Pressure at the channel inlet p'_0 versus the flow rate. The values given in the legend represent the dimensional channel length l' in mm. The pressure for $Q' = 0$ corresponds to the pressure boundary condition at the channel inlet ($p'_0 = -1.07$ Pa, as in the compensation tube in the CCF experiment). The critical flow rate Q'_c corresponds to the highest computed value before the pressure "jump" occurs.

the pressure at the inlet ($x = 0$) decreases (same trend for all channel lengths). The critical flow rate is defined where the pressure "jump" occurs, which can be easily determined in Figure 9.12(b). During unstable flow (gas ingestion), an increase of the flow rate at the outlet does not influence the flow condition (pressure) at the channel inlet.

Furthermore, a series of simulations with a constant flow rate is performed in order to accurately determine the critical flow rates. First, the flow rate determined with the "coarse" approach is set as a fixed value at the domain outlet. Second, the flow rate is varied with $\Delta Q'_c = 0.1$ ml s^{-1} (in the vicinity of the flow rate classified as critical with the "coarse" approach) until the last stable interface, for which the critical flow rate is defined, is determined. Figure 9.13 shows an overview of the steady flow simulations with the fixed flow rate performed for parallel plates. The filled circles represent the values of the critical flow rate. An average of 3-4 runs per length are carried out. The simulations are run for 10 s (real time), which is assumed to be enough to determine if the free surface remains stable. A comparison with the experimental results is shown in Section 6.2.

As already mentioned, OpenFOAM can be used to study the behavior of stable and unstable flow. An example for the unstable flow in the groove with $l' = 25$ mm is shown in Figure 9.14.

The flow rate is increased dynamically with the acceleration $\Delta Q'/\Delta t' = 0.1$ ml/s^2. The free surface is stable in the subcritical regime (a-b). The last stable interface is depicted in Figure 9.14(c). Further increase of the flow rate leads to the collapse of the free surfaces and to gas ingestion.

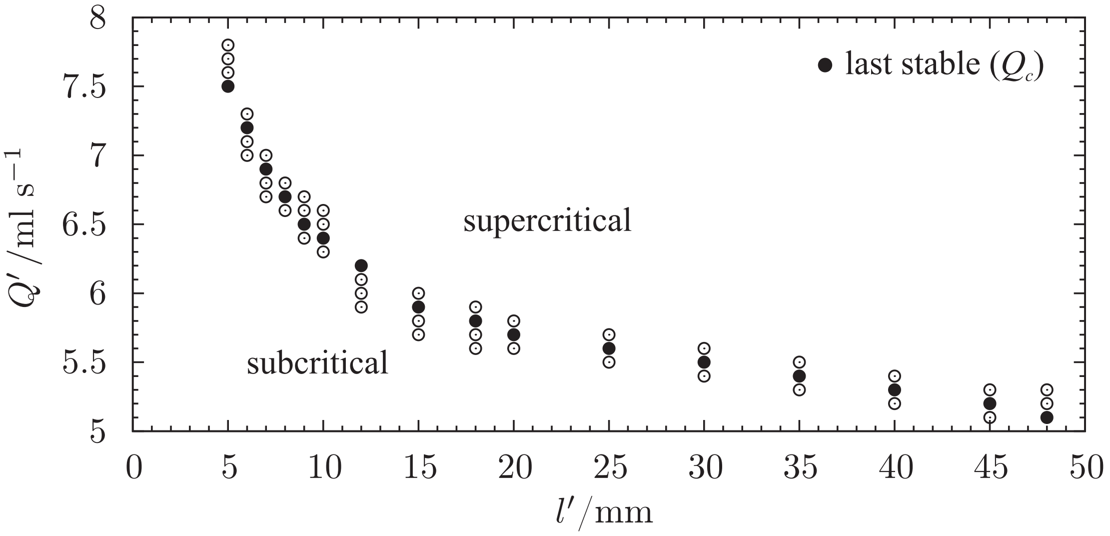

Figure 9.13: Summary of steady flow simulations with the fixed flow rate Q' for parallel plates. Each circle represents a single simulation. Filled circles represent simulations for which last stable free surfaces are observed (critical flow rate).

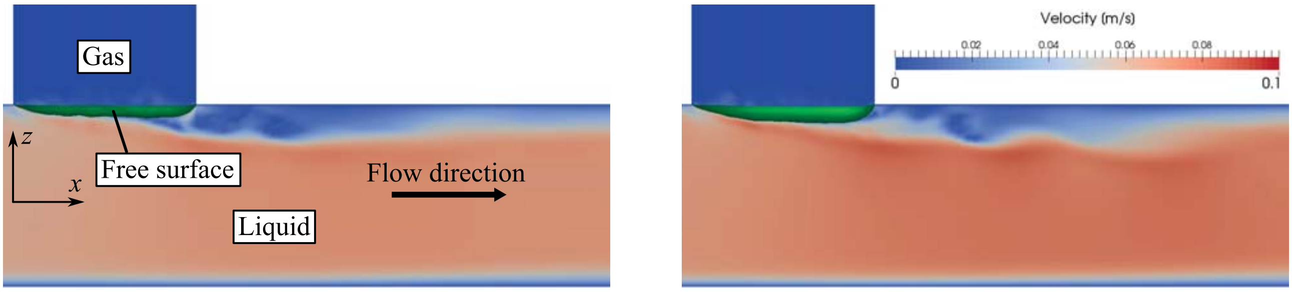

(a) $t' = 0$, $Q' = 5.2$ ml/s

(b) $t' = 6$ s, $Q' = 5.8$ ml/s

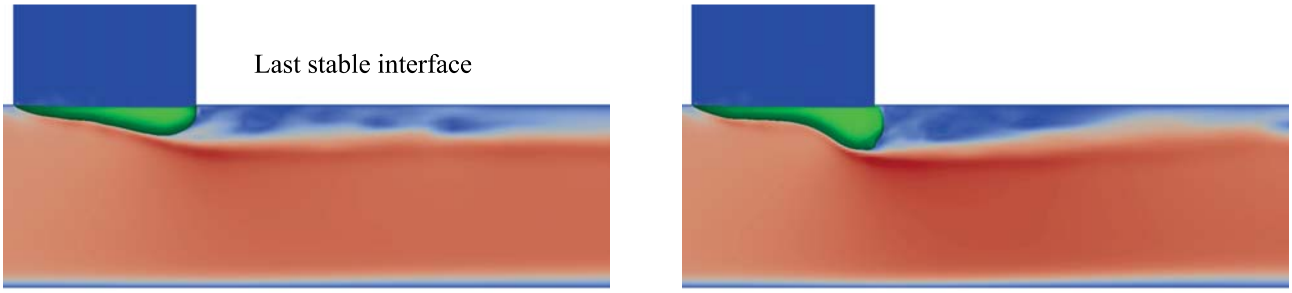

(c) $t' = 8$ s, $Q' = 6.0$ ml/s

(d) $t' = 9$ s, $Q' = 6.1$ ml/s

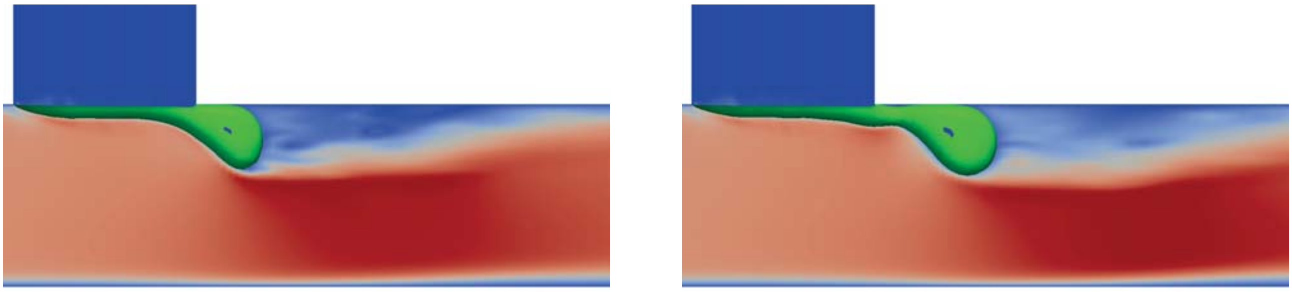

(e) $t' = 10$ s, $Q' = 6.2$ ml/s

(f) $t' = 10.4$ s, $Q' = 6.24$ ml/s

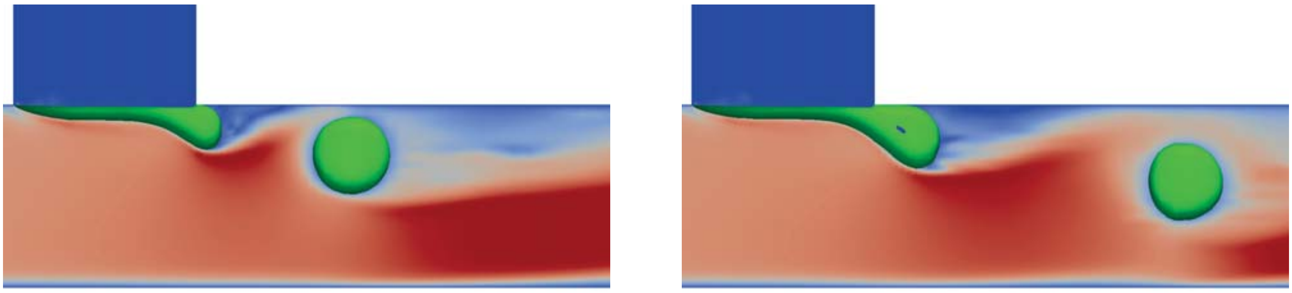

(g) $t' = 10.7$ s, $Q' = 6.27$ ml/s

(h) $t' = 11.1$ s, $Q' = 6.31$ ml/s

Figure 9.14: Time sequence showing the results of the OpenFOAM flow simulations in the groove channel with $l' = 25$ mm ($l = 10$). Flow is from left to right. The liquid velocity is shown at the symmetry x, z-plane ($y = 0$). The green color represents the free surface (whole free surface is depicted). In (c) the last stable interface with corresponding critical flow rate $Q_c^{\prime OF} = 6.00$ ml/s (experimental value is $Q_c^{\prime EXP} = 5.93$ ml/s) is shown.

Chapter 10

Conclusions

In this work forced flow through a partially open capillary channel in compensated gravity environment is investigated experimentally, theoretically, and numerically. The shape of the channel resembles the capillary vanes commonly used in propellant management devices applied in satellite surface tension tanks (Figure 1.1). The experimental unit contains a test channel composed of two parallel glass walls with a fixed gap distance and height (channel aspect ratio $\Lambda = 5$). The liquid flow is driven by a pump, and the length of the channel's open section is adjusted with movable slide bars. The length of the channel's open section is varied in the range $2 \leq l \leq 19.2$ ($5.64 \times 10^{-4} \leq \tilde{l} \leq 5.96 \times 10^{-3}$ with a constant OHNESORGE number $\mathrm{Oh} = 2.26 \times 10^{-3}$). Two channel configurations were considered during the first series of the Capillary Channel Flow experiment (CCF EU#1): the groove (one free liquid surface) and the parallel plates (two free liquid surfaces). The CCF experimental unit (EU#1) was installed for over 60 days into the Microgravity Science Glovebox in the Destiny module aboard the International Space Station. The CCF experiment was the first long-term experiment conducted in space and controlled from a ground station via telescience (real time operation). The capillary test channel was implemented into a closed fluid loop system (the hardware was introduced in Chapter 4) and the test section was observed with two cameras: High Speed High Resolution Camera and standard definition camera (live view). The total of 2139 (PP: 187, GR: 1952) data points was achieved, thereof 846 (PP: 187, GR: 659) with included HSHR camera images. The main goal of the CCF experiment (EU#1) was to validate the recently developed theoretical flow models. Contrarily to previously performed short time experiments (drop tower and suborbital rocket flights), a broader parameter space could be investigated now.

A literature survey was performed and the mathematical flow model for both geometries (GR and PP) was reviewed and outlined (Chapter 3). The one-dimensional, steady model comprises both radii of curvature, the convective acceleration due to the change in cross-section, and the viscous pressure loss within the channel. The stability of steady and unsteady flow is based on the pressure interactions at the interface's minimum contour point (point of the minimum cross-section, Figure 2.2). It is assumed that the capillary pressure (surface tension) enhance the stability of the free surface, whereas the convective pressure and the effect of the local acceleration act contrarily. In the Transient Stability Model, which is an extension of the steady model, the inertia of the accelerated liquid column and the geometry of the free surface are taken into account. A graphical illustration of the Transient Stability Model was demonstrated in the form of a generic stability diagram (Figure 3.8(b)). The 1D flow model was solved with finite differences with the numerical tool ccFlow (developed at ZARM). Additionally, 3D CFD simulations were performed with OpenFOAM to study the flow behavior within the inlet section of the experimental setup. Both tools were introduced in Chapter 5.

The steady flow results served for verification of the flow model. In the steady flow experiments, the critical flow rate Q_c (defined as the maximum measured flow rate at which stable interfaces are observed) was determined for both geometries in the dimensionless channel lengths range $2 \leq l \leq 19.2$ (Figure 6.4). It was shown that the choking effect defines the limit of steady stable flow. Exceeding the critical flow rate leads to the collapse of the free surface and to gas ingestion into the flow path. It was found that the critical flow rate is a function of the channel length l. With increasing l the critical flow rate decreases. This decrease appears hyperbolic for channels with $l \leq 8$ and almost linear for channels with $l > 8$. A comparison of experimental and the 1D computational results shows very good agreement for channels $l > 7.2$ with a deviation less than 5%. The discrepancy between the experiment and 1D model increases for short channels. This behavior is attributed to the additional flow effects, which are not included in the mathematical model. A comparison of experimental and 3D results shows very good agreement (deviation less than 5 %) for the entire range of lengths l. The 3D solver OpenFOAM solves the full NAVIER-STOKES flow equations in the three-dimensional domain (more accurately resembling the real setup), which is believed to explain the better performance of the 3D solver for short channels. Furthermore, it was shown that the values of experimentally determined critical flow rate for the groove are higher than for the parallel plates. This is attributed to the smaller flow cross-section area between parallel plates, due to the two-sided indentation of the surfaces (Figure 3.1). Higher flow rates can be achieved for the groove channel before the curvature fails to balance the pressure difference $p - p_a$. Furthermore, it was shown that the flow development condition at the inlet of the capillary channel influences the critical flow rate. Critical flow rates computed with ccFlow for the developed flow (parabolic velocity profile) are 10 % higher (for channels with $l > 8$) compared to undeveloped flow assumption (uniform velocity profile). This difference decreases with decreasing channel length l. These two cases represent two extremes of the inlet flow conditions, which bracket all intermediate scenarios of a developing flow (e.g. flow in the CCF setup). Furthermore, a parametric study with ccFlow shows that an increase of the channel length l (beyond the CCF experiment capabilities) leads to a further decrease of the critical flow rate Q_c (Figure 6.6(a)).

HSHR camera images were evaluated with a contour detection algorithm, aiming at the determination of the time averaged free surface contours k along the channel x-axis. Inspection of the evaluated profiles shows that the shape of the free surface depends on the length of the channel's open section (Figure 6.7). For channels with $l = 2$ (for both PP and GR), the contours of the free surface are almost symmetric with respect to the plane $x = 0.5$. For channels with $l = 19.2$ (maximum length investigated in the CCF experiment), the contours are highly asymmetric. The changing shape of the free surface with increasing channel length is found to be a consequence of different physical regimes that influence the flow. A comparison of the experimentally determined contours with the numerical predictions (1D model) shows a good agreement (Figures 6.10 and 6.11), for the whole range of length l. However, 1D profiles are slightly shifted towards the channel inlet ($x = 0$). For the groove channel, also lower values of k are obtained compared to the experiment. A minimum contour point $k_{min}(x^*, k^*)$ is found to be a characteristic point of the contour, aiding the examination of the free surface profiles (Figure 6.12). The point k_{min} is located in the vicinity of $x = 0.5$ for short channels, which is typical for convective dominated quasi-symmetrical profiles. As the channel length is increased, longitudinal coordinate x^* of k_{min} shifts towards the channel outlet. As the channel length increases, the asymmetry of the free surface also increases due to the shifting of k_{min} towards the channel outlet. In the experiments, k^* increases with l for channels with $l > 3.6$. The same trend is observed for results of the 1D computation, albeit for channels with $l > 4.8$. In both cases, k^* seems to tend towards a value of 4. It is found that for sufficiently long channels $k^* = 4$ is a minimum value, based on the channel geometry. Furthermore, the "sensitivity" of the free liquid surface was demonstrated with the experimental results (reproducibility measurements, Figures 6.8 and 6.9), and with results of a parametric study with ccFlow. It is found that for the flow in the critical regime, a small change (even below 2 %) in the value of the flow rate leads to a significant change of the shape of the free surface profiles. Small fluctuations of the flow rate in the vicinity of the stability limit result in significant differences in the plot $k = f(x)$ (Figure 7.5(a)).

In the transient flow experiments, the flow rate was increased with a well defined flow acceleration $\delta = \Delta Q/\Delta t$ and time constant $\Delta = 1$. It was determined experimentally that this value corresponds with the natural time constant of the CCF system. The acceleration δ was varied until a clear limit between stable and unstable accelerations was resolved. The experimental results (1403 data points) were evaluated and presented in the form of Transient Stability Diagrams (Figures 8.2 and 8.3). A comparison to the theoretically determined transient stability limit shows a good agreement. The transient stability model accounts for the additional effects related to the geometric properties of the free surface (flexibility effects) and feedback effects of the fluid loop. It was found that both effects lead to an enhancement of the free surface stability. The evaluation of the experimental results illustrates that both effects are modeled well with the Transient Stability Model. The proposed scaling provides (Figure 8.4) a common description of the Transient Stability Diagrams in which the flexibility and feedback effects are eliminated.

The evaluation of the critical flow rate and the free surface contours underlines the good agreement between the experiment and the mathematical model. Hence, the model is verified and assumed to be valid for both geometries. After the verification of the mathematical model, the numerical tool ccFlow was employed for further investigation of the general behavior of gas-liquid interfaces in open capillary channels. It was shown that the shape of the free surface is influenced by the flow conditions, geometric constraints, and by the system pressure. The flow between parallel plates was solved for a static and for a dynamic case. In the zero flow (static) case the free surface possesses a constant mean curvature dependent on the boundary conditions (system pressure). It was shown that the maximum curvature of the free surface is a geometric property (Figure 7.3). For sufficiently long channels ($l > 7.2$), the middle part of the profile was identified where only the first principal radius contributes to the curvature (the free surface is supported by only one radius). It was demonstrated that the maximum curvature resulting in the pinned free surface is a purely geometric quantity. The dynamic solution was calculated for subcritical and critical (main focus of the CCF experiment) flow conditions. Two scenarios were considered: (i) flow rate variation and (ii) channel length variation. The different behavior of free surfaces in "short" and "long" channels was addressed. It was found that the deformation (asymmetry) of the free surface and its curvature are influenced by flow conditions (in addition to geometric constraints). Furthermore, two major flow effects i.e., convective acceleration and viscous pressure loss, and their influence on the shape of the interface were investigated. It was shown that for sufficiently short channels convective effects are dominant ($\tilde{l} < 4.5 \times 10^{-3}$), whereas for sufficiently long channels the frictional pressure loss dominates ($\tilde{l} > 4.5 \times 10^{-3}$). Irreversible pressure loss leads to the interface asymmetry and the minimum contour point is shifted towards the channel exit. Different physical flow regimes (purely convective, convective dominated, transition regime, viscous dominated, and purely viscous) were identified in relation to the dimensionless flow length $\tilde{l}$ (Figure 7.10). Finally, it was proven that the mathematical model is valid and applicable for a wider range of geometric configurations (different aspect ratios) and model parameters.

Finally, it was shown that the flow in the capillary channel and its inlet section can be modeled three-dimensionally with an open source code OpenFOAM. Besides the determination of the critical flow rate, simulations were employed to study the general flow behavior in the inlet section (flow preparation chamber and the entrance nozzle). There is no experimental apparatus enabling the measurement of the pressure losses in the said section and the flow development ratio at the capillary channel entrance. However, knowledge of the flow behavior in the inlet section is essential for the proper application of the boundary conditions required for the 1D model. The flow development ratio at the channel inlet is found to be in the range $1.2 < \gamma < 1.4$ for flow rates corresponding to the CCF experiment. As expected, the flow at the capillary channel inlet $x = 0$ is not fully developed. Furthermore, the pressure loss upstream from the channel inlet was evaluated and the pressure loss coefficients $K_1 = 527.4$ and $K_2 = 1.68$, required for the 1D model, were determined. Due to the applied scaling of the flow equations, the presented coefficients are valid for both geometries (groove and parallel plates). Finally, it was shown that OpenFOAM can be employed to study the flow in the unstable regime (choking process can be investigated, Figure 9.14).

Appendix A

CCF Experiment

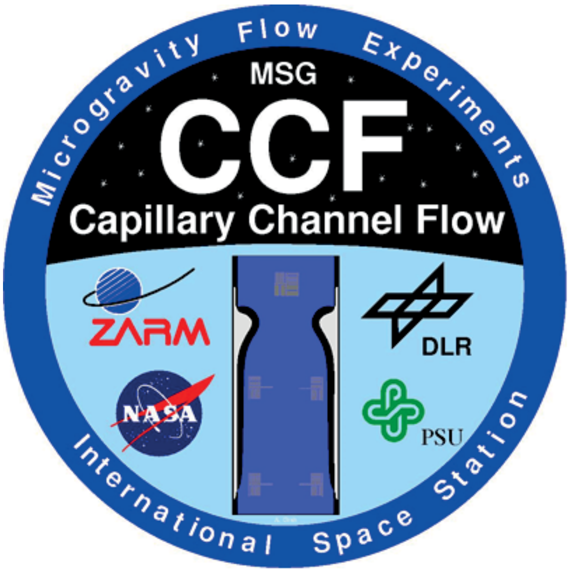

Figure A.1: The patch of the CCF experiment.

A.1 Test Fluid

The properties of the test liquid 3M™Novec™Engineered Fluid HFE-7500 can be described as a function of temperature T (in °C) [7]

$$\rho \;=\; 1670.98 - 2.02 \cdot \mathrm{T} \quad \frac{\mathrm{kg}}{\mathrm{m}^3} \quad , \tag{A.1}$$

$$\nu \;=\; \exp\left(-3.2319 + \frac{555.62}{\mathrm{T} + 161.83}\right) \cdot 10^{-6} \quad \frac{\mathrm{m}^2}{\mathrm{s}} \quad , \tag{A.2}$$

$$\sigma \;=\; (19.12025 - 0.09863 \cdot \mathrm{T}) \cdot 10^{-3} \quad \frac{\mathrm{N}}{\mathrm{m}} \quad , \tag{A.3}$$

where ρ, ν, and σ are density, viscosity, and surface tension, respectively. The liquid temperature evolution during the CCF (EU#1) experiment and the dependency of the OHNESORGE number on the liquid temperature are shown in Figure A.2.

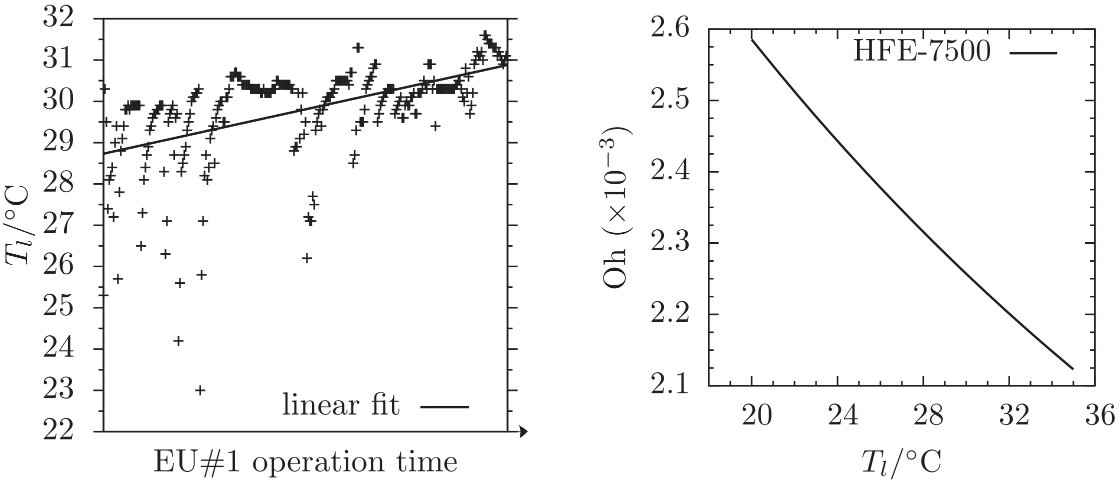

(a) Liquid temperature evolution.

(b) Oh versus the temperature.

Figure A.2: (a) Liquid temperature evolution during the CCF experiment. Each cross represents a single data point for which the liquid temperature was measured at the channel inlet and outlet. The average temperature is displayed. (b) OHNESORGE number Oh as a function of the liquid temperature.

A.2 Software

The CCF ground station in Bremen (Figure 4.6(b)) is equipped with a workstation and software designated to fully control (real-time) the experimental setup aboard the ISS via telescience. During the operation, the sensors readings are received via telemetry with frequency of 1 Hz and plotted on the EGSE display as shown in Figure A.3. All data are saved throughout the entire operation. The most adequate values are recorded in the test matrix. An overview of the monitored parameters is given in Table A.1.

Table A.1: Experiment parameters monitored in real-time during the CCF operation. Values in the left column are recorded for every data point (test matrix). Readings of the senors presented in the right column are used for the house keeping.

Recorded		Observed	
Parameter	Description	Parameter	Description
`EUTemp2SW`	Gas temperature in the TU	`PlungK2Position`	Position of the liquid plunger K2
`EUTemp5SW`	Liquid temperature at the channel inlet	`PlungK3Position`	Position of the gas plunger K3
`EUTemp6SW`	Liquid temperature at the channel outlet	`PlungK1Frequency`	Frequency of the plunger K1 (oscillator)
`PressureC9`	Liquid pressure	`PlungK1Amplitude`	Amplitude of the plunger K1 (oscillator) †
`PressureC3`	Gas pressure in the Plunger K3 section	`PlsLedCurrent`	Intensity of the parallel light source
`Pressure1TU`	Ambient pressure in the Test Unit	`BubbleSens1Mon`	Fluid temperature (innermost bubble sensor)
`FlowSensSig`	Flow meter reading	`BubbleSens2Mon`	Fluid temperature (intermediate bubble sensor)
`Slider1Position`	Position of the first slider	`BubbleSens3Mon`	Fluid temperature (outermost bubble sensor)
`Slider2Position`	Position of the second slider		

† Not subject of present work.

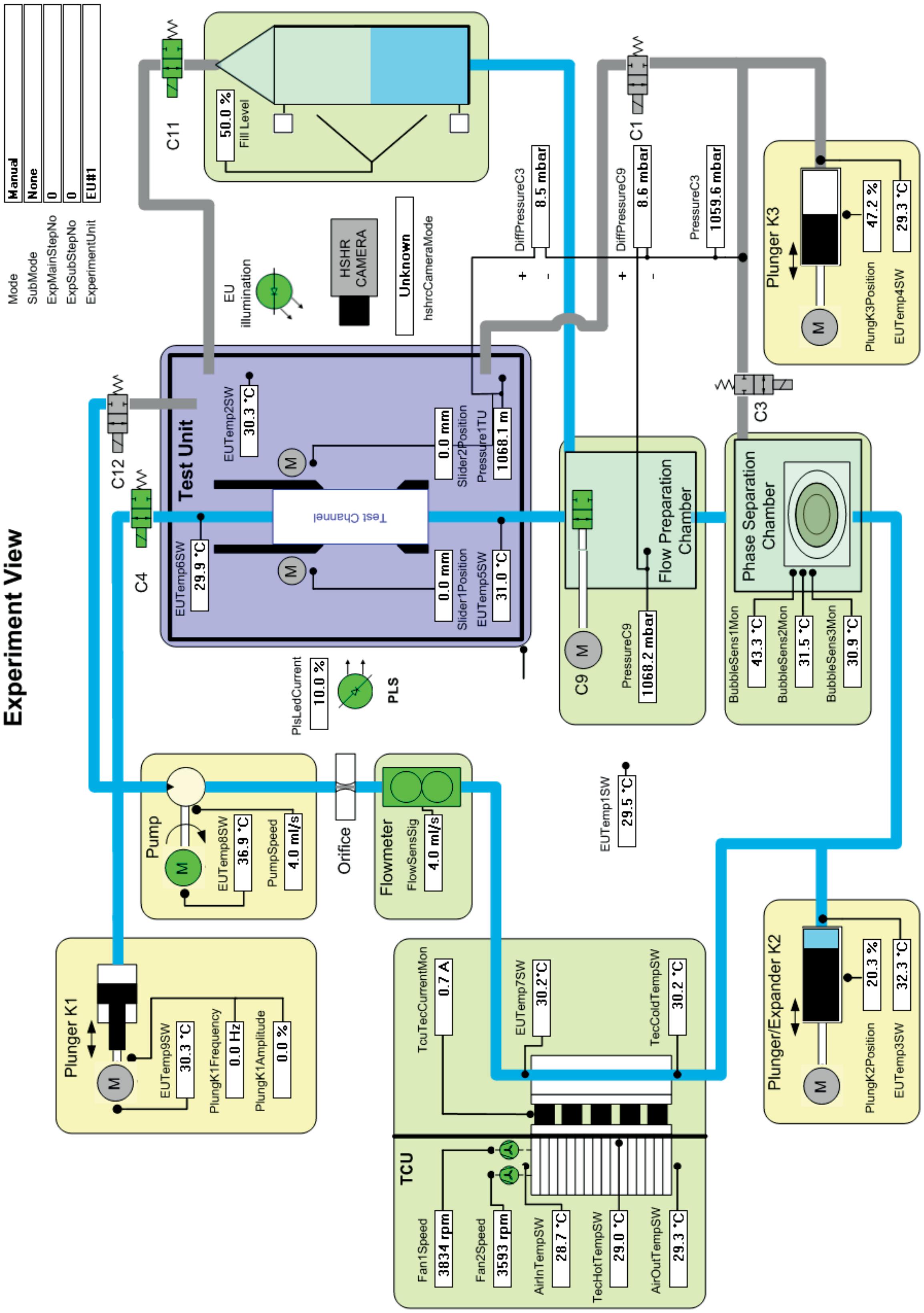

Figure A.3: EGSE experiment view display containing a generic view of Experiment Unit EU#1. Readings of the hardware senors are plotted in-real time. Cyan and grey colors represent liquid and gas, respectively. An overview of the monitored parameters is given in Table A.1.

Appendix B

CCF Experiment Results

B.1 Critical Flow Rate

All gathered experimental data of a steady flow at the critical rate (last stable interface) for both geometries are summarized in Tables B.1 and B.2.

Table B.1: Experimentally determined values of the critical flow rate $Q_{c,PP}^{EXP}$ for the **parallel plates** channel. n is the number of data points recorded with the HSHR camera. Corresponding HSHRC images and evaluated free surface contours can be found on the website `http://ccf.zarm.uni-bremen.de/`.

l' /mm	l	$Q_{c,PP}^{EXP}$	n	$s_{Q_{c,PP}^{EXP}}$	Experiment ID
1	0.4	1.48	1	-	653
2	0.8	1.25	2	0.01	722; 654
3	1.2	1.15	1	-	655
4	1.6	1.07	1	-	656
5	2	0.99	5	0.01	726; 736; 746; 642; 657
6	2.4	0.95	1	-	658
7	2.8	0.91	1	-	659
8	3.2	0.88	1	-	660
9	3.6	0.86	1	-	661
10	4	0.83	5	0.02	727; 737; 747; 643; 662
11	4.4	0.81	1	-	663
12	4.8	0.80	1	-	664
13	5.2	0.79	1	-	666
14	5.6	0.78	1	-	667
15	6	0.77	5	0.01	728; 738; 752; 645; 668

Continued on next page

Table B.1 – continued from previous page

l' /mm	l	$Q_{c,PP}^{EXP}$	n	$s_{Q_{c,PP}^{EXP}}$	Experiment ID
16	6.4	0.76	1	-	669
17	6.8	0.76	1	-	670
18	7.2	0.75	1	-	671
19	7.6	0.75	1	-	672
20	8	0.74	5	0.01	729; 739; 753; 646; 673
21	8.4	0.73	1	-	674
22	8.8	0.74	1	-	675
23	9.2	0.72	1	-	676
24	9.6	0.73	1	-	677
25	10	0.72	5	0.01	730; 740; 754; 647; 678
26	10.4	0.71	1	-	679
27	10.8	0.71	1	-	680
28	11.2	0.71	1	-	681
29	11.6	0.70	1	-	682
30	12	0.71	4	0.01	731; 741; 648; 683
31	12.4	0.70	1	-	684
32	12.8	0.69	1	-	685
33	13.2	0.69	1	-	686
34	13.6	0.69	1	-	688
35	14	0.70	3	0.01	732; 649; 689
36	14.4	0.70	1	-	690
37	14.8	0.69	1	-	691
38	15.2	0.69	1	-	692
39	15.6	0.68	1	-	693
40	16	0.68	4	0.01	733; 743; 650; 694
41	16.4	0.68	1	-	695
42	16.8	0.68	1	-	696
43	17.2	0.68	1	-	697
44	17.6	0.68	1	-	698
45	18	0.67	4	0.01	734; 744; 651; 699
46	18.4	0.66	1	-	701
47	18.8	0.67	1	-	702
48	19.2	0.67	4	0.01	735; 745; 652; 703

Table B.2: Experimentally determined values of the critical flow rate $Q_{c,GR}^{EXP}$ for the **groove** channel. n is the number of data points recorded with the HSHR camera. Corresponding HSHRC images and evaluated free surface contours can be found on the website `http://ccf.zarm.uni-bremen.de/`.

l' /mm	l	$Q_{c,GR}^{EXP}$	n	$s_{Q_{c,GR}^{EXP}}$	Experiment ID
2	0.8	1.35	1	-	723
3	1.2	1.15	1	-	724
4	1.6	1.07	1	-	725
5	2	1.00	2	0.01	28; 29
6	2.4	0.96	2	0.002	30; 31
7	2.8	0.96	1	-	32
8	3.2	0.92	1	-	33
9	3.6	0.89	1	-	34
10	4	0.87	5	0.005	26; 35; 86; 99; 105
11	4.4	0.84	1	-	36
12	4.8	0.83	1	-	37
14	5.6	0.81	2	0.004	39; 40
15	6	0.80	2	0.003	25; 42
16	6.4	0.79	1	-	43
17	6.8	0.78	1	-	44
18	7.2	0.78	1	-	45
19	7.6	0.77	1	-	46
20	8	0.76	5	0.003	22; 47; 89; 100; 106
21	8.4	0.76	1	-	48
22	8.8	0.76	2	0.004	49; 52
23	9.2	0.76	1	-	53
24	9.6	0.76	1	-	54
25	10	0.75	1	-	55
26	10.4	0.75	1	-	56
27	10.8	0.74	1	-	57
29	11.6	0.74	1	-	60
30	12	0.73	5	0.01	27; 61; 90; 101; 108
31	12.4	0.73	1	-	62
33	13.2	0.72	1	-	64
34	13.6	0.72	1	-	65
35	14	0.71	1	-	66

Continued on next page

Table B.2 – continued from previous page

l' /mm	l	$Q_{c,GR}^{EXP}$	n	$s_{Q_{c,GR}^{EXP}}$	Experiment ID
37	14.8	0.71	1	-	68
38	15.2	0.71	1	-	69
39	15.6	0.71	2	0.002	71; 73
40	16	0.70	5	0.01	74; 91; 97; 102; 109
41	16.4	0.71	1	-	77
42	16.8	0.70	1	-	78
43	17.2	0.68	1	-	79
44	17.6	0.69	1	-	80
45	18	0.69	1	-	82
46	18.4	0.70	1	-	83
47	18.8	0.69	1	-	84
48	19.2	0.68	5	0.02	85; 92; 98; 103; 110

B.2 HSHR Camera Images

Examples of the unprocessed HSHR camera images downlinked from the ISS are shown in Figure B.1. The flow is steady at the critical flow rate (last stable interface). Four cases are presented: groove with $l = 6$, groove with $l = 19.2$, parallel plates with $l = 6$ and parallel plates with $l = 19.2$. The time evolution is depicted with the time stamps. The free surfaces remain stable throughout the entire experiment. Minor oscillations can be observed on the free surfaces, which were discussed in Section 6.1.

B.3 MSG Camera View

During the operation, the MSG camera is used to observe the test channel and the compensation tube. An example of unsteady flow behavior in the groove channel recorded with the MSG camera is shown in Figure B.2. In (a) the flow is stable. Increasing the flow rate above the critical rate leads to the instability. This is indicated by the free surface which is being pulled into the test channel. In general, the MSG camera view is used for qualitative analysis of the free surface behavior. The position of the meniscus in the compensation tube is monitored and used to evaluate the amount of gas ingested (choked) into the flow path. The Δh_{CT} in Figure B.2(b) depicts the fill level change in the CT, which was discussed in Section 6.1.

B.4 Symmetry in the Free Surface Contours

During the CCF experiments with the parallel plates channel, it was observed that both free surfaces behave identically during subcritical flow with $Q \leq Q_c$. An example of the evaluated profiles is shown in Figure B.3.

B.5 Flexibility Function - Transient Stability Model

The additional stabilization of the free surface during transient flow is caused by the flexibility of the flat part of the surface (was discussed in Section 3.5.2). Evaluation of the CCF experiment results confirms this assumption (stability diagrams in Figures 8.2 and 8.3). The "long channel effect" is modeled with the flexibility function f (Equation (3.67)). The dependency of of the f function on the channel length l is shown in Figure B.4.

(a) groove (ID 00025) $l = 6$ ($l' = 15$ mm)

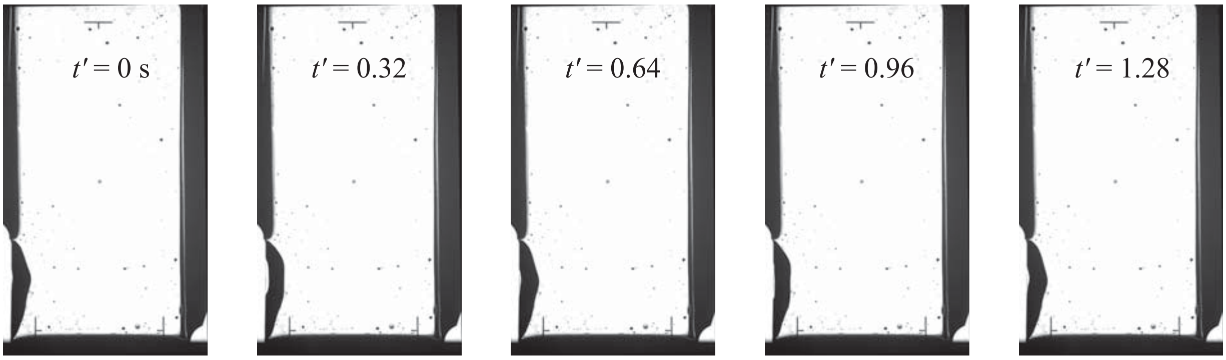

(b) groove (ID 00085) $l = 19.2$ ($l' = 48$ mm)

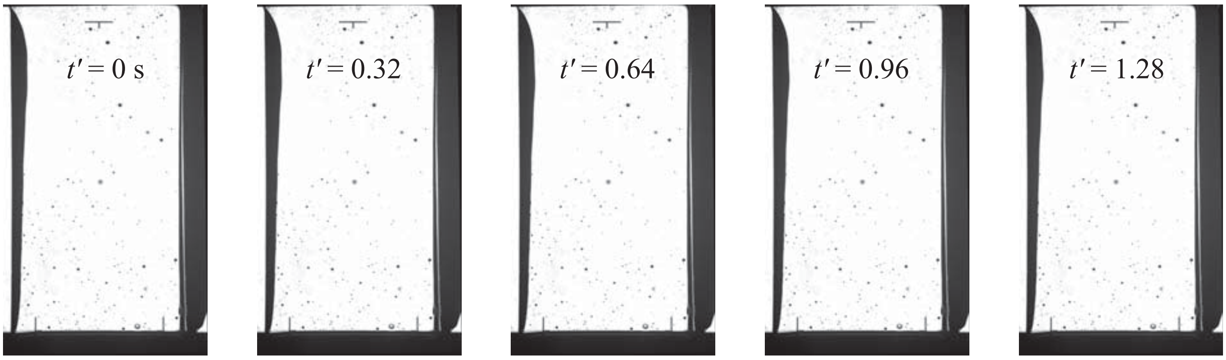

(c) parallel plates (ID 00645) $l = 6$ ($l' = 15$ mm)

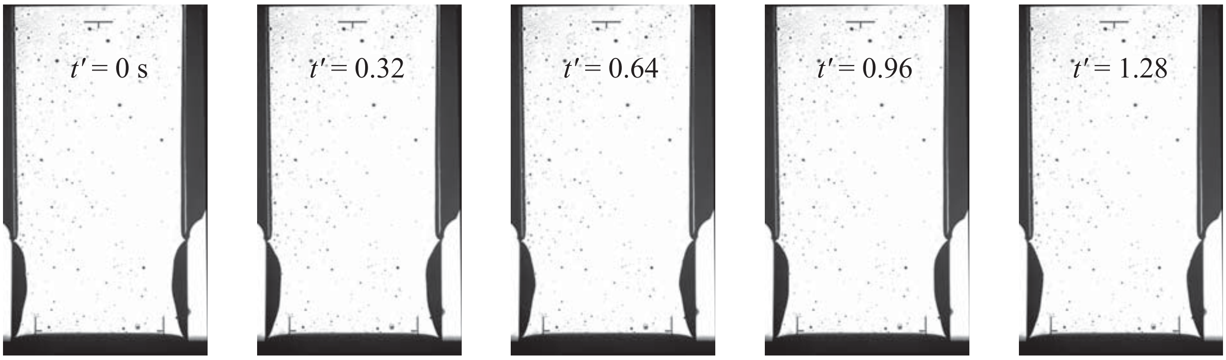

(d) parallel plates (ID 00652) $l = 19.2$ ($l' = 48$ mm)

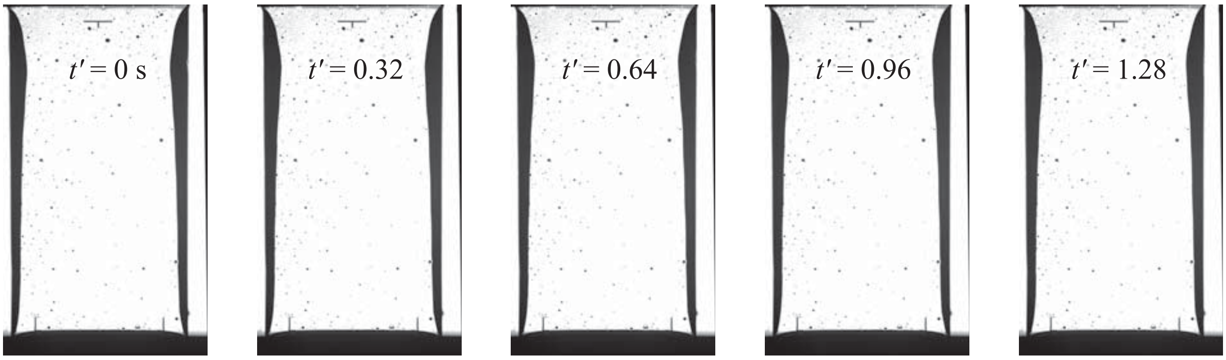

Figure B.1: Examples of unprocessed HSHRC images showing the last stable free surfaces recorded for steady flow. Flow is from bottom to top.

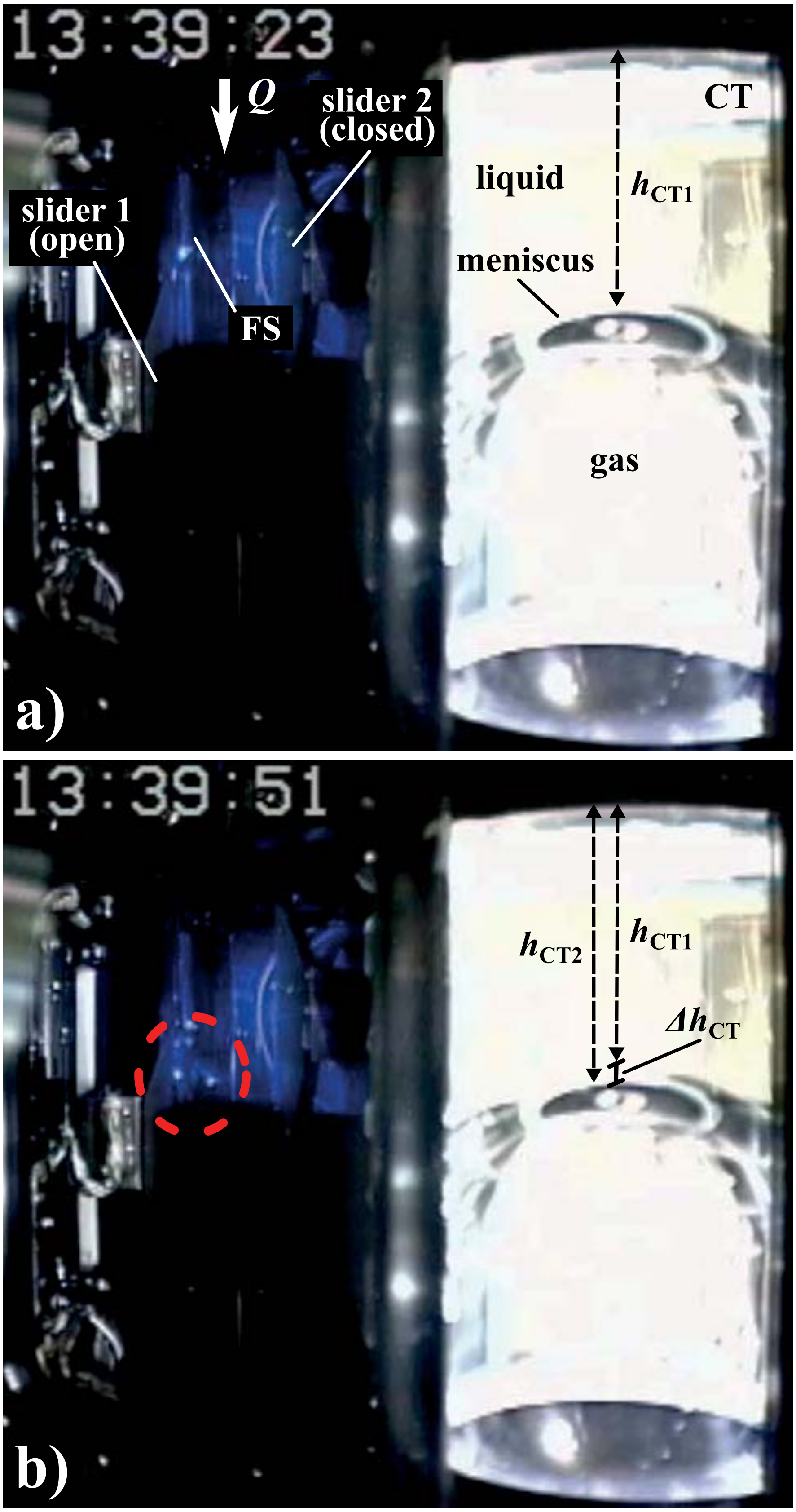

Figure B.2: Unstable flow in the groove recorded with the MSG camera. The channel length is $l = 12$ ($l' = 30$ mm) and the flow rate $Q/Q_c = 1.19$ (ID 00821). The red circle marks the free surface which is being withdrawn into the test channel.

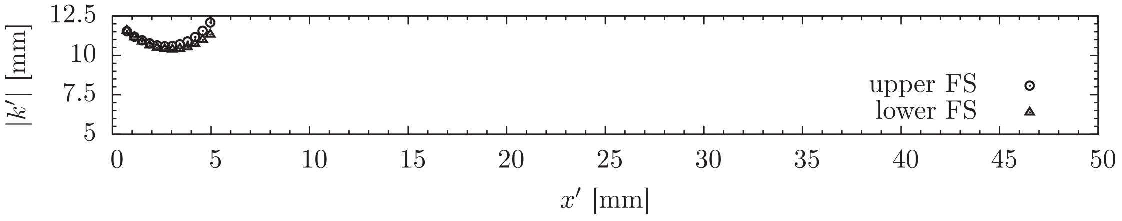

(a) $l' = 5$ mm (EXP 00746)

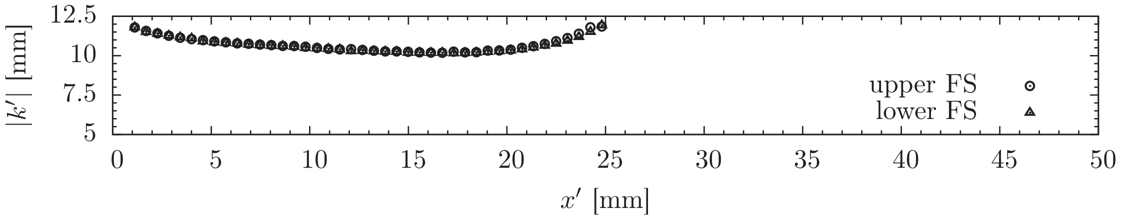

(b) $l' = 25$ mm (EXP 00754)

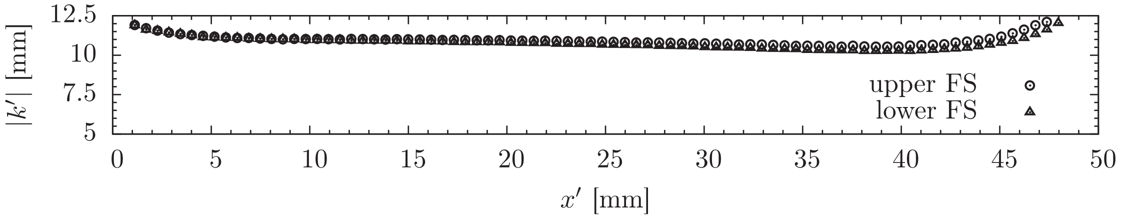

(c) $l' = 48$ mm (EXP 00652)

Figure B.3: Evaluated free surface (FS) contour k' along the parallel plates channel x'-axis. Both, lower (z' negative) and upper (z' positive) profiles are depicted for three characteristic channel lengths. Dimensional values are shown for the sake of comparison. Maximum stable (critical flow) interfaces are depicted.

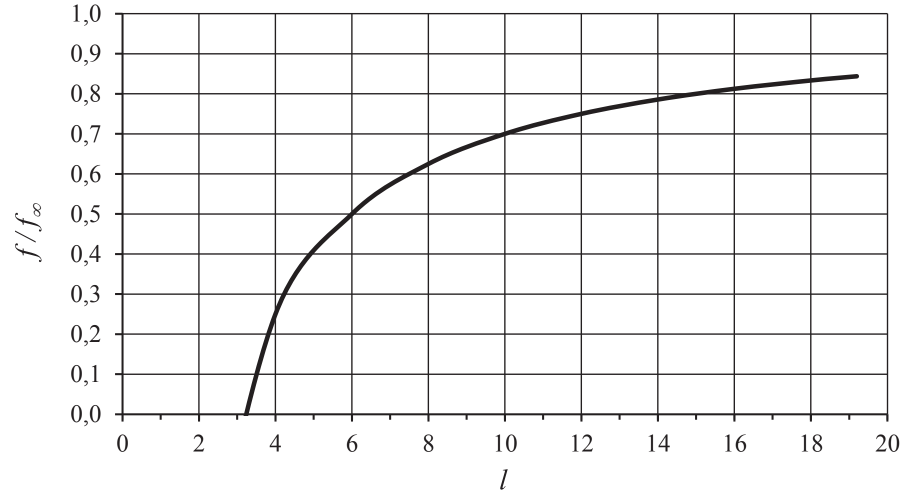

Figure B.4: Normalized flexibility function versus the channel length. f/f_∞ defines the relative compensatory capability of a surface of minimum length $l > l_{f0}$ $(l > 3)$.

Appendix C

ccFlow Results

The one-dimensional flow simulations are carried out with the `ccFlow` toll (version 5.3). The simulation parameters are listed in Table 5.2.

C.1 Critical Flow Rate

A complete list of the simulation results for all considered channel lengths is given in Tables C.1 (parallel plates) and C.2 (groove).

Table C.1: Results of the ccFlow computations for the **parallel plates** channel. Critical flow rate $Q^{1D}_{c,GR}$ is the mean value between the critical flow rate computed for undeveloped ($L_0 = 1$) and developed flow ($L_0 = 0$) assumptions. The v^*, A^*, h^*, k^* are the flow velocity, cross-sectional area, mean curvature, and the vertical coordinate of the k_{min} point, respectively at the point of the minimum cross-section point. The model parameters are given in Table 5.2.

		undeveloped					developed					
l'/mm	l	$Q^{L_0=1}_{c,PP}$	v^*	A^*	h^*	k^*	$Q^{L_0=0}_{c,PP}$	v^*	A^*	h^*	k^*	$Q^{1D}_{c,PP}$
5	2	1.18	1.37	0.86	2.06	4.08	1.22	1.42	0.86	2.06	4.07	1.20
6	2.4	1.1	1.3	0.84	1.88	4	1.14	1.35	0.84	1.88	4	1.12
7	2.8	1.03	1.24	0.83	1.74	3.94	1.08	1.3	0.83	1.74	3.94	1.06
8	3.2	0.98	1.2	0.82	1.64	3.88	1.03	1.25	0.82	1.64	3.88	1.01
9	3.6	0.94	1.16	0.81	1.56	3.84	0.99	1.22	0.81	1.56	3.84	0.97
10	4	0.9	1.12	0.8	1.49	3.8	0.95	1.18	0.8	1.49	3.81	0.93
11	4.4	0.87	1.09	0.8	1.43	3.78	0.92	1.15	0.8	1.43	3.79	0.90
12	4.8	0.85	1.06	0.8	1.38	3.77	0.9	1.12	0.8	1.38	3.78	0.88
14	5.6	0.81	1.01	0.8	1.3	3.78	0.86	1.07	0.8	1.29	3.79	0.84
15	6	0.79	0.99	0.8	1.26	3.79	0.85	1.05	0.8	1.25	3.8	0.82
16	6.4	0.78	0.97	0.8	1.23	3.8	0.83	1.03	0.81	1.22	3.82	0.81
17	6.8	0.77	0.95	0.81	1.21	3.82	0.82	1.01	0.81	1.2	3.84	0.80
18	7.2	0.76	0.93	0.81	1.18	3.83	0.81	0.99	0.81	1.17	3.86	0.79
19	7.6	0.75	0.92	0.81	1.16	3.85	0.8	0.98	0.82	1.15	3.88	0.78
20	8	0.74	0.9	0.82	1.15	3.87	0.79	0.96	0.82	1.13	3.9	0.77
22	8.8	0.72	0.88	0.82	1.12	3.9	0.78	0.94	0.83	1.11	3.94	0.75
24	9.6	0.71	0.86	0.83	1.1	3.93	0.77	0.92	0.84	1.08	3.97	0.74
25	10	0.71	0.85	0.83	1.09	3.94	0.77	0.91	0.84	1.08	3.98	0.74
28	11.2	0.69	0.83	0.84	1.08	3.96	0.75	0.9	0.84	1.06	4	0.72
30	12	0.69	0.82	0.84	1.07	3.97	0.75	0.89	0.84	1.05	4.01	0.72
32	12.8	0.68	0.81	0.84	1.06	3.98	0.74	0.88	0.85	1.05	4.01	0.71
34	13.6	0.67	0.8	0.84	1.06	3.98	0.74	0.87	0.85	1.05	4.01	0.71
35	14	0.67	0.8	0.84	1.06	3.98	0.73	0.87	0.85	1.05	4.01	0.70
36	14.4	0.67	0.79	0.84	1.06	3.98	0.73	0.87	0.85	1.04	4.01	0.70
38	15.2	0.66	0.79	0.84	1.05	3.99	0.73	0.86	0.85	1.04	4.02	0.70
40	16	0.66	0.78	0.84	1.05	3.99	0.72	0.85	0.85	1.04	4.02	0.69
42	16.8	0.65	0.78	0.84	1.05	3.99	0.72	0.85	0.85	1.04	4.01	0.69
45	18	0.65	0.77	0.84	1.05	4	0.71	0.84	0.85	1.04	4.01	0.68
46	18.4	0.64	0.77	0.84	1.05	4	0.71	0.84	0.85	1.04	4.01	0.68
48	19.2	0.64	0.76	0.84	1.05	4	0.7	0.83	0.85	1.04	4.01	0.67

Table C.2: Results of the ccFlow computations for the **groove** channel. Critical flow rate $Q_{c,GR}^{1D}$ is the mean value between the critical flow rate computed for undeveloped ($L_0 = 1$) and developed flow ($L_0 = 0$) assumptions. The v^*, A^*, h^*, k^* are the flow velocity, cross-sectional area, mean curvature, and the vertical coordinate of the k_{min} point, respectively at the point of the minimum cross-section point. The model parameters are given in Table 5.2.

		undeveloped					developed					
l'/mm	l	$Q_{c,GR}^{L_0=1}$	v^*	A^*	h^*	k^*	$Q_{c,GR}^{L_0=0}$	v^*	A^*	h^*	k^*	$Q_{c,GR}^{1D}$
2	0.8	1.67	1.72	0.97	3.2	4.6	1.7	1.75	0.97	0.32	4.6	1.69
3	1.2	1.44	1.5	0.96	2.56	4.41	1.48	1.55	0.96	2.57	4.4	1.46
4	1.6	1.31	1.39	0.94	2.24	4.23	1.36	1.44	0.94	2.25	4.2	1.34
5	2	1.22	1.31	0.93	2.03	4.06	1.26	1.36	0.92	2.03	4.03	1.24
6	2.4	1.14	1.25	0.91	1.87	3.92	1.19	1.3	0.91	1.86	3.91	1.17
7	2.8	1.08	1.2	0.9	1.75	3.8	1.13	1.25	0.9	1.74	3.79	1.11
8	3.2	1.03	1.16	0.89	1.65	3.68	1.08	1.22	0.89	1.65	3.68	1.06
9	3.6	0.99	1.12	0.88	1.58	3.59	1.04	1.19	0.88	1.58	3.58	1.02
10	4	0.95	1.1	0.87	1.52	3.5	1.01	1.16	0.87	1.52	3.5	0.98
11	4.4	0.93	1.07	0.86	1.47	3.43	0.98	1.14	0.86	1.47	3.43	0.96
12	4.8	0.9	1.05	0.86	1.43	3.37	0.96	1.12	0.86	1.42	3.37	0.93
14	5.6	0.86	1.01	0.85	1.36	3.29	0.92	1.08	0.85	1.35	3.29	0.89
15	6	0.84	0.99	0.85	1.33	3.26	0.91	1.07	0.85	1.32	3.27	0.88
16	6.4	0.83	0.98	0.85	1.3	3.24	0.89	1.05	0.85	1.29	3.25	0.86
17	6.8	0.81	0.96	0.84	1.28	3.23	0.88	1.04	0.85	1.27	3.25	0.85
18	7.2	0.8	0.95	0.84	1.26	3.23	0.87	1.02	0.85	1.25	3.25	0.84
19	7.6	0.79	0.93	0.85	1.24	3.24	0.86	1.01	0.85	1.23	3.26	0.83
20	8	0.78	0.92	0.85	1.22	3.25	0.85	1	0.85	1.21	3.28	0.82
21	8.4	0.77	0.91	0.85	1.2	3.26	0.84	0.98	0.85	1.19	3.31	0.81
22	8.8	0.76	0.9	0.85	1.19	3.29	0.83	0.97	0.86	1.17	3.34	0.80
23	9.2	0.75	0.88	0.85	1.17	3.31	0.82	0.96	0.86	1.16	3.37	0.79
24	9.6	0.75	0.87	0.86	1.16	3.34	0.82	0.95	0.86	1.14	3.41	0.79
25	10	0.74	0.86	0.86	1.15	3.36	0.81	0.94	0.87	1.13	3.45	0.78
30	12	0.72	0.82	0.87	1.11	3.5	0.79	0.89	0.89	1.08	3.64	0.76
35	14	0.7	0.79	0.88	1.08	3.59	0.77	0.86	0.9	1.06	3.76	0.74
40	16	0.68	0.77	0.89	1.07	3.64	0.76	0.84	0.9	1.05	3.82	0.72
45	18	0.67	0.76	0.89	1.07	3.66	0.75	0.83	0.9	1.05	3.82	0.71
48	19.2	0.66	0.75	0.89	1.06	3.66	0.74	0.82	0.9	1.05	3.82	0.70

Appendix D

OpenFOAM

D.1 simpleFOAM Input Files - Cylindrical Tube

The numerical schemes dictionary `system/fvSchemes`:

```
/*--------------------------------*- C++ -*----------------------------------*\
| =========                 |                                                 |
| \\      /  F ield         | OpenFOAM: The Open Source CFD Toolbox           |
|  \\    /   O peration     | Version:  2.0.x                                 |
|   \\  /    A nd           | Web:      www.OpenFOAM.com                      |
|    \\/     M anipulation  |                                                 |
\*---------------------------------------------------------------------------*/
FoamFile
{
    version     2.0;
    format      ascii;
    class       dictionary;
    location    "system";
    object      fvSchemes;
}
// * * * * * * * * * * * * * * * * * * * * * * * * * * * * * * * * * * * * * //
ddtSchemes
{
    default         steadyState;
}
gradSchemes
{
```

```
    default         Gauss linear;
    grad(p)         Gauss linear;
    grad(U)         Gauss linear;
}
divSchemes
{
    default         none;
    div(phi,U)      Gauss upwind;
    div(phi,k)      Gauss upwind;
    div(phi,epsilon) Gauss upwind;
    div(phi,R)      Gauss upwind;
    div(R)          Gauss linear;
    div(phi,nuTilda) Gauss upwind;
    div((nuEff*dev(T(grad(U))))) Gauss linear;
}
laplacianSchemes
{
    default         none;
    laplacian(nuEff,U) Gauss linear corrected;
    laplacian((1|A(U)),p) Gauss linear corrected;
    laplacian(DkEff,k) Gauss linear corrected;
    laplacian(DepsilonEff,epsilon) Gauss linear corrected;
    laplacian(DREff,R) Gauss linear corrected;
    laplacian(DnuTildaEff,nuTilda) Gauss linear corrected;
}
interpolationSchemes
{
    default         linear;
    interpolate(U)  linear;
}
snGradSchemes
{
    default         corrected;
}
fluxRequired
{
    default         no;
```

```
    p               ;
}
// ************************************************************************* //
```

The solution and algorithm control settings dictionary `system/fvSolution`:

```
/*--------------------------------*- C++ -*----------------------------------*\
| =========                 |                                                 |
| \\      /  F ield         | OpenFOAM: The Open Source CFD Toolbox           |
|  \\    /   O peration     | Version:  2.0.x                                 |
|   \\  /    A nd           | Web:      www.OpenFOAM.com                      |
|    \\/     M anipulation  |                                                 |
\*---------------------------------------------------------------------------*/
FoamFile
{
    version     2.0;
    format      ascii;
    class       dictionary;
    location    "system";
    object      fvSolution;
}
// * * * * * * * * * * * * * * * * * * * * * * * * * * * * * * * * * * * * * //
solvers
{
    p
    {
        solver          GAMG;
smoother GaussSeidel;
agglomerator faceAreaPair;
nCellsInCoarsestLevel 100;
mergeLevels 1;
        preconditioner  DIC;
        tolerance       1e-06;
        relTol          0.05;
    }
    U
    {
        solver          PBiCG;
        preconditioner  DILU;
```

```
        tolerance       1e-05;
        relTol          0.1;
    }

    k
    {
        solver          PBiCG;
        preconditioner  DILU;
        tolerance       1e-05;
        relTol          0.1;
    }
}
SIMPLE
{
    nNonOrthogonalCorrectors 1;

   residualControl
    {
        p               1e-3;
        U               1e-4;
        "(k|epsilon|omega)" 1e-3;
    }
}
relaxationFactors
{
    p               0.6;
    U               0.7;
    k               0.7;
    epsilon         0.7;
    R               0.7;
    nuTilda         0.7;
}
// ************************************************************************* //
```

D.2 Cluster - Technical Specification

Computational Nodes:

Number of nodes: 8
Number of CPUs per node: 2
Number of cores per CPU/node: 8/16
Total number of cores: 128

Technical data:
CPU: Intel XEON E5-2670 2.6 GHz
RAM: 32 GB (8 × 4 GB DDR3-1333)
HDD: 1 × 500 GB SATA2
LAN: 2 × GBit LAN onboard; 1 × 40 Gbit QDR Infiniband (Interconnect)

Headnode:

CPU: Intel XEON E5-2670 2.0 GHz
RAM: 64 GB (8 × 8 GB DDR3-1333)
HDD: 2 × 500 GB SATA3 RAID1 for System; 7 × 2 TB SATA3 RAID6 for /home
LAN: 2 × GBit LAN onboard

D.3 Velocity Distribution

Velocity field in the inlet section of the CCF setup for three different flow rates (corresponding with the CCF experiment range) is shown in Figure D.1. Simulations are carried out with the simpleFOAM solver and the fine type of numerical mesh (shown in Figure 9.6).

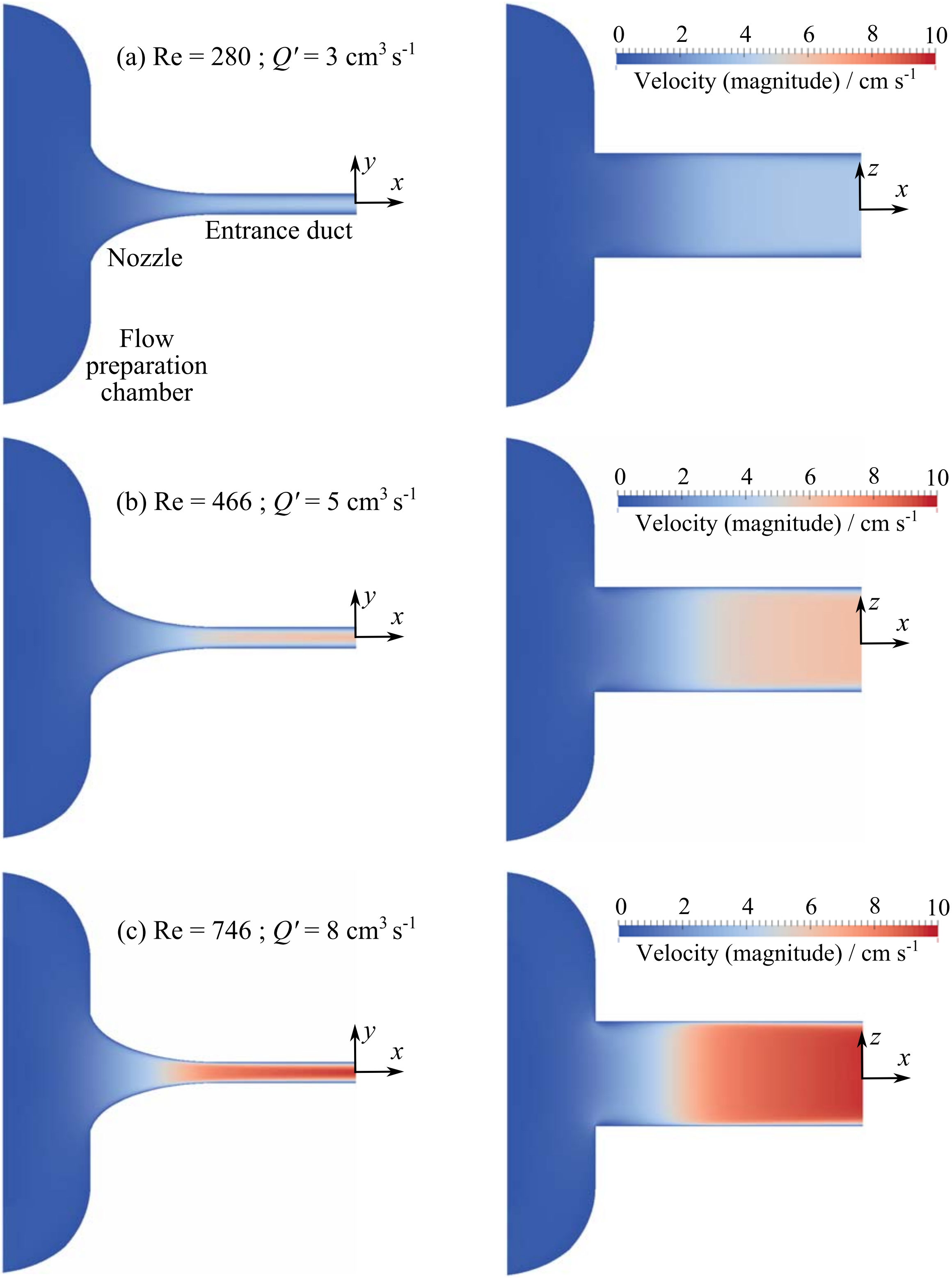

Figure D.1: Numerically (simpleFOAM) determined velocity field in the CCF inlet section. Flow is from left to the right. The velocity distribution at the xy symmetry plane ($z = 0$) and at the xz symmetry plane ($y = 0$) is shown in the left and right column, respectively.

List of Figures

List of Tables

Bibliography

[1] Artemov, V., Beale, S., de Vahl Davis, G., Escudier, M., Fueyo, N., Launder, B., Leonardi, E., Malin, M., Minkowycz, W., Patankar, S., Pollard, A., Rodi, W., Runchal, A., and Vanka, S. A tribute to D.B. spalding and his contributions in science and engineering. *Int. J. Heat Mass Transfer 52* (2009).

[2] Ayyaswamy, P. S., Catton, I., and Edwards, D. K. Capillary flow in triangular grooves. *J. Appl. Mech.* (1974), 332–336.

[3] Berthier, J., Brakke, K., and Berthier, E. A general condition for spontaneous capillary flow in uniform cross-section microchannels. *Microfluidics and Nanofluidics 16*, 4 (2014), 779–785.

[4] Brackbill, J. U., Kothe, D. B., and Zemach, C. A continuum method for modeling surface tension. *J. Comput. Phys. 100*, 2 (1992), 335–354.

[5] Bronowicki, P., Canfield, P., Grah, A., and Dreyer, M. E. Free surfaces in open capillary channels-parallel plates. *Phys. Fluids 27*, 012106 (2015), 1–21.

[6] Bronstein, I. N., and Semendjajew, K. A. *Taschenbuch der Mathematik*. Teubner, 1985.

[7] C. Ihmels, R. P., and Fischer, K. Messung der kinematischen Viskositäten von HFE-7500. Tech. rep., Laboratory for Thermophysical Properties GmbH, 2003.

[8] Canfield, P. J., Bronowicki, P. M., Chen, Y., Kiewidt, L., Grah, A., Klatte, J., Jenson, R., Blackmore, W., Weislogel, M. M., and Dreyer, M. E. The capillary channel flow experiments on the International Space Station: Experiment set-up and first results. *Exp. Fluids 54*, 1519 (2013), 1–14.

[9] Canny, J. A computational approach to edge detection. *Pattern Analysis and Machine Intelligence, IEEE Transactions on PAMI-8*, 6 (1986), 679–698.

[10] Chato, D. J., and Martin, T. A. Vented tank resupply experiment. Flight test results. *J. Spacecraft Rockets 43*, 5 (2006), 1124–1130.

[11] Chen, Y., and Collicott, S. H. Investigation of the symmetric wetting of vane-wall gaps in propellant tanks. AIAA J. 42, 2 (2004), 305–314.

[12] Chen, Y., Jenson, R., Weislogel, M., and Collicot, S. Capillary wetting analysis of the CFE-Vane gap geometry. In 46th AIAA Aerospace Sciences Meeting and Exhibit (2008), AIAA.

[13] Conrath, M., Canfield, P. J., Bronowicki, P. M., Dreyer, M. E., Weislogel, M. M., and Grah, A. Capillary channel flow experiments aboard the international space station. Phys. Rev. E 88, 063009 (2013), 1–8.

[14] Der, J. A linearized theory for unsteady surface tension driven flow along supercritical vane-formed fillets. In 27th Joint Propulsion Conference (Sacramento, CA, 1991), AIAA, pp. 1–5.

[15] Deshpande, S. S., Anumolu, L., and Trujillo, M. F. Evaluating the performance of the two-phase flow solver interFOAM. Computational Science and Discovery 5, 1 (2012).

[16] Deshpande, S. S., Trujillo, M. F., Wu, X., and Chahine, G. Computational and experimental characterization of a liquid jet plunging into a quiescent pool at shallow inclination. Int. J. Heat Fluid Flow 34 (2012), 1 – 14.

[17] Dietze, G. F., Rohlfs, W., Nährich, K., Kneer, R., and Scheid, B. Three-dimensional flow structures in laminar falling liquid films. J. Fluid Mech. 743 (2014), 75–123.

[18] Doro, E. O., and Aidun, C. K. Interfacial waves and the dynamics of backflow in falling liquid films. J. Fluid Mech. 726 (2013), 261–284.

[19] Dreyer, M. E., Delgado, A., and Rath, H. J. Capillary rise of liquid between parallel plates under microgravity. J. Colloid Interface Sci. 163, 1 (1994), 158–168.

[20] Dreyer, M. E., Rosendahl, U., and Rath, H. J. Experimental investigation on flow rate limitations in open capillary flow. In 34th AIAA/ASME/SAE/ASEE Joint Propulsion Conference (1998), AIAA 98-3165.

[21] Ducret, E., Arnaud, R., and Rigollet, R. Design and development of the eurostar 2000+ propellant tank. In 32nd ASME, SAE, and ASEE, Joint Propulsion Conference and Exhibit (1996), AIAA 96-3289.

[22] Durst, F., Ray, S., Uensal, B., and Bayoumi, O. A. The development lengths of laminar pipe and channel flows. J. Fluids Eng. 127 (2005), 1154–1160.

[23] Ferziger, J. H., and Peric, M. Computational Methods for Fluid Dynamics. Springer, 1996.

[24] Frank, J., Morris, P., Green, J., and Hall, T. The challenge of evolving mission operations tools for manned spaceflight. In 9th International Symposium on Artifical Intelligence, Robotics and Automation in Space (2008), AIAA.

[25] Gast, F. U., and Fiehn, H. The development of integrated microfluidic systems at GeSiM. Lab Chip 3 (2003), 6N–10N.

[26] Geuzaine, C., and Remacle, J. F. Gmsh Reference Manual, 2012.

[27] Gopala, V. R., and van Wachem, B. G. Volume of fluid methods for immiscible-fluid and free-surface flows. Chemical Engineering Journal 141 (2008), 204 – 221.

[28] Grah, A. ccFlow 5.3 - Benutzerhandbuch. ZARM, University of Bremen, 2013.

[29] Grah, A., Canfield, P. J., Bronowicki, P. M., Dreyer, M. E., Chen, Y., and Weislogel, M. M. Transient capillary channel flow stability. Microgravity Sci. Technol. 26, 6 (2014), 385–396.

[30] Grah, A., and Dreyer, M. E. One-dimensional and three-dimensional computation of free surface flow. In Interdisciplinary Transport Phenomena VI: Fluid, Thermal, Biological, Materials and Space Sciences (2009).

[31] Grah, A., and Dreyer, M. E. Dynamic stability analysis for capillary channel flow: One-dimensional and three-dimensional computations and the equivalent steady state technique. Phys. Fluids 22, 014101 (2010), 1–11.

[32] Grah, A., Haake, D., Rosendahl, U., Klatte, J., and Dreyer, M. Stability limits of unsteady open capillary channel flow. J. Fluid Mech. 600 (2008), 271–289.

[33] Groll, M., Schneider, M., Sartre, V., Zaghdoudi, M. C., and Lallemand, M. Thermal control of electronic equipment by heat pipes. Rev. Gen. Therm. 37, 5 (1998), 323 – 352.

[34] Haake, D., Klatte, J., Grah, A., and Dreyer, M. E. Flow rate limitation of steady convective dominated open capillary channel flows through a groove. Microgravity Sci. Technol. 22, 2 (2010), 129–138.

[35] Haake, D., Rosendahl, U., Ohlhoff, A., and Dreyer, M. E. Flow rate limitation in open capillary channel flows. Ann. NY Acad. Sci. 1077 (2006), 443–458.

[36] Haeberle, S., and Zengerle, R. Microfluidic platforms for lab-on-a-chip applications. Lab Chip 7 (2007), 1094–1110.

[37] Hancock, M. J., and Bush, J. W. M. Fluid pipes. J. Fluid Mech. 466 (2002), 285–304.

[38] Harlow, F. H., and Welch, J. E. Numerical calculation of time-dependent viscous incompressible flow of fluid with free surface. Phys. Fluids 8, 12 (1965), 2182–2189.

[39] Hess, J. L., and Smith, A. M. O. Calculation of potential flow about arbitrary bodies. Progress in Aerospace Sciences 8 (1967), 1–138.

[40] Hirt, C. W., and Nichols, B. D. Volume of fluid (VOF) method for the dynamics of free boundaries. J. Comput. Phys. 39, 1 (1981), 201–225.

[41] Hoang, D. A., van Steijn, V., Portela, L. M., Kreutzer, M. T., and Kleijn, C. R. Benchmark numerical simulations of segmented two-phase flows in microchannels using the volume of fluid method. Computers & Fluids 86 (2013), 28–36.

[42] Hysing, S., and Turek, S. Evaluation of commercial and academic CFD codes for a two–phase flow benchmark test case. Int. J. Comput. Sci. Eng. 10, 4 (2015), 387–394.

[43] Jaekle, D. E. Propellant management device conceptual design and analysis: Vanes. In AIAA/SAE/ASME/ASEE 27th Joint Propulsion Conference (Sacramento, CA, 1991), AIAA, pp. 1–13.

[44] Jasak, H., Jemcov, A., and Tukovic, Z. OpenFOAM: A C++ library for complex physics simulations. In International workshop on coupled methods in numerical dynamics (2007), vol. 1000, pp. 1–20.

[45] Jenson, R. M., Weislogel, M. M., Klatte, J., and Dreyer, M. E. Dynamic fluid interface experiments aboard the International Space Station: Model benchmarking dataset. J. Spacecraft Rockets 47, 4 (2010), 670–679.

[46] Johnson, C., and Hansen, C. Visualization Handbook. Academic Press, Inc., Orlando, FL, USA, 2004.

[47] Kamath, A., Bihs, H., Chella, M. A., and Arntsen, A. CFD simulations of wave propagation and shoaling over a submerged bar. Aquatic Procedia 4 (2015), 308–316.

[48] Kawaguti, M. Numerical solution of the navier-stokes equations for the flow around a circular cylinder at reynolds number 40. Journal of the Physical Society of Japan 8, 6 (1953), 747–757.

[49] Kiewidt, L. CCF ISS experiments. Image processing (steady flow). Tech. rep., ZARM Institute, University of Bremen, 2011.

[50] Klatte, J. Capillary Flow and Collapse in Wedge-Shaped Channels. PhD thesis, University of Bremen, 2011.

[51] Klatte, J., Haake, D., Weislogel, M. M., and Dreyer, M. E. A fast numerical procedure for steady capillary flow in open channels. Acta Mech. 201, 1-4 (2008), 269–276.

[52] Kranz, M. Numerische Untersuchung der Strömung in einem kapillaren Kanal mit variierender Querschnittsfläche. Bachelor Thesis, University of Bremen, Germany, 2014.

[53] Maiwald, A., and Schwarze, R. Numerical analysis of flow-induced gas entrainment in roll coating. Appl. Math. Model. 35, 7 (2011), 3516 – 3526.

[54] Martin, M., Defraeye, T., Derome, D., and Carmeliet, J. A film flow model for analysing gravity-driven, thin wavy fluid films. Int. J. Multiphas. Flow 73 (2015), 207–216.

[55] Melin, J., van der Wijngaart, W., and Stemme, G. Behaviour and design considerations for continuous flow closed-open-closed liquid microchannels. Lab Chip 5 (2005), 682–686.

[56] Netter, G., Renner, U., and Dreyer, M. Design and verification of a standard surface tension propellant tank. In 35th Joint Propulsion Conference (1999), AIAA 99-2178, pp. 1–11.

[57] Netter, G., Renner, U., Gerstmann, J., and Dreyer, M. E. Design of a new refillable reservoir or a standard surface tension tank. In 36th AIAA/ASME/ASEE Joint Propulsion Conference and Exhibit (2000), AIAA 2000-3446, pp. 1–21.

[58] Ohlhoff, A., Rosendahl, U., and Dreyer, M. E. Test-case no 35: Flow rate limitation in open capillary channels (PE). Multiphase Science and Technology 16, 1-3 (2004), 259–271.

[59] OpenCFD. OpenFOAM - The Open Source CFD Toolbox - Programmer's Guide. OpenCFD Ltd., United Kingdom, 2012.

[60] OpenCFD. OpenFOAM - The Open Source CFD Toolbox - User's Guide. OpenCFD Ltd., United Kingdom, 2012.

[61] Palacios, F., Colonno, M. R., Aranake, A. C., Campos, A., Copeland, S. R., Economon, T. D., Lonkar, A. K., Lukaczyk, T. W., Taylor, T. W., and

Alonso, J. J. Stanford University unstructured (SU2): An open-source integrated computational environment for multi-physics simulation and design. AIAA Paper 287 (2013), 2013.

[62] Popinet, S. An accurate adaptive solver for surface-tension-driven interfacial flows. J. Comput. Phys. 228, 16 (2009), 5838–5866.

[63] Ransohoff, T. C., and Radtke, C. J. Laminar flow of a wetting liquid along the corners of a predominantly gas-occupied noncircular pore. J. Colloid Interf. Sci. 121, 2 (1988), 392–401.

[64] Richardson, L. F. Weather Prediction by Numerical Process. Cambridge University Press, 1922.

[65] Rollins, J. R., Grove, R. K., and Jaekle, D. E. Twenty-three years of surface tension propellant management system design, development, manufacture, test, and operation. In 21st Joint Propulsion Conference (1985), AIAA 85-1199, pp. 1–9.

[66] Rosendahl, U., and Dreyer, M. E. Design and performance of an experiment for the investigation of open capillary channel flows. Exp. Fluids 42, 5 (2007), 683–696.

[67] Rosendahl, U., Dreyer, M. E., Rath, H. J., and Motil, B. Critical velocities in open capillary channel flows. In Conference and Exhibit on International Space Station Utilization (2001).

[68] Rosendahl, U., Fechtmann, C., and Dreyer, M. E. Sounding rocket experiment on capillary channel flow. In Proceedings of the 17th ESA Symposium on European Rocket and Balloon Programmes and Related Research (2005), vol. ESA SP-590, pp. 551–556.

[69] Rosendahl, U., Grah, A., and Dreyer, M. E. Convective dominated flows in open capillary channels. Phys. Fluids 22, 052102 (2010), 1–13.

[70] Rosendahl, U., Ohlhoff, A., and Dreyer, M. E. Choked flows in open capillary channels: theory, experiment and computations. J. Fluid Mech. 518 (2004), 187–214.

[71] Rosendahl, U., Ohlhoff, A., Dreyer, M. E., and Rath, H. J. Investigation of forced liquid flows in open capillary channels. Microgravity Sci. Technol. 13, 4 (2002), 53–59.

[72] Rusche, H. Computational Fluid Dynamics of Dispersed Two-Phase Flows at High Phase Fractions. PhD thesis, University of London, Imperial College of Science, Technology and Medicine, Department of Mechanical Engineering, 2002.

[73] RUYTERS, G., AND FRIEDRICH, U. From the Bremen drop tower to the International Space Station ISS - ways to weightlessness in the German space life sciences program. Signal Transduction 6 (2006), 397–405.

[74] SAFAVIEH, R., AND JUNCKER, D. Capillarics: pre-programmed, self-powered microfluidic circuits built from capillary elements. Lab Chip 13 (2013), 4180–4189.

[75] SAHA, A., MITRA, S., TWEEDIE, M., ROY, S., AND MCLAUGHLIN, J. Experimental and numerical investigation of capillary flow in SU8 and PDMS microchannels with integrated pillars. Microfluidics and Nanofluidics 7, 4 (2009), 451–465.

[76] SALIM, A., COLIN, C., AND DREYER, M. Experimental investigation of a bubbly two-phase flow in an open capillary channel under microgravity conditions. Microgravity Sci. Technol. 22, 1 (2010), 87–96.

[77] SALIM, A., COLIN, C., GRAH, A., AND DREYER, M. E. Laminar bubbly flow in an open capillary channel in microgravity. Int. J. Multiphas. Flow 36, 9 (2010), 707–719.

[78] SCHLICHTING, H. Boundary Layer Theory. Springer-Verlag, 2000.

[79] SPARROW, E. M., HIXON, C. W., AND SHAVIT, G. Experiments on laminar flow development in rectangular ducts. J. Basic Eng.-T. ASME 89 (1967), 116–124.

[80] SPARROW, E. M., LIN, S. H., AND LUNDGREN, T. S. Flow development in the hydrodynamic entrance region of tubes and ducts. Phys. Fluids 7, 3 (1964), 338–347.

[81] SPIVEY, R. A., SHEREDY, W. A., AND FLORES, G. An overview of the Microgravity Science Glovebox (MSG) facility, and the gravity-dependent phenomena research performed in the MSG on the International Space Station (ISS). In 46th AIAA Aerospace Sciences Meeting and Exhibit (Reno, Nevada, 2008), AIAA, pp. 1–18.

[82] SRINIVASAN, R. Estimating zero-g flow rates in open channels having capillary pumped vanes. Int. J. Numer. Meth. Fl. 41, 4 (2003), 389–417.

[83] SRINIVASAN, V., SALAZAR, A. J., AND SAITO, K. Modeling the disintegration of modulated liquid jets using volume-of-fluid (VOF) methodology. Applied Mathematical Modelling 35, 8 (2011), 3710 – 3730.

[84] SUMAN, B., AND KUMAR, P. An analytical model for fluid flow and heat transfer in a micro-heat pipe of polygonal shape. Int. J. Heat Mass Transfer 48, 21-22 (2005), 4498 – 4509.

[85] Teles, J., Samii, M., and Doll, C. Overview of TDRSS. Advances in Space Research 16, 12 (1995), 67 – 76.

[86] Thom, A. The flow past circular cylinders at low speeds. Proceedings of the Royal Society of London. Series A, Containing Papers of a Mathematical and Physical Character 141, 845 (1933), 651–669.

[87] Ubbink, O. Numerical prediction of two fluid systems with sharp interfaces. PhD thesis, University of London, Imperial College of Science, Technology and Medicine, Department of Mechanical Engineering, 1997.

[88] Ubbink, O., and Issa, R. A method for capturing sharp fluid interfaces on arbitrary meshes. J. Comput. Phys. 153, 1 (1999), 26 – 50.

[89] van der Wijngaart, W. Capillary pumps with constant flow rate. Microfluidics and Nanofluidics 16, 5 (2014), 829–837.

[90] Vazquez, M., and Paull, B. Review on recent and advanced applications of monoliths and related porous polymer gels in micro-fluidic devices. Analytica Chimica Acta 668, 2 (2010), 100 – 113.

[91] Vosughian, B. Surface waves in open capillary channels under conditions of microgravity. Bachelor Thesis, University of Bremen, Germany, 2012.

[92] Warsi, Z. Fluid Dynamics. Theoretical and Computational Approaches. CRC Press, 1999.

[93] Weislogel, M. M., and Collicott, S. H. Capillary rewetting of vaned containers: Spacecraft tank rewetting following thrust resettling. AIAA J. 42, 12 (2004), 2551–2561.

[94] Weislogel, M. M., Jenson, R. M., Chen, Y., Collicott, S. H., Bunnell, C. T., Klatte, J., and Dreyer, M. E. Postflight summary of the Capillary Flow Experiments aboard the International Space Station. In 59th International Astronautical Congress-2008 (2008), pp. 1–11.

[95] Weislogel, M. M., and Lichter, S. Capillary flow in an interior corner. J. Fluid Mech. 373 (1998), 349–378.

[96] Weislogel, M. M., Thomas, E. A., and Graf, J. C. A novel device addressing design challenges for passive fluid phase separations aboard spacecraft. Microgravity Sci. Technol. 21, 3 (2009), 257–268.

[97] Weller, H. G., Tabor, G., Jasak, H., and Fureby, C. A tensorial approach to computational continuum mechanics using object-oriented techniques. Computers in physics 12, 6 (1998), 620–631.

[98] White, F. M. Fluid Mechanics. McGraw Hill, 2006.

[99] White, F. M. Viscous Fluid Flow. McGraw Hill, 2006.

[100] Zhang, J., Watson, S. J., and Wong, H. Fluid flow and heat transfer in a dual-wet micro heat pipe. J. Fluid Mech. 589 (2007), 1–37.

[101] Zimmermann, M., Schmid, H., Hunziker, P., and Delamarche, E. Capillary pumps for autonomous capillary systems. Lab Chip 7, 1 (2007), 119–125.